Aus dem Institut für Stammzellforschung
Helmholtz-Zentrum München
und
Aus dem Physiologischen Institut
Lehrstuhl: Physiologische Genomik
der Ludwig-Maximilians-Universität München

Direktorin: Prof. Dr. Magdalena Götz

Dissection and identification of cellular contexts that determine sensitivity to ferroptosis in human mammary epithelial cells and breast cancer

Dissertation
zum Erwerb des Doktorgrades der Naturwissenschaften
an der Medizinischen Fakultät
der Ludwig-Maximilians-Universität zu München

vorgelegt von
Elena Panzilius

aus
Karaganda, Kasachstan

2019

Mit Genehmigung der Medizinischen Fakultät
der Universität München

Betreuerin: Prof. Dr. rer. nat. Magdalena Götz

Zweitgutachterin: Prof. Dr. rer. nat. Regina Fluhrer

Dekan: Prof. Dr. med. dent. Reinhard Hickel

Tag der mündlichen Prüfung: 20.04.2020

Parts of this thesis have been published as a pre-print on bioRxiv
(Panzilius et al., 2018)

Dedicated to my mother

Table of contents

Summary

Breast cancer is the most frequently diagnosed cancer and the leading cause of cancer-related death among women. When metastatic disease is present, i.e. where cancer cells disseminate and start proliferating in distant organs, treatment options remain very limited. Ferroptosis is a newly identified form of regulated, iron-dependent cell death. Inhibition of the ferroptotic key enzyme glutathione peroxidase 4 (GPX4) induces the accumulation of high cellular levels of lipid hydroperoxides within cellular membranes, initiating signaling that ultimately leads to cell death. Recent studies begun to identify genetic and metabolic contributors to the execution of ferroptosis. However, the exact molecular determinants that dictate sensitivity of cells to ferroptosis in different cellular contexts remain unclear.

In my thesis, I set out to study ferroptosis in human mammary epithelial cells (HMECs). Thus, my goal was to determine whether ferroptosis plays a role during metastatic progression, thereby testing whether targeted induction of ferroptosis might provide a new therapeutic strategy specifically against advanced breast cancer. Therefore, I initially set out to assess how induction of the Epithelial-Mesenchymal Transition (EMT) impacts ferroptosis sensitivity. EMT is a process implicated in tumor progression and metastasis which is orchestrated by pleiotropic transcription factors such as TWIST1. Instead of identifying a link between EMT and ferroptosis, I discovered that cell density, or more specifically proximity determined by seeding density, is a critical factor determining sensitivity to ferroptosis irrespective of cellular state. More precisely, low cell-seeding density sensitized cells to ferroptosis while high cell-seeding density, resulting in high cell-cell proximity, induced resistance. Experiments with ferroptosis inhibitors like Liproxstatin-1 and Ferrostatin-1, and genetic interference with GPX4 confirmed ferroptosis as the cell death-modality. Moreover, I discovered that cell density-dependent ferroptosis is an intrinsic trait of primary HMECs that occurs irrespective of the immortalization process and oncogenic signaling (i.e. $HRAS^{G12V}$ and HER2/Neu). Furthermore, cell density-dependent ferroptosis could be observed in more physiological conditions as well (i.e. low oxygen pressure and three-dimensional organoid culture). Further, by using an E-cadherin neutralizing antibody and by co-culture experiments, I excluded cell-cell adhesion signaling as well as secreted factors as mediators of ferroptosis resistance at high cell densities. Although I was able to unequivocally

demonstrate that cell proximity dictates ferroptosis sensitivity, elucidation of the exact mechanism of proximity-sensing constitutes the aim for future studies. By conducting a proteomics screen which assessed regulated protein levels affected both by cell density and upon GPX4-inhibition, I discovered adipose triglyceride lipase (ATGL) as a determinant of cell density-dependent ferroptosis. In particular, ATGL-upregulation by low cell density triggered the lipolytic breakdown of fatty acids (FAs) from triacylglycerides stored in lipid droplets. Then, I elucidated that low cell density induces a metabolic switch to fatty acid oxidation which is fueled by ATGL-liberated FAs. This in turn, increased lipid-mediated stress at low density inducing a vulnerable cell state towards GPX4 inhibition.

In conclusion, cell density as a predictor of ferroptosis sensitivity in HMECs has implications for considering ferroptosis as treatment modality for cancer. Hence, single, disseminated cancer cells and small cancer cell clusters might be targeted by inducing ferroptosis during early stages of metastasis and before the onset of outgrowth of dormant cancer cells. Future studies will determine whether the mechanism of low cell density ferroptosis also has a physiological role to protect epithelial tissue maintenance as well as a role in other cellular contexts *in vivo*, where cells are disseminated, i.e. during neural crest migration.

Zusammenfassung

Brustkrebs ist sowohl die am häufigsten, diagnostizierte Krebsart als auch die häufigste, krebsbedingte Todesursache bei Frauen. Sobald Metastasen festgestellt werden, d.h. wenn sich Krebszellen verteilen und in anderen Organen zu wachsen beginnen, sind die Behandlungsmöglichkeiten stark eingeschränkt. Ferroptose ist eine neu entdeckte, regulierte Zelltodart, die Eisen-abhängig ist. Die Hemmung des ferroptotischen Schlüsselenzymes Glutathionperoxidase 4 (GPX4) führt zur Anhäufung von Phospholipid Hydroperoxiden in Zellmembranen, wodurch eine Signalkaskade eingeleitet wird, die letztendlich zum Zelltod führt. Jüngste Studien haben genetische und metabolische Regulatoren während des Ferroptose Prozesses untersucht. Allerdings sind die genauen molekularen Faktoren, die die Ferroptose-Sensitivität in unterschiedlichen zellulären Kontexten bestimmen, weitgehend unbekannt.

Ziel meiner Arbeit war die Untersuchung von Ferroptose in humanen Brust-epithelzellen (HMECs). Dabei wurde geklärt, ob Ferroptose während der Metastasierung eine Rolle spielt und ob die gezielte Aktivierung von Ferroptose eine neuartige Behandlungsmöglichkeit von fortgeschrittenem Brustkrebs darstellen könnte. Zu Beginn wurde untersucht, wie sich die Aktivierung der Epithelialen-Mesenchymalen Transition (EMT) auf Ferroptose-Sensitivität auswirkt. EMT ist ein Prozess, der mit Tumorprogression und Metastasierung assoziiert wird und durch pleiotrope Transkriptionsfaktoren, wie zum Beispiel TWIST1, reguliert wird. Ein direkter Zusammenhang zwischen EMT und Ferroptose konnte nicht gezeigt werden. Stattdessen wurde, unabhängig vom zellulären Phänotyp, die Zelldichte und die daraus resultierende Nähe der Zellen zueinander als entscheidendes Kriterium für Ferroptose-Sensitivität identifiziert. Dabei zeigte sich, dass Zellen in niedriger Zelldichte Ferroptose-sensitiv sind, wohingegen eine hohe Zelldichte zu Resistenz gegenüber Ferroptose führt. Durch Experimente mit Ferroptose-Hemmern, wie zum Beispiel Liproxstatin-1 und Ferrostatin-1, und durch genetische Manipulation von GPX4 wurde Ferroptose als Zelltodart bestätigt. Darüber hinaus wurde festgestellt, dass Zelldichte-abhängige Ferroptose eine intrinsische Eigenschaft von primären HMECs ist, die unabhängig vom Immortalisierungsprozess und onkogenen Signalkaskaden (wie zum Beispiel $HRAS^{G12V}$ und HER2/Neu) ist. Zudem kann Zelldichte-abhängige Ferroptose unter

physiologischeren Konditionen, wie zum Beispiel bei niedrigem Sauerstoffdruck und in drei-dimensionalen Organoidkulturen, beobachtet werden. Mit Hilfe eines E-cadherin neutralisierenden Antikörpers und Ko-Kulturen wurden Zell-Zell-Adhesion und sezernierte Faktoren als Vermittler von Ferroptose-Resistenz bei hoher Zelldichte ausgeschlossen. Obwohl gezeigt werden konnte, dass die Zelldichte und die damit resultierende Nähe der Zellen zueinander Ferroptose-Sensitivität bestimmt, bleiben die genauen Mechanismen, wie Zellen diese Nähe signalisiert wird, Bestandteil weiterführender Studien. Mittels einer Proteomik-Analyse wurden Proteine bestimmt, die sowohl durch die Zelldichte als auch durch GPX4-Hemmung reguliert wurden. Hierbei wurde die Adipozyten-Triglycerid-Lipase (ATGL) als ein Regulator der Zelldichte-abhängigen Ferroptose identifiziert. In niedriger Zelldichte wurde ATGL hochreguliert, was wiederum zum lipolytischen Abbau von Fettsäuren aus Triacylglyceriden führte, welche in Lipidtropfen gespeichert werden. Durch die ATGL-vermittelte Fettsäuremobilisierung wurde der zelluläre Stoffwechsel bei niedriger Zelldichte vermehrt auf Fettsäureoxidation umgestellt. Dadurch erhöhte sich der Lipid-induzierte Stress, welcher zu einem Anstieg der Sensitivität der Zellen gegenüber GPX4-Hemmung führte.

Zusammenfassend wurde die Zelldichte als Indikator für Ferroptose-Sensitivität von HMECs identifiziert. Darauf basierend könnte man Ferroptose als eine mögliche Krebsbehandlungsmodalität in Betracht ziehen. Hierbei könnten einzelne, disseminierte Krebszellen sowie kleine Gruppen von Krebszellen durch das Auslösen von Ferroptose während frühen Stadien der Metastasierung am Auswachsen gehindert werden. Zukünftige Studien werden zeigen, ob der Ferroptosemechanismus, induziert durch niedrige Zelldichte, eine physiologische Rolle beim Schutz von epithelialen Geweben spielt. Weiterhin ist es von Interesse herauszufinden, ob dieser Mechanismus auch in anderen zellulären Kontexten *in vivo* bedeutsam ist, bei denen disseminierte Zellen vorzufinden sind, wie zum Beispiel während der Neuralleistenmigration.

Abbreviations

°C	Degree Celsius
µ	micro
2D/3D	2/3 dimensional
7-AAD	7-Aminoactinomycin D
A	Ampere
Å	Ångström
AA	Arachidonic acid
ABDH5	1-acylglycerol-3-phosphate O-acyltransferase
ACC-1	Acetyl-CoA Carboxylase 1
ACSF2	Acyl-CoA synthetase family member 2
ACSL4	Acyl-CoA synthetase long chain family member 4
AdA	Adrenic Acid
AKR1C	Aldo-Keto Reductase Family 1 Member
AKT	Protein kinase B
AMPK	AMP-activated protein kinase
ANT	adenine nucleotide translocase
APS	Ammonium peroxydisulphate
Atg	Autophagy-related gene
ATGL	Adipose triglyceride lipase
ATGLi	Atglistatin
ATM	ATM serine/threonine kinase
ATP	Adenosine triphosphate
B+	CD10-positive basal cell
BACE1	β-site amyloid precursor protein cleavage enzyme 1
BL	Burkitt' Lymphoma
BL1/2	Basal-like 1/2
Blast	Blastidicin
bp	Base pair
BPE	Bovine Pituitary Extract
BRCA	Breast Cancer, early onset
BSA	Bovine serum albumin
BSL	Biosafety level
BSO	L-buthionine sulfoximine
BVR	biliverdin reductase
cAMP	cyclic adenosine monophosphate
CARS	Cysteinyl-tRNA synthetase
Cas	CRISPR associated
Casp3	Caspase 3
CDH1	Cadherin 1
cDNA	complementary DNA
CH	Cumene hydroperoxide
cm	Centimeter
CMA	chaperone-mediated autophagy

CMV	Cytomegalovirus
CO2	carbon dioxide
CoA	Coenzyme A
CoQ_{10}	Coenzyme Q_{10}
CPT1A	Carnitine Palmitoyltransferase 1A
CPX	Ciclopirox
CRISPR	Clustered regularly interspaced short palindromic repeats
CS	Citrate synthase
Ct	Cycle threshold
CTC	Circulating tumor cells
CTG	CellTiter-Glo
Ctrl	Control
d	days
DAG	Diacylglycerol
DAPI	4′,6-diamidino-2-phenylindole
DAVID	Database for Annotation, Visualization and Integrated Discovery
DCIS	Ductal carcinoma in situ
DDA	Data dependent
DFO	Deferoxamine
DGAT-1	Diacylglycerol acyltransferase1
DLBCL	Diffuse large B cell lymphoma
DMEM	Dulbecco's Modified Eagle Medium
DMEM/F12	Dulbecco's Modified Eagle Medium F-12 Nutrient Mixture
DMSO	Dimethyl sulfoxide
DMT1	Divalent metal transporter 1
DNA	Deoxyribonucleic acid
DNase	Deoxyribonuclease
dNTP	Deoxyribonucleotide
Dox	Doxycycline
DOXO	Doxorubicin
DPYD	dihydropyrimidine dehydrogenase
DS	Donkey serum
dT	Deoxythymine
DTNB	5,5′-Dithiobis(2-nitrobenzoic acid)
EB	Elution buffer
E-cad	E-cadherin
ECL	Enhanced chemoluminescence
ECM	Extracellular matrix
EDTA	Ethylendiaminetetraacetic acid
EGF	Epidermal Growth Factor
EMT	Epithelial-Mesenchymal Transition
ER	Estrogen receptor
ERA	Erastin
ERK	Extracellular signal-regulated kinase
ESR1	Estrogen receptor 1

ETC	electron transport chain
Ex	Exon
FA	Fatty Acid
FACS	Fluorescent-activated cell sorting
FAO	fatty acid oxidation
FASP	Filter-aided sample preparation
FCS	Fetal calf serum
FDR	False discovery rate
Fe^{2+}	ferrous iron
Fe^{3+}	ferric iron
Fer1	Ferrostatin-1
FIN	Ferroptosis-inducing agent
FOXA1	Forkhead Box A1
FBP1	Fructose-1,6-biphosphatase
Fsk	Forskolin
FTH1	Ferritin heavy chain 1
FTL	Ferritin light chain
fwd	forward
g	Gram
g	Gravitational force
GATA3	GATA Binding Protein 3
GC	Guanine-Cytosine
GCL	Glutamate-cysteine ligase
GCLC	Glutamate-cysteine ligase catalytic subunit
gDNA	genomic DNA
GFP	Green fluorescent protein
GO-term	Gene ontology term
GPX4	Glutathione peroxidase 4
gRNA	guide RNA
GSH	Glutathione
GSS	Glutathione synthetase
GSSG	Glutathione disulfide
h	hours
H+L	Heavy and light chain
HCC	Hepatocellular carcinoma cell lines
HCl	hydrochloric acid
HEPES	N-2-hydroxyethylpiperazine-N-2-ethane sulfonic acid
Her2/neu	Human epidermal growth factor receptor 2
HF	high-fidelity
hGX sPLA2	human group X secreted phospholipase
hi	high
HMEC	Human mammary epithelial cells
HMLE	Immortalized human mammary epithelial cells
HMOX1/2	Heme oxygenase 1/2
HPLC	High-performance liquid chromatography
HR	Hormone receptor

HRP	Horseradish peroxidase
HSL	Hormone-sensitive lipase
hTERT	Human telomerase reverse transcriptase
HTwist1	HMLE-Twist1
hU6	human U6 promoter
i.e.	id est: that is
I/R	Ischemia/reperfusion
IBC	Invasive breast cancer
IC50	Inhibitory concentration 50
ID	Inner diameter
IDC	Invasive ductal carcinoma
IgG	Immunoglobulin G
IREB2	Iron response element binding protein 2
IRES	Internal ribosomal entry site
IU	International enzyme unit
kb	Kilo base
KCl	Potassium chloride
kDA	Kilo Dalton
KO	Knockout
KRT18	Keratin 18
l	liter
LAA	alkyne-modified linoleic acid
LAR	Luminal androgen receptor
LB	Lysogeny broth
LD	Lipid Droplet
LDAH	LD-associated hydrolase
LIP	Labile iron pool
Lip1	Liproxstatin-1
LKB1	Liver Kinase B1
log2	Binary logarithm
L-OOH	Lipid hydroperoxides
LOX	Lipoxygenase
LP	Luminal progenitor
LPCAT3	Lysophosphatidylcholine acyl-transferase 3
M	Molar
m	milli
m/v	mass/volume
m/z	mass-to-charge ratio
MAGL	Monoacylglycerol lipase
MAPK	mitogen-activated protein kinase
MDA157	MDA-MB-157
MDA231	MDA-MB-231
MDA468	MDA-MB-468
MECGM	Mammary epithelial cell growth medium
med	intermediate
MEF	Mouse embryonic fibroblast

MEK	Mitogen-Activated Protein Kinase Kinase
MET	Mesenchymal-Epithelial Transition
Milli-Q	Ultrapure water
min	Minutes
miR-200	microRNA 200 family
Mito	Mitochondrial
MOI	Multiplicity of infection
mRNA	messenger RNA
MS	Mass spectrometry
MS/MS	Tandem mass spectrometry
mTOR	Mammalian target of rapamycin
n	number
n	nano
n.d.	not detected
n.s.	not significant
N20	20-nucleotide
NaCl	Sodium chloride
NADPH	reduced Nicotinamide adenine dinucleotide phosphate
NaOH	sodium hydroxide
NCOA4	Nuclear receptor coactivator 4
Nec1-S	7-Cl-O-Nec1 (Necrostatin1-S)
nm	Nanometer
NP40	Nonidet P40
NQO1	Quinone oxidoreductase-1
NRF2	Nuclear factor erythroid 2-related factor 2
NSCLC	Non-small cell lung cancer
nt	nontargeting
O_2	Oxygen
OA	Oleic Acid
OE	Overexpression
Oligo	Oligonucleotide
ON	over night
OXPHOS	Oxidative phosphorylation
p	phospho
p53	Tumor suppressor 53
PARP	Poly(ADP-ribose) polymerase
PBS	Phosphate buffered saline
PC	PromoCell
PCOOH	Phosphatidylcholine hydroperoxide
PCR	Polymerase chain reaction
pCR	Pathologic complete response rate
PE	Phosphatidylethanolamine
PEI	Polyethleneimine
Pen/Strep	Penicillin/Streptomycin
PFA	Paraformaldehyde

PGC-1α	Peroxisome proliferator-activated receptor gamma coactivator 1 alpha
PI	Propidium Iodide
PI3K	phosphoinositide 3-kinase
PIK3CA	Phosphatidylinositol-4,5-Bisphosphate 3-Kinase Catalytic Subunit Alpha
PKA	Protein kinase A
PLIN	Perilipin
PNPLA2	Patatin Like Phospholipase Domain Containing 2 (ATGL)
PPAR	peroxisome proliferator-activated receptor
PR	Progesterone receptor
PTEN	Phosphatase and tensin homolog
PUFA	Polyunsatured fatty acid
Puro	Puromycin
PVDF	Polyvinylidene fluoride
PyMT	Polyoma middle T antigen
QE	Q Exactive
qPCR	real-time semi-quantitative PCR
RB	Retinoblastoma
rev	reverse
RFP	Red fluorescent protein
RIPA	Radioimmunoprecipitation assay
RIPK1	Receptor-interacting serine/threonine-protein kinase 1
RISC	RNA-induced silencing complex
RLU	Relative light units
RNA	Ribonucleic acid
RNase	Ribonuclease
ROS	Reactive oxygen species
ROSI	Rosiglitazone
RPL32	Ribosomal protein 32
rpm	revolutions per minute
RSL3	(*1S,3R*)-Ras selective lethal 3
RT	Room temperature
−RT	without reverse transcriptase
SCC	Single-cell clone
SCD	Stearoyl-CoA Desaturase
SD	Standard deviation
SDS-Page	Sodium dodecyl sulfate polyacrylamide gel electrophoresis
sec	Seconds
SEM	Standard error of the mean
Ser	Serine
sgRNA	Single guide RNA
sh-GPX4	shRNA against GPX4
sh-nt	shRNA nontargeting
shRNA	short hairpin RNA
SIRT1	Sirtuin1

SLC7A11	Solute Carrier Family 7 Member 11
SOD	Superoxide dismutase
StagR	String assembly gRNA
STEAP	Six-transmembrane epithelial antigen of prostate protein family
SV40	Simian Virus 40
TAE	Tris-acetate-EDTA
TAG	Triacylglyceride
TAM	4-Hydroxytamoxifen
TBS	Tris-buffered saline
TBS/T	Tris-buffered saline with Tween-20
TCA	Trichloroacetic acid
TE	Tris-EDTA
TEMED	Tetramethylendiamine
TF	Transcription factor
TF	Transferrin
TFR1	Transferrin receptor 1
TNB^-	2-nitro-5-thiobenzoate
TNBC	Triple-negative breast cancer
TNS	Trypsin Neutralizing Solution
TP53	Tumor protein p53
tRNA (Sec)	selenocysteine tRNA
TU	Transduction Unit
TXNRD1	Thioredoxin reductase 1
TZN	Thiazolidinedione
U	Units
UV	Ultraviolet
V	Voltage
v/v	Volume fraction (volume/volume)
vs	versus
VSV-G	Vesicular stomatitis Indiana virus glycoprotein
WT	Wildtype
Zeb1/2	Zinc finger E-box-binding homeobox 1/2
zVAD	zVAD-fmk
α-Toc	α-Tocopherol
Δ	Delta
λ	Lambda, wavelength

1 Introduction

1.1 Breast cancer

1.1.1 Epidemiology

The most frequently diagnosed cancer among women worldwide is breast cancer with an estimated number of almost 2.1 million new cases in 2018, accounting for approximately 25% of all cancers in women (Bray et al., 2018). Breast cancer is the main cause of cancer-related death in women, leading to about 0.7 million cases of death with higher relative mortality rates in less developed countries (Bray et al., 2018). Lower mortality rates were linked to early diagnosis, for example by screening mammography, and the application of adjuvant treatment (Berry et al., 2005; Richards et al., 1999). While localized breast cancer shows a 5-year survival rate of almost 100% (Noone et al., 2017), advanced disease and the presence of distant metastases decrease 5-year survival rates of women below 20% (Allemani et al., 2013). Therefore, it is very important to predict the progression of the disease and apply beneficial treatment.

1.1.2 Heterogeneity in breast cancer

1.1.2.1 Intertumor heterogeneity

Breast cancer is a highly heterogeneous disease at the clinical, histopathological and molecular level (Zardavas et al., 2015). Main clinical parameters include age, axillary lymph node status, tumor size and histological grade, but also the expression status of histological markers such as estrogen receptor (ER), progesterone receptor (PR) and human epidermal growth factor receptor 2 (HER2) (Schnitt, 2010). The mammary gland is composed of a complex network of epithelial branching ducts arising from the nipple and terminating in alveoli which expand and produce milk during pregnancy. Thereby, luminal epithelial cells face the inner lumen of the ducts and alveoli while contractile myoepithelial, also termed basal cells, are located at an outer position next to the basement membrane. This network is embedded in stroma consisting of adipocytes, fibroblasts, endothelial cells and immune cells (Visvader, 2009). At the histopathological level, most breast cancers are divided either into in situ carcinoma, where cancer cells expand within the ducts or alveoli, or into invasive, infiltrating carcinoma, where cancer cells have broken through the basement and grown into the adjacent stroma. Invasive breast cancer

(IBC) accounts for 80% of diagnosed breast cancer (American Cancer Society, 2017). The majority of invasive breast cancer arise within the ducts (73.4%) and only about 10% arise in the lobules (alveoli cluster) or show a mixed ductal/lobular phenotype (Noone et al., 2017). Another level of heterogeneity at the biological level is added by the classification into molecular subtypes. Global gene expression profiling of human breast cancer samples revealed five molecular intrinsic subtypes: luminal A, luminal B, normal breast-like, HER2-enriched and basal-like (Perou et al., 2000; Sørlie et al., 2001, 2003). Luminal A and B breast cancer belong to the group of ER-positive cancer which account for approximately 80% of IBC and are characterized by the expression of a gene signature of luminal mammary epithelial cells like *ESR1* (encoding for ER), *GATA3*, *FOXA1* and *KRT18* (American Cancer Society, 2017; Perou et al., 2000; Sørlie et al., 2001). However, a distinct proliferation signature signifying luminal B subtype, for example, high KI67 expression, discriminates luminal A and B subtypes, directly relating to a poorer outcome of luminal B classified tumors (Hu et al., 2006; Perou et al., 1999; Sørlie et al., 2003). Both HER2-enriched and basal-like tumors display low expression of ER and ER-associated genes and are associated with poorer survival than luminal A tumors (Sørlie et al., 2001, 2003). The HER2-enriched subset is a rare group of IBC (5%) amplified in the *HER2* locus and therein associated genes (American Cancer Society, 2017; Perou et al., 2000; Sørlie et al., 2001). A gene signature associated with basal epithelial cells like expression of cytokeratin 5 and 7 or laminin defines the basal-like subtype (Perou et al., 2000; Sørlie et al., 2001). The normal-breast like subtype showed a distinct gene expression pattern characterized by high expression of basal epithelial genes and genes associated with adipose tissue and non-epithelial cell types (Sørlie et al., 2001). Further, the claudin-low subtype as another molecular subtype was described for both human and murine breast cancer data sets characterized by low expression of tight junction proteins claudin 3,4 and 7 as well as E-cadherin (E-cad), an important cell adhesion protein, but was enriched for the expression of mesenchymal and stem cell markers (Herschkowitz et al., 2007; Prat et al., 2010). Clinically, IBC lacking hormone receptor- (HR) and HER2-expression are grouped as triple-negative breast cancer (TNBC), occurring in approximately 12% of cases (American Cancer Society, 2017). At the molecular level, most TNBCs are classified as the basal-like subtype (70-80%) (Koboldt et al., 2012; Sabatier et al., 2014). However, within the claudin-low subtype, about 50% of

tumors are also TNBC and have a poor prognosis similar to that of basal-like tumors (Sabatier et al., 2014). In general, apart from the molecular subtype, tumors classified as TNBC are more likely to be associated with a higher stage and risk for metastases, thus resulting in a worse prognosis and reduced overall survival compared to HR+ tumors (Lin et al., 2012). Within the clinical group of TNBC tumors, another study identified six different TNBC subtypes based on gene expression profiling that were refined into four different TNBC subtypes five years later showing distinct sensitivities to chemotherapy (Lehmann et al., 2016, 2011). Along these lines, further genomic and transcriptomic analyses of about 2000 breast cancer samples through the Molecular Taxonomy of Breast Cancer International Consortium (METABRIC) yielded ten different subtypes with distinct disease-free survival probabilities (Curtis et al., 2012), adding further complication to breast cancer classification and heterogeneity. In contrast, the Cancer Genome Atlas Network (TCGA) combined integrative information on primary breast cancer samples derived by different molecular techniques (genomic DNA copy number arrays, DNA methylation, exome sequencing, messenger RNA arrays, microRNA sequencing and reverse-phase protein arrays) and thereby, portrayed four main breast cancer classes (Luminal A and B, HER2-enriched and Basal-Like) that were highly heterogeneous within each class. Importantly, while only a few genes such as *TP53*, *PIK3CA* or *GATA3* were frequently mutated across all breast cancer patients (>10%), subtypes were enriched for these mutations. For example, *PIK3CA* is mutated in half of luminal A tumors and only in 7% of basal-like tumors which harbor a *TP53* mutation at a high frequency (84%) in contrast to luminal A tumors (12%) (Koboldt et al., 2012). Together, these data indicate a tremendous intertumor heterogeneity of breast cancer linked to different treatment and prognostic outcome implying the need for precise patient stratification.

1.1.2.2 Intratumor heterogeneity

Tumors are not only heterogeneous between different patients, but can be also heterogeneous within one patient at a spatial and temporal level. Recent studies analyzing different areas at the genetic level in breast cancer samples identified several clonal cell lineages present within one tumor. Matched lymph node metastases showed further genomic variability (Ellsworth et al., 2015; Torres et al., 2007). A more detailed study showed that clonal subpopulations could be located in

distinct areas or be intermixed within the tissue (Navin et al., 2010). Single-nucleus-sequencing of 100 cells from one polygenomic TNBC suggested the emergence of three clonal expansions at an early stage with subsequent genetic variations. Thereby, intratumoral heterogeneity was illustrated by the presence of a KRAS-amplified subpopulation intermixed with one without KRAS amplification at the same anatomical area (Navin et al., 2011). With regard to frequently mutated genes in breast cancer such as *TP53* and *PIK3CA*, TNBCs showed a clonal dominance for these mutations, but low- and high clonal tumors with a diverse spectrum of mutations could exist as well (Shah et al., 2012). Further, the appearance of both ductal carcinoma in situ (DCIS) and invasive ductal carcinoma (IDC) components in the same breast cancer tissue sections reflects heterogeneity at the phenotypic level (Wong et al., 2010). Compared to size-matched pure IDC, DCIS-IDC were associated with less metastatic potential and lower proliferation (Wong et al., 2010). Interestingly, studies analyzing synchronous DCIS-IDC showed that they share some genetic similarities, but the progression from DCIS to IDC can also select for clones. For instance, *CDH1*, the gene coding for E-cadherin, was most commonly lost, while, at the same time, *MYC*-amplified clones emerged (Hernandez et al., 2012; Heselmeyer-Haddad et al., 2012). Temporal intratumoral heterogeneity can also arise as a consequence of innate tumor progression from primary to metastatic disease or due to therapeutic interventions. Therapy-naïve primary breast cancer and synchronous metastases shared 60% of somatic mutations, especially frequently mutated genes like *TP53*, *PIK3CA* and *GATA3*, but gained additional mutational burden, for example affecting genes related to the epithelial-mesenchymal transition (EMT), a process implied in metastasis (Ng et al., 2017). Similarly, metastases detected 9 years after the removal of primary lobular breast cancer had acquired a significant amount of novel somatic coding mutations compared to the primary tumor while only some mutations, present in minor subclones of the primary tumor, were enriched in metastatic cells (Shah et al., 2009). Conclusively, intratumoral heterogeneity further complicates treatment since sensitivities towards therapeutic interventions might greatly differ between subclones and therefore, one general treatment regimen might not fit for the whole tumor.

1.2 Breast cancer treatment

Currently, IBC is removed by surgery followed by radiation therapy. To reduce the risk of recurrence or if metastatic disease is present at diagnosis, chemotherapy, anti-hormone therapy and/or targeted therapy are applied at a systemic level (American Cancer Society, 2017). Both radiation and chemotherapy induce unspecific DNA damage like double-strand breaks or DNA crosslinks, which ultimately lead to cell death if they accumulate (Cheung-Ong et al., 2013; Lomax et al., 2013). In order to shrink the tumor prior to surgery, chemotherapy can be also applied in a neoadjuvant setting that does neither impact survival nor overall disease progression compared to surgery followed by adjuvant chemotherapy (Mauri et al., 2005). Since HR+ breast cancer patients express ER, these patients are eligible to targeted adjuvant endocrine therapy, including tamoxifen and aromatase inhibitor treatment, which modulate estrogen receptor effects and estrogen levels (American Cancer Society, 2017). For example, 5-year adjuvant tamoxifen therapy was shown to reduce recurrence risk by about 40% within the first ten years and mortality risk by one third within 15 years (Abe et al., 2011). Further, patients with HER2-amplified breast cancer benefit from a HER2-targeted therapy using specific anti-HER2 antibodies such as trastuzumab, thus inhibiting the highly proliferative and survival signaling induced by *HER2* amplification (Ménard et al., 2003). Addition of trastuzumab to chemotherapy reduced the risk of recurrence and death for early-stage as well as metastatic disease compared to adjuvant chemotherapy alone (Romond et al., 2005; Slamon et al., 2001). Since patients with TNBC lack expression of HR and HER2, therapy is mainly based on surgery, radiotherapy and chemotherapy (Wahba et al., 2015). Although pathologic complete response rates (pCR) to neoadjuvant chemotherapy are significantly higher in TNBC compared to non-TNBC (22% vs 11%) (Liedtke et al., 2008), TNBC generally display a more aggressive phenotype with a higher risk recurrence and reduced overall survival (Lin et al., 2012). However, if pCR is achieved, TNBC and non-TNBC patients have a similar prognosis irrespective of HR status (Guarneri et al., 2006; Liedtke et al., 2008). Importantly, distant relapse after therapy is still associated with poor survival without any superior improvement over the last decades (Tevaarwerk et al., 2013). Likewise, only a small proportion of patients (3.1%) with metastatic breast cancer at diagnosis showed a complete response to chemotherapy for more than 5 years (Greenberg et al., 1996). Since chemotherapy induces adverse side effects such

nausea, fatigue and hair loss, but can also impact the quality of life by inducing long-term effects such as cardiovascular toxicity or loss of fertility (Agrawal, 2014; Kayl and Meyers, 2006), recent studies aim to stratify patients to avoid over- or under-treatment. For example, gene expression profiling was employed to predict the occurrence of metastasis in breast cancer based on a 70-gene prognosis profile, linking it to a decreased overall 10-year survival and providing a strategy to stratify patients for beneficial adjuvant therapy (van 't Veer et al., 2002; van de Vijver et al., 2002). Along these lines, another study, predicting prognosis using a 21-gene expression profile, emphasized that HR-positive, HER2-negative breast cancer patients with low risk of recurrence do not benefit from additional adjuvant chemotherapy, but endocrine treatment alone is sufficient (Sparano et al., 2015). Accordingly, dividing TNBC into molecular subtypes further enabled to evaluate the probability of achieving a pCR by neoadjuvant chemotherapy (Lehmann et al., 2016, 2011). Exemplarily, TNBC belonging to the subgroup of basal-like 1 (BL1 and BL2) were shown to highly express genes involved in cell cycle and DNA damage response such as BRCA, therefore presenting a highly proliferative subtype which lost cell-cycle checkpoint control, but in turn increased DNA damage response. Accordingly, antimitotic chemotherapeutics such as paclitaxel and DNA-damaging agents such radiotherapy induced significantly higher pCR in TNBC patients with BL1 or BL2 subtypes than in a mesenchymal-like or luminal androgen receptor (LAR) TNBC subtype (Lehmann et al., 2011). In line with these data, chemical inhibition of poly(ADP-ribose) polymerase1 (PARP1), involved in DNA strand-break repair, specifically killed BRCA1-deficient tumors in mice (Rottenberg et al., 2008) and in combination with chemotherapy resulted in a better overall response rate and progression-free-survival compared to chemotherapy alone in a clinical trial with metastatic TNBC patients (O'Shaughnessy et al., 2009). Mutations in BRCA1 or BRCA2 have been linked to a higher risk of developing breast cancer (Easton et al., 1995; Ford et al., 1998) and since BRCA1 and 2 are involved in DNA double-strand break repair and PARP is a key enzyme therein, additional PARP inhibition further damages DNA and thereby induces cell cycle arrest and apoptosis (Bryant et al., 2005; Farmer et al., 2005). Although there are several compounds available for the treatment of breast cancer, targeted therapies, especially for TNBC, are still limited. Further, novel treatment strategies are urgently needed for recurrent breast cancer and metastatic disease since metastatic disease highly impacts survival.

1.3 Epithelial-Mesenchymal Transition is essential for developmental and pathological processes

The Epithelial-Mesenchymal Transition (EMT) is a process by which epithelial cells are transdifferentiated in a mesenchymal cell state. Epithelial cells show a cobblestone-like morphology with an apicobasal polarity and tight cell-cell adhesion. When EMT is induced, epithelial cells downregulate proteins involved in cell-cell adhesions like E-cadherin, thereby loose detachment to each other. Subsequently, mesenchymal proteins like N-cadherin or fibronectin are upregulated accompanied by the acquisition of a single, spindle-shaped and front-to-back polarized cell morphology. Additionally, EMT-converted mesenchymal cells gain migratory abilities that enable the invasion through the adjacent extracellular matrix (ECM) (Hay, 1995; Yang and Weinberg, 2008). The process of EMT was first observed and described for cell movements in the primitive streak in chick embryos (Hay, 1968; Trelstad et al., 1967). During embryonic gastrulation, leading to the development of the three germ layers (ectoderm, mesoderm and endoderm), epithelial cells invaginate at the primitive streak in the primitive ectoderm. After the reorganization of cellular shape and cell organelles, cells detach from the primitive streak by locally breaking the basement membrane and then migrate underneath the primitive ectoderm to form the mesoderm (Yang and Weinberg, 2008). Apart from mesoderm formation, EMT processes and its reverse process, mesenchymal-epithelial transition (MET), are crucial for neural crest formation and the generation of tissues like the pancreas, reproductive tracts and the heart (Thiery et al., 2009). However, EMT can be reactivated in both physiological processes like tissue regeneration and wound healing or during pathological processes such as fibrosis, cancer progression and metastasis (Kalluri and Weinberg, 2009; Thiery et al., 2009).

EMT programs enable epithelial cancer cells to detach from the primary tumor by loosening cell-cell adhesions and gaining the ability to break the basement membrane and invade into the adjacent stroma (Figure 1). Thereby, cancer cells obtain access to surrounding blood vessels which facilitate systemic dissemination. Extravasation at distant sites allows the formation of non-proliferating micrometastases which eventually grow out as detectable macrometastases (Scheel and Weinberg, 2012).

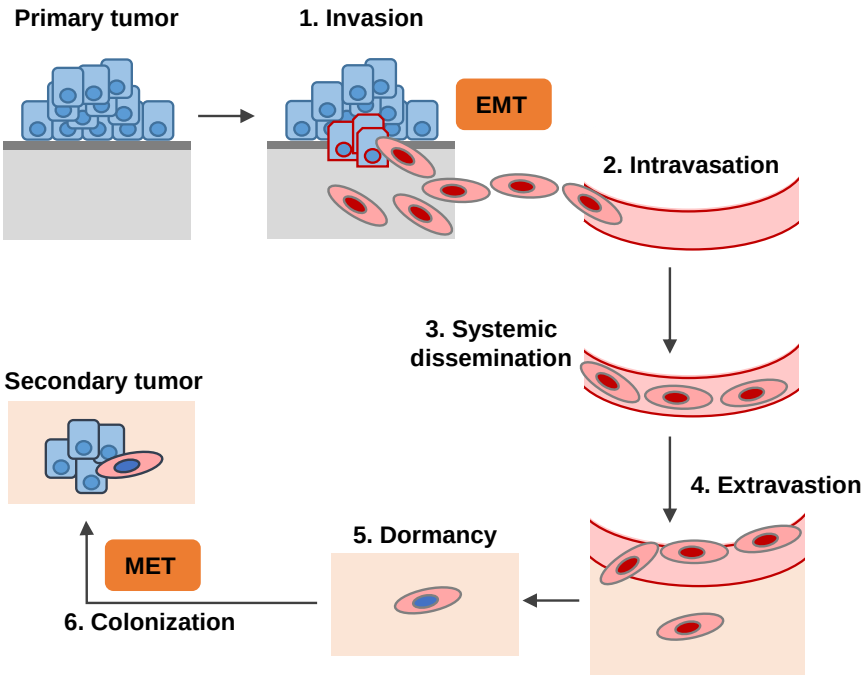

Figure 1: **The metastatic cascade**
Early steps of metastasis are enabled by the Epithelial-Mesenchymal Transition (EMT). During EMT, epithelial cancer cells (blue) are converted to invasive, migratory mesenchymal cells (red cells) that are able to invade into the surrounding tissue (grey) and intravasate into blood circulation. Upon systemic dissemination and extravasation at distant sites (beige), cells reside in a non-proliferating cell state (Dormancy). The outgrowth of cancer cells as secondary tumors is thought to require the reversion back to an epithelial cell state by the Mesenchymal-Epithelial-Transition (MET). Figure was adapted from (Scheel and Weinberg, 2012).

1.3.1 EMT in cancer progression and metastasis

The process of EMT is mediated by a group of transcription factors like TWIST1, SNAI1/2 (Snail1/Slug), ZEB1/2, Goosecoid and FOXC2 that interact together to induce phenotypic, transcriptional and functional changes. Together, they induce the repression of epithelial and upregulation of mesenchymal genes (De Craene and Berx, 2013). Thereby, E-cadherin (*CDH1*), the main component of epithelial cell-cell adherens junctions, is transcriptionally repressed by direct binding of EMT-TFs like Snail1, Slug, ZEB1 or ZEB2 to the *CDH1* promotor (Batlle et al., 2000; Cano et al., 2000; Comijn et al., 2001; Hajra et al., 2002; Shirakihara et al., 2007). Other EMT-TFs like TWIST1 induce EMT without directly binding to the *CDH1* promoter and instead mediate its repression through induction of other EMT-TFs such as Slug (Casas et al., 2011; De Craene and Berx, 2013). Further, epithelial dedifferentiation is accompanied by the downregulation of desmosomal junctions as well tight

junctional proteins like claudins by EMT-TFs (Cano et al., 2000; Ikenouchi et al., 2003; Martínez-Estrada et al., 2006; Moreno-Bueno et al., 2006; Vandewalle et al., 2005). In turn, mesenchymal markers, for example vimentin, N-cadherin and fibronectin, are upregulated, along with a gain in single cell motility and invasive capabilities (Cano et al., 2000; Casas et al., 2011; Shirakihara et al., 2007; Vandewalle et al., 2005; Yang et al., 2004). In several mouse models, forced expression of EMT-TFs induced the dissemination and the appearance of metastatic cells (Casas et al., 2011; Mani et al., 2007; Moody et al., 2005; Yang et al., 2004). Further, EMT-TF expression was observed at the invasive front of primary tumors formed in xenograft experiments (von Burstin et al., 2009; Cano et al., 2000) Similarly, loss of E-cadherin was shown to induce metastasis (Onder et al., 2008; Wendt et al., 2011). Mechanistically, early studies suggested that EMT leads to tumorigenic potential by conferring stem-cell-like traits to cells. Thereby, mesenchymal immortalized mammary epithelial cells (HMLE) undergoing EMT by EMT-TF activation acquired a $CD44^{high}/CD24^{-/low}$ cell surface profile which was associated with tumor-initiating capacity both *in vitro* and *in vivo* (Mani et al., 2008; Morel et al., 2008). A prior study showed that as few as 100 $CD44^{high}/CD24^{-/low}$ cells isolated from metastases of breast cancer patients engrafted in immunodeficient and –compromised mice and could be serially passaged in mice while $CD44^{+}/CD24^{+}$ cells failed to do so (Al-Hajj et al., 2003). However, there is recent experimental evidence that for successful outgrowth as macroscopically visible metastases, the reversion of the mesenchymal to an epithelial phenotype by MET is required at the distant site (Celià-Terrassa et al., 2012; Ocaña et al., 2012; Schmidt et al., 2015; Tsai et al., 2012), contrasting the stemness hypothesis. These observations are in line with clinical data showing that both primary tumors, as well as metastases of IDC, express E-cadherin, although expression was often weaker in the primary tumor compared to metastases (Bukholm et al., 2000; Jeschke et al., 2007; Kowalski et al., 2003). A decrease in E-cadherin levels could be explained by the finding that *CDH1* promotor hypermethylation is dynamically increased during malignant progression in primary ductal breast cancer (Graff et al., 2000; Nass et al., 2000; Shargh et al., 2014). However, there are also seemingly contradictory observations about EMT-TFs and EMT in patient samples. Another report associated Snail1 and Slug overexpression in primary breast cancer samples with lymph node metastasis, although Snail1 and Slug were shown to co-localize with E-cadherin-positive tumor

cells (Côme et al., 2006). Yet, in another study, nuclear Snail1 expression was linked to higher tumor grade, stage and size as well as lymph node metastasis. Further, high Snail1 expression correlated with basal-like subtypes and served as an independent prognostic factor for overall survival for luminal B and basal-like subtypes (Muenst et al., 2013). Along these lines, EMT marker genes were correlated with the basal-like subtypes of IBC (Sarrió et al., 2008), but were also shown to be enriched in claudin-low subtypes (Herschkowitz et al., 2007; Prat et al., 2010; Taube et al., 2010). Interestingly, recent data suggest that dissemination does not necessarily require a full EMT, i.e. repression of E-cadherin. For instance, Twist1 expression leads to disseminated mammary epithelial cells both in *in vitro* and *in vivo* without the repression of epithelial adherens junctions (Shamir et al., 2014). Similarly, circulating tumor cells (CTC) clusters are highly metastatic compared to single CTCs, whereby intracellular adhesion mediated by plakoglobin within these cluster is crucial for their metastatic ability (Aceto et al., 2014). These observations are in line with another report showing that cells of an oncogene-induced breast cancer mouse model (polyoma middle T antigen (PyMT) mice) spontaneously undergo EMT. However, both epithelial and mesenchymal cells have been shown to be equally able to form E-cadherin positive metastases, indicating a high plasticity of both cell states (Beerling et al., 2016).

1.3.2 Roles of EMT-TF beyond EMT

In a model of skin cancer, Twist1 expression was shown to be required for tumor initiation and p53-dependent apoptosis resistance, a programmed form of cell death, irrespective of E-cadherin repression. However, high levels of Twist1 were necessary for the malignant progression of benign tumors (Beck et al., 2015). Similarly, sequential Zeb1 induction following mutation of the tumor suppressor Retinoblastoma 1 (RB1) and tumor oncogene Ras were necessary to overcome oncogene-induced senescence and thus initiate tumor formation and progression of mouse embryonic fibroblasts (MEFs) in nude mice (Liu et al., 2013). In line with these data, comparable effects in overriding Ras-induced senescence by disrupting p53 and RB pathways were described for Twist1, which was shown to induce transformation and invasiveness in cooperation with Ras (Ansieau et al., 2008). These results were corroborated by another study showing cooperative effects between EMT-TFs like Zeb1 and Twist1 with Ras in malignant transformation of

mammary epithelial cells. Further, the combined expression of Twist1 and oncogenic Ras in murine luminal mammary epithelial cells induced claudin-low, basal breast tumors (Morel et al., 2012). Apart from the effects on overcoming cellular senescence, several reports suggest that EMT-TFs confer radio- and chemoresistance as well (Cheng et al., 2007; Kajita et al., 2004; Kurrey et al., 2009; Li et al., 2009; Vega et al., 2004). For instance, hyperactivation of the ATM serine/threonine kinase (ATM) and upregulated Zeb1 levels were observed in radioresistant breast cancer cells both in *in vitro* and *in vivo*. Thereby, ionizing radiation induces inducing single- and double-strand DNA break which activates ATM. ATM in turn was shown to stabilize Zeb1 which subsequently promotes homologous recombination-dependent DNA repair by interacting with downstream effectors of the DNA-damage response (Zhang et al., 2014). Resistance to chemotherapy which specifically targets actively proliferating cells, might be explained due to reduced proliferation of cells undergoing EMT (Mejlvang et al., 2007; Schmidt et al., 2015; Vega et al., 2004). Accordingly, cancer cells deleted in Snail1 or Twist1 were more proliferative without any effects on invasiveness in an invasive pancreatic ductal adenocarcinoma mouse model. However, EMT-TF deletion induced increased sensitivity to gemcitabine chemotherapy and improved the overall survival of mice (Zheng et al., 2015b). Another study showed that lung metastases emerged from non-EMT cells that were targetable by cyclophosphamide treatment in a spontaneous breast cancer metastasis model. In contrast, chemotherapy-resistant recurrent metastases were generated by EMT-induced breast cancer cells (Fischer et al., 2015). Likewise, an enrichment of a $CD44^{high}/CD24^{-/low}$ gene signature, linked to stem-cell-like traits and EMT, was connected with the claudin-low subtype. Similarly, enrichment of this stem-cell signature as well as an enrichment of EMT-associated genes was observed in residual cells of ER+ breast cancer surviving both endocrine treatment and chemotherapy (Creighton et al., 2009). High expression of EMT-TFs like Twist1 was further associated with reduced relapse-free survival (Grzegrzolka et al., 2015; Van Nes et al., 2012). Together, EMT-TF and thereby EMT might contribute to tumor progression and metastasis predominantly by driving therapy resistance and tumor recurrence. Therefore, employing and studying models for EMT might unravel novel treatment options for basal-like and claudin-low subtypes, but might also identify mechanisms to avoid recurrence or to treat recurrent breast cancer.

1.3.3 Redox regulation, metabolism and EMT

To accomplish the process of EMT and acquire migratory and invasive properties, several studies suggest that profound changes at the metabolic level occur during EMT-TF activation and EMT. For instance, it was found that a set of high-grade carcinoma cell lines showing a mesenchymal gene signature were marked by high expression of 44 metabolic genes involved in several pathways like nucleotide, amino acid, lipid and redox metabolism. Genes of this “mesenchymal metabolic signature” were induced during Twist1-induced EMT in HMLE cells (Shaul et al., 2014). Further, dihydropyrimidine dehydrogenase (DPYD), a pyrimidine-degrading enzyme, was shown to be required for EMT *in vitro* and for metastasis to the lungs *in vivo*, but did not generally impact cell viability or proliferation (Shaul et al., 2014). Another group reported that Snail1 leads to a metabolic switch to glycolysis through epigenetic silencing of fructose-1,6-biphosphatase (FBP1), an enzyme involved in gluconeogenesis. This process was shown to be involved in the development of basal-like breast cancer and associated with the maintenance of stem-cell-like traits by lowering reactive oxygen species (ROS), presumably generated by oxidative phosphorylation (OXPHOS) in the mitochondria (Dong et al., 2013). Accordingly, reducing the content of mitochondrial DNA generated an EMT-like phenotype characterized by the suppression of E-cadherin, upregulation of EMT-TFs and mesenchymal markers and a gain in migratory and invasive properties in human mammary epithelial cells and a breast cancer cell line (Guha et al., 2014). However, the impact of ROS and mitochondria on metastasis is not clear yet. For example, an increase in mitochondria and thus OXPHOS by higher expression of the peroxisome proliferator-activated receptor gamma, coactivator 1 alpha (PGC-1α) was implicated in promoting invasiveness and metastasis. Indeed, knockdown of PGC-1α inhibited invasive properties and metastasis but did not impact primary tumor growth or the process of EMT (LeBleu et al., 2014). Mitochondrial ROS, especially superoxide, generated during the electron transport chain (ETC) during OXPHOS, were implicated to be necessary for tumor cell migration, invasion and metastasis. Thereby, either overload of the ETC or partial ETC inhibition yielded higher mitochondrial superoxide levels (Porporato et al., 2014), possibly explaining the seemingly contradictory observations mentioned before. Further, oxidative stress was shown to be increased in metastatic cells. However, metastatic outgrowth was shown to require metabolic changes that limit oxidative stress at the distant site

(Piskounova et al., 2015). Interestingly, a recent report identified that loss of fumarate hydratase, an enzyme of the tricarboxylic cycle, led to the accumulation of fumarate which in turn induced EMT by epigenetic suppression of the miR-200 microRNA family which targets the EMT-TF Zeb1 (Sciacovelli et al., 2016). However, fumarate accumulation was connected with increased oxidative stress, inducing cellular senescence *in vitro* and *in vivo*. Overcoming oxidative stress-induced senescence initiated renal cancer (Zheng et al., 2015a), hinting to the possibility that EMT-TF activation and EMT might be a mechanism to promote tumorigenesis by bypassing premature oncogene-senescence as suggested earlier (Ansieau et al., 2008). Conclusively, these studies indicate some connections of EMT-TFs and EMT to metabolic pathways and ROS generation while the exact contribution to tumor initiation, progression and metastasis remain unresolved.

1.4 Ferroptosis

One of the hallmarks of cancer is the resistance to cell death. In 2011, Hanahan and Weinberg described the evasion of apoptosis as one of the important mechanisms for the malignant progression of cancer cells. Further, cancer cells obtain advantages for tumor progression by exploiting autophagy, the recycling of cell organelles in nutrient-limited conditions, or by switching necrotic cell death to a pro-tumorigenic mode (Hanahan and Weinberg, 2011). Recently, another regulated cell-death modality termed ferroptosis was revealed in specific cancer entities (Dixon et al., 2012; Lachaier et al., 2014; Miess et al., 2018; Yang et al., 2014), thus offering novel opportunities to tackle otherwise resistant cancer cells. The term ferroptosis was introduced in 2012 by Dixon and colleagues, describing an iron-dependent and lipid-mediated mode of cell death induced by the small molecule Erastin (ERA) (Dixon et al., 2012) (Figure 2). Two years later in 2014, glutathione peroxidase 4 (GPX4) which removes lipid hydroperoxides (L-OOH), was shown to be a central regulator of ferroptosis. Consequently, inhibition of GPX4 by the small molecule (*1S,3R)*-RSL3 (RSL3) or genetic interference with GPX4 led to an aberrant accumulation of L-OOH in membrane phospholipids, ultimately resulting in ferroptosis (Yang et al., 2014) (Figure 2).

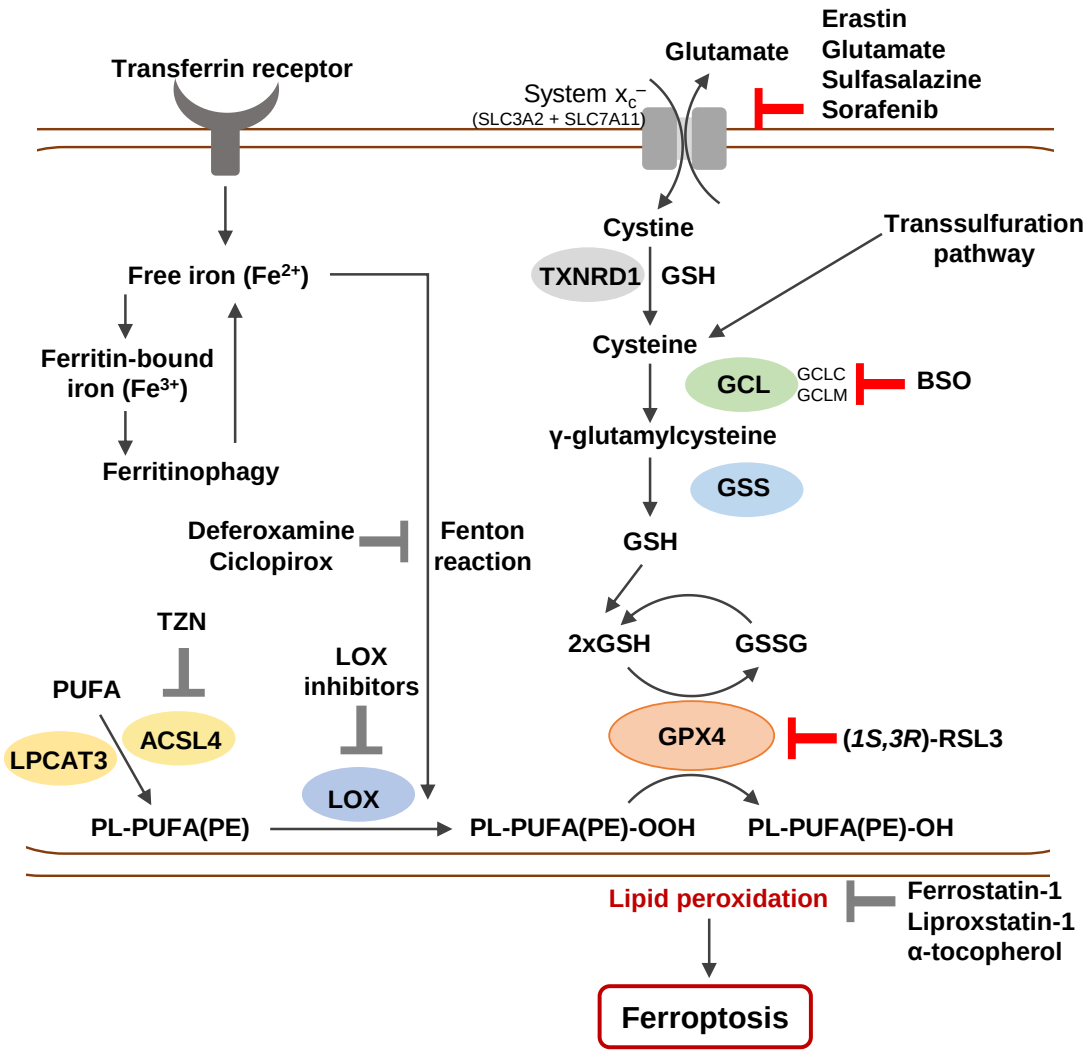

Figure 2: Overview of signaling pathways and regulators involved in ferroptosis
Accumulation of high lipid peroxidation (-OOH) levels in phospholipids (PL), unless reduced by glutathione peroxidase 4 (GPX4) to the corresponding alcohol (-OH), results in ferroptosis. Ferroptosis is induced by direct inhibition of GPX4, i.e. by (*1S,3R*)-RSL3 or by depleting glutathione (GSH) upstream of GPX4 by inhibition of system x_c^-, supplying cysteine for GSH synthesis, by Erastin, Glutamate, Sulfasalazine or Sorafenib or by inhibition of glutamate-cysteine ligase (GCL) by buthionine sulfoximine (BSO). Reduction of cystine to cysteine is mediated by GSH or by thioredoxin reductase 1 (TXNRD1) and cysteine can be supplied by the transsulfuration pathway as well. Ferrous iron (Fe^{2+}) via Fenton reaction and lipoxygenases (LOX) contribute to lipid peroxidation during ferroptosis and iron chelators like deferoxamine and ciclopirox and LOX-inhibitors are able to rescue ferroptosis. Iron levels are controlled by transferrin receptor-mediated import of iron and storage and release (ferritinophagy) of iron from ferritin. Susceptibility to ferroptosis is regulated by the amount of esterified polyunsaturated fatty acids (PUFAs) into PLs or specifically in phosphatidylethanolamines (PEs) by PUFA-related-enzymes like lysophosphatidylcholine acyl-transferase 3 (LPCAT3) and acyl-CoA synthetase long-chain family member 4 (ACSL4). Inhibition of ACSL4 by thiazolidinediones (TZN) and likewise the inhibition of lipid peroxidation by lipophilic antioxidants like Ferrostatin-1, Liproxstatin-1 and α-tocopherol protects from ferroptosis. GSS: glutathione synthetase. Figure was adapted from (Conrad et al., 2016; Stockwell et al., 2017) with modifications.

Initially, ERA and RSL3 were identified through genetic screens to selectively kill tumorigenic fibroblast expressing Small T oncoprotein and oncogenic $HRAS^{G12V}$ without affecting their normal counterparts (Dolma et al., 2003; Yang and Stockwell, 2008). These early studies already ruled out caspase activation and thus apoptosis as cell-death modality, but showed an involvement of iron and lipid reactive oxygen species (ROS) by the ability of rescuing the cell death with deferoxamine (DFO), an iron chelator, and vitamin E, a lipophilic antioxidant (Dolma et al., 2003; Yagoda et al., 2007; Yang and Stockwell, 2008). Since then, several molecular mechanisms such as the enrichment of oxidation-prone polyunsaturated fatty acids (PUFA) within cellular membranes by the enzyme acyl-CoA synthetase long-chain family member 4 (ACSL4) and biomarkers like NADPH levels as a predictor for ferroptosis sensitivity were identified (Doll et al., 2017; Shimada et al., 2016a). However, in contrast to apoptosis, ferroptosis has not yet been linked to normal physiological function (Stockwell et al., 2017). Thus far, mechanistic insights were predominantly achieved by inducing ferroptosis in cancer cells or by studying the role of ferroptosis in other pathological conditions such as ischemia/reperfusion (I/R) injury in liver, heart and kidney (Friedmann Angeli et al., 2014; Gao et al., 2015; Jiang et al., 2015; Linkermann et al., 2014; Yang et al., 2014). Therefore, current research aims to further describe and define biological contexts and signaling pathways involved in ferroptosis.

1.4.1 Molecular mechanisms involved in ferroptosis

1.4.1.1 Thiol and Glutathione metabolism

Ferroptosis is triggered when GPX4 function is impaired and consequently, a deadly threshold of L-OOH is exceeded (Stockwell et al., 2017). Almost four decades ago, GPX4 was isolated from pig liver and shown to reduce phospholipid hydroperoxides to the corresponding alcohols in presence of glutathione (GSH) (Ursini et al., 1982, 1985). During this reaction, two molecules of GSH are oxidized to glutathione disulfide (GSSG), highlighting the importance of GSH for maintaining GPX4 function (Brigelius-Flohé and Maiorino, 2013). In the context of ferroptosis, the system x_c^- plays an important role to supply cysteine for GSH biosynthesis and was identified to modulate GPX4 function (Friedmann Angeli et al., 2014; Yang et al., 2014). The system x_c^- is an antiporter consisting of a light chain xCT and a heavy chain 4F2hc which imports one molecule cystine (oxidized form of two molecules cysteine

connected via a disulfide bridge) in exchange for glutamate (Bannai, 1986; Sato et al., 1999). Imported cystine is readily reduced to cysteine by GSH or thioredoxin reductase 1 (TXNRD1) (Bannai, 1986; Mandal et al., 2010). Thereby, cysteine availability directly controls GSH biosynthesis (Ishii et al., 1987). The rate-limiting reaction catalyzed by the glutamate-cysteine ligase (GCL) yields γ-glutamylcysteine and addition of glycine by glutathione synthetase (GSS) forms GSH in a second reaction (Bannai and Tateishi, 1986). Thereby, compounds initiating ferroptosis through GSH depletion were classified as class I ferroptosis-inducing agents (FINs) (Yang et al., 2014). ERA, glutamate, sulfasalazine and sorafenib deplete GSH indirectly by targeting the system x_c^- while buthionine sulfoximine (BSO) inhibits GCL, the rate-limiting enzyme for GSH synthesis (Dixon et al., 2012, 2014; Seiler et al., 2008; Yang et al., 2014). A recent study showed that knockdown of CARS, a cysteinyl-tRNA synthetase, protects from ERA-induced ferroptosis by supplying cysteine from methionine via the transsulfuration pathway (Hayano et al., 2016), thus reflecting a mechanism to bypass dependence on system x_c^-. Interestingly, sensitivity to ERA-induced ferroptosis is also regulated by the tumor suppressor p53 which represses xCT (*SLC7A11*) expression, thereby reducing cysteine availability and conferring tumor suppressive activities (Jiang et al., 2015). However, murine p53 with four mutated acetylation sites was unable to transcriptionally repress *SLC7A11* in tumor cells, resulting in resistance to ERA-induced ferroptosis and entailing important implications for tumor progression (Wang et al., 2016). In contrast to Class I FINs, Class II FINs directly impair GPX4 function. This can be achieved by covalent GPX4 inhibitors such as RSL3 or by GPX4-degrading compounds such as FIN56 (Shimada et al., 2016b; Yang et al., 2014).

1.4.1.2 Lipid-related metabolism

Downstream of the direct or indirect impairment of GPX4 function results in the accumulation of lipid peroxidation, leading to ferroptosis (Dixon et al., 2012; Yang et al., 2014). However, there is still uncertainty about the precise mechanism of how and where lipid peroxidation is initiated and how exactly it induces cell death (Yang and Stockwell, 2016). For sure, lipid peroxidation is a critical event in ferroptosis since its prevention by administration of lipophilic antioxidants such as α-tocopherol (α-toc), ferrostatins like ferrostatin-1 (Fer1) and liproxstatin-1 (Lip1) rescue ferroptosis induced by chemical compounds or genetic knockout of GPX4 (Dixon et

al., 2012; Friedmann Angeli et al., 2014; Seiler et al., 2008; Skouta et al., 2014; Yang et al., 2014). In this context, recent studies highlight the importance of polyunsaturated fatty acids (PUFA) metabolism and oxidation in ferroptosis execution (Doll et al., 2017; Kagan et al., 2017). For example, a haploid screen identified the involvement of two PUFA metabolism-linked enzymes, namely ACSL4 and lysophosphatidylcholine acyl-transferase 3 (LPCAT3), in RSL3- and ML162-induced ferroptosis, but not in ERA-induced ferroptosis (Dixon et al., 2015). ACSL4 activates preferentially arachidonic acid (AA) or other long-chain fatty acids (FAs) by ligating them with free coenzyme A, thus generating acyl-CoAs (Van Horn et al., 2005; Soupene and Kuypers, 2008). In turn, LPCAT3 re-esterifies these acyl-CoAs into membrane phospholipids (Shindou and Shimizu, 2009). ACSL4 but not LPCAT3 expression was further established as a critical player in ferroptosis sensitivity in MEFs as well as in a panel of breast cancer cell lines (Doll et al., 2017). Mechanistically, ACSL4 yields long chain acyl-CoAs containing AA or adrenic acid (AdA) that are enriched in phosphatidylethanolamines (PE) which presents a specific class of phospholipids. Ferroptosis induction occurs through oxidation of these AA- or AdA-containing PEs, thus serving as an execution signal (Doll et al., 2017; Kagan et al., 2017). Genetic deletion or pharmacological inhibition of ACSL4 by thiazolidinediones conferred increased resistance to ferroptosis *in vitro* and delayed mortality in a ferroptosis mouse model *in vivo* (Doll et al., 2017). Enzymes such as lipoxygenases (LOX) are implicated in inducing these lipid peroxidation death signals in ferroptosis (Kagan et al., 2017; Seiler et al., 2008; Yang et al., 2016). LOX enzymes dioxygenate PUFAs like AA and linoleic acid at different positions to the corresponding hydroperoxide which in turn serve as bioactive lipid mediators or impact diverse biological processes (Kuhn et al., 2015). Blocking LOX activity by small molecules such as PD146176 or BWA4C was shown to protect from ferroptosis *in vitro* (Friedmann Angeli et al., 2014; Yang et al., 2016). Knockdown of all LOX enzymes using a pool of siRNAs or knockdown of specific LOX enzymes such as ALOX15B and ALOXE3 rescued the fibrosarcoma cell line HT1080 from ERA-induced ferroptosis (Yang et al., 2016). Likewise, genetic deletion of a specific LOX (*ALOX15*) induced resistance to BSO-induced ferroptosis *in vitro* (Seiler et al., 2008). However, *ALOX15* knockout (KO) did not rescue from ferroptosis-induced-acute renal failure and mortality in a tamoxifen (TAM)-inducible *GPX4*-KO mouse model. Further, knockdown of ALOX5, which could possibly compensate for

ALOX15-KO, did not protect these *ALOX15*/*GPX4*-double KO cells from ferroptosis *in vitro* (Friedmann Angeli et al., 2014). Together, the role of LOX enzymes in ferroptosis remains obscure and further research is required to establish the exact source of death signals. Since supplementation of cells with AA or other PUFAs was shown to elicit ferroptosis sensitivity (Yang et al., 2016), the oxidation of PUFA-containing lipids by whatever means seems to be indeed a hallmark in ferroptosis. This notion is further supported by the finding that several aldo-keto reductase members of the AKR1C family, which detoxify reactive aldehyde species occurring as end-products during lipid peroxidation, are highly overexpressed in ERA-selected resistant DU-145 prostate cancer cell clones (Dixon et al., 2014). However, it still has to be elucidated to what extent these pathways downstream of lipid peroxidation depend on cellular context and the means of ferroptosis-induction.

1.4.1.3 Iron-related metabolism

Earlier studies suggested iron-dependence in ferroptosis (Dixon et al., 2012; Yang and Stockwell, 2008). This was determined by rescue experiments with iron chelators such as deferoxamine and the observation that ferroptosis sensitive cell lines had higher iron levels, ultimately impacting the terminology of ferroptosis (Dixon et al., 2012; Yang and Stockwell, 2008). However, the mechanistic role of iron in ferroptosis remains obscure (Doll and Conrad, 2017). In a model of oncogenic Ras-expressing fibroblasts, ferroptosis-sensitive cells showed higher expression of transferrin receptor 1 (TFR1), leading to increased iron uptake into cells, while iron storage-related genes such as ferritin heavy chain 1 (FTH1) and ferritin light chain (FTL) were downregulated compared to the parental cells (Yang and Stockwell, 2008). 30% of circulating ferric iron (Fe^{3+}) is bound to transferrin (TF) and this complex is internalized via endocytosis upon binding to TFR1. Acidification of the early endosome induces the release of iron from TF and a subsequent reduction to ferrous iron (Fe^{2+}) by the six-transmembrane epithelial antigen of prostate protein family (STEAP). This is followed by the transport into the cytosol via DMT1 (divalent metal transporter 1). Fe^{2+} contributes to the labile iron pool (LIP) in the cytosol which is used for storage as Fe^{3+} bound to ferritin, exported as Fe^{3+} via Ferroportin (FPN) or for metabolic pathways, for example in heme or iron-sulfur cluster-containing enzymes (Muckenthaler et al., 2017). In accordance with earlier findings, a recent study demonstrated that TF-bound iron import is required for ferroptosis induction in

amino acid-starved MEFs (Gao et al., 2015). Likewise, the release of iron from ferritin involved an autophagic/lysosomal process termed ferritinophagy and was shown to contribute to ERA- and RSL3-induced ferroptosis in N-Ras mutated HT1080 cells (Torii et al., 2016). Additionally, expression of the heme oxygenase 1 (HMOX1) was implicated in ERA-mediated ferroptosis sensitivity of HT1080 cells (Kwon et al., 2015). HMOX1 releases iron by the degradation of heme or heme-containing proteins (Poss and Tonegawa, 1997a). Accordingly, silencing the iron response element binding protein 2 (IREB2), a master regulator of iron metabolism, resulted in resistance to ERA- or sorafenib-induced ferroptosis in different cancer cell lines (Dixon et al., 2012; Louandre et al., 2013). An explanation of how iron contributes to ferroptosis might be the initiation of lipid peroxidation by the Fenton reaction, further supported by the ability of iron chelators to bind the redox active LIP (Cao and Dixon, 2016). The reaction of Fe^{2+} of the LIB with hydrogen peroxide results in the generation of Fe^{3+} and a highly reactive hydroxyl radical ($OH^{\bullet}$) which in turn initiates a damaging oxidation cascade in lipids, but also in proteins and DNA (Doll and Conrad, 2017; Torii et al., 2016). Another explanation why iron chelation rescues from ferroptosis might be the inhibition of iron-containing enzymes. For instance, LOX enzymes contain iron in their active site that can be chelated by DFO, thereby inhibiting their activity (Abeysinghe et al., 1996; Barradas et al., 1989).

1.4.1.4 Additional pathways regulating ferroptosis

Several other pathways were shown to regulate ferroptosis sensitivity. For instance, L-glutamine was shown to induce ferroptosis in amino-acid-deprived MEFs via the process of glutaminolysis (Gao et al., 2015). Glutamine is converted to glutamate by glutaminases and subsequently to a-ketoglutarate which is used in the tricarboxylic acid cycle for diverse metabolic pathways such as mitochondrial respiration, fatty acid synthesis or NADPH production (Yang et al., 2017). Inhibition of glutaminases by Compound 968 also ameliorated ferroptosis-induced I/R injury in an *ex vivo* heart model (Gao et al., 2015). Along these lines, genes involved in mitochondrial fatty acid metabolism like acyl-CoA synthetase family member 2 (ACSF2) and citrate synthase (CS), which partly depend on glutaminolysis, were shown to be required for ferroptosis induction by ERA (Dixon et al., 2012). Interestingly, the amount of NADPH, which is an important reductant within cells, was established as a biomarker for ferroptosis sensitivity in a large panel of cancer cell lines. Thereby,

high levels of NADPH correlated with resistance to FINs (Shimada et al., 2016a). Another study showed that increasing cellular coenzyme Q_{10} (CoQ_{10}) concentrations inhibit ERA-, RSL3- and FIN56-induced ferroptosis in HT1080 cells which is most likely independent from the mitochondrial function of CoQ_{10} (Shimada et al., 2016b). CoQ_{10} is important for mitochondrial respiration as an electron carrier and further has antioxidant activity. Production of CoQ_{10} occurs within the mevalonate pathway which is inhibited by Statins (Deichmann et al., 2010). Likewise, treatment with Statins elicits ferroptosis-sensitivity, possibly by reducing CoQ_{10} levels and reduced GPX4 abundance (Shimada et al., 2016b; Viswanathan et al., 2017). Biosynthesis of selenoproteins like GPX4 is controlled by a selenocysteine tRNA (tRNA (Sec)) that requires isopentenylation for proper function. Inhibition of the mevalonate pathway by Statins was shown to impair tRNA(sec) maturation and therefore selenoprotein synthesis (Kryukov et al., 2003; Warner et al., 2000). The presence of oncogenic Ras was described to induce a selective susceptibility to FINs and employing MEK inhibitors, thereby disrupting Ras signaling, rescued cell death (Dixon et al., 2012; Dolma et al., 2003; Yang and Stockwell, 2008; Yang et al., 2014). However, an association between *RAS* mutational status and ferroptosis sensitivity was not observed when analyzing 117 cancer cell lines (Yang et al., 2014). Further, sensitivity to sorafenib- and ERA-induced ferroptosis is not dictated by common tumor mutations like *RAS*, *RAF*, *PIK3CA* and *TP53* in a panel of cancer cell lines (Lachaier et al., 2014). For hepatocellular carcinoma cell lines (HCC), the nuclear factor erythroid 2-related factor 2 (NRF2) was shown to preserve ferroptosis protection (Sun et al., 2016). NRF2 is a master regulator in inducing the transcription of a variety of genes all involved in the cellular response against oxidative damage (Jaramillo and Zhang, 2013). Knockdown of downstream targets of NRF2 such as quinone oxidoreductase-1 (NQO1), FTH1 or HMOX1 increased ferroptosis sensitivity in HCC cells *in vitro* and knockdown of NRF2 augmented ferroptosis induction by ERA and sorafenib *in vivo*, leading to smaller tumors formed by Hepa1-6 cells compared to the control group (Sun et al., 2016). This is in contrast to the finding that the presence of HMOX1 increases ferroptosis-sensitivity to ERA treatment in HT1080 cells (Kwon et al., 2015), indicating that the cellular signaling context strongly influences ferroptosis sensitivity, and single genes and proteins might differently contribute therein.

1.4.2 Relevance of ferroptosis for human diseases

Since ferroptosis was not yet directly linked to a normal physiological function, the relevance of ferroptosis for human diseases comes mainly from *in vitro* and *in vivo* studies in mouse models (Stockwell et al., 2017). Systemic deletion of *GPX4* results in an embryonic lethal phenotype during gastrulation stage (Imai et al., 2003; Yant et al., 2003), highlighting that GPX4 function is indeed necessary for embryonic development. Further, numerous studies observed an important role of GPX4 in neuronal development and homeostasis. Conditional knockout of *GPX4* leads to neurodegeneration in the cerebral cortex and hippocampus (Seiler et al., 2008; Wirth et al., 2010, 2014; Yoo et al., 2012). Along these lines, a reduction of GPX4 levels, thereby increasing lipid peroxidation, were implicated in mouse models of the neurodegenerative disease Alzheimer's (Chen et al., 2008; Yoo et al., 2010). Mechanistically, higher lipid peroxidation levels might lead to upregulation of the β-site amyloid precursor protein cleavage enzyme 1 (BACE1) which is required for the generation of β-amyloid plaques, a fundamental cause in Alzheimer's disease (Chen et al., 2008). Likewise, Parkinson's disease was associated with a regulation of GPX4 levels and increased ferroptosis in dopaminergic neurons (Bellinger et al., 2011; Do Van et al., 2016). *In vitro*, reprogramming of astrocytes into neurons was shown to be accompanied by increased lipid peroxidation induced by the switch from glycolytic to oxidative energy metabolism. Reducing these levels by the ferroptosis inhibitor Lip1 or the lipophilic antioxidant α-toc ameliorated reprogramming into neurons (Gascón et al., 2016). Additionally, ferroptosis inhibitors such as Fer1 and Lip1 alleviated injuries in mouse models induced by I/R of the liver, heart, brain and kidney, indicating that ferroptosis contributes in I/R injuries as a harmful mechanism (Dixon et al., 2012; Friedmann Angeli et al., 2014; Gao et al., 2015; Linkermann et al., 2014; Skouta et al., 2014; Tuo et al., 2017). Accordingly, GPX4 was shown to be essential for hepatocellular survival and function. Thus, diminishing *GPX4*-KO-induced lipid peroxidation by α-toc supplementation counteracted GPX4-mediated hepatocyte loss (Carlson et al., 2016). Interestingly, GPX4 activity is also critical for hair follicle morphogenesis in the skin (Sengupta et al., 2013), for the maturation of photoreceptor cells (Ueta et al., 2012) and for the expansion of T-cells in the periphery in response to acute infections (Matsushita et al., 2015). Possible ferroptosis-sensitive tumor entities might be diffuse large B cell lymphoma (DLBCL) and renal cell carcinomas (RCCs), assessed by *in vitro* sensitivity towards ERA-

induced ferroptosis in the NCI-60 cell line panel (Yang et al., 2014). In experiments using tumor xenografts, ferroptosis induction reduced tumor growth and led to cell death induction (Jiang et al., 2015; Sun et al., 2016; Yang et al., 2014). In contrast, TAM-inducible GPX4-ablated fibroblasts, transformed with c-Myc and HRas oncogenes, were able to generate subcutaneous tumors similar to GPX4 wildtype (WT) cells while survival was highly impacted in 2D cultures *in vitro* (Schneider et al., 2010). Together, these studies show an important role of GPX4 and ferroptosis for development as well for pathological conditions. Especially when it comes to neoplastic diseases such as cancer, further research is necessary to describe and understand the conditions conferring sensitivity or resistance to ferroptosis.

1.5 Aim of the study

Breast cancer is a frequently diagnosed cancer among women, leading to the highest mortality rate across all cancer entities in women (Bray et al., 2018). Particularly, the presence of metastatic disease drastically decreases 5-year survival to less than 30% (Noone et al., 2017). Currently, treatment options for metastatic disease are limited, especially for the subset of TNBC (Zeichner et al., 2016). EMT-TF and the process of EMT were linked to tumor progression and metastasis. Additionally, EMT was shown to induce resistance to therapeutic interventions and thus cancer recurrence (Ansieau et al., 2014; Nieto et al., 2016). As recent reports suggested a connection between EMT and metabolic rewiring, including redox regulation and lipid metabolism (Dong et al., 2013; Sciacovelli and Frezza, 2017; Shaul et al., 2014), I hypothesized that ferroptosis might be employed as a potential cell death mechanism to target otherwise resistant cells, i.e. induced by EMT. Ferroptosis was identified as a novel iron-dependent cell death mechanism, involving the lethal accumulation of lipid peroxidation. Mechanistically, ferroptosis is distinct to known other cell death modalities like apoptosis or necrosis and relies on the proper function of GPX4 which reduces lipid peroxides within membranes. Several cancer entities like diffuse large B cell lymphoma and renal cell carcinomas were shown to be particularly sensitive to ferroptosis (Dixon et al., 2012; Yang et al., 2014). Several genetic and metabolic contributors involved in ferroptosis and predicting ferroptosis sensitivity and resistance were identified. However, there are still many open questions about the determinants of ferroptosis, especially when it comes to different cellular contexts. Therefore, I aimed to study ferroptosis in human

mammary epithelial cells and to elucidate whether EMT-induction by TWIST1 expression, leading to mesenchymal transdifferentiation, impacts ferroptosis susceptibility. Throughout the study, I established cell density as a critical determinant of ferroptosis sensitivity in human mammary epithelial cells. Therefore, I extended the aim to determine the molecular mechanisms underlying cell density-dependent ferroptosis in human mammary epithelial cells.

2 Materials

2.1 Cell lines

HMLE (Immortalized human mammary epithelial cells): Primary mammary epithelial cells were transduced with retroviruses containing the SV40 large T early region, leading to inactivation of the tumor suppressor proteins p53 and RB as well as Protein Phosphatase 2, thus driving progression through cell cycle. Additionally, they were transduced retrovirally with the telomerase catalytic subunit of the hTERT gene, which is sufficient to induce telomerase activity (Elenbaas et al., 2001). HMLE cells are neither tumorigenic nor express the estrogen receptor (Ince et al., 2007). Cells were kindly provided by Robert A. Weinberg (Massachusetts Institute of Technology, USA).

HMLE-Twist1: HMLE cells were transduced with a pBabe-Puro-Twist1 vector, thereby leading to constitutive overexpression of TWIST1 and thus induction of an EMT (Mani et al., 2008; Yang et al., 2004a). Cells were kindly provided by Robert A. Weinberg (Massachusetts Institute of Technology, USA).

HMLE-Ras: HMLE cells were transduced with a pBabe-Puro-Ras (V12H) retroviral vector, leading to the overexpression of a constitutively active form of HRAS (Elenbaas et al., 2001). Cells were kindly provided by Robert A. Weinberg (Massachusetts Institute of Technology, USA).

HMLE-neuNT: HMLE cells were transduced with a pWZL vector containing a mutated, constitutively active form of the HER2/neu oncogene (Mani et al., 2008). Cells were kindly provided by Robert A. Weinberg (Massachusetts Institute of Technology, USA).

HMLE-Twist1-Ras: HMLE-Twist1 cells were transduced with a pWZL retroviral vector containing V12H-RAS oncogene, leading to the overexpression of a constitutively active form of hRas (Mani et al., 2008). Cells were kindly provided by Robert A. Weinberg (Massachusetts Institute of Technology, USA).

HMLE-Twist1-ER: HMLE cells were transduced with a pWZL-Blast-Twist1-ER vector and are cultured in growth medium containing 10 µg/ml blasticidin, leading to the constitutive overexpression of an inducible TWIST1 protein. For this purpose, Twist1 was fused to a mutated estrogen ligand binding-domain that keeps Twist1 inactive unless 4-hydroxytamoxifen is added (Casas et al., 2011; Mani et al., 2008). Cells were kindly provided by Robert A. Weinberg (Massachusetts Institute of Technology, USA). The $CD44^{+}/CD24^{high}$ population, termed HMLE-Twist1-ER 24^{hi}, was derived by FACS-sorting and was kindly provided by Dr. Johanna Schmidt (Schmidt et al., 2015).

HMLE-Snail1-ER: HMLE cells were transduced with a pWZL-Blast-Snail1-ER vector, resulting in the overexpression of a 4-hydroxytamoxifen inducible Snail1 protein (see also HMLE-Twist1-ER) (Mani et al., 2008). Cells were kindly provided by Robert A. Weinberg (Massachusetts Institute of Technology, USA). The $CD44^{+}/CD24^{high}$ population, termed HMLE-Snail1-ER 24^{hi}, was derived by FACS-sorting and was generated during my master thesis (Schmidt et al., 2015).

Breast cancer cell line panel: MCF7 (ATCC® HTB-22™), T-47D (ATCC® HTB-133™), MDA-MB-468 (ATCC® HTB-132), MDA-MB-231 and MDA-MB-157 (both from panel ATCC® TCP-1002™) cell lines were purchased from ATCC.

HEK293T: Human embryonic kidney cells containing the SV40 T-antigen that were employed for production of lentivirus and were purchased from ATCC (CRL-3216™) (DuBridge et al., 1987; Pear et al., 1993).

HMLE-Twist1-ER 24^{hi}_PTEN_wt and HMLE-Twist1-ER 24^{hi}_PTEN_KO clones: Single-cell clones were derived from HMLE-Twist1-ER 24^{hi} expressing wildtype (wt) PTEN or containing homozygous PTEN-deletions (Knockout, KO) generated by CRISPR/Cas9 genome-editing. For this purpose, cells were transduced with lentiviruses containing a doxycycline-inducible Cas9 protein (pCW-Cas9, Addgene #50661) and with the pLX-sgRNA vector (Addgene#50662) containing the sgRNA PTEN target sequence TGTGCATATTTATTACATCG. Cells were kindly generated and provided by Hilary M. Ganz (Mammary Stem Cells, Institute of Stem Cell

Research, Helmholtz Center Munich) according to published protocols (Wang et al., 2014).

2.2 Primary mammary epithelial cells

Primary mammary epithelial cells were kindly provided by Lisa Meixner (Mammary Stem Cells, Institute of Stem Cell Research, Helmholtz Center Munich), who isolated, processed and banked these cells from reduction mammoplasties according to a published protocol (Stingl et al., 2005) with modifications (Linnemann et al., 2015) and in accordance with the regulations of the ethics committee of the Ludwig-Maximilians-University Munich (ethics vote EK397-12). Luminal progenitor (LP) and basal B+ subpopulations were sorted and provided by Lisa Meixner as described (Linnemann et al., 2015).

Donors used in this study: M16, M19 and M29

2.3 Cell culture media and solutions

Product	Supplier (Catalog No)
Dulbecco's Modified Eagle Medium (DMEM)	Gibco®, Life Technologies™; Thermo Fisher Scientific (41965-039)
Dulbecco's Modified Eagle Medium F-12 Nutrient Mixture (DMEM/F12)	Gibco®, Life Technologies™; Thermo Fisher Scientific (11320-074)
fetal calf serum (FCS)	PAN-Biotech (30-2602)
Mammary Epithelial Cell Growth Medium (MECGM) including Mammary Epithelial Cell Growth Medium SupplementPack: 0.004 ml/ml Bovine Pituitary Extract (BPE) 10 ng/ml Epidermal Growth Factor (EGF, recombinant human) 5 µg/ml Insulin (recombinant human) 0.5 µg/ml Hydrocortisone	PromoCell (C-21010, C-39115)
Penicillin/Streptomycin (10,000 U/ml)	Gibco®, Life Technologies™; Thermo Fisher Scientific (15140122)
Trypsin-EDTA 0.05%, 0.25%	Gibco®, Life Technologies™; Thermo Fisher Scientific (25300, 25200)
Trypsin Neutralizing Solution (TNS)	PromoCell (C-41120)

2.4 Reagents and chemicals

Reagent	Supplier (Catalog No)
1,7-Dichloro-octamethyltetrasiloxane	Santa Cruz (sc-229834)
1S,3R-RSL3	Cayman Chemicals (Cay19288)
2-Mercaptoethanol	Sigma (63689)
2-Propanol	Roth (9866)
5,5′-Dithiobis(2-nitrobenzoic acid)	Sigma (D8130)
7-Cl-O-Nec1	Abcam (ab221984)
α-tocopherol	Sigma (258024)
β-Nicotinamide adenine dinucleotide 2′-phosphate reduced tetrasodium salt hydrate (NADPH)	Sigma (N1630)
Acetic acid (glacial)	Th.Geyer (2234)
Agarose, universal, peqGOLD	VWR (35-1020)
Albumin Fraction V (BSA)	Roth (8076)
Aluminum potassium sulfate	Sigma (A-7167)
Ammonium peroxydisulphate (APS)	Roth (9592)
Ampicillin sodium salt	Roth (K029)
Ampicillin sodium salt	Serva Electrophoresis (13399)
Aqua-Poly/Mount	Polysciences (18606)
Atglistatin	Sigma (SML1075)
Blasticidin S HCl (10 mg/ml)	Gibco®, Life Technologies™; Thermo Fisher Scientific (A1113903)
Bromophenol Blue	Sigma (B0126)
Buffer P1 (500 ml)	Qiagen (19051)
Buffer P2 (500 ml)	Qiagen (19052)
Buffer P3 (500 ml)	Qiagen (19053)
BW A4C	Sigma (B7559)
Carmine	Sigma (C-1022)
Ciclopirox	Sigma (SML2011)
CHAPS hydrate	Sigma (C9426)
cOmplete™ Protease Inhibitor Cocktail	Sigma (11697498)
Collagen type I rat tail	Corning (354236)

Reagent	Supplier (Catalog No)
DAPI	Sigma (D9542)
Deferoxamine	Sigma (D9533)
Deoxynucleotide (dNTP) Solution Mix	NEB (N0447)
Dimethyl sulfoxide (DMSO)	Sigma (D8418)
Doxorubicin hydrochloride	Sigma (D1515)
Doxycycline Hydrochloride (Dox)	Sigma (D3072)
Erastin	Sigma (E7781)
Ethanol	Merck (100983)
Ethylenediaminetetraacetic acid (EDTA)	Roth (X986)
Ethylene glycol-bis(2-aminoethylether)-N,N,N′,N′-tetraacetic acid	Sigma (O3778)
Etomoxir	Sigma (E1905)
Ferrostatin-1	Sigma (SML0583)
Forskolin	Biomol (AG-CN2-0089)
Gelatin, powdered	Applichem (147116)
Gel Loading Dye, Orange (6X)	New England Biolabs (B7022S)
Glycerol	Roth (3783)
Glycine	Roth (3790)
Hoechst 33342 Solution (20 mM)	Thermo Fisher Scientific (62249)
Hydrochloric acid 32% (HCl)	Merck (100319)
Inactive stereoisomer of RSL3	Kind gift of Dr. Marcus Conrad
Kanamycin sulfate	Sigma (60615)
LB Broth (Lennox)	Roth (X964)
LB Broth with agar (Lennox)	Sigma (L2897)
L-α-Phosphatidylcholine	Sigma (P7443)
L-Glutathione (reduced) (GSH)	Sigma (G6013)
Linoleic Acid	Sigma (L1012)
Liproxstatin-1	Sigma (SML1414)
Methanol	Roth (4627)
Mirus TransIT-X2® dynamic delivery system	Mirus Bio LLC (MIR 6003)

Reagent	Supplier (Catalog No)
N-2-hydroxyethylpiperazine-N-2-ethane sulfonic acid, 1M HEPES	Gibco®, Life Technologies™; Thermo Fisher Scientific (15630)
n-heptane	Applichem (1948)
non-fat dried milk powder	Roth (T145)
Normal donor donkey serum	GeneTex (GTX73205)
Normal goat serum	GeneTex (GTX73206)
Nonidet® P40 (NP40)	Applichem (A1694)
Oleic Acid-Albumin from bovine serum (OA)	Sigma (O3008)
PageRuler™ Plus protein ladder	Thermo Fisher Scientific (26619)
Paraformaldehyde 16% (w/v) (PFA)	VWR International (43368.9M)
PD 146176	Sigma (P4620)
Phosphate Buffered Saline (PBS) pH 7.4	Gibco®, Life Technologies™; Thermo Fisher Scientific (10010-015)
Phosphatase Inhibitor Cocktail 2	Sigma (P5726)
Phosphatase Inhibitor Cocktail 3	Sigma (P0044)
Polyethyleneimine (PEI), linear	Alfa Aesar (43896)
Potassium chloride (KCl)	Sigma (4504)
Potassium phosphate dibasic (K_2HPO_4)	Sigma (P3786)
Potassium phosphate monobasic (KH_2PO_4)	Sigma (P5655)
Protease Inhibitor Cocktail	Sigma (P8340)
Puromycin Dihydrochloride	Gibco®, Life Technologies™; Thermo Fisher Scientific (A1113803)
Rosiglitazone	Sigma (R2408)
Rotiphorese® Gel 30	Roth (3029)
S.O.C. Medium	Invitrogen™, Thermo Fisher Scientific (15544034)
Sodium chloride (NaCl)	Roth (P029)
Sodium Deoxycholate	Applichem (A1531)
Sodium dodecyl sulfate (SDS)	Roth (4360)
Sodium hydroxide	Merck (30620-M)

Reagent	Supplier (Catalog No)
Sucrose	Sigma (16104)
SYBR™ Safe DNA Gel Stain	Invitrogen™, Thermo Fisher Scientific (S33102)
TE Buffer	Invitrogen™, Thermo Fisher Scientific (12090015)
TEMED	Roth (2367)
Thymol	Sigma (T0501)
TransIT-X2® Transfection Reagent	Mirus Bio LLC (MIR 6003)
Trichloroacetic acid (TCA)	Sigma (T6399)
TriDye™ 1 kb Plus DNA Ladder	New England Biolabs (N3270S)
Triton X-100	Sigma (T8787)
Tris (Trizma base)	Sigma (T1503)
TWEEN® 20	Sigma (P1379)
UltraPure™ DNase/RNase-Free Distilled Water	Thermo Fisher Scientific (10977035)
Water (sterile-filtered)	Sigma (W3500)
Y-27632	Biomol (AG-CR1-3564)
(Z)-4-Hydroxytamoxifen	Sigma (H7904)
z-VAD-fmk	R&D Systems (FMK001)

2.5 Flow cytometry dyes

Dye	Supplier (Catalog No)	Laser (nm)	Filter (nm)
7-Amino-Actinomycin D (7-AAD)	BD (559925)	488	695/40
BODIPY™ 493/503	Molecular Probes®, Life Technologies™, Thermo Fisher Scientific (D3922)	488	530/30I
BODIPY® 581/591 C11	Molecular Probes®, Life Technologies™, Thermo Fisher Scientific (D3861)	488	530/30I
CellROX™ Deep Red for oxidative stress	Molecular Probes®, Life Technologies™, Thermo	640	660/20

Dye	Supplier (Catalog No)	Laser (nm)	Filter (nm)
detection/Flow Cytometry Assay Kit	Fisher Scientific (C10422, C10491)		
MitoSOX™ Red Mitochondrial Superoxide Indicator	Molecular Probes®, Life Technologies™, Thermo Fisher Scientific (M36008)	561	586/15
Propidium Iodide (PI)	Molecular Probes®, Life Technologies™, Thermo Fisher Scientific (P3566)	561	610/20
SYTOX® Blue	Molecular Probes®, Life Technologies™, Thermo Fisher Scientific (S34857)	405	450/40
ThiolTracker™ Violet (glutathione detection reagent)	Molecular Probes®, Life Technologies™, Thermo Fisher Scientific (T10096)	405	530/30II

2.6 Antibodies

2.6.1 Primary Antibodies

Epitope [Clone]	Host	Supplier (Catalog No)	Application, Dilution
ACSL4 [A5]	Mouse	Santa-Cruz (sc-271800)	WB, 1:100
ATGL	Rabbit	Cell Signaling Technology (2138)	WB, 1:1000
beta-actin (AC-15)	Mouse	Abcam (ab6276)	WB, 1:6000
Caspase 3	Rabbit	Cell Signaling Technology (9662)	WB, 1:1000
cleaved Caspase 3 Asp175 (5A1E)	Rabbit	Cell Signaling Technology (9664)	WB, 1:1000
E-cadherin (EP700Y)	Rabbit	GeneTex (GTX61329)	WB, 1:25000
E-cadherin (HECD-1)	Mouse	Thermo Fisher Scientific (13-1700)	Inhibition Assay, 1 µg/ml
ERK1/2 (137F5)	Rabbit	Cell Signaling Technology (4695)	WB, 1:1000

Epitope [Clone]	Host	Supplier (Catalog No)	Application, Dilution
GPX4 (EPNCIR144)	Rabbit	Abcam (ab125066)	WB, 1:2000
HMOX1 (EPR1390Y)	Rabbit	Abcam (ab68477)	WB, 1:10000
Ki67	Rabbit	Abcam (ab15580)	IF, 1:300
pan Akt (C67E7)	Rabbit	Cell Signaling Technology (4691)	WB, 1:1000
PARP	Rabbit	Cell Signalling Technology (9542)	WB, 1:1000
phospho-Akt Ser473 (D9E)	Rabbit	Cell Signalling Technology (4060)	WB, 1:2000
phospho-ERK1/2 Thr202/Tyr204 (D13.14.4E)	Rabbit	Cell Signaling Technology (4370)	WB, 1:2000
Vimentin (V9)	Mouse	Abnova (MAB3578)	IF, 1:100
Zeb1	Rabbit	Sigma (HPA027524)	WB, 1:5000

2.6.2 Secondary Antibodies

Host	Epitope	Conjugation	Supplier (Catalog No)	Application, Dilution
Donkey	Mouse IgG	Alexa Fluor 488	Thermo Fisher Scientific (A21202)	IF, 1:250
Donkey	Rabbit IgG	Alexa Fluor 546	Thermo Fisher Scientific (A10040)	IF, 1:250
Goat	Mouse IgG (H+L)	HRP-conjugated	Jackson ImmunoResearch (115-036-062)	WB, 1:12500
Goat	Rabbit IgG (H+L)	HRP-conjugated	Jackson ImmunoResearch (111-036-045)	WB, 1:12500

2.7 Oligonucleotides

Oligonucleotides used as primers and templates for PCR reactions and for sequencing were purchased from Eurofins. Sequences of oligonucleotides are listed in the respective sections of the methods.

2.8 Mixtures and Kits

Kit	Supplier (Catalog No.)
Amersham™ ECL™ Prime Western Blotting Reagent	GE Healthcare (RPN2232)
CellTiter-Glo® Luminescent Cell Viability Assay	Promega (G7572)
Click-iT™ Lipid Peroxidation Imaging Kit - Alexa Fluor™ 488	Thermo Fisher Scientific (C10446)
DNA Clean & Concentrator™-5	Zymo Research (D4014)
DC™ Protein Assay	Bio-Rad Laboratories (5000112)
Hemacolor® Rapid Staining	Merck (111661)
Mix2Seq Kit	Eurofins (3094-000MSK)
Monarch® DNA Gel Extraction Kit	New England Biolabs (T1020)
QIAGEN Plasmid Midi Kit	Qiagen (12143)
RNase-Free DNase Set	Qiagen (79254)
RNeasy Mini Kit	Qiagen (74106)

2.9 Enzymes

Enzyme/Enzyme Mix	Supplier (Catalog No.)
AgeI-HF	New England Biolabs (3552S)
BamHI-HF	New England Biolabs (R3136S)
DpnI, recombinant	New England Biolabs (R0176)
Gibson Assembly® Master Mix	New England Biolabs (E2611)
Glutathione Reductase	Sigma (G3664)
MluI-HF	New England Biolabs (R3198S)
NotI-HF	New England Biolabs (R3189S)
OneScript® Plus cDNA Synthesis Kit	Applied Biological Materials (G236)
Phusion® High-Fidelity DNA Polymerase	New England Biolabs (M0530)
Power SYBR™ Green PCR Master Mix	Applied Biosystems (4367659)

Enzyme/Enzyme Mix	Supplier (Catalog No.)
Q5® High-Fidelity DNA Polymerase	New England Biolabs (M0491)
RNase A (17,500 U)	Qiagen (19101)
RNase A (10 mg/ml)	Thermo Fisher Scientific (EN0531)
T4 DNA Ligase	New England Biolabs (M0202S)
Taq DNA Polymerase with ThermoPol® Buffer	New England Biolabs (M0267)
PvuI-HF	New England Biolabs (R3150S)
SalI	New England Biolabs (R0138S)
XbaI	New England Biolabs (R0145S)
XhoI	New England Biolabs (R0146S)

2.10 Bacterial Strains

Bacterial Strain	Manufacturer
XL10-Gold Ultracompetent Cells	Agilent Technologies (200314)
MAX Efficiency™ Stbl2™ Competent Cells	Invitrogen™, Thermo Fisher Scientific (10268019)

2.11 Plasmids

Plasmid	Description	Source
StagR_Neo	Backbone vector for StagR cloning, Ampicillin resistance	Kindly provided by Christopher Breunig and Stefan Stricker (Addgene #102992) (Breunig et al., 2018)
STAGR_gRNAScaffold_hU6	template for StagR cloning to generate StagR fragments, Kanamycin resistance	kindly provided by Christopher Breunig and Stefan Stricker (Addgene #102840) (Breunig et al., 2018)
pSpCas9(BB)-2A-GFP (PX458)	Transfectable Cas9 expression plasmid fused to 2A-GFP as a selection marker. There is the possibility to directly clone and	Gift from Christopher Breunig and Stefan Stricker (Addgene #48138) (Breunig et al., 2018)

Plasmid	Description	Source
	express a sgRNA, Ampicillin resistance	
pGIPZ GPX4 targeting shRNAs V2LHS_228172 (sh#1) V3LHS_310275 (sh#2) V3LHS_332098 (sh#3) V3LHS_332100 (sh#4)	Lentiviral vector expressing turboGFP and connected through an IRES element puromycin. In addition, single shRNA against GPX4 are expressed, Ampicillin resistance	Dharmacon (RHS4531-EG2879)
pTRIPZ nontargeting shRNA control	Lentiviral expression vector where turboRFP and shRNA expression is driven by a tetracycline-inducible promoter, Ampicillin resistance	Dharmacon (RHS4743)
pLVX-puro vector	Lentiviral expression vector, Ampicillin resistance	Clontech Laboratories (632164)
pCMV-VSV-G	Plasmid expressing VSV-G envelope protein necessary for retro- or lentiviral particle assembly, Ampicillin resistance	Kindly provided by Robert A. Weinberg (Addgene #8454)
pCMV-dR8.2 dvpr	2nd generation lentiviral packaging plasmid, Ampicillin resistance	Kindly provided by Robert A. Weinberg (Addgene #8455)

2.12 Consumables

Product	Supplier
15mL Conical Centrifuge Tubes	Corning
25 Culture-Inserts 2 Well for self-insertion	Ibidi
384 PCR Plates	Kisker Biotech
6-, 12-, 24-, 96-well plates (Falcon)	Becton Dickinson
Falcon® Permeable Support for 24 well plates, 8 µm pore (Inserts)	Corning
Cell culture flasks (T75, T175)	Greiner Bio-One
Cell Scraper lila, UltraCruz® Cell Lifter	Santa Cruz
Cell Strainer Snap 40µM	Corning
Cover Glasses, 13 mm, round	VWR International

Product	Supplier
Falcon Round-Bottom Polypropylene Tubes	Corning
KOVA™ Glasstic™ Slide 10 with Grids	Kova International
Micro cover glasses 22 mm x 40 mm	VWR International
Microlite 1+ Plate white flat bottom	Fisher Scientific
Microscopy slides, cut edges, matt strip	Thermo Fisher Scientific
Millex 33mm Durapore PVDF 0.22 µm	Merck
Millex 33mm Durapore PVDF 0.45µm	Merck
Mr. Frosty™ Freezing Container	Thermo Fisher Scientific
Nitril® NextGen® Gloves	Meditrade
Nunc® CryoTubes®	Thermo Fisher Scientific
Nunc™ Cell Culture Dishes (6-cm, 15-cm)	Thermo Fisher Scientific
PCR Tubes, 0.5 mL, PCR clean	Eppendorf
Petri dish, polystyrene (for Agar plates)	Greiner Bio-One
Pipette tips (filtered)	Starlab
Pipette tips (unfiltered)	Starlab
Protein LoBind Tubes, 1.5 ml	Eppendorf
PVDF blotting membrane	GE Healthcare
QIAshredder	Qiagen
Reagent reservoirs	Corning
Rotilabo® Blotting papers, thick 1.5 mm, 580x600 mm	Roth
Safe-Lock Tubes 1.5ml PCRclean	Eppendorf
Safe-Lock Tubes 2.0ml	Eppendorf
Scalpels	VWR International
Sterile Serological Pipets (2, 5, 10, 25, 50 ml)	Greiner Bio-One
TC-flask T175	Sarstedt
TC-treated Cell Culture Dish (10-cm)	Corning
Test Tube with Cell Strainer Snap Cap (FACS tube)	Corning
TUBE, 50 ML, PP	Greiner Bio-One
Ultra - Clear - Film for RT - PCR	Kisker Biotech
X960 PCR TUBE STRIPS EPPENDORF 8 TUBES	Eppendorf

2.13 Instruments

Instrument	Manufacturer
2D Rocker	IKA®
Blue light table, LED transilluminator	Serva Electrophoresis
ChemiDoc™ MP Imaging System	Bio-Rad Laboratories
Eppendorf Mastercycler® nexus gradient	Eppendorf AG
FACSAria IIIu	Becton Dickinson
FLUOVIEW FV1200 inverted Confocal Laser Scanning Microscope	Olympus
HERAcell® 240i incubator	Thermo Fisher Scientific
Heraeus™ Fresco™ 21	Thermo Fisher Scientific
Heraeus™ Megafuge™ 40R centrifuge	Thermo Fisher Scientific
Heraeus™ Pico™ 21	Thermo Fisher Scientific
Horizontal Roller	CAT
iMark Microplate Absorbance Reader	Bio-Rad Laboratories
Leica DFC 450 C camera module	Leica Microsystems
Leica DM IL LED microscope	Leica Microsystems
Luminometer Centro XS3 LB 960	Berthold Technologies
Mini-PROTEAN® Tetra System	Bio-Rad Laboratories
NanoDrop® ND 1000 Spectrophotometer	Thermo Fisher Scientific
Orbital Multi Bio 3D Shaker	Biosan
PerfectBlue™ gel system	Peqlab
PowerPac™ HC	Bio-Rad Laboratories
QuantStudio™ 12K Flex qPCR System	Applied Biosystems™, Thermo Fisher Scientific
Safe 2020 Class II Biological Safety Cabinet	Thermo Fisher Scientific
SteREO Lumar V.12	Carl Zeiss Microscopy
ThermoMixer® C 1.5 ml	Eppendorf
Zeiss Axio Imager M.2 with Colibri 7	Carl Zeiss Microscopy

2.14 Software

Product	Manufacturer
FACS Diva™ v6.1.3	Becton Dickinson
FlowJo® 10.5.0	FlowJo, LLC
FV10-ASW software Ver 4.2.b	Olympus
GIMP 2.8.22	The GIMP Team
GraphPad Prism 7	GraphPad Software
Hugin (2018.0.0.5abfb4de7961)	GPL, Free Software Foundation
Image Composite Editor 2.0.3.0	Microsoft Corporation
Image Lab 5.2.1	Bio-Rad Laboratories
ImageJ 1.52	NIH
Leica Application Suite 4.2	Leica Microsystems
MikroWin, v4.41	Mikrotek Laborsysteme GmbH
MS Office 2016	Microsoft Corporation
QuantStudio™ 12K Flex Real-Time PCR System 1.2.2	Applied Biosystems™, Thermo Fisher Scientific
ZEN pro 2.3	Carl Zeiss Microscopy

3 Methods

3.1 Cultivation of cells

Cell culture and cell culture-related experiments were performed in a sterile safety cabinet. For maintenance, cells (see *Section 2.1*) were cultured in 6- or 10-cm diameter cell culture dishes in a 37°C HERAcell 240i incubator with a humidified atmosphere of 5% CO_2 at ambient oxygen levels (20% O_2). Primary cells (see *Section 2.2*) were maintained at 3% O_2, mimicking physiological tissue pressure (normoxia). Composition of media employed for maintenance culture is shown in Table 1. Cells were grown until they reached 70-80% confluence. For passaging, media was aspirated from dishes, cells were washed with PBS and then 0.15% Trypsin-EDTA was applied to cells with subsequent incubation for 10 min at 37°C. After visually confirming detachment of cells, the trypsinization process was stopped using 3 volumes of TNS. The cell suspension was transferred to 15 ml falcon tubes and pelleted by centrifugation at 490 x g in a Heraeus Megafuge for 5 minutes at 4°C. The supernatant was aspirated, cells suspended in their respective growth medium and transferred to plates at 1:4-1:10 dilutions.

HMLE-Twist1-ER and HMLE-Snail1-ER cells were kept in growth medium containing blasticidin (Blast-maintenance medium, Table 1). For activation of the respective EMT-TF, growth medium containing tamoxifen was applied (usually for 15 days, EMT-induction medium, Table 1). After thawing or sorting primary mammary epithelial cells into subpopulations, cells were plated in survival medium for five days in 2D culture for establishment prior to changing medium to primary cell maintenance medium and subsequent experimental usage such as seeding into cell viability assays (Linnemann et al., 2015).

Table 1: Composition of cell culture media for cells used in this study

Name	Composition	Cell line
Standard PC-medium	MECGM (0.004 ml/ml BPE, 10 ng/ml EGF, 5 µg/ml Insulin, 0.5 µg/ml Hydrocortisone), 1% Pen/Strep	HMLE, HMLE-Twist1, HMLE-Ras, HMLE-Twist1-Ras, HMLE-neuNT
Blast-maintenance medium	Standard PC-medium, 10 µg/ml blasticidin	HMLE-Twist1-ER, HMLE-Snail1-ER and derivatives (sorted populations, PTEN-KO

Name	Composition	Cell line
		and PTEN-WT single cell clones)
EMT-Induction medium	Standard PC-medium, 10 µg/ml Blasticidin, 20 nM 4-hydroxytamoxifen	HMLE-Twist1-ER, HMLE-Snail1-ER and derivatives (sorted populations, PTEN-KO and PTEN-WT single cell clones) during EMT-induction
GPX4-KO maintenance medium	Standard PC-medium, 1 µM Liproxstatin	*GPX4*-KO and *GPX4*-WT single cell clones of HMLE and HMLE-Twist1 cells
Puromycin-selection medium	Standard PC-medium, 1 µg/ml puromycin	HMLE-derivatives transduced with pLVX-puro or pTRIPZ-vectors
shRNA-induction medium	Standard PC-medium, 1 µg/ml puromycin, 0.5 µg/ml doxycycline	HMLE-derivatives transduced with pTRIPZ-vectors
Standard DMEM	DMEM, 10% FCS, 1% 1% Pen/Strep	HEK293T
Standard DMEM/F12	DMEM/F12, 10% FCS, 1% Pen/Strep	MCF7, T-47D, MDA-MB-468, MDA-MB-231, MDA-MB-157
Survival Medium	Standard PC-medium, 0.5% FCS, 10 µM Forskolin, 3 µM Y-27632	Primary mammary epithelial cells for first 5 days of initial seeding (after thawing and sorts in 2D and 3D)
Primary cell maintenance Medium	Standard PC-medium, 10 µM Forskolin	Primary mammary epithelial cells after 5 days of initial seeding

3.2 Cell Counting

For experiments that required specific cell numbers, a 10 µl aliquot of cell suspension was pipetted into the grid chamber of a KOVA Glasstic Slide and live cells of three large grids, discriminated based on morphology and intracellular granularity, were counted using a 10x objective on a Leica DM IL Led light microscope. The number of cells per ml was determined by counting three aliquots

of cell suspension, averaging the counted three large grids within each aliquot and then averaging the means of the three aliquots multiplied by 10^4.

3.3 Freezing and thawing of cells

After centrifugation of the desired amount of passaged cells, cells were resuspended in ice-cold Freezing Medium, 1 ml cell suspension per cryotube was added on ice and cooled to -80°C in ice-cold freezing containers. For long-term storage, cells were transferred to liquid nitrogen. For re-cultivation, cells were quickly thawed in a 37°C water bath, transferred to 3 ml cell culture medium and centrifuged. After aspirating the supernatant, cells were resuspended in medium and plated in 6-cm dishes. The next day, the medium was refreshed in order to remove dead cells and cells were cultivated as described.

Freezing Medium: 50% FCS, 40% respective cell culture medium, 10% DMSO

3.4 3D-culture in collagen gels

To model growth in a physiological environment, cells were grown in a 3D-environment in a collagen-based matrix (3D collagen gels). 3D collagen gels were prepared and cultured as previously described with some minor modifications (Linnemann et al., 2015). 24-well plates were coated for 30 sec with a siloxane coating solution and rinsed three times with PBS and once with sterile Milli-Q water. After trypsinization, cells were filtered through a 40 µm cell strainer to remove cell clumps. The desired number of cells in growth medium was mixed with neutralizing solution (one-tenth of the volume of collagen I) and collagen I at a final concentration of 1.3 mg/ml. 400 µl of this mixture was pipetted per well into siloxane-pre-coated 24-well plates and allowed to polymerize for 1h at 37°C. 500 µl medium and if necessary, 100 µl 10x concentrated supplements were carefully added to the solidified collagen gels to reach a final concentration of 1x of the respective supplements (total volume of gel and medium 1 ml). Detachment of 3D collagen gels was achieved by surrounding the gel with a pipet tip prior to carefully shaking the plate. For each experimental condition, three to four collagen gels were prepared. For primary cells, 5000 primary bulk cells or sorted luminal progenitor (LP) or basal B+ were seeded in 3D collagen gels and survival medium (see *Table 1*)

was added for five days before starting any treatment in primary cell maintenance medium. Seeding of primary cells into 3D collagen gels was kindly performed by Lisa Meixner (Mammary Stem Cells, Institute of Stem Cell Research, Helmholtz-Center Munich). For *GPX4*-knockdown cells, 500 cells were seeded per gel in Standard PC-medium containing DMSO as solvent control or in sh-RNA induction medium containing 0.5 µg/ml doxycycline (Dox). For *GPX4*-knockout cells, 675, 225 and 75 cells were seeded per gel in Standard PC-medium (−Lip1) or supplemented with 500 nM Lip1 (+Lip1) and after three days, all gels were washed twice with PBS. For the +/−Lip1 condition, supplementation with 500 nM Lip1 was removed from the Standard PC-medium. For 3D-collagen gels, treatment medium was replaced every 2-3 days and cells were cultured for 8-12 days. Pictures of single colonies grown in 3D collagen gels were taken on a Leica DM IL Led microscope using 5- to 10-fold magnification.

Siloxane coating solution: n-heptane, 25 g/l 1,7-Dichlorooctamethyltetrasiloxane

Neutralizing Solution: 500 mM HEPES in 11x PBS

3.5 Cell density experiments

For initial cell density experiments, cells were seeded in 96-well plates at a cell density of 3000 (high, hi), 1000 (intermediate, med) and 333 (low) cells. For cell density experiments in other well sizes and in dishes, if not otherwise stated, the number of cells to be seeded in a particular format [a] at a high, intermediate or low cell density was calculated using the following equation:

$$Number\ of\ cells\ to\ be\ seeded\ in\ [a] = \frac{Growth\ area\ [a]}{Growth\ area\ [96-well]} \times Reference\ cell\ number\ [96-well]$$

Table 2 shows the cell culture format with respective growth areas and the calculated seeding number (rounded), using 3000 seeded cells (high cell density) in a 96-well as reference cell number.

Table 2: Overview of calculated cell densities depending on the cell culture format and growth area

Format [a]	Growth area [cm^2]	Number of cells to be seeded in [a]
96-well (reference)	0.32	3×10^3
24-well	1.9	1.8×10^4
12-well	3.8	3.6×10^4
6-well	9.5	9×10^4
6-cm	21	2×10^5
10-cm	55	5.16×10^5
15-cm	145	1.4×10^6

3.6 Cell viability assay in 96-well plates

Cell viability assays using CellTiter-Glo were performed to determine the viability of cells upon treatment with chemical compounds such as small molecule inhibitors or upon genetic manipulations such as knockout, knockdown or overexpression of genes. The CellTiter-Glo assay is a luciferase-based assay that determines the number of viable cells by measuring ATP levels, which correlate with the amount of metabolically active cells. For this purpose, 100 µl cell suspension at respective, indicated cell density was seeded per well in a 96-well plate (3-6 technical replicates). For cell lines, the respective treatment was started the next day for 20-24h while for primary cells, treatment was performed 48h after seeding. Solvent control, usually DMSO, served as a control treatment. For *GPX4*-knockout cell lines, that were maintained in GPX4-KO maintenance medium (Table 1) which served as a control treatment, Lip1 was removed from culture medium on the day of plating into viability assays. For rescue-experiments, chemical compounds were added during RSL3-treatment with the exception of Rosiglitazone (ROSI), Oleic Acid (OA), and Atglistatin (ATGLi). For these compounds, cells were additionally pre-treated for 24-48h in 96-wells and/or prior to seeding into the viability assay. For cell scattering experiments using the E-cadherin neutralizing antibody HECD-1, cells were 24h pre-treated with 1 µg/ml HECD-1 prior to plating cells into the viability assay. HECD-1 treatment was applied during viability assay as well. For *GPX4*-knockdown experiments, sh-nt and sh-GPX4 containing HMLE 24^{hi} cells were seeded at indicated cell densities in 96-wells in respective medium (Table 1). The next day, 0.5 µg/ml Dox-treatment was applied for 48h prior to the addition of 10 nM RSL3 or 0.01% DMSO for 24h in presence of Dox. For all experiments using cell

lines, except for *GPX4*-knockdown cells, 48h after plating and after visual inspection, cell viability was measured using the CellTiter-Glo assay with a slightly modified protocol. The assessment of cell viability was performed 72h after plating for primary cells and 96h after plating for Dox-induced *GPX4*-knockdown HMLE 24^{hi} cells. To do so, the growth medium was removed and replaced by 50 µl DMEM/F12 and 50 µl (1 volume) CellTiter-Glo reagent was added. The contents of the well were mixed for 2 min at RT on an orbital shaker, followed by an incubation of 30-40 min at RT in the dark to allow sufficient lysis of the adherent cells and stabilization of the luminescent signal. After an additional 2 min mixing on an orbital shaker, 95 µl of the supernatant was transferred to white opaque 96-well plates and the luminescence signal was immediately measured on a luminometer using luciferase-specific settings and an integration time of 0.25 sec per well. Wells without supernatant served as blank control. Measured blank controls were averaged and subtracted from measured RLU values. Then, obtained RLUs of technical replicates were averaged and normalized to respective solvent control (mostly DMSO) or Lip1 control.

CellTiter-Glo reagent: 1 mix of CellTiter-Glo buffer and CellTiter-Glo substrate

3.7 Cell viability assay in 24-well plates

Cell viability of HMLE 24^{hi} cells containing Dox-inducible shRNA against GPX4 was assessed by counting viable cells (see *Section 3.22.3* and *3.23.2)*. To do so, HMLE 24^{hi} cells containing shRNAs (sh-nt and sh-GPX4) were seeded in triplicates in 24-well plates at a low (1200 cells) or intermediate (3600 cells) cell density in puromycin selection medium (Table 1). The next day, shRNA expression was induced by 0.5 µg/ml Dox-treatment. After 48h Dox-treatment, cells were additionally treated with 10 nM RSL3 or 0.01% DMSO (solvent control), the next day trypsinized and total cell number assessed by counting (see *Section 3.1* and *3.2*).

3.8 Cell proliferation in 96-well plates

To measure cell proliferation, HMLE and HMLE-Twist1 cells were plated at low, intermediate and high cell density in 96-wells (10 technical replicates per timepoint and cell density) (see *Section 3.5*). Proliferation was monitored every 24h over a

period of 96h using CellTiter-Glo assay (see *Section 3.6*). Growth medium was refreshed every 24h. Data obtained was normalized to the 24h time point for every cell density within each cell line.

3.9 Co-culture

Co-culture experiments were employed to assess whether cells seeded at high cell density secrete a soluble factor protecting them from cell death. To do so, a co-culture system using transwell inserts with 8 µm pore size was employed, thereby separating cells seeded at the bottom well from those seeded into the upper transwell. Of note, HMLE 24^{hi} cells containing shRNAs against GPX4 or non-targeting shRNAs were first plated in 6-well plates and the next day treated with 0.5 µg/ml Dox for 24h to induce shRNA expression prior to seeding cells into co-culture experiments with further Dox-stimulation. For co-culture experiments, 500 µl cell suspension of 2 x 10^3 cells (low cell density) was seeded in triplicates into 24-well plates. After 1h, transwell inserts were placed into the well and 500 µl of 2 x 10^4 cells (slightly more than high cell density) were added into the transwell inserts for co-culture, while 500 µl medium was added to control wells containing only cells in the bottom well. The next day, complete medium was replaced with treatment medium (0.1% DMSO or 100 nM RSL3 for HMLE and HMLE-Twist1 cells and 0.01% DMSO or 10 nM RSL3 for HMLE 24^{hi} cells containing shRNAs) and cells were treated for 20-24h. After visual inspection, inserts were fixed and stained with the Hemacolor Rapid staining set and cell viability assessed using CellTiter-Glo assay as described in *Section 3.6* with minor modifications. 100 µl basal DMEM/F12 together with 100 µl CellTiter-Glo reagent was applied to 24-well plates. After incubation, 50 µl of supernatant was diluted in 50 µl basal DMEM/F12 in white opaque 96-well plates before measuring luminescence as described. For Hemacolor Rapid staining of insert, cells grown in inserts were fixed by applying the methanol-based Fixing Solution for 30 sec. After a brief wash in Milli-Q water, Staining Solution 1 was added to inserts for 2 min to stain the cytoplasm and after washing with Milli-Q, Staining Solution 2 was employed for another 2 min to stain nuclei. Inserts were washed using a buffer sold with the Kit and inserts air-dried overnight prior to taking pictures on a Leica DM IL LED microscope.

3.10 Viability assays using sticky Culture-Inserts with 2 wells

In order to assess whether resistance mechanisms to RSL3 were related to cell-cell adhesions or depended on the size of growing colonies, $3x10^4$ cells were either seeded triplicates in one well of a sticky culture-insert (Ibidi) with a growth area of 0.22 cm^2 placed in 6-cm dishes (to yield one large dense, compact colony) or the same cell number was directly plated in 6-cm dishes (to yield several sparse, small colonies). 3 $x10^4$ cells represents approximately 450 seeded cells in a 96-well (see *Section 3.5*), thus at an intermediate-low seeding density at which cells were sensitive to RSL3 treatment. The next day, the cell culture-inserts were removed and 0.1% DMSO or 100 nM RSL3 treatment applied for 18h. Viability was assessed by CellTiter-Glo assay applying 200 µl basal DMEM/F12 and 200 µl CellTiter-Glo reagent as described in *Section 3.6*. For measurement, 20 µl of supernatant were diluted in 80 µl basal DMEM/F12 in white opaque 96-well plates.

3.11 Methods working with 3D collagen gels

3.11.1 Fixation of 3D collagen gels

After a period of 8-12 days of culturing cells in 3D-collagen gels, growth medium was removed and gels were washed with 1 ml PBS. All subsequent steps were performed using an orbital shaker. After removal of PBS, gels were fixed with 1 ml 4% PFA for 15 min, washed again briefly with PBS prior to three subsequent PBS washing steps for 10 min each. Gels were kept in PBS at 4°C until further use.

4% PFA: 1:4 dilution of 16% paraformaldehyde in PBS

3.11.2 Carmine Staining

To visualize colonies grown in 3D collagen gels, PFA-fixed gels were stained with 1 ml carmine solution overnight at RT on an orbital shaker and kept in carmine solution at 4°C until further use. To image colonies, gels were transferred to microscopy slides and excess solution removed with a pipette and a kimwipe tissue. 6-8 images per gel were taken on a Zeiss SteREO Lumar.V12 microscope with a NeoLumar S 0.8 objective with a 10- to 20-fold magnification. Images were stitched using Hugin or Image Composite Editor Software to obtain a whole mount picture and colonies were counted using ImageJ software. First, a binary image (black/white) was

produced and then, by setting a manual threshold, areas containing colonies (black) were extracted from the background. Colonies were automatically counted by using the “Analyze particles” feature setting the area between 400 and 90000 μm^2 (20 – 300 µM diameter) and a circularity of 0.5-1.

Carmine solution: 1g carmine, 2.5 g aluminum potassium sulfate in 500 ml Milli-Q water, 1 crystal of Thymol

3.11.3 3D immunofluorescence

All steps were carried out on an orbital shaker and each washing step with 1 ml PBS washing was performed for 10 min. First, cells within collagen gels were permeabilized for 10 min using 1 ml permeabilization solution and washed twice with PBS before applying 1 ml blocking solution for 2-3h. Gels were washed with PBS prior to incubation with 100 µl primary antibody solution overnight at 4°C. After three PBS washing steps, respective secondary antibody solutions (100 µl) were applied for 2-3h at RT, followed by washing gels twice with PBS. To stain nuclei, 100 µl of DAPI solution was added for 5 min before washing gels two times with PBS and once with Milli-Q water for 5 min. Collagen gels were placed on microcopy slides and excess water was carefully removed using a pipette and kimwipe tissues. Two drops of Aqua-Poly/Mount mounting medium were applied to gels prior to covering with a cover slip. Slides were dried for 1-2 days in the dark at RT before sealing with nail polish and storing at -20°C until imaging. Images were taken on an FLUOVIEW FV1200 inverted Confocal Laser Scanning Microscope using FV10-ASW software and 20-fold magnification (UPlanSApo 20x objective lense). Images were processed with Gimp 2.8.22.

Permeabilization solution: 0.2% Triton X-100, PBS

Blocking Solution: 10% donkey serum, 0.1% BSA, PBS

Antibody solution: Respective antibody diluted in 0.1% BSA in PBS

DAPI Solution: 167 ng/ml DAPI in PBS

3.12 Methods working with proteins

3.12.1 Protein Isolation

To assess protein expression levels, whole cell lysates using RIPA buffer lysis were prepared. To do so, cells were seeded in 10- or 15-cm dishes at indicated cell densities as calculated in *Section 3.5*. If cells were treated or starved, cells were washed once with PBS 24h after seeding and the medium was changed to respective treatment medium or starvation medium for another 20-24h. 48h after seeding, proteins were isolated with all subsequent steps performed on ice. Cells were washed once with PBS, then 1 ml PBS was applied to cells to facilitate scraping with a cell scraper prior to collection of cells in 1.5 ml Eppendorf tubes. Cells were pelleted by centrifuging at 4°C at 2500 x g in Heraeus Fresco 21 centrifuge for 5 min. The supernatant was removed and protein lysis buffer, usually 30 – 200 µl depending on cell pellet, was applied and vigorously mixed by vortexing. To further increase lysis, samples were frozen for at least 1h at -80°C. Then, samples were thawed on ice and cell debris pelleted by centrifugation at 4°C at 14000 x g for 10 min. The supernatant containing the protein fraction was transferred to a clean tube. Protein extracts were stored at -80°C.

Starvation medium: basal DMEM/F12

RIPA buffer: 50 mM Tris pH 8.0, 150 mM NaCl, 1% (w/v) NP-40, 0.5% (w/v) sodium deoxycholate, 0.1% (w/v) SDS, 5 mM EDTA pH 8.0, Milli-Q water

Lysis buffer: RIPA buffer, freshly added Phosphatase Inhibitor Cocktail 2 and 3 and Protease Inhibitor Cocktail (each 1:100), 4°C

3.12.2 Protein concentration measurement

Protein concentration was measured using the colorimetric, detergent-compatible DC Protein Assay which is based on the Lowry method (Lowry et al., 1951). Protein standards (0.5 µg, 1 µg, 2 µg, 5 µg, 7.5 µg, 10 µg, and 25 µg) from 1 mg/ml BSA/RIPA stock, 3 µl RIPA buffer as well as 3 µl of each sample were pipetted in duplicate into a 96-well plate. The assay was then performed according to the manufacturer's instructions and the absorbance was measured at 750 nm on a microplate reader. The concentration of the protein samples was calculated from a standard curve that was obtained using the RIPA buffer only as blank and the protein standard as a reference.

3.12.3 SDS-PAGE

SDS-PAGE is used to separate proteins samples based on their molecular weight. A 12.5% separating SDS-polyacrylamide gel was prepared in glass plates of the Mini-PROTEAN Tetra Cell system and then overlaid with isopropanol until polymerization. Then, isopropanol was removed and the stacking gel, as well as a 10-well or 15-well comb, were added. 10-20 µg of each protein sample was mixed with 5x SDS loading buffer and then proteins were denatured for 5 min at 95°C. Gels were loaded with samples and with 8 µl of PageRuler Prestained Protein ladder serving as a reference for protein size. Gel electrophoresis was run for 60-90 min in 1x Running buffer for 120V.

12.5% separating gel: 1.95 ml 30% Rotiphorese, 2.75 ml Milli-Q water, 1.25 ml 1 M Tris pH 8.8, 50 µl 10% (w/v) SDS, 3.75 µl Temed, 37.5 µl 10% (w/v) APS

Stacking gel: 416.5 µl 30% Rotiphorese, 1.73 ml Milli-Q water, 312.5 µl 1 M Tris pH 6.8, 25 µl 10% (w/v) SDS, 2.5 µl Temed, 12.5 µl 10% (w/v) APS

5x SDS loading buffer: 30% (v/v) Glycerol, 10% (w/v) SDS, 0.25 M Tris/HCl pH 6.8, 0.05% (w/v) bromophenol blue, 10% (v/v) β-Mercaptoethanol, Milli-Q water

1x Running buffer: 25 mM Tris, 192 mM Glycine, 0.1% (w/v) SDS, Milli-Q water

3.12.4 Immunoblotting

Proteins separated by SDS-PAGE were transferred to a PVDF membrane using a Tank/Wet Blotting System from Bio-Rad. The PVDF membrane was activated in methanol prior to assembling the wet blot according to manufacturer's instructions. Electroblotting was performed with 300 mA for 1.5 to 2 hours in an ice-cooled chamber using ice-cold 1x Transfer buffer. The PVDF membrane was briefly washed with TBS/T on a 2D Rocker and subsequently, depending on the antibody requirements, blocked with 5% milk or 5% BSA for 1h. Membranes were incubated in a 50 ml falcon with primary antibody solution according to manufacturer's requirements overnight at 4°C on a horizontal roller. The next day, membranes were washed three times with TBS/T for 10 min and respective HRP-conjugated secondary antibodies were applied in 5% milk or 5% BSA for 1h at RT. Membranes were again washed three times with TBS/T and once with TBS for 10 min prior to applying 600 µl ECL Prime Western Blotting Detection Reagent per membrane according to manufacturer's instructions. Chemiluminescence was visualized on a

ChemiDoc Imaging System using the Image Lab software. ImageJ software was used for densitometric analysis of protein bands. Briefly, the grey mean value was measured using the same frame for the background above each protein band and each protein band across one protein lane. The measured values were first inverted (255-grey mean value) and then the background value subtracted from the respective protein band value. Obtained values were normalized to values of beta-actin loading control.

1x Transfer buffer: 25 mM Tris, 192 mM Glycine, 20 % (v/v) Methanol

10x TBS: 1.5 M NaCl, 0.1 M Tris, MilliQ-water, pH 7.2-7.4 with HCl

1x TBS/T: 10% (v/v) 10x TBS, 0.1% (v/v) Tween 20, MilliQ-water

5% skim milk: 5% (m/v) non-fat dried milk powder in 1x TBS/T

5% BSA: 5% (m/v) bovine serum albumin fraction V in 1x TBS/T

3.13 Proteomics

To assess changes in the proteome of cells seeded in cell density and upon RSL3-treatment, a proteomic study was kindly performed by Dr. Christine von Toerne and Dr. Ann-Christine Koenig at the Research Unit Protein Science headed by Dr. Stefanie Hauck at the Helmholtz Center Munich. For each condition in the study, four independent biological replicates were prepared, measured and analyzed.

3.13.1 Conditions for proteomics

HMLE and HMLE-Twist1 cells were seeded in 10-cm dishes in a cell density that corresponds to 3000 (high), 1000 (med) and 333 (low) seeded cells in 96-well plates (see *Section 3.5*). For high cell density, cells were seeded in one 10-cm dish. For intermediate cell density, cells were seeded in five 10-cm dishes, two serving as cell density control and three for RSL3 treatment. For low cell density, cells were plated in four 10-cm dishes. The next day, cells seeded in three 10-cm dishes at intermediate cell density were treated for 5h with 100 nM RSL3 before isolating proteins. For all other conditions, the medium was refreshed and protein isolation was performed 48 hours after plating into dishes. Proteins extracts from the same condition were pooled during protein isolation. Protein isolation and concentration measurement were carried out as indicated in *Sections 3.12.1* and *3.12.2*. Of each

sample, 10 µg protein were pipetted into Protein LoBind 1.5 ml Eppendorf tubes, resuspended with 20 µl lysis buffer (see *Section 3.12.1*) and stored at -80°C until the proteomic study was performed.

3.13.2 Sample preparation for mass spectrometry

A modified filter-aided sample preparation (FASP) protocol was used to enzymatically digest each sample (10 µg) according to published protocols (Grosche et al., 2016; Wiśniewski et al., 2009). Peptides were frozen at -20°C until the measurement by mass spectrometry.

3.13.3 Measurement by mass spectrometry

The measurements by mass spectrometry (MS) were carried out in data dependent (DDA) mode. A Q Exactive (QE) high field (HF) mass spectrometer (Thermo Fisher Scientific) was used to obtain MS data. Briefly, about 0.5 µg of each sample was automatically supplied to the online coupled RSLC (Ultimate 3000, Thermo Fisher Scientific) HPLC system. A nano trap column was employed (300 µm inner diameter (ID) × 5 mm, packed with Acclaim PepMap100 C18, 5 µm, 100 Å; LC Packings, Sunnyvale, CA) prior to separation by reversed phase chromatography (Acquity UPLC M-Class HSS T3 Column 75µm ID x 250mm, 1.8µm; Waters, Eschborn, Germany) at 40°C. Peptides were eluted from the column at a rate of 250 nl/min applying a gradient of increasing acetonitrile concentrations in 0.1% formic acid ranging from 3% to 41 % over 105 min. A high-resolution (60 000 full width at half-maximum) MS spectrum was obtained with a mass range from 300 to 1500 m/z. The value for the automatic gain control target was 3 x 106 and the maximum injection time was 50 ms. From the high-resolution MS prescan, the ten most abundant peptide ions were chosen for fragmentation (MS/MS) in case that they were at least doubly charged, with a dynamic exclusion of 30 sec. The record of MS/MS spectra was performed at 15 000 resolution whereby automatic gain control target was set to 1 x 105 and a maximum of 100 msec injection time. All spectra were run at a normalized collision energy set to 28 and acquired in profile type.

3.13.4 Label-free quantification

The recorded spectra of each sample were analyzed with the Progenesis QI software for proteomics (Version 3.0, Nonlinear Dynamics, Waters, Newcastle upon

Tyne, U.K.) for label-free quantification according to a previous description (Grosche et al., 2016) with a modification regarding peptide identification. Briefly, after export of MS/MS spectra from the Progenesis QI software, peptide identification occurred against the SwissProt human database (Release 2017.02, 553473 sequences). Search parameters employed were 10 ppm peptide mass tolerance, 20 mmu fragment mass tolerance and only one missed cleavage site was allowed.
Cysteine carbamidomethylation was set as fixed modification while methionine oxidation and deamidation of asparagine and glutamine were permitted as variable modifications. A false discovery rate (FDR) of 1% was used in the Mascot integrated decoy database search.

3.13.5 Analysis of proteomics

For data analysis, normalized abundances were averaged between the four replicates for each protein. Within each cell line (HMLE and HMLE-Twist1), a ratio of the averaged abundances between low and high cell density conditions as well as between 5h RSL3-treated and intermediate control cell density condition was calculated. Then, proteins were filtered for a regulation of at least 1.5-fold up- or downregulation within each ratio (for upregulation ratio higher than 1.5, for downregulation ratio below 0.67). Statistical analysis was performed using log2 transformed normalized abundances and an unpaired, two-tailed T-test with Welch's correction was applied.
Proteins with a p-value below 0.05 and a 1.5-fold up or downregulation for both cell lines were considered for GO term enrichment analysis using DAVID (Huang et al., 2009b, 2009a). Interesting GO terms and potential hit proteins were submitted to extensive literature research prior to validation and further functional analyses.

3.14 Flow cytometry

3.14.1 Analysis of cells by flow cytometry using fluorescent probes

Flow cytometry was employed to assess ROS levels (lipid ROS, mitochondrial ROS, and general ROS) by fluorescent dyes that increase or shift fluorescence upon oxidation by ROS and therefore serve as a proxy measure of ROS levels. Further, ThiolTracker Violet was employed to assess reduced glutathione levels. Glutathione represents the majority of free thiols and Thioltracker Violet reacts with free thiols, therefore it can be used a proxy for reduced glutathione content. In addition, the

neutral triacylglyceride (TAG) content, which represents the lipid droplet (LD) content of cells, was measured by staining with BODIPY 493/503. Cells were seeded in 6-cm dishes at indicated cell densities (see *Section 3.5*), the next day medium was refreshed and 48h after plating, cells were analyzed. Treatment with RSL3, oleic Acid and cumene hydroperoxide (CH), serving as a positive control for lipid peroxidation, was performed 24h to 48h after plating for the indicated time points. For *GPX4*-knockout clones which were plated in 1 µM Lip1-containing medium or in medium not containing Lip1 for induction of ferroptosis, the analysis was performed 24h after plating. For the respective staining, cells were washed once with PBS before applying 1 ml 2 µM BODIPY-C11 581/591, 5 µM MitoSox or 5 µM CellROX Deep Red staining solution in medium for 30 min at 37°C in a tissue incubator to assess lipid peroxidation, mitochondrial ROS or general ROS respectively. For assessment of reduced glutathione, cells were stained with 10 µM ThiolTracker Violet in PBS for 30 min at 37°C and for LD staining, 2 µM BODIPY 493/503 staining solution in medium was applied for 15 min at 37°C. One sample per cell line was not stained in order to serve as a reference to draw negative and positive gates. Cells were washed with PBS, harvested by trypsinization, resuspended in 120-150 µl ice-cold FACS buffer and filtered through a 35 µm cell strainer into 5 ml round-bottom FACS tubes on ice. To distinguish between live and dead cells, cells were incubated for 5 min with 1 µM Sytox blue prior to analysis. For Thioltracker Violet staining, live/dead cell discrimination was performed by 1 µg/ml Propidium iodide (PI) staining for 5 min. Cells were analyzed on a FACSAria IIIu using laser and filters according to manufacturer's recommendations (see *Section 2.5*). First, cell doublets and debris were excluded by applying forward and side scatter gates and then cells were gated on the live population (Sytox-negative or PI-negative gates). At least 10000 events per sample were recorded for the live population. Data analysis was conducted using FlowJo Software.

FACS buffer: 1% bovine serum albumin fraction V in PBS, sterile filtered

3.14.2 Fluorescence-activated cell sorting (FACS)

Fluorescence-activated cell sorting is a method to separate single cells based on fluorescent labeling. FACS was performed on a FACSAria IIIu flow cytometer using

the 70 µm nozzle and set-ups according to manufacturer's recommendations. 7-AAD employed for live/dead cell discrimination was excited using the 488 nm laser and detected by the 695/40 nm filter, while GFP, also excited by the 488 nm laser, was detected by the 530/30 nm filter. Transfected cells (see *Section 3.23.1*) were trypsinized, collected in 500 µl ice-cold FACS buffer and strained through a 35 µm filter. 5 µl 7-AAD staining solution was applied for at least 10 min and gating was performed as described in *Section 3.14.1*. Gates for GFP were drawn using non-transfected cells (GFP-negative) and GFP-positive cells were sorted into 2 ml complete growth medium using purity mode. Sorted cells were centrifuged for 5 min at 490 x g at 4°C and resuspended in complete growth medium prior to subsequent experiments.

3.15 Cell cycle analysis

For cell cycle analysis, HMLE and HMLE-Twist1 cells were seeded at low, intermediate or high cell density in 10-cm dishes (see *Section 3.5*). After 48h, cells were harvested by trypsinization. Cells were resuspended in 600 µl PBS and then fixed by adding drop-wise 1.4 ml ice-cold (-20°C) 100% ethanol while mixing cells by vortexing. Cells were incubated overnight at -20°C. The next day, fixed cells were pelleted by centrifugation at 850 x g for 10 min, washed twice with PBS and resuspended in 100 µl PBS. To remove RNA, fixed cells were incubated with 50 µg/ml RNase A for 20 min at 37°C prior to staining of DNA with 50 µg/ml PI at 4°C overnight. The next day, fixed and PI-stained cells were washed 1x with PBS, resuspended in FACS buffer and analyzed by flow cytometry as described in *Section 3.14.1*. A linear scale was used to visualize PI staining, thus cell cycle distribution.

3.16 Detection of lipid peroxidation using the Click-iT™ Lipid Peroxidation Imaging Kit

The Click-iT™ Lipid Peroxidation Imaging Kit is a method to detect lipid-peroxidation-derived protein modifications. To do so, cells are incubated with an alkyne-modified linoleic acid (LAA, Component A) which is a polyunsaturated fatty acid that incorporates into cell membranes. In the presence of lipid peroxidation, oxygenation of LAA leads to chemical reactions with intracellular proteins. Modified proteins can be subsequently detected with Click-iT® chemistry. As a result, the

fluorophore Alexa Fluor 488 yields green fluorescence. All steps were performed according to the manufacturer's instructions.

3.16.1 Detection of lipid peroxidation by immunofluorescence

For detection of lipid peroxidation by immunofluorescence, coverslips were placed into 24-well plates, covered with 1% gelatin and then incubated overnight at 4°C. The next day, gelatin was removed and coverslips were washed three times with PBS. Then, 1.5 x 10^4 HMLE or HMLE-Twist1 cells were seeded in 24-well plates containing gelatin-coated coverslips and were grown for 48h. Cells were incubated for 1.5h with 50 µM LAA together with 0.1% DMSO, 100 nM RSL3, 500 nM Fer1 or with a combination of RSL3 and Fer1 at 37°C in a tissue incubator. As a positive control, cells were incubated for 1.5h with 50 µM LAA together with 100 µM CH with or without 500 nM Fer1. After three washing steps with PBS, cells were fixed for 15 min with 4% PFA at RT followed by three subsequent washing steps using PBS. After applying the permeabilization solution for 2 min at RT and three additional washing steps, blocking solution was applied for 1 hour at RT to reduce nonspecific background. Meanwhile, Click-iT™ reaction cocktail was freshly prepared in the order as listed in Table 3 according to manufacturer's instructions. After two washing steps, 300 µl of the Click-iT™ reaction cocktail was added per coverslip and incubated for 30 min at RT protected from light. The reaction cocktail was removed and coverslips were washed four times with PBS. DAPI solution was applied to stain nuclei and then coverslips were dipped 10 times in PBS followed by dipping the coverslips 10 times in Milli-Q water. Coverslips were mounted on microscopy slides using Aqua-Poly/Mount mounting medium and dried at RT prior to storage at -20°C. Images were acquired on a Zeiss Axio Imager M.2 microscope using Zen Pro Software and 20-fold magnification. Images were edited with Gimp 2.8.22.

Table 3: Composition of Click-iT™ reaction cocktail

Click-iT™ reaction cocktail	**1x**
1X Click-iT® reaction buffer (Component C)	258 µl
CuSO4 (Component D)	12 µl
Alexa Fluor® 488 azide (Component B)	0.72 µl
1X Click-iT® buffer additive (Component E)	30 µl
Total Volume	300 µl

4% PFA: 1:4 dilution of 16% paraformaldehyde in PBS

Permeabilization solution: 0.2% Triton X-100, PBS

Blocking Solution: 10% goat serum, 0.1% BSA, PBS

DAPI Solution: 167 ng/ml DAPI in PBS

3.16.2 Detection of lipid peroxidation by flow cytometry

For detection of lipid peroxidation by flow cytometry, 8 x 10^4 HMLE or HMLE-Twist1 cells were seeded per well of a 6-well plate. After 48h, cells were treated for 1.5h with 50 µM LAA together with 0.1% DMSO, 100 nM RSL3, 500 nM Fer1 or with a combination of RSL3 and Fer1 at 37°C in a tissue incubator. Then, cells were washed three times with PBS, harvested by trypsinization and transferred into 5 ml round-bottom FACS tubes on ice. All subsequent steps were performed in FACS tubes, washed each time with PBS and pellet by centrifugation prior to the next step. Cells were fixed, permeabilized and blocked as described in *Section 3.16.1*. Then, 300 µl of the Click-iT™ reaction cocktail (Table 3) was added per FACS tubes as described in *Section 3.16.1*. After 30 min incubation at RT, protected from light, cells were washed twice with PBS and pelleted. Cells were resuspended in 120-150 µl ice-cold FACS buffer and filtered through a 35 µm cell strainer into 5 ml round-bottom FACS tubes on ice. Then, FACS analysis was performed as described in *Section 3.14.1*. Alexa Fluor 488 fluorescence was analyzed with the 488 nm laser and detected by the 530/30I filter.

FACS buffer: 1% bovine serum albumin fraction V in PBS, sterile filtered

3.17 GPX4-specific enzyme activity

The GPX4-specific enzyme activity was kindly measured by Dr. Irina Ingold from the group of Dr. Marcus Conrad at the Institute of Developmental Genetics at the Helmholtz Center Munich. GPX4-activity was determined in an enzymatically coupled test of whole cell lysates as previously described (Roveri et al., 1994). Thereby, GPX4 reduces phosphatidylcholine hydroperoxide (PCOOH), a GPX4-specific substrate. GPX4 is recycled by reduced GSH which in turn gets oxidized. Oxidized GSH (GSSG) is reduced by glutathione reductase in presence of non-limiting concentrations of NADPH which gets oxidized. During the reaction, a

decrease in reduced NADPH can be measured spectrometrically at λ=340 nm. To do so, 2-4 x 10^6 epithelial (–TAM) and TAM-induced mesenchymal HMLE-Twist1-ER 24^{hi} cells were seeded in 15-cm dishes (4 technical replicates per cell line). When cells reached 80% confluency, cells were washed twice with ice-cold PBS prior to harvest cells by scraping in PBS. After pelleting cells and removing the supernatant, cell pellets were snap-frozen in liquid nitrogen to retain GPX4 enzymatic activity and were stored at -80°C. After resuspension of cell pellets in 100 µl protein lysis buffer and incubation for 15 min on ice, homogenate was centrifuged for 10 min at 18400 x g at 4°C followed by a transfer of the supernatant to a new tube. A reaction mix was prepared consisting of 1 ml assay buffer, 200 µM NADPH, 3 mM GSH, 0.6 U/ml glutathione reductase and 20-30 µM PCOOH. 50 µl of protein supernatant was added to the reaction mix. GPX4 enzyme activity was determined spectrometrically at λ=340 nM for 10 min on a SpectraMax microplate reader (Molecular Device GmbH), thereby measuring the decrease in NADPH concentration. GPX4-specific activity was calculated by subtracting a background measurement of NADPH without PCOOH addition from measurements containing the reaction mix and protein supernatant. For data normalization, protein concentration was measured of each sample using the Pierce 660 nm Protein Assay Reagent (Thermo Fisher Scientific) according to manufacturer's instructions.

PCOOH: enzymatically oxidized phosphatidylcholine as previously described (Roveri et al., 1994)

Protein lysis buffer: 100 mM KH_2PO_4/K_2HPO_4 (pH7.4), 150 mM KCl, 0.05% CHAPS, 2 mM β-mercaptoethanol, 1% protease inhibitor cocktail

Assay buffer: 100 mM Tris (pH 7.8), 5 mM EDTA, 0.1% Triton X-100

3.18 Assessment of free total thiols and GSH

The measurements of free total thiols and GSH were kindly performed by Dr. José-Pedro Friedman Angeli form the group of Dr. Marcus Conrad at the Institute of Developmental Genetics at the Helmholtz Center Munich.

3.18.1 Assessment of free total thiols

1.5 – 1.6 x 10^5 parental (–TAM) and 1.9 – 2.1 x 10^5 15d TAM-induced mesenchymal

HMLE-Twist1-ER 24^{hi} cells were plated in triplicates in 12-well plates. Two days later, cells were washed twice with PBS prior to addition of 1 ml serum-free and phenol red-free DMEM. 2 µM ERA was applied to wells as a positive control to inhibit x_c^- and thus thiol release. The release of free total thiols into the cell culture medium was assessed at desired time points by collecting 60 µl aliquots and measured as previously described (Bannai and Ishii, 1982). For background measurements, the collected supernatants were mixed with an equal volume of thiol assay buffer and absorbance was directly measured at λ=412 nm on a SpectraMax microplate reader (Molecular Device GmbH). Then, 10 µl of 10 mM 5,5'-dithiobis (2-nitrobenzoic acid) (DTNB) was added on ice to samples and incubated for 2 min prior to a second measurement at 412 nm. As a blank measurement, thiol assay buffer was mixed with serum-free and phenol red-free DMEM. A standard curve to calculate the amount of released thiols was generated by measuring reduced GSH. In order to normalize data, cells were harvested by trypsinization and cell numbers were determined by counting.

Thiol assay buffer: 0.2 M KH_2PO_4/K_2HPO_4, 10 mM EDTA, pH 7.2

3.18.2 Assessment of intracellular total GSH levels

$1.5 – 1.6 \times 10^5$ parental (–TAM) and $1.9 – 2.1 \times 10^5$ 15d TAM-induced mesenchymal HMLE-Twist1-ER 24^{hi} cells were plated in triplicates in 12-well plates. The next day, 2 µM ERA was applied to wells as a positive control to inhibit x_c^- and thus GSH metabolism. After 48h, cells were washed twice with ice-cold PBS. Then, 5% tricholoacetic acid (TCA) was added to cells for 30 min to enable membrane permeabilization of cells that allows the release of low molecular proteins like reduced and oxidized GSH. The supernatant was collected in tubes and TCA was removed by ether extraction. Total GSH levels were measured in the aqueous phase using an enzymatic method as previously described (Tietze, 1969). Thereby, the reduction of 5,5'-dithiobis (2-nitrobenzoic acid) (DTNB) to 2-nitro-5-thiobenzoate (TNB^-) at the expense of NADPH by GSH was measured. To do so, 500 µl of the aqueous phase of each sample was mixed with 1.2 ml thiol assay buffer (see *Section 3.18.1*), 10 µM DTNB, 1 IU glutathione reductase and 3.62 mg/ml NADPH. The total GSH content was measured by assessing the reduction of DTNB to TNB^-, resulting

in a colorimetric intensity change, over a period of 5 min at λ=412 nm absorbance. A GSH standard curve was used to determine the total GSH content. For normalization, proteins content was determined in cells permeabilized with TCA. Therefore, 0.5 M NaOH was added to cells overnight to disrupt cellular membranes to enable the release of proteins. Then, protein concentration was measured using the Pierce 660 nm Protein Assay Reagent (Thermo Fisher Scientific) according to manufacturer's instructions.

3.19 RNA-related methods

3.19.1 RNA Isolation and cDNA synthesis

Cells were grown in 6-well to 6-cm dishes at respective densities. To isolate total RNA, the RNeasy Mini Kit was employed. Briefly, cells were washed once with PBS on ice and 300-350 µl RLT buffer containing 10 µl β-mercaptoethanol per ml RLT was added to dishes on ice. Cells/lysate were scraped using a cell scraper, collected in nuclease-free Eppendorf tubes and shortly frozen at -80°C to enable disruption of cells. Lysates were thawed on ice, loaded on Qiashredder columns to further lyse cells and centrifuged at 14000 x g for 2 min. RNA isolation of homogenized lysates was performed according to the manufacturer's instruction for the RNeasy Mini Kit. In addition, an on-column DNase digestion step to minimize potential DNA contamination using the RNase-free DNase Set was performed. RNA was eluted in 30 µl RNase-free water. RNA concentration and quality was measured on a NanoDrop spectrophotometer at λ=260 nm. Isolated RNA was stored at -80°C.

Up to 1 µg total RNA was reverse transcribed into complementary DNA (cDNA) using the OneScript® Plus cDNA Synthesis Kit according to manufacturer's instruction. For priming, Oligo(dT) primers were used and for quality control, a control without RNA (water control) and one control without the reverse transcriptase (−RT) was run. The reverse transcription reaction was performed in a thermocycler for 60 min at 50°C and terminated at 85°C for 5 min. cDNA was stored at -20°C.

3.19.2 Real-time semi-quantitative PCR (qPCR)

To measure and quantify the expression of different transcripts in a cDNA sample a qPCR reaction using the Power SYBR Green PCR Master Mix was performed. A 10 µl reaction consisting of 2 µl (10 ng) cDNA, 0.25 µl (500 nM) of each, respective

forward and reverse primer, 5 µl 2x SYBR Green reagent and 2.5 µl nuclease-free water was prepared in triplicates for each cDNA sample and primer pair in 384-well plates. The gene *RPL32* was used as internal control to normalize data. For quality controls, cDNA of the water control and –RT control (see *Section 3.19.1*) were included for *RPL32* primers and for each primer pair a water control without any cDNA was prepared. Samples were run in triplicates on a QuantStudio 12K Flex qPCR system using the cycling steps shown in Table 4. By checking the obtained values from control samples and the melting curve for each reaction, quality as well as reaction specificity was assessed and ensured. Obtained data were analyzed using the ΔC_T method (Livak and Schmittgen, 2001; Schmittgen and Livak, 2008) by subtracting the C_T value of the gene of interest from the C_T value of the internal control *RPL32*. The relative fold change of the gene of interest compared to the internal control *RPL32* was calculated with the formula $2^{\Delta CT}$. For illustration of the relative gene expression, the obtained values were multiplied by 1000. Primer sequences used in qPCR reactions were obtained from a public available resource for PCR Primer (PrimerBank: https://pga.mgh.harvard.edu/primerbank/) and are listed in Table 5.

Table 4: Cycling steps for qPCR

Step	Temperature	Duration	Cycles
Initialization	95°C	10 min	1x
Denaturation	95°C	15 sec	40x
Annealing	60°C	30 sec	
Extension	72°C	16 sec	
Melting Curve	70 to 95°C		

Table 5: Primer sequences used for qPCR

Target	Sequence (Forward, Reverse)
ABDH5	ACAGACCTGTCTATGCTTTTGAC, AGGGCACATCTCCACTCTTCA
ACAA2	CTGCTCCGAGGTGTGTTTGTA, GGCAGCAAATTCAGACAAGTCA
CPT1A	ATCAATCGGACTCTGGAAACGG, TCAGGGAGTAGCGCATGGT
GCLC	CTTTCTCCCCAGACAGGACC, CAAGGACGTTCTCAAGTGGG
GPX4	GAGGCAAGACCGAAGTAAACTAC, CCGAACTGGTTACACGGGAA
HMOX1	AAGACTGCGTTCCTGCTCAAC, AAAGCCCTACAGCAACTGTCG

Target	Sequence (Forward, Reverse)
PNPLA2	ATGGTGGCATTTCAGACAACC, CGGACAGATGTCACTCTCGC
SLC7A11	TCTCCAAAGGAGGTTACCTGC, AGACTCCCCTCAGTAAAGTGAC
RPL32	CAGGGTTCGTAGAAGATTCAAGGG, CTTGGAGGAAACATTGTGAGCGATC

3.20 Methods working with bacteria

3.20.1 Transformation of chemically competent bacteria

XL10-Gold and Stabl2 bacteria were stored at -80°C. One aliquot of ultracompetent bacteria of the strains XL10-Gold or Stabl2, if plasmids larger than >10kb were used, were thawed on ice for 5-10 min. Meanwhile, plasmid DNA (less than 1 µg, usually 0.5-1 µl) was placed on the bottom of a fresh 1.5 ml Eppendorf tube on ice. 25 µl bacteria were added to the DNA and incubated for 10 min on ice. Bacteria were exposed to a 30 sec heat shock in a 42°C water bath and immediately placed on ice for 2 min. To allow regeneration of bacteria, 200 µl S.O.C. medium was added prior to incubation on a Thermomixer for at least 60 min at 37°C with constant shaking (1000 rpm). Afterwards, bacteria were plated on LB agar plates containing the appropriate antibiotics (50 µg/ml Kanamycin or 100 µg/ml Ampicillin) for selection and incubated overnight at 37°C for colony formation.

LB Agar: 35 g/l LB Broth with agar powder in MilliQ-water, autoclaved, addition of antibiotics prior to pouring of plates, stored at 4°C

3.20.2 Isolation of bacterial plasmid DNA

A single colony was picked from an LB agar plate (see *Section 3.20.1*) and used to inoculate 3 ml (Mini preparation) or 100 ml (Midi preparation) LB medium containing the appropriate selection antibiotic (50 µg/ml Kanamycin or 100 µg/ml Ampicillin). Cultures were incubated overnight at 37°C with vigorous shaking (120 rpm). Plasmid DNA from the Midi preparation was isolated using the QIAGEN plasmid midi kit according to the manufacturer's instructions and resuspended in 150-200 µl TE buffer. Plasmid DNA from the Mini preparation was isolated using buffers supplied by the QIAGEN Midi Kit. Briefly, 2 ml of overnight grown bacterial culture was transferred to a 2 ml Eppendorf tube and centrifuged for 5 min at 18000 x g at 4°C. After removing the supernatant, cells were resuspended in 300 µl 100 µg/ml RNase

A containing Buffer P1, followed by addition of 300 µl lysis Buffer P2 and lysis of bacteria for 5 min at RT. The lytic process was neutralized by the addition of 300 µl Buffer P3. After centrifugation for 10 min at 18000 x g at 4°C, the supernatant containing plasmid DNA was transferred to a clean, nuclease-free 1.5 ml Eppendorf tube and 600 µl isopropanol was added. The tube was inverted four to five times to precipitate the plasmid DNA prior to pelleting the plasmid DNA for 30 min at 18000 x g at 4°C. The supernatant was removed and plasmid DNA washed once with 500 µl 70% ethanol for 5 min at 18000 x g at 4°C. The supernatant was removed and the open tubes were placed briefly in a thermoblock at 85°C in order to allow the ethanol to evaporate and the pellet to dry. Plasmid DNA was resuspended in 30 µl elution buffer. The concentration of plasmid DNA was measured on a NanoDrop spectrophotometer at λ=260 nm. Only DNA with a purity greater than 1.8 based on 260/280 nm ratio was used for subsequent experiments.

LB medium: 20 g/l LB Broth (Lennox) powder in MilliQ-water, autoclaved, respective antibiotics were freshly added to bacterial cultures

3.21 Methods working with DNA

3.21.1 Genomic DNA (gDNA) extraction from single-cell clones and cell lines

Single-cell clones (SCCs) and cell lines were grown in 12-well plates until they were at least 60% confluent. Cells were washed once with PBS and 200 µl DNAzol reagent was added per well and cell culture plates were agitated to facilitate lysis. DNA isolation was either immediately performed or plates were stored for 1-2 days sealed with parafilm at 4°C. DNA was precipitated by addition of 125 µl 100% ultra-pure ethanol per well and plates were agitated and incubated for 5 min. 500 µl 70% ethanol was pipetted in nuclease-free 1.5 ml Eppendorf tubes and DNA, becoming visible as a cloudy precipitate, was swirled with a pipet tip and transferred to the tube. After centrifugation for 1 min at 18000 x g, the supernatant was carefully removed and DNA was washed one more time with 500 µl 70% ethanol. The supernatant was again removed and the remaining ethanol evaporated by placing the open tube for 1 min at 85°C on a thermoblock. DNA was dissolved in 30 µl 8 mM NaOH, adjusted for a final pH of 7.5 with 0.1 M HEPES. DNA concentration was measured on a NanoDrop spectrophotometer at λ=260 nm and a 260/280 ratio greater than 1.8 was considered as pure. DNA was stored at -20°C.

3.21.2 Restriction digest

Restriction endonucleases were purchased from New England Biolabs and restrictions digestions were used to either prepare DNA (for example bacterial plasmids or PCR products) for cloning or to monitor cloning accomplishments. 20-50 µl reactions were set up to digest DNA according to the manufacturer's protocol.

3.21.3 Agarose gel electrophoresis

Agarose gel electrophoresis is used to separate DNA fragments based on their size alongside with a molecular weight marker allowing analysis of the length of the fragment. Agarose gel electrophoresis was used to purify respective DNA fragments from gels for cloning purposes or to monitor for example restriction digestions or PCR amplification reactions. Agarose powder at a concentration of 0.8 to 1.2% was dissolved in 1X TAE buffer, SYBR Safe DNA stain was added at a ratio of 1:10000 and the gel solution was poured into gel carriers applying appropriate gel combs. After solidification, gels were placed in gel running system, filled with 1x TAE buffer and the gel comb was carefully removed. 6x orange loading dye was added to DNA samples before loading samples and the DNA weight marker into the gel pockets. DNA fragments were separated at 120 V for 30-60 min. For cloning and subsequent purification of plasmid DNA from the gel, DNA fragments were visualized using a blue light table. For all other purposes, pictures of gels were taken on a ChemiDoc UV transilluminator.

10x TAE: 0.4 M Tris, 0.2 M acetic acid, 10 mM EDTA

3.21.4 Gel extraction of DNA fragments

For cloning purposes, digested bacterial plasmids or amplified PCR products were run on an agarose gel and separation of DNA fragments visualized on a blue light table (see *Section 3.21.3*). Fragments of interest were cut out from the gel using a scalpel and purified from the gel using the Monarch Gel Extraction Kit according to the manufacturer's instructions. DNA was eluted using 15 µl of 50°C pre-heated EB and concentration measured on a NanoDrop spectrophotometer.

3.21.5 Ligation of DNA fragments using T4-DNA-Ligase

Digested and purified DNA fragments were used for a ligation reaction using T4-DNA-ligase according to manufacturer's instructions. 50-200 ng backbone DNA and insert DNA fragment at a molar ratio of 1:3 to 1:10 (backbone:insert) were used. The required amount of insert was calculated using the NEBioCalculator for DNA ligation (*http://nebiocalculator.neb.com/#!/ligation*) which is based on the following formula:

$$mass(insert) = desired\ molar\ ratio \frac{insert}{backbone} \times mass(backbone) \times length \frac{insert}{backbone}$$

The ligation reaction was mixed and incubated overnight for 16h at 4°C in a thermoblock and 4 µl ligation reaction were transformed into 25 µl competent bacteria (see *Section 3.20.1*).

3.21.6 Ligation of DNA using Gibson assembly

Gibson assembly is a method to connect DNA fragments with overlapping ends of at least 15 bp. In this study, Gibson assembly was used to assemble PCR products into a vector backbone with 1-4 insert fragments of 16 to 25 bp homology (see *Section 3.22.1*). A Gibson Assembly reaction was set up using the 2x Gibson Assembly Master Mix together with 50-100 ng purified vector backbone PCR and 1-4 insert fragments (StagR or oligo fragments, 2-3 fold molar excess) according to the manufacturer's instructions. The reaction was incubated for 45-60 min at 50°C on a thermoblock and afterward diluted 1:4 in nuclease-free water prior to transformation of 2 µl diluted Gibson reaction added to 25 µl competent bacteria (see *Section 3.20.1*).

3.21.7 Colony-PCR

Colony-PCR was utilized to screen clones containing Gibson assembled plasmids with the desired amount of sgRNA flanked by the hU6 promotor and sgRNA scaffold (see *Section 3.21.6*). At least 24 single bacterial clones were analyzed by picking a single bacterial clone, smearing it to the bottom of a single PCR reaction tube prior to inoculation with 2 ml LB medium containing 100 µg/ml Ampicillin. In accordance with the published protocol for StagR cloning (Breunig et al., 2018), a 10 µl PCR mix using Taq polymerase and primers binding within the vector backbone was prepared, added to each PCR reaction tube prior to run the PCR with the published settings. PCR products were analyzed on a 1% agarose gel and clones showing a

PCR product of the desired length were used to inoculate cultures for mini preparations (see *Section 3.21.3* and *3.20.2*).

Primer used for colony-PCR: StAgR_seq_fwd2 (ACTGGATCCGGTACCAAGG), StAgR_seq_rev (TTACGGTTCCTGGCCTTTTG)

Expected PCR products containing sgRNAs: hU6 265 bp, gRNA scaffold 83 bp, 1 sgRNA ~370 bp, 2 sgRNAs ~740 bp, 3 sgRNAs ~1.1kb, 4 sgRNAs ~1.5kb

3.21.8 Genotyping of single-cell clones

SCCs were analyzed at the genomic level in order to assess genetic insertions or deletions introduced by CRISPR/Cas9 technology. To do so, PCR reactions were performed using primers flanking the exon or exons of a gene of interest that was targeted by sgRNAs during CRISPR/Cas9 genome-editing (Table 6). For each new primer pair, respective annealing temperatures were established with the help of a temperature gradient using isolated gDNA from bulk cells. For genotyping, 25 µl reactions using 200 ng gDNA of each SCCs were mixed with nuclease-free water and the following reagents at a final concentration of 1x Q5 reaction buffer, 200 µM dNTPs, 0.5 µM of each primer and 20 Units/ml Q5 high-fidelity polymerase. The cycling program shown in Table 9 was run on a Thermocycler with the adjusted annealing temperature shown below (Table 6). As primers were designed to yield small PCR fragments and thereby allowing visualization of small insertions and deletions on 1 to 1.5% agarose gels, genotyping served as a method to screen for modified SCCs prior to subsequent analyses such as sequencing, immunoblotting and functional assays.

Table 6: Primer sequences used for genotyping of single-cell clones

Gene	Primer (for, rev)	Product length (wt)	Annealing Temp
ACSL4, gDNA Exon 4/5	AACTGCCTTGGCTGTACTGCTA, ATGCAAGCAAAGACCCTCCTCT	940 bp	70°C
HMOX1, gDNA Exon3	AGGGATTACAGGGGTTTGAGCC, CTCACCTGGATGTTGAGCAGGA	808 bp	70°C

3.22 Cloning

3.22.1 Cloning of two to four sgRNAs into the StagR_neo vector using StagR cloning

String assembly gRNA cloning (StagR) was employed to generate vectors containing two to four sgRNAs targeting several critical exons of individual genes. The strategy of using two to four sgRNAs per gene simultaneously was employed to increase the probability of generating genomic deletions flanked by the sgRNAs. StagR cloning was performed according to a recently published protocol (Breunig et al., 2018). Critical exons of individual human genes were identified using the Ensembl genome browser 94 (https://www.ensembl.org/index.html) and sgRNAs targeting these exons were designed using the MIT CRISPR tool (http://crispr.mit.edu/) and the Benchling platform (https://benchling.com/). A distance of about 120 bp to a maximum of 250 bp was chosen between the target sequences of single sgRNAs within one gene (Table 7). The StagR_neo backbone vector was used for StagR cloning where expression of the sgRNA target sequence and scaffold sequence is driven by a hU6 promoter. Therefore, primer pairs of each sgRNA target sequence with the addition of either scaffold (forward primer) or hU6 (reverse primer) overlapping overhangs were ordered from Eurofins as followed (see Table 7 for sgRNA target sequence):

Forward primer: 5‘$N_{20(\text{sgRNA target sequence})}$GTTTTAGAGCTAGAAATAGCAAGTT3‘
Reverse primer: 5‘$N_{20(\text{complementary to sgRNA forward target sequence})}$CGGTGTTTCGTCCTTT3‘

Lyophilized primers were dissolved in nuclease-free water to a final concentration of 100 µM. PCRs using the Phusion High-Fidelity Polymerase to achieve maximal sequence accuracy were performed according to the published PCR protocols (Breunig et al., 2018). Briefly, depending on the desired order of sgRNA within the vector, the forward primer of the last sgRNA target sequence and reverse primer of the first sgRNA target sequence were used to amplify the StagR_neo backbone. For amplification of StagR fragments, the forward primer of the first target sequence and reverse primer of the second sgRNA target sequence and so on are combined for PCRs using the STAGR_gRNAScaffold_hU6 plasmid as template. Thereby, overhangs for Gibson Assembly were generated. The backbone PCR reaction was digested using DpnI enzyme according to manufacturer’s instructions for at least 1h

at 37°C in a thermoblock to digest methylated template plasmid. DpnI-digested backbone PCR and StagR fragments were separated on a 1% agarose gel and purified by gel extraction prior to ligation using Gibson assembly and transformation into XL10-Gold competent bacteria. Bacterial clones containing the plasmid with the desired amount of sgRNAs were identified by Colony-PCR (see *Section 3.21.7*). Plasmids were isolated by mini preparations and cleaned up using the Zymo DNA Clean & Concentrator-5 Kit according to the manufacturer's instructions. The correct sequence was validated via sequencing by Eurofins using the Mix2SeqKit according to manufacturer's instructions using the listed sequencing primer prior to amplification of correct plasmids by midi preparations.

Sequencing primers: StAgR_seq_fwd2 (ACTGGATCCGGTACCAAGG), StAgR_seq_rev (TTACGGTTCCTGGCCTTTTG)

Table 7: sgRNA target sequences cloned into the StagR_neo vector using StagR cloning

Gene	Oligo label	Target Sequence
ACSL4	ACSL4_Ex4_sg1	ATTGTTATTAACAAGTGGAC
	ACSL4_Ex4_sg2	CTAGCTGTAATAGACATCCC
	ACSL4_Ex5_sg2	TGCAATCATCCATTCGGCCC
GPX4	Gpx4_Ex2_gRNA2	TTTCCGCCAAGGACATCGAC
	Gpx4_Ex4_gRNA4	ACTCAGCGTATCGGGCGTGC
HMOX1	HO1_Ex_gRNA19	CACATAGATGTGGTACAGGG
	HO1_Ex3_gRNA2	CTATGTGAAGCGGCTCCACG

3.22.2 Cloning one sgRNA into the StagR_neo vector

To generate constructs targeting only one sequence within a gene of interest, one sgRNA was cloned into the StagR_neo vector using a slightly altered protocol kindly provided by Christopher Breunig, from the group of Dr. Stefan Stricker (Functional Epigenetics, Institute of Stem Cell Research, Helmholtz-Center Munich). Briefly, in a 50 µl reaction, 5 µg of StagR_neo vector were digested with 2.5 µl AgeI in 1x CutSmart buffer overnight at 37°C. Linearization of the vector was confirmed by a 1% test agarose gel and digestion reaction was cleaned up using the Zymo DNA Clean & Concentrator-5 Kit. sgRNA target sequences were designed as described in *Section 3.22.1* and an oligo containing the GPX4 sgRNA target sequence (see

below) flanked by the addition of overhangs (partial sequences of hU6 and Scaffold) was ordered from Eurofins:

Oligo: TCTTGTGGAAAGGACGAAACACCG$N_{20(sgRNA\ target\ sequence)}$GTTTTAGAGCTAGAAATAGCAAGTTAAAATAAGGCT

50 ng of the oligo template were amplified using the Phusion high-fidelity DNA polymerase and primers annealing to the flanking sequences in a 50 µl reaction according to manufacturer's protocol using the cycling protocol shown in Table 8. Upon column-based cleanup of the PCR product using the Zymo DNA Clean & Concentrator-5 Kit, purified AgeI-digested vector backbone and PCR fragment containing the sgRNA were submitted to Gibson Assembly (see *Section 3.21.6*). After transformation and isolating plasmids from approximately 12 mini-cultures, plasmids were screened for sgRNA containing bacterial clones by a test endonuclease restriction. 2 µl of plasmid DNA were digested using AgeI and PvuI double digest in a 10 µl reaction according to manufacturer's protocol and analyzed on a 1% agarose gel. This strategy yields two fragments for negative clones and one fragment for sgRNA positive clones as AgeI restriction site should be lost during Gibson assembly. Positive clones were sequenced (Mix2SeqKit, Eurofins) using StagR_seq_fwd1 primer and a plasmid containing the correct sequence amplified by midi preparation.

GPX4 sgRNA target sequence: Gpx4_Ex3_gRNA3TP (CGTGTGCATCGTCACCAACG)

PCR primer: LibGen_U6_fwd (CTTGTGGAAAGGACGAAACA), LibGen_Scaffold_rev (GCCTTATTTTAACTTGCTATTTCTAGC)

Sequencing primer: StAgR_seq_fwd1: GAGTTAGGGGCGGGACTATG (for 1 sgRNA),

Table 8: Cycling program to amplify oligo template for cloning of one sgRNA into StagR_neo

Step	Temperature	Duration	Cycles
Initialization	98°C	30 sec	1x
Denaturation	98°C	10 sec	35x
Annealing	66°C	10sec	
Extension	72°C	10 sec	
Final Extension	72°C	10 min	1x

3.22.3 Cloning of GPX4 shRNAs from pGIPZ into the doxycycline-inducible pTRIPZ vector

Since a doxycycline-inducible pTRIPZ vector containing shRNAs against GPX4 was not available, GPX4 shRNAs were subcloned from purchased pGIPZ vectors to the nontargeting shRNA containing pTRIPZ vector (see *Section 2.11*). Cloning was performed as recommended by the manufacturer's protocol. Briefly, midi cultures containing 100 µg/ml Ampicillin were inoculated from purchased glycerol stocks, plasmids isolated using QIAGEN Plasmid Midi Kit and quality of plasmids controlled by SalI restriction followed by agarose gel visualization. 10 µg of each shRNA containing pGIPZ and control pTRIPZ vector were digested using MluI and XhoI for 2h at 37°C in a 20 µl reaction, followed by purification of GPX4 shRNAs (345 bp) and pTRIPZ backbone (13061 bp) from 1.2% agarose gels. Ligation reactions of each GPX4 shRNA with the digested pTRIPZ backbone were performed using 300 ng pTRIPZ backbone and 79.24 ng insert (1:10 ratio) in 20 µl T4-ligase reactions overnight at 16°C (see *Section 3.21.5*). Stabl2 competent bacteria were transduced prior to preparing 6-10 mini-cultures for bacterial colonies for each construct. 2 µl of isolated plasmids were test-digested with combinations of either NotI/MluI or XhoI/MluI (in case MluI/XhoI restriction sites got lost during cloning) in 20 µl reactions according to manufacturer's instructions for 20 min at 37°C. After a cleanup with Zymo DNA Clean and Concentrator Kit 5, plasmids showing the correct fragment sizes on agarose gels were sequenced to validate correct sequence using pTRIPZ_seq primer. pTRIPZ plasmids containing shRNAs against GPX4 were amplified by Midi cultures prior to subsequent experiments.

Sequencing primer: pTRIPZ_seq (GGAAAGAATCAAGGAGG)

3.22.4 Cloning of HMOX1 cDNA into the pLVX-puro vector

The pLVX-puro vector was used to express HMOX1 cDNA in HMLE cells via lentiviral gene transfer. cDNAs transcribed from RNA isolated from HMLE-Twist1 cells at low cell density in 6-cm dishes (see *Section 3.5* and *3.19.1*) were purified using the Zymo DNA Clean and Concentrator 5 Kit. 5 ng of purified cDNAs were used to amplify full-length HMOX1 cDNA in 50 µl reactions using Q5 high-fidelity DNA polymerase and 1x Q5 high GC enhancer according to manufacturer's protocol

with the cycling steps shown in Table 9. Primers employed annealed to sequences containing the start and stop codons flanked by BamHI and XbaI recognition sites which were not present in HMOX1 cDNA. The PCR product as well as 3 µg of pLVX-puro vector were digested with XbaI/BamHI in 20 µl reactions for 1.5h at 37°C. A 1.2% test agarose gel was run to assess digestion efficiency of vector and HMOX1 PCR amplification specificity prior to purification using Zymo DNA Clean and Concentrator 5 Kit. 200 ng purified and digested vector backbone were ligated to HMOX1 cDNA inserts at 1:3 and 1:5 ratios using a T4-ligase reaction overnight at 16°C (see *Section 3.21.5*). Stabl2 competent bacteria were transformed, plasmids of 14 mini-cultures screened by XbaI/BamHI test-digest and positive plasmids sequenced using the following primer prior to amplification by Midi cultures.

PCR Primer: For_XbaI_Hmox1 (CCTCTAGAATGGAGCGTCCGCAACCCGACA), Rev_BamHI_Hmox1 (AAGGGATCCTTACTGCATTCACATGGCATAAAGCCCTACAGC)

Sequencing primer: Seq_pLVX_HMOX1_For1 (GTTTAGTGAACCGTCAGATCGC), Seq_pLVX_HMOX1_For2 (CTGCCCTGGAGCAGGACC), Seq_pLVX_HMOX1_For3 (GAGGGTGATAGAAGAGGCCA)

Table 9: Cycling program used to amplify HMOX1 cDNA

Step	Temperature	Duration	Cycles
Initialization	98°C	3 min	1x
Denaturation	98°C	20 sec	35x
Annealing	72 °C	20 sec	
Extension	72°C	40 sec	
Final Extension	72°C	5 min	1x

3.23 Delivery methods into human cells

3.23.1 Transfection of vectors expressing Cas9 and sgRNAs for CRISPR/Cas9-mediated gene knockout

For CRISPR/Cas9-mediated gene knockout, cells were transiently transfected with the Cas9/GFP expressing pSpCas9(BB)-2A-GFP plasmid (Ran et al., 2013) together with a cloned gRNA_neo construct containing 1-4 sgRNAs targeting genes of interest (see *Section 3.22.1* and *3.22.2*). This strategy allows CRISPR/Cas9 modification in the target locus only in a short period without possible, undesired long-term effects introduced by stable lentiviral transductions. For transfection, 1.5

to 2 x 10^5 cells were seeded per well in a 6-well plate. The next day, the medium was replaced with 1.8 ml with respective complete growth medium. 200 µl basal DMEM was mixed with 1 µg of pSpCas9(BB)-2A-GFP plasmid and the gRNA_neo vector with sgRNAs at a molar ratio of 1:3 (in total approximately 2-2.5 µg) prior to addition of 7.5 µl room-temperature equilibrated TransIT-X2 transfection reagent according to manufacturer's protocol. The transfection mix was vortexed and incubated for 15-30 min at RT prior to drop-wise addition to cells. After overnight incubation of cells at the 37°C cell incubator, the transfection medium was replaced by respective complete growth medium and two days later, GFP-positive cells were sorted by FACS as described in *Section 3.14.2*.

3.23.2 Viral transduction

Viral transduction was employed to stably introduce DNA into target cells and handled in agreement with recommended guidelines for working with BSL-2 safety class.

3.23.2.1 Lentiviral production, concentration, and titration

HEK293T were used to produce replication-incompetent viral particles by transfection of lentiviral vectors (pLKO-puro and pTRIPZ based vector) together with the second generation packaging plasmid pCMV-dR8.2 dvpr and envelope plasmid pCMV-VSV-G. 2 x 10^6 HEK293T cells (passage below 20) were seeded in a T175 cm^2 cell culture flask in standard DMEM. A transfection mix in 1500 µl basal DMEM was prepared consisting of 18 µg lentiviral vector, 6.3 µg pCMV-VSV-G, 11.7 µg pCMV-dR8.2 dvpr and 108 µl PEI, followed by extensive mixing and incubation for 15-30 min at RT. The transfection mix was added drop-wise to HEK293T cells, incubated overnight prior to refreshing with standard DMEM medium. 24h later, viral particles contained in the medium supernatant were filtered through a 0.45 µm PVDF filter to remove cell fragments and concentrated by applying 30 ml filtered viral supernatant on 6 ml 20% sucrose in single-use ultracentrifugation tubes. After high-speed ultracentrifugation for 2-3h at 50000 x g at 4°C, the supernatant was completely removed and pelleted viral particles were resuspended in 75-120 µl medium of target cells and aliquots of 25 µl were frozen to -80°C. For titration of the virus, 5 x 10^4 HMLE cells were seeded into 24-well plates and the next day, different amounts of thawed virus aliquot were added per well overnight (10-fold dilutions

ranging from 10 µl to 0.001 µl, one well without virus). Then, cells were replated in a 6-well plate and after attachment of cells (3-4h later), antibiotic selection with 1 µg/ml puromycin was started. Total colonies of wells with distinguishable colonies were counted once non-transduced cells were completely killed by puromycin and viral titer (averaged from different wells) calculated using the following formula:

$$Titer\ (Transduction\ Units(TU)\ per\ ml) = colonies\ per\ well\ \times dilution\ factor \frac{volume\ of\ medium}{volume\ of\ viral\ supernatant}$$

Standard DMEM: DMEM, 10% FCS, 1% Pen/Strep

3.23.2.2 Transduction of target cells with lentivirus

Multiplicities of infection (MOI) between 0.2 and 10 were used to transduce target cells. The volume of virus required for transduction was dependent on the virus titer and the number of seeded cells and was calculated adjusting the following formula:

$$MOI = \frac{volume\ of\ virus\ x\ virus\ titer}{number\ of\ seeded\ cells}$$

Target cells at respective cell densities were seeded into 24-well to 6-well to reach a 60-70% confluency one day before overnight viral transduction. Cells were passaged and after attachment, selected with 1 µg/ml puromycin selection until non-transduced control cells were completely killed. Selected, transduced cells were frozen to generate cell stocks prior to subsequent experimental procedures and analyses.

3.24 Isolation of single-cell clones (SCCs)

In order to purify clones derived from one single cell in order to isolate one specific genotype (for example after CRISPR/Cas9 genome-editing), single cells were seeded in 96-wells. Specifically, a cell suspension consisting of 0.5 to 1 cell per 100 µl was prepared and seeded into each well of five 96-well plates. After 3-4 days, each well was visually inspected for single cells giving rise to one small colony. Wells containing one colony were passaged and expanded to 6-well prior to genotyping (see *Section 3.21.8*) and freezing into 1-2 cryotubes (see *Section 3.3*).

3.25 Data presentation and statistical analyses

Data presented show the mean ± SEM of n=x independently performed experiments, with x values indicated in the respective figure legends, unless stated otherwise. Within each independent experiment, 3-10 technical replicates per

condition were employed. An unpaired, two-tailed student's t-test with Welch's correction was used to compare two groups and a p-value below 0.05 was considered significant. Statistical analyses were conducted using Excel 2016 and GraphPad Prism 7.0 software.

4 Results

4.1 Initial induction of ferroptosis in HMLE-Twist1-ER 24^{hi} cells

The activation of the EMT program has been associated with the induction of resistance to conventional therapies (Ansieau et al., 2014; Nieto et al., 2016). Several reports have suggested a connection between EMT and the upregulation or loss of metabolic genes regulating the generation of ROS (Dong et al., 2013; Masin et al., 2014; Shaul et al., 2014). As ferroptosis has been introduced as a newly recognized cell death modality reported to involve mitochondrial damage as well as lipid ROS-mediated toxicity (Dixon et al., 2012; Yagoda et al., 2007), I was interested whether epithelial and Twist1-induced mesenchymal cells are differentially affected by ferroptosis inducers. As an experimental EMT model, I used immortalized human mammary epithelial cells (HMLE) (Elenbaas et al., 2001) that express an inducible Twist1 protein (HMLE-Twist1-ER) (Mani et al., 2008). Therein, Twist1 is fused to a mutated estrogen receptor (ER) ligand domain keeping the EMT-TF in an inactive conformation until 4-hydroxytamoxifen (TAM) is added (Casas et al., 2011; Schmidt et al., 2015). Derived thereof, HMLE-Twist1-ER 24^{hi} cells are a purified epithelial subpopulation based on the CD44^{+}/CD24^{high} cell surface marker expression (Schmidt et al., 2015). In an initial experiment, 2.5 x 10^{3} epithelial or 15d TAM-induced mesenchymal HMLE-Twist1-ER 24^{hi} cells were seeded in 96-well plates and 48h later, the cells were treated with 3-fold dilutions of ferroptosis-inducing compounds such as RSL3 and ERA for 24h (Figure 3).

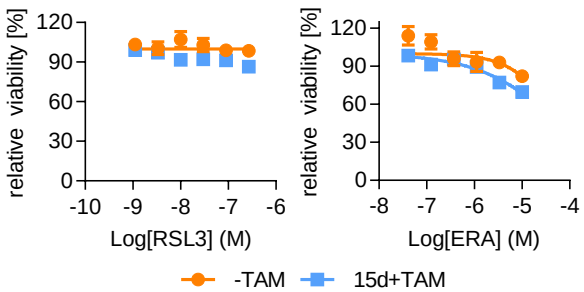

Figure 3: HMLE-Twist1-ER 24^{hi} cells are resistant to ferroptosis inducers

Dose-response curves: epithelial (−TAM, orange) and 15d TAM-induced mesenchymal (15d+TAM, blue) HMLE-Twist1-ER 24^{hi} cells were seeded at a cell density of 2500 cells per well in 96-well plates. 48h after plating, cells were treated with 3-fold dilutions of RSL3 or Erastin (ERA) for 24h prior to the assessment of cell viability using CellTiter-Glo assay. Data was normalized to DMSO control and show mean ± SD of n=5 wells.

However, neither RSL3 nor ERA affected cell viability in epithelial (–TAM) or mesenchymal (15d+TAM) HMLE-Twist1-ER 24^{hi} compared to untreated control (Figure 3): Earlier studies using chemotherapeutics such as doxorubicin have shown a correlation between cell density and drug efficacy (Ohnuma et al., 1986; Takemura et al., 1991). Hence, I speculated that cell density might influence sensitivity to ferroptosis-inducing compounds. Therefore, 333, 1000 and 3000 cells were seeded in 96-well plates prior to incubation for 24h with abovementioned compounds (Figure 4). Applied drug concentrations were chosen from dose-response curves shown in (Figure 3), in order to allow assessment of differences in cell death induction at lower seeding densities. While I did not observe major differences in cell viability at different seeding numbers when 3 µM ERA treatment was applied, RSL3 induced a reduction in cell viability that depended on seeded cell numbers in both epithelial and 15d TAM-induced mesenchymal HMLE-Twist1-ER 24^{hi} cells (Figure 4). Both cell lines showed resistance to 300 nM RSL3 treatment at high density (3000 cells seeded per well in a 96-well plate). However, viability was decreased by 92-97% at low density (333 seeded cells) in comparison to the DMSO control. Interestingly, at an intermediate seeding density of 1000 seeded cells, a differential sensitivity between epithelial and 15d TAM-induced mesenchymal HMLE-Twist1-ER 24^{hi} cells was observed, with mesenchymal cells showing increased sensitivity. The initial observation of cell density-dependent cell death induction by RSL3 was an unexpected and intriguing finding. Therefore, I decided to first validate this

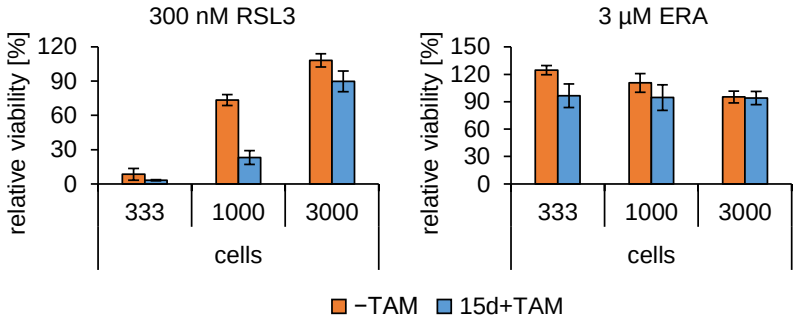

Figure 4: Sensitivity to RSL3 treatment depends on seeding density in HMLE-Twist1-ER 24^{hi} cells

Viability assays: treatment of epithelial (−TAM, orange) and 15d TAM-induced mesenchymal (15d+TAM, blue) HMLE-Twist1-ER 24^{hi} cells seeded at three different cell densities (333, 1000 and 3000 cells) in 96-well plates. One day later, treatment with RSL3 or ERA at indicated concentrations was applied for 24h prior to measuring cell viability using CellTiter-Glo assay. Data was normalized to DMSO control within each cell density and cell line and show mean ± SD of n=5 wells.

observation and then to determine the mechanisms of cell density-dependent cell death induction by RSL3.

4.2 RSL3 induces cell death in a cell density-dependent manner in both epithelial and Twist1-induced mesenchymal HMLE cells

RSL3 induces ferroptosis by directly inhibiting the central ferroptosis regulator glutathione peroxidase 4 (GPX4) (Yang et al., 2014). For validation of above-mentioned observations, viability assays with epithelial and Twist1-induced mesenchymal cells at different cell densities were repeated. In the following, high (hi), intermediate (med) and low cell density refers to 3000, 1000 and 333 cells seeded per well in a 96-well plate, if not otherwise indicated. Cell numbers were adjusted accordingly to other well and dish formats as described in *Section 3.5*. One day after plating, cells were treated for 24h with 300 nM RSL3 and cell viability was measured using the CellTiter-Glo assay. I observed a statistically significant cell density-dependent induction of cell death in both epithelial and Twist1-induced cells, with cells being highly sensitive at low cell density and resistant at high cell density. RSL3 treatment decreased cell viability by 90-93% at low cell density compared to DMSO treated control (Figure 5A). Again, I observed an increased sensitivity to RSL3-treatment in HMLE cells where Twist1 was induced for 15 days. Here, RSL3 treatment diminished cell viability by 69% in HMLE-Twist1 cells, but only by 8% in HMLE cells compared to DMSO treated control (Figure 5A). Of note, an inactive diastereomer of RSL3 (inactive RSL3), used as a control for off-target effects (Yang et al., 2014), did not induce cell death at any cell density (Figure 5A).

Next, HMLE-Snail1-ER 24^{hi} cells that express the Snail1 EMT-TF which results in EMT induction upon TAM treatment (Mani et al., 2008; Schmidt et al., 2015), were also treated with RSL3. Again, RSL3 induced cell death in a cell density-dependent manner, but activation of Snail1 did not alter this sensitivity at intermediate seeding densities (Figure 5B). These data suggested on one hand that sensitivity to ferroptosis was not generally connected to EMT-induction, but in some conditions, i.e. at intermediate seeding density, Twist1 expression might increase sensitivity to ferroptosis (Figure 5A) . To further support these findings, I used parental epithelial HMLE and HMLE-Twist1 cells, which constitutively express Twist1 and are fixed in the mesenchymal state (Mani et al., 2008). Using viability assays, I determined that

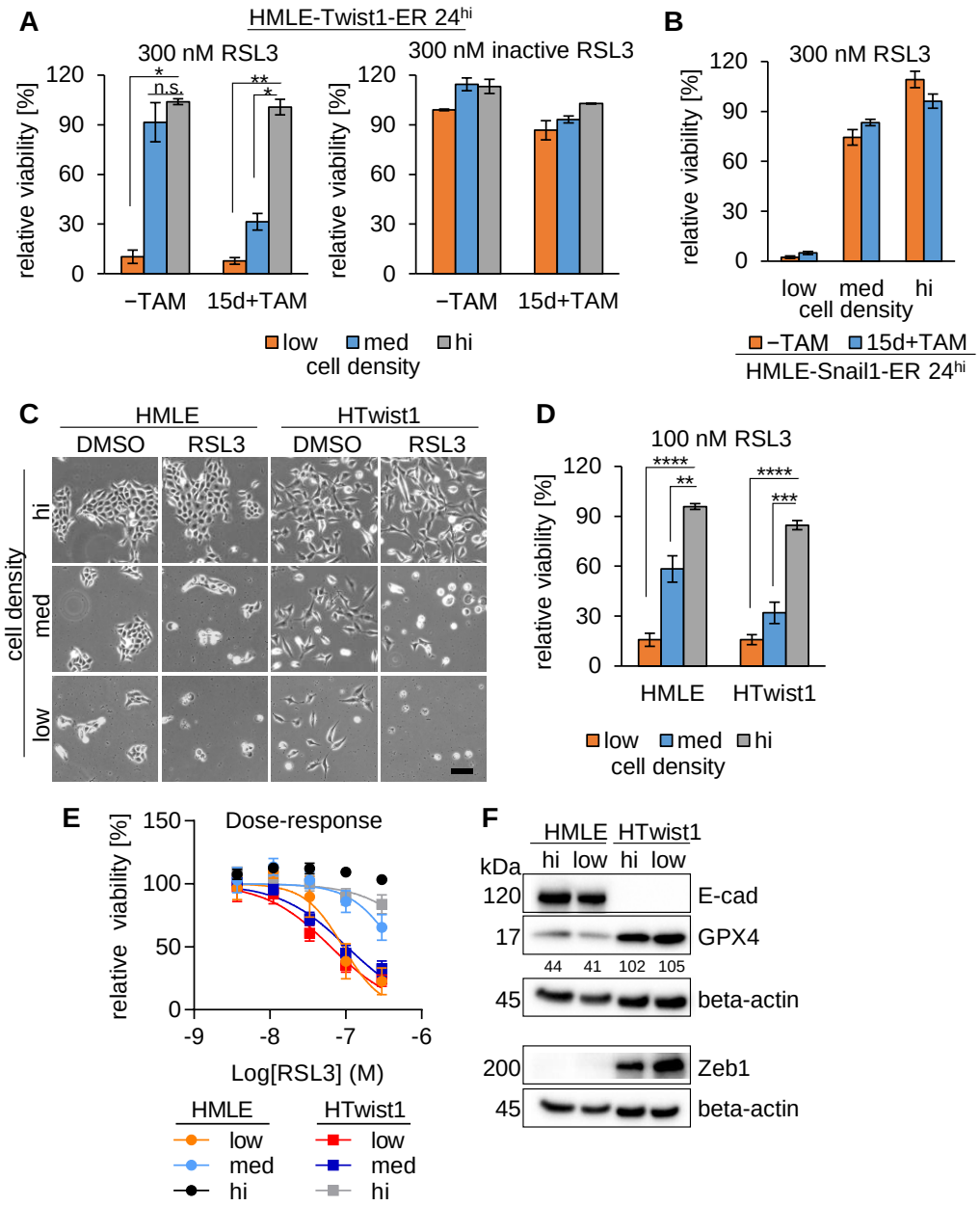

Figure 5: RSL3 induces cell density-dependent cell death in both epithelial and Twist1-induced mesenchymal HMLE cells

(A) Viability assay: treatment of epithelial (−TAM) or 15d TAM-induced mesenchymal (15d+TAM) HMLE-Twist1-ER 24^{hi} cells seeded the day before at low (orange, 333 cells), med (blue, 1000 cells) or hi (grey, 3000 cells) cell density in 96-well plates with 0.3% DMSO, 300 nM RSL3 or inactive RSL3 for 24h. n=3. (B) Viability assay: treatment of epithelial (−TAM) or 15d TAM-induced mesenchymal (15d+TAM) HMLE-Snail1-ER 24^{hi} cells as described in A. Data show mean ± SEM of n=5 wells. (C) Bright-field microscopy: representative pictures of epithelial HMLE and mesenchymal HMLE-Twist1 (HTwist1) cells seeded at indicated cell densities in 6-well plates 24h before treating cells with 0.1% DMSO control or 100 nM RSL3 for 24h and imaging. Scale bar: 200 µm. (D) Viability assay: treatment of HMLE and HTwist1 cells seeded at indicated densities in 96-well plates with 0.1% DMSO or 100 nM RSL3. n=6. Data were partly generated by Marie Bannier-Hélaouët (Intern). (E) Dose-response curves: treatment of HMLE and HTwist1 cells plated in 96-well plates with 3-fold dilutions of RSL3. n=4. (F) Immunoblot: protein expression of E-cadherin (E-cad), GPX4, Zeb1 and beta-actin in HMLE and HMLE-

Twist1 seeded at high (hi) and low cell density in 10-cm dishes. Upper beta-actin protein band serves as a loading control for E-cad and GPX4, lower beta-actin protein band for Zeb1. Densitometric ratios of detected proteins bands of GPX4 to beta-actin are indicated in percent. kDa = kilo Dalton. Data (A, D, E) represent mean ± SEM. Viability was normalized to respective DMSO control within each cell density and cell line. Statistics: two-tailed, unpaired T-test with Welch's correction (p-value: *<0.05, **<0.01, ***0.001, ****<0.0001, n.s. = not significant).

treatment with 100 nM RSL3 for 24h again significantly induced cell death in a cell density-dependent manner (Figure 5C and D). Moreover, cells plated at an intermediate cell density also showed intermediate levels of cell death (Figure 5D). Dose-response curves using 3-fold dilutions of RSL3 further supported the finding of a cell density-dependent induction of cell death by RSL3 (Figure 5E). A comparison of the calculated IC50 values at intermediate seeding densities for HMLE and HMLE-Twist1 showed an increased sensitivity of HMLE-Twist1 cells towards RSL3 treatment (449 nM vs 104 nM). These results suggested that activation of Twist1 increased sensitivity to ferroptosis.

Since RSL3 directly inhibits GPX4 (Yang et al., 2014), immunoblotting for GPX4 was performed to assess whether GPX4 expression levels were dependent on cell density. GPX4 was expressed in both HMLE and HMLE-Twist1 cells at the same level irrespective of low or high cell density (Figure 5F). However, GPX4 expression levels were generally around 2.5-fold higher in HMLE-Twist1 compared to HMLE cells. As described previously, HMLE cells display an epithelial morphology and express the epithelial marker E-cadherin, whereas Twist1-overexpression induces an EMT, resulting in downregulation of E-cadherin and expression of the mesenchymal marker Zeb1 (Figure 5F) (Mani et al., 2008; Yang et al., 2004).

Taken together, I validated my initial findings, showing that cell density is a critical factor that sensitized both epithelial and mesenchymal HMLE cells to GPX4 inhibition by RSL3. In addition, Twist1-expression increased sensitivity towards RSL3 treatment at intermediate seeding densities.

4.3 Ferroptosis is the cell death-modality in cell density-dependent cell death

As GPX4 is a known key regulator of ferroptotic cell death (Yang et al., 2014), I wanted to further specify whether cell density sensitized cells specifically to this mode of cell death. To do so, cells were plated at a lower seeding density (600 cells) in 96-well plates and treated with RSL3 alone or in combination with compounds

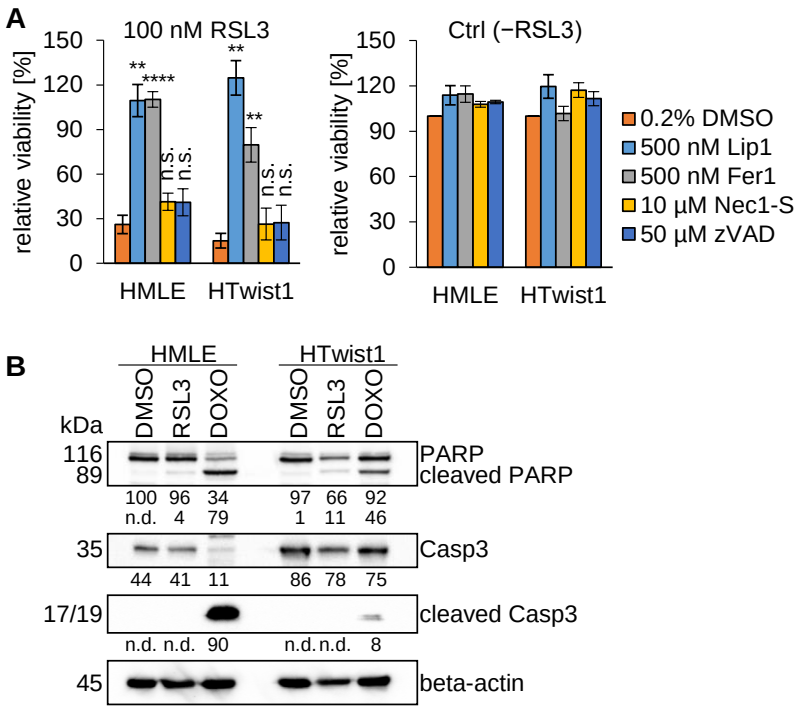

Figure 6: The cell death-modality in cell density-dependent cell death induced by RSL3 is ferroptosis.

(A) Rescue-viability assay: HMLE and HMLE-Twist1 cells were seeded at 600 cells (intermediate-low cell density) in 96-well plates and treated for 20-24h with DMSO control or 100 nM RSL3 alone or in combination with 500 nM Liproxstatin (Lip1), 500 nM Ferrostatin-1 (Fer1), 10 µM Necrostatin1-S (Nec1-S) or 50 µM zVAD-fmk (zVAD). n=3-5. Data shown represent mean ± SEM. Viability was normalized to respective DMSO control within each cell line. Statistics: two-tailed, unpaired T-test with Welch's correction (p-value: *<0.05, **<0.01, ***0.001, ****<0.0001, n.s. = not significant). (B) Immunoblot: protein expression of uncleaved and cleaved PARP and Caspase 3 (Casp3) upon 20h 100 nM RSL3 or 10 µM Doxorubicin (DOXO) treatment of HMLE and HTwist1 cells seeded at intermediate cell density in 15-cm dishes. 0.1% DMSO treatment served as negative control while DOXO served as positive control for PARP and Casp3 cleavage. Beta-actin was used as loading control. Numbers shown indicate densitometric ratios of detected proteins (PARP, cleaved PARP, Casp3, cleaved Casp3) to respective beta-actin protein band in percent (from top to bottom). kDa= kilo Dalton, n.d. = not detectable. Immunoblot shown is representative for n=3 (PARP) and n=1 (Casp3). Data from rescue-viability assay were partly generated by and immunoblot analysis was performed by Felix Holstein (Master Student).

inhibiting either apoptosis, necroptosis or ferroptosis. zVAD-fmk (zVAD) inhibits apoptosis by inhibiting caspase activity necessary for apoptosis execution (SLEE et al., 1996). Nec1-S is a more potent derivative of Necrostatin-1 which inhibits the receptor-interacting protein kinase 1 (RIPK1), thereby blocking regulated necrosis (Degterev et al., 2005). For ferroptosis inhibition, Ferrostatin1 (Fer1) and Liproxstatin1 (Lip1) were employed (Dixon et al., 2012; Friedmann Angeli et al., 2014). Upon 20-24h of RSL3-treatment, cell viability was decreased by 74-85% in HMLE and HMLE-Twist1 cells compared to the DMSO control (Figure 6A). When

cells were co-treated with either 500 nM Fer1, 500 nM Lip1, 10 µM Nec1-S or 50 µM zVAD, only Fer1 and Lip1 fully rescued RSL3-induced cell death (Figure 6A). Neither zVAD nor Nec1-S protected cells significantly from RSL3-induced cell death (Figure 6A). Importantly, the applied inhibitor concentrations were not toxic to the cells (Figure 6A) and were previously shown to be protective against the respective mode of cell death (Friedmann Angeli et al., 2014). To further rule out apoptosis as cell death modality, immunoblotting for the apoptosis markers Caspase 3 (Casp3) and PARP was performed. During the process of apoptosis, Casp3 is cleaved into its active isoform, inducing a process leading to DNA fragmentation (Fernandes-Alnemri et al., 1994; Nicholson et al., 1995; Tewari et al., 1995; Wolf et al., 1999). PARP is involved in DNA repair and DNA stability, unless it is inactivated by Casp3 cleavage, thereby leading to accumulation of double strand breaks and thus contribution to apoptosis (Boulares et al., 1999; Nicholson et al., 1995). For this purpose, HMLE and HMLE-Twist1 cells were seeded at an intermediate cell density and treated with 100 nM RSL3 for 20h. I could neither detect a cleavage of Casp3 nor pronounced cleavage of its downstream target PARP (Figure 6B). In contrast, when cells were treated with 10 µM Doxorubicin (DOXO), both PARP and Casp3 were cleaved, thus serving as a positive control (Figure 6B). DOXO is a chemotherapeutic agent that intercalates into DNA and compromises DNA synthesis, ultimately leading to apoptosis (Fornari et al., 1994; Tacar et al., 2013).
Together, these data suggested that cell death induced by RSL3 treatment was mediated through ferroptosis and that thereby cell density sensitized both HMLE and HMLE-Twist1 to ferroptosis.

4.4 Cell density-dependent ferroptosis is not directly linked to thiol and glutathione metabolism

Previous reports have shown that reducing GSH levels by inhibiting the system x_c^- by ERA treatment or by direct interference with GSH synthesizing enzymes (for example by BSO) indirectly impairs GPX4 function and thus leads to ferroptosis (Friedmann Angeli et al., 2014; Yang et al., 2014). Therefore, I wanted to elaborate in more detail whether thiol and GSH metabolism upstream of GPX4 contributed to cell density-dependent ferroptosis induced by RSL3-treatment. To address this question, I again exposed epithelial and TAM-induced HMLE-Twist1-ER 24^{hi} cells, seeded at an intermediate-low density (600 cells) in 96-well plates, to 3-fold

dilutions. In line with my initial observations when exposing cells to ERA treatment (Figure 3 and Figure 4), I observed that ERA treatment for 24h did not influence cell viability in HMLE-Twist1-ER 24^{hi} cells (Figure 7A). Importantly, ferroptosis was efficiently induced by RSL3 treatment in both HMLE and HMLE-Twist1 cells at this cell density (Figure 6A). Next, I assessed the expression of the substrate specific light chain subunit *SLC7A11* of system x_c^- (Lewerenz et al., 2012), and the expression of the catalytic subunit *GCLC* of GCL, the rate-limiting enzyme in GSH biosynthesis (Franklin et al., 2009). qPCR analysis revealed a reduction of both *GCLC* and *SLC7A11* transcript levels in mesenchymal HMLE-Twist1 cells compared to parental epithelial HMLE cells. However, this reduction occurred irrespective of cell density (Figure 7B and C), indicating that *GCLC* and *SLC7A11* expression were not directly regulated by cell density, but rather by Twist1 expression.

To determine whether this reduction in gene expression was functionally relevant, I assessed thiol release as a proxy for system x_c^- activity and total GSH levels in collaboration with Dr. José-Pedro Friedman Angeli (Bannai and Ishii, 1980, 1982; Ishii et al., 1987). System x_c^- activity was 2-fold and total GSH levels were 1.5-fold reduced in 17d TAM-induced mesenchymal HMLE-Twist1-ER 24^{hi} cells compared to parental epithelial HMLE cells (Figure 7D and E). These results suggested a lower abundance of reducing equivalents in Twist1-induced mesenchymal cells. Importantly, ERA treatment, serving as a control, completely abolished system x_c^- activity and depleted GSH content, which was expected since the cysteine that is necessary for GSH synthesis is derived via cystine import by system x_c^- (Figure 7D and E) (Ishii et al., 1987). Accordingly, Thioltracker Violet staining by flow cytometry revealed that reduced Thiols, serving as a proxy for reduced GSH content, were decreased upon Twist1-expression, both in HMLE-Twist1-ER 24^{hi} cells and in HMLE-Twist1 cells compared to the parental, epithelial HMLE cells (Figure 7F). Again, these data indicated that Twist1-induced mesenchymal cells might have less reducing equivalents. Since both thiol and glutathione metabolism are connected with GPX4 function (Friedmann Angeli et al., 2014; Yang et al., 2014), GPX4 activity, measured by the specific reduction of phosphatidylcholine hydroperoxide (PCOOH), was assessed in collaboration with Dr. Irina Ingold. Surprisingly, GPX4 activity was not altered upon 17d TAM-induction compared to the parental cells (Figure 7G).

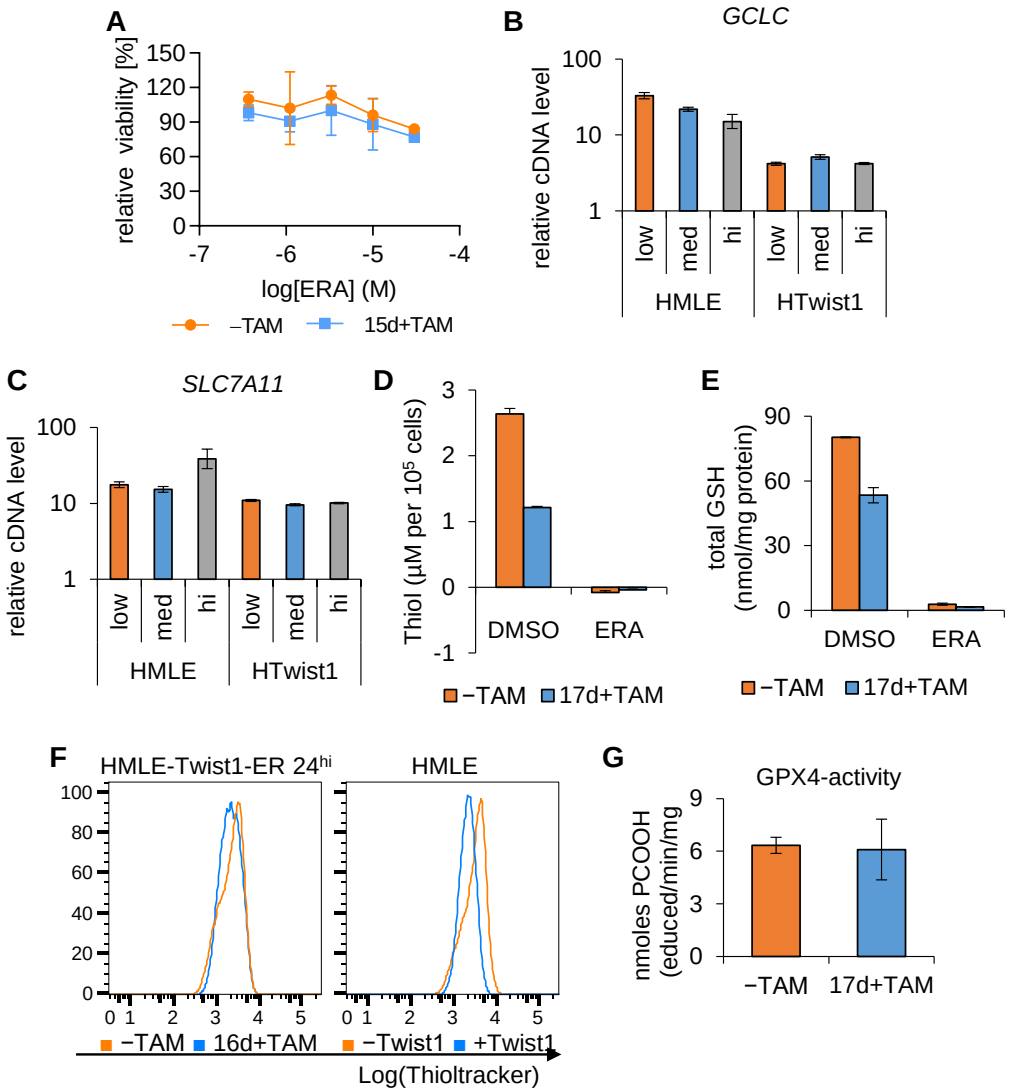

Figure 7: Thiol and glutathione metabolism are not directly linked with cell density-dependent ferroptosis

(A) Dose-response curves: treatment of epithelial (−TAM) or 15d TAM-induced mesenchymal (15d+TAM) HMLE-Twist1-ER 24^{hi} cells seeded at 600 cells in 96-well plates with 3-fold dilutions of Erastin (ERA) for 24h. Data show mean ± SD. n=2. Viability was normalized to respective DMSO control within each cell line. (B) and (C) qPCR: relative (B) *GCLC* and (C) *SLC7A11* mRNA expression of HMLE and HMLE-Twist1 cells seeded at different cell densities in 6-cm dishes. Data show mean ± SEM. (D) Thiol release measurement as a proxy for system x_c^- activity in epithelial (−TAM) or 17d TAM-induced mesenchymal (17d+TAM) HMLE-Twist1-ER 24^{hi} cells plated in 12-well plates. ERA treatment (inhibiting system x_c^-) served as positive control. Data shown quantified thiol release at 4h and represent mean ± SD. (E) GSH levels were measured as described in D. ERA treatment served as positive control to inhibit system x_c^- and thus cystine uptake necessary for GSH metabolism. Data show mean ± SD. n=2. (F) Flow cytometry: Thioltracker Violet staining of epithelial (−TAM, −Twist1 orange) and Twist1-induced mesenchymal (16d+TAM, +Twist1 blue) HMLE-Twist1-ER 24^{hi} and HMLE cells seeded at 1 x 10^5 cells in a 6-well. X-axis: log10 of Thioltracker fluorescence, Y-axis: percentage of maximum count. (G) GPX4-specific activity measurement in epithelial (−TAM) or 17d TAM-induced mesenchymal (17d+TAM) HMLE-Twist1-ER 24^{hi} cells. Data show mean ± SD of n=4 samples obtained from confluent 15-cm dishes. Data (B, C, D, F) show one representative

experiment performed independently two (D, F) or three (B, C) times. Data (D, E, G) were kindly provided (D, E) by Dr. José Pedro Friedmann Angeli and (G) by Dr. Irina Ingold.

Overall, these data suggested that system x_c^- activity as well as GSH levels were decreased upon Twist1-expression, but not by cell density. However, these changes did not seem to be sufficient to impact GPX4 activity, since both epithelial and Twist1-induced cells showed a similar GPX4 activity. Conclusively, upstream mechanisms did not directly influence cell density-dependent ferroptosis observed upon GPX4-inhibition.

4.5 Cell density-dependent ferroptosis occurs upon *GPX4*-knockdown and knockout

As described above, RSL3, but not ERA, led to cell density-dependent cell death and by using ferroptosis inhibitors, I specified the mode of cell death as ferroptosis. To pinpoint that the induced ferroptosis is dependent on GPX4-inhibition, I sought to confirm genetically that GPX4-inhibition led to cell density-dependent ferroptosis. To do so, I pursued two different strategies because CRISPR/Cas9 technology, used as a second approach to knockout GPX4, had to be established in our laboratory first. First, *GPX4* expression was ablated by short hairpin RNA (shRNA)-mediated gene silencing. Thereby, mRNA is degraded by the endogenous RNA-induced silencing complex (RISC) loaded with the respective shRNA (Paddison et al., 2002). shRNAs were cloned from the pGIPZ lentiviral vectors containing shRNAs against GPX4 into the pTRIPZ lentiviral vectors (Dharmacon). The pTRIPZ lentiviral vector system enabled Dox-inducible shRNA expression and thus inducible *GPX4* knockdown. This strategy facilitated long-term culture of cells in the absence of Dox since a genetic knockout of GPX4 was shown to be lethal (Imai et al., 2003; Yant et al., 2003). HMLE 24^{hi} cells were transduced with pTRIPZ lentiviral vectors containing non-targeting shRNAs (sh-nt) or GPX4-targeting shRNAs (sh-GPX4) at a MOI of 0.7. Induction of shRNAs against GPX4 for 72h with 0.5 µg/ml Dox led to a reduction of *GPX4* transcript levels of about 90% compared to untransduced control cells as assessed by qPCR (Figure 8A). Moreover, nt shRNA did not influence *GPX4* transcript levels (Figure 8A). To determine the impact on cell viability, viability assays were performed by counting the cells seeded in 24-well plates and by

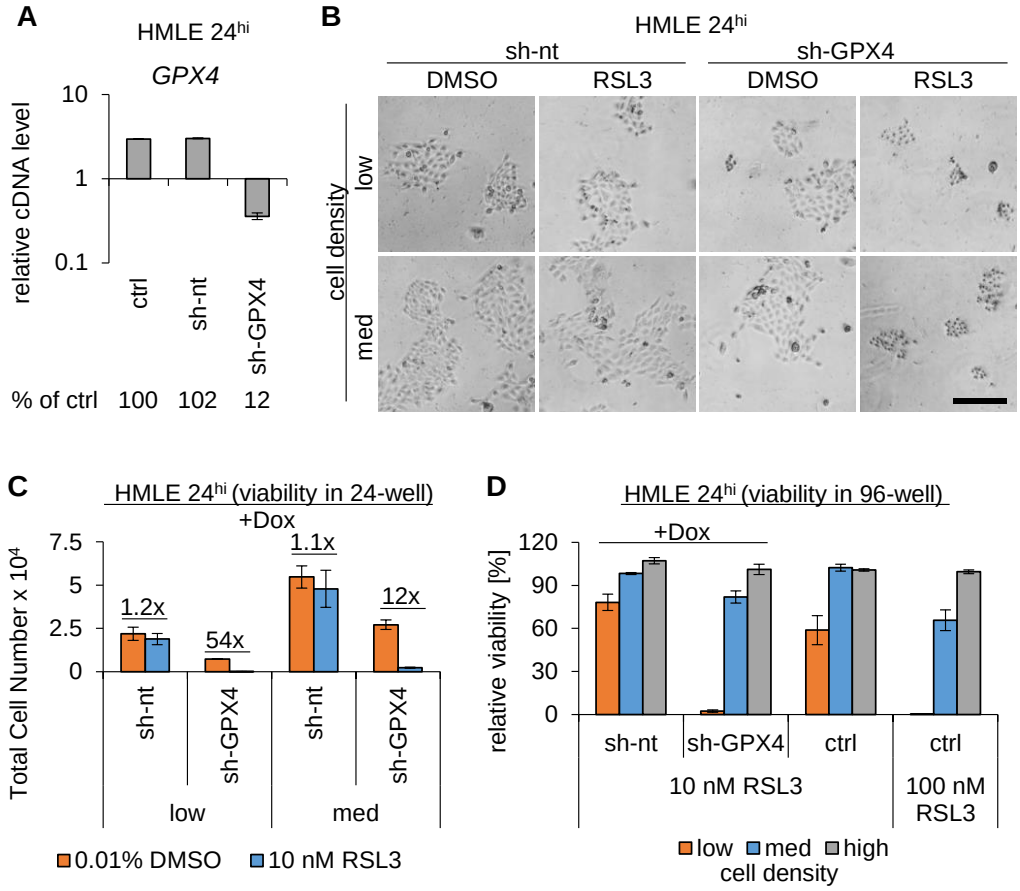

Figure 8: Cell density-dependent ferroptosis occurs upon *GPX4*-knockdown
(A) qPCR: relative *GPX4* mRNA expression of non-transduced, control (ctrl) or pTRIPZ lentiviral vectors containing Dox-inducible non-targeting shRNAs (sh-nt) or *GPX4*-targeting shRNAs (sh-GPX4) HMLE 24^{hi} cells induced for 72h with 0.5 µg/ml doxycycline (Dox). Numbers indicate *GPX4* levels normalized to control in percent. Data show mean ± SEM. (B) Bright-field microscopy: representative pictures of 96h Dox-treated HMLE 24^{hi} cells expressing sh-nt and sh-GPX4 seeded at low (1200 cells) or intermediate (3600 cells) cell density in 24-well plates and treated for 24h with 0.01% DMSO or 10 nM RSL3. Scale bar: 200 µm. (C) Viability assay: assessment of cell viability by counting HMLE 24^{hi} cells plated and treated as described in B. Data shown represent mean ± SD of one representative experiment performed independently two times. (D) Viability assay: control (ctrl) and Dox-inducible sh-nt or sh-GPX4 HMLE 24^{hi} cells plated at different cell densities (167-500-2000 cells, low-med-hi) in 96-well plates were treated with 0.5 µg/ml Dox for 96h. During the last 24h, DMSO, 10 nM or 100 nM RSL3 treatment was applied. Data shown represent mean ± SEM. n=2. Viability was normalized to respective DMSO control within each cell line and cell density.

performing CellTiter-Glo assays. Since GPX4 might have residual activity after a 10-fold decrease (Yang et al., 2014), low-dose RSL3 treatment was applied during viability assays using *GPX4* knockdown cells. Importantly, in this case, RSL3 treatment was used at a dosage previously shown to be non-toxic to cells with intact GPX4 expression (Figure 5E). To assess viability, HMLE 24^{hi} cells containing shRNAs were seeded in 24-well plates at a low (1200 cells) or intermediate (3600

cells) cell density and the next day, shRNA expression was induced by Dox-treatment. After 48h Dox-treatment, cells were additionally treated with 10 nM RSL3 or 0.01% DMSO (solvent control), the next day trypsinized and total cell number assessed by counting (Figure 8B). As expected, a similar cell number compared to DMSO control was counted when 10 nM RSL3 treatment was applied to sh-nt expressing cells at a low and at an intermediate seeding density (Figure 8C). In contrast, compared to the DMSO control, RSL3-treatment reduced cell numbers by 54-fold at low and by 12-fold at intermediate density in HMLE 24^{hi} cells with *GPX4* knockdown (Figure 8C).

In a second line of experiments, untransduced control (ctrl), sh-nt or sh-GPX4 HMLE 24^{hi} cells were seeded in 96-well plates at 167, 500 and 2000 cells (low, med, high cell density). Of note, cell numbers were lower than those used in previous viability assays because cells were grown for 72h prior to RSL3 treatment. Cells were treated with Dox and 10 nM RSL3 as described for viability assays performed in 24-well plates, but instead of counting cells, viability was measured by the CellTiter-Glo assay. As a control, cells were not treated with Dox, but instead with 100 nM RSL3, which was shown to efficiently induce cell density-dependent ferroptosis (Figure 8D). Again, I noticed that 10 nM RSL3 induced cell density-dependent ferroptosis upon *GPX4* knockdown to a similar extent as in control cells that were treated with 100 nM RSL3. However, cell viability was only slightly impacted by 10 nM RSL3 treatment in sh-nt expressing cells which was comparable to the viability of 10 nM RSL3-treated control cells (Figure 8D). Together, these data indicated that GPX4 was the regulator of cell density-dependent ferroptosis.

However, although RSL3 was used at a low-dose during *GPX4* knockdown experiments, off-target effects of RSL3 could not be excluded. Furthermore, the ratio of RSL3 molecules to the numbers of seeded cells might be altered in cell density experiments, thereby explaining the observed effects. Therefore, to establish a stronger genetic link between GPX4 and cell density-dependent ferroptosis, I knocked out *GPX4* in HMLE and HMLE-Twist1 cells using the CRISPR/Cas9 system. For this purpose, plasmids containing Cas9 and sgRNAs targeting *GPX4* were transiently transfected into both cell lines to avoid long-term off-target effects. Transfections of only the plasmid containing Cas9 served as a control for wild-type GPX4 expression. After single cell seeding and expansion, I derived several single-

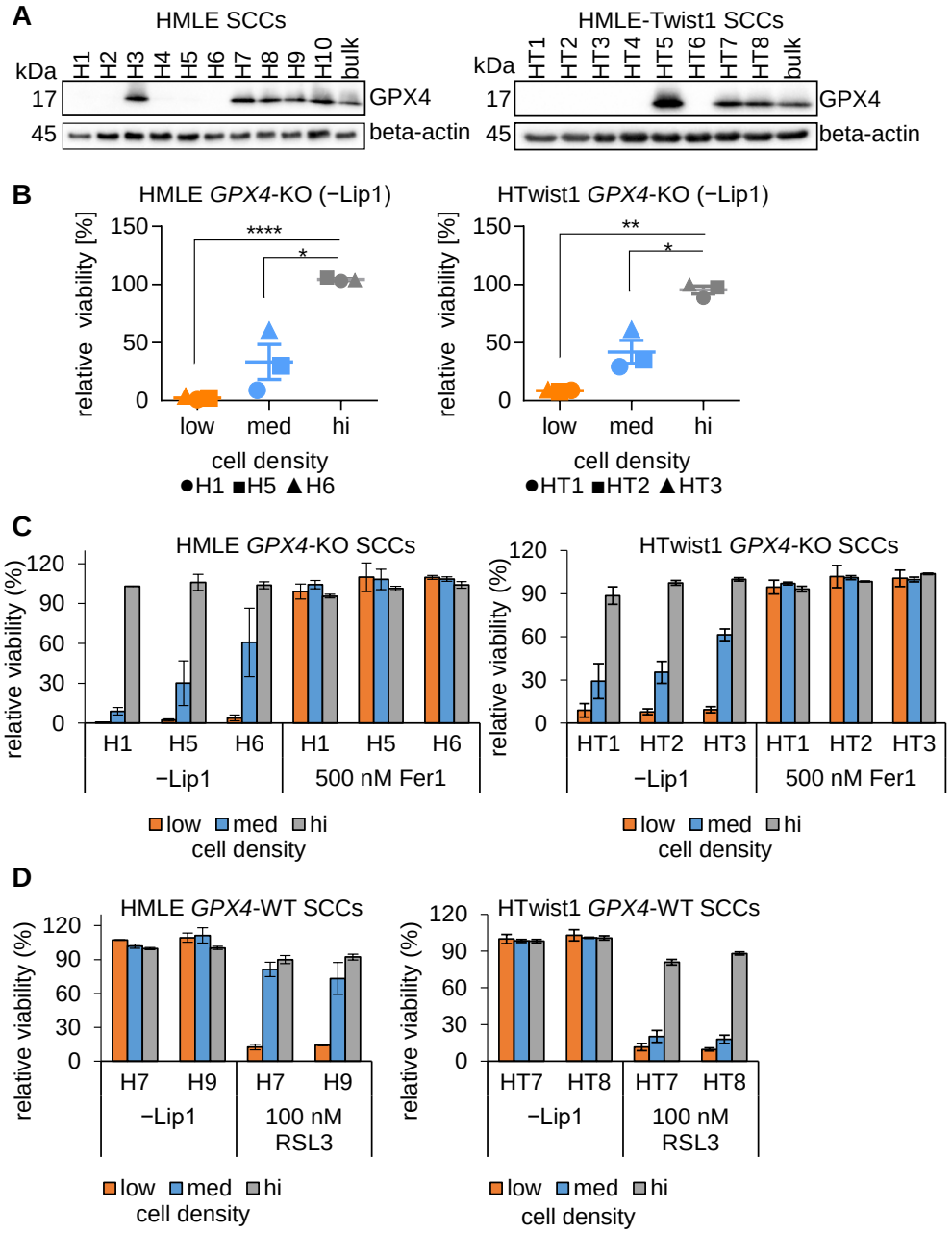

Figure 9: Cell density-dependent ferroptosis occurs upon *GPX4*-knockout

(A) Immunoblot: GPX4 and beta-actin (loading control) protein expression in single-cell clones (SCCs) derived by CRISPR/Cas9 genome-editing in the *GPX4* locus of bulk HMLE and HMLE-Twist1 cells. kDa= kilo Dalton. One representative immunoblot performed independently two times is shown. (B) Viability assay: treatment of SCCs with *GPX4*-knockout (KO) plated at indicated cell densities in 96-well plates in presence or absence of 1 µM Liproxstatin-1 (Lip1) for 48h. n=2 for HMLE SCCs, n=4 for HMLE-Twist1 SCCs. Statistics: two-tailed, unpaired T-test with Welch's correction (p-value: *<0.05, **<0.01, ****<0.0001). (C) Viability assay: assessment of cell viability, including a treatment with 500 nM Fer1, as described in B. n=2 for HMLE SCCs, n=3-4 for HMLE-Twist1 SCCs. (D) Viability assay: treatment of CRISPR/Cas9-derived control SCCs with intact GPX4 expression (wildtype = WT) plated at indicated cell densities in 96-well plates with 1 µM Lip1, 100 nM RSL3 or without Lip1 (–Lip1) for 48h. n=2 for HMLE SCCs, n=2-4 for HMLE-Twist1 SCCs. Data shown (B, C, D) represent mean ± SEM. Viability was normalized to respective Lip1 control within each cell line and cell density.

cell clones (SCCs) with no detectable GPX4 protein (*GPX4*-KO) or with intact GPX4 expression (*GPX4*-WT) (Figure 9A). Since the lethal effect of the full knockout of GPX4 (Imai et al., 2003; Yant et al., 2003) can be rescued by Lip1 (Friedmann Angeli et al., 2014) (Figure 6A), SCCs were kept in 1 µM Lip1-containing medium. Next, I conducted viability assays using three HMLE (H1, H5, H6) and HMLE-Twist1 (HT1, HT2, HT3) SCCs with a full GPX4 knockout (*GPX4*-KO) and challenged them by withdrawal of Lip1 for 48h upon seeding. Again, I noticed that cell death was induced in a cell density-dependent manner: cells seeded at low cell density were highly susceptible to cell death induced by *GPX4* loss while high cell density induced complete resistance (Figure 9B). At intermediate seeding densities, an intermediate cell death induction was observed. However, in contrast to treatment with RSL3, I did not detect a pronounced difference in cell death induction at intermediate cell densities between HMLE and HMLE-Twist1 SCCs (Figure 9B and C). Importantly, addition of 500 nM Fer1 rescued cell death induction upon *GPX4*-KO to a similar extent as 1 µM Lip1 (Figure 9C), further supporting that ferroptosis was the observed cell death modality (Dixon et al., 2012; Friedmann Angeli et al., 2014). In order to ensure that analyzed SCCs were representative of the bulk population, two control SCCs with intact GPX4 expression of HMLE and HMLE-Twist1 cells were applied to 100 nM RSL3 treatment in viability assays. Again, RSL3 treatment elicited cell density-dependent ferroptosis (Figure 9D). In contrast to a full genetic knockout of *GPX4*, I observed an increased sensitivity of HMLE-Twist1 SCCs to GPX4 inhibition at intermediate seeding densities compared to HMLE SCCs (Figure 9D).

In summary, a full genetic knockout of *GPX4* confirmed that GPX4 function directly mediated cell density-dependent ferroptosis both in epithelial and in Twist1-induced mesenchymal HMLE cells. Cell death induction occurred to a similar extent in epithelial HMLE and mesenchymal HMLE-Twist1 upon *GPX4* knockout without any major differences at intermediate cell densities. These results suggested that similar pathways contributed to cell density-dependent ferroptosis in both cell lines that were most likely downstream of GPX4. Therefore, I focused on elucidating the pathways that might contribute to cell density-dependent ferroptosis.

4.6 Oncogenic signaling does not affect cell density-dependent ferroptosis

Recent studies have shown that RSL3 induces oncogenic-RAS-synthetic lethality in hTERT immortalized and SV40 large and small T containing fibroblasts (Yang and

Stockwell, 2008). Furthermore, MEK inhibitor that target mitogen-activated protein kinase (MAPK) signaling downstream of Ras, rescue RSL3-induced ferroptosis (Yang and Stockwell, 2008; Yang et al., 2014). Similar to these engineered fibroblasts (Hahn et al., 1999; Yang and Stockwell, 2008), HMLE cells were derived by introducing vectors expressing hTERT and the SV40 large T early region, containing both large T and small T, into primary human mammary epithelial cells. To transform cells and acquire tumorigenic cells, oncogenic $HRAS^{G12V}$ needs to be expressed (HMLE-Ras) (Elenbaas et al., 2001; Ince et al., 2007). Since both epithelial and Twist1-induced mesenchymal HMLE cells are equally susceptible to GPX4 inhibition or knockout, irrespective of the cellular phenotype, I hypothesized that the genetic background of these cells might influence cell density-dependent ferroptosis. To test whether oncogenic transformation also impacted cell density-dependent ferroptosis, I assessed RSL3-sensitivity in oncogene-transformed HMLE cells overexpressing HRAS or neuNT oncogenes (Mani et al., 2008), the latter serving as a model for Her2 overexpressing breast cancer (Chen et al., 2005b). Again, RSL3 induced cell death in a cell density-dependent manner in HMLE cells, but neither overexpression of HRAS nor of neuNT oncogenes altered sensitivity of the cells to RSL3 (Figure 10A). Likewise, overexpression of HRAS in HMLE-Twist1 cells did not confer any additional sensitivity to cell density-dependent ferroptosis induced by RSL3 treatment (Figure 10B).

PTEN is another frequently mutated or deleted gene in cancer, leading to tumor progression and poor prognosis (Chen et al., 2005b; Jones et al., 2013; Li et al., 1997; Steck et al., 1997). PTEN opposes phosphoinositide 3-kinase (PI3K) signaling which regulates proliferation, survival and metabolism via the downstream targets AKT, a serine/threonine kinase and the mammalian target of rapamycin (mTOR) pathway (Yu and Cui, 2016). Phosphorylation of AKT at Ser473 indicates active PI3K signaling (Hyun et al., 2000; Wan and Helman, 2003). Since PTEN-deleted cancer cells are selectively lethal to compounds targeting mTOR, for instance to CCI-779 (Neshat et al., 2001), I wondered whether PTEN deletion might also influence RSL3 sensitivity. CRISPR/Cas9 *PTEN*-deleted HMLE-Twist1-ER 24^{hi} cells were kindly generated and provided by Hilary Ganz, a PhD student in the Scheel laboratory (Mammary Stem Cells, Helmholtz-Center Munich). First, I confirmed the *PTEN* deletion in SCCs KO-1 and KO-2 by immunoblotting for phosphorylated AKT.

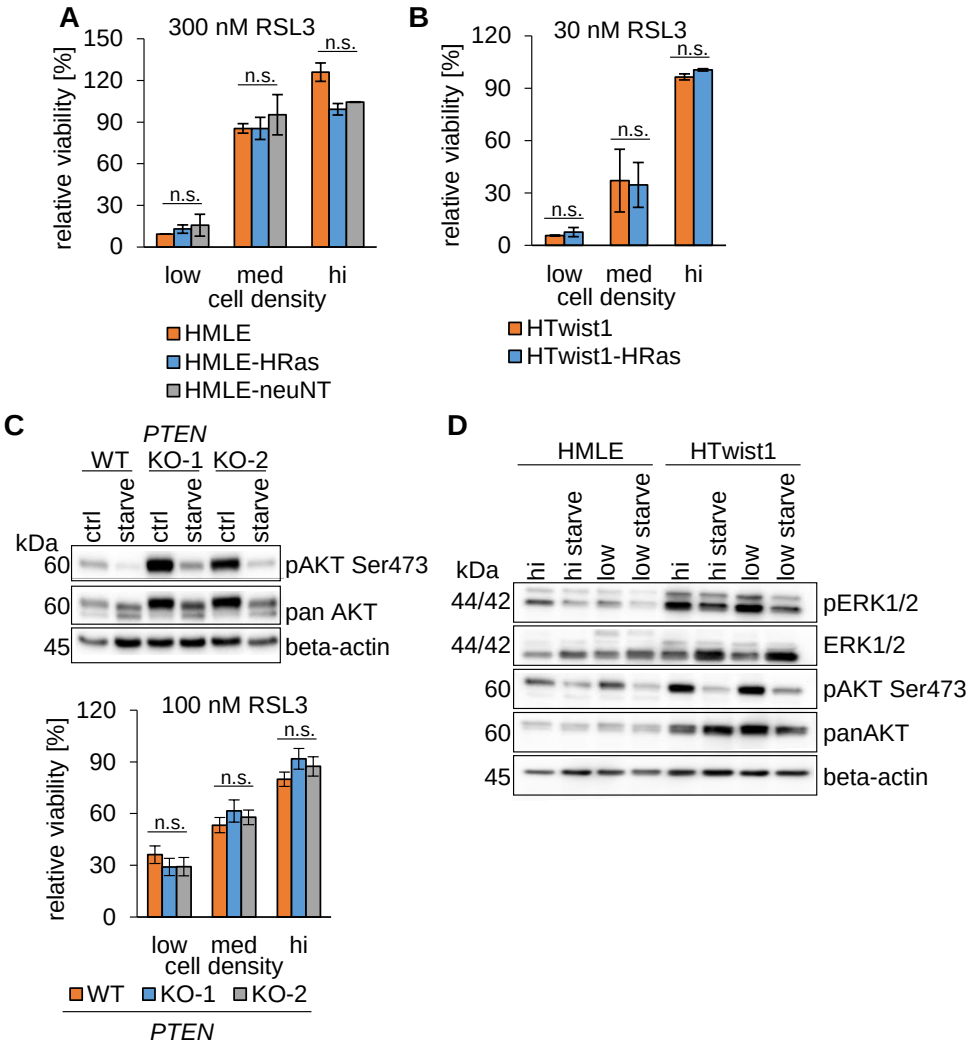

Figure 10: Cell density-dependent ferroptosis is not affected by oncogenic signaling

(A) Viability assay: treatment of HMLE, HMLE-HRas^{G12V} and HMLE-neuNT cells plated at indicated cell densities in 96-well plates with 0.3% DMSO or 300 nM RSL3 for 24h. n=2. (B) Viability assay: treatment of HMLE-Twist1 and HMLE-Twist1-Ras^{G12V} with 30 nM RSL3 for 24h as described in A. n=2. (C) Immunoblot (upper part): protein expression of phosphorylated AKT at serine residue 473 (pAKT Ser473), total AKT 1 and 2 isoforms (pan AKT) and beta-actin (loading control) in CRISPR/Cas9-derived *PTEN*-wildtype (WT) and *PTEN*-knockout single-cell clones (SCCs, KO-1 and KO-2) of HMLE-Twist1-ER 24^{hi} cells plated in 10-cm dishes. Cells were grown in growth-factor containing medium (PC-medium, ctrl) or starved overnight in basal DMEM/F-12 medium (starve) prior to protein extraction. kDa = kilo Dalton. Cell viability (lower part): treatment of *PTEN*-WT, KO-1 and KO-2 SCCs with 0.1% DMSO or 100 nM RSL3 for 24h as described in A. n=3. (D) Immunoblot: protein expression of phosphorylated ERK1/2 (pERK 1/2), total ERK, pAKT Ser473, pan AKT and beta-actin (loading control) in HMLE and HMLE-Twist1 cells plated at high or low cell density in 10-cm dishes. Starvation as described in C. Data shown represent one representative experiment performed independently two times. Data shown (A, B, C) represent mean ± SEM. Viability was normalized to respective DMSO control within each cell line and cell density. Statistics: two-tailed, unpaired T-test with Welch's correction (p-value: *<0.05, n.s. = not significant).

Indeed, I observed an upregulation of AKT phosphorylation at Ser473 in *PTEN*-deleted SCC KO-1 and KO-2 compared to a control SCC (WT) (Figure 10C). However, when I submitted *PTEN*-deleted SCCs to viability assays, I did not observe an effect beyond cell density-dependent ferroptosis upon treatment with 100 nM RSL3. Moreover, RSL3 treatment induced cell death in *PTEN*-deleted SCCs to a similar extent as in the *PTEN*-WT SCC (Figure 10C). Finally, to exclude any contribution of MAPK and PI3K signaling to cell density-dependent ferroptosis, I assessed whether cell density impacted MAPK signaling, activated downstream of RAS (McCubrey et al., 2007), and PI3K signaling in HMLE and HMLE-Twist1 cells. To this end, immunoblots for phosphorylated ERK1/2 (pERK1/2) and phosphorylated AKT at Ser473, as readouts for active MAPK and PI3K signaling, respectively (McCubrey et al., 2007; Yu and Cui, 2016), were performed. As expected, I did not observe a cell density-dependent regulation of pERK1/2 or pAKT Ser473 in HMLE and HMLE-Twist1 cells (Figure 10D). Compared to parental HMLE cells, Twist1-expression elevated total ERK1/2 and AKT levels (Figure 10D).
Conclusively, these data suggested that changes in MAPK or PI3K signaling that occur during oncogenesis did not modulate cell density-dependent ferroptosis.

4.7 Cell density-dependent ferroptosis is present in primary mammary epithelial cells

HMLE cells were immortalized and had undergone subsequent selection processes (Elenbaas et al., 2001), raising the question whether cell density-dependent ferroptosis-sensitivity depended on the immortalization process or whether it constituted an intrinsic property of human mammary epithelial cells. To address this question, primary human mammary epithelial cells (HMECs) were isolated from three breast reduction mammoplasties donated by healthy women. After establishing primary HMECs in an initial 2D culture, cells were plated in 96-well plates at different densities and treated for 24h with 100 nM RSL3. Interestingly, RSL3 treatment led to cell density-dependent ferroptosis in bulk cells of all three donors M16, M29 and M19 respectively (Figure 11A). All samples were similarly sensitive to RSL3 treatment and cell death was induced at both ambient oxygen atmosphere (20%) as well as 3% oxygen, the latter mimicking physiological tissue pressure (Figure 11A). Furthermore, I observed a comparable cell density-dependent cell death induction by RSL3 when CD10-positive HMEC of the basal

lineage (B+, CD10^{+}/CD49f^{hi}/EpCAM^{-}) prospectively isolated from donor M16 were submitted to viability assays (Figure 11B).

Together, these data indicated that cell density-dependent ferroptosis-sensitivity was a trait that was not acquired during the immortalization process, but that was already present in HMECs.

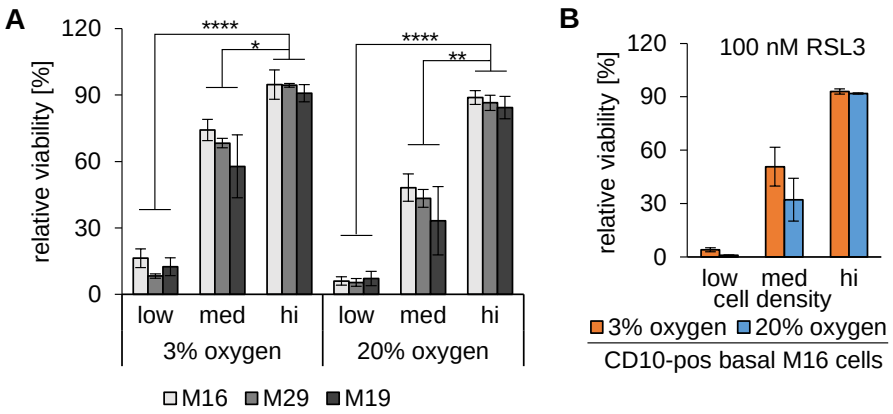

Figure 11: Cell density-dependent ferroptosis is a trait of primary HMECs

(A) Viability assay: treatment of bulk primary human mammary epithelial cells (HMECs) of three different donors (M16, M29, M19) plated at indicated cell densities in 96-well plates with 0.1% DMSO or 100 nM RSL3 for 24h at oxygen levels present in tissues (normoxia 3%) or at ambient oxygen level (20%). n=3. Statistics: two-tailed, unpaired T-test with Welch's correction (p-value: *<0.05, **<0.01, ****<0.0001). (B) Viability assay: treatment of prospectively, sorted CD10-positive primary HMECs of the basal lineage of donor M16 with 0.1% DMSO or 100 nM RSL3 as described in A. n=2. Data shown (A, B) represent mean ± SEM. Viability was normalized to respective DMSO control within each donor and cell density.

4.8 GPX4 inhibition by RSL3 prevents organoid formation in 3D collagen gels by primary HMECs

As described above, upon inhibition of GPX4 in 2D cultures, cell density-dependent ferroptosis was induced in both immortalized and primary HMECs. It has been reported that absence of GPX4 does not impact colony formation of transformed MEFs in Matrigel which provides an ECM enabling three dimensional (3D) growth. In contrast, 2D viability has been highly impaired in the absence of GPX4 (Schneider et al., 2010). Therefore, I wanted to assess how a 3D-environment impacted sensitivity towards ferroptosis in primary as well as immortalized HMECs.

To do so, primary HMECs were plated as single cells in floating 3D-collagen gels as recently described (Linnemann et al., 2015). In this organoid assay, Collagen I provides an ECM that mimics a physiological environment, thereby allowing the formation of organoids by primary HMECs. More precisely, prospectively isolated

cells of the basal lineage (B+, $CD10^{+}/CD49f^{hi}/EpCAM^{-}$) form branched organoids that resemble mammary gland architecture. In contrast, prospectively isolated progenitor cells of the luminal lineage (LP, $CD49f^{+}/EpCAM^{+}$) mainly form spheres (Linnemann et al., 2015). For viability assays, primary bulk HMECs as well as sorted B+ and LP cells were seeded as single cells into 3D collagen gels. After five days of an initial survival culture, allowing the establishment of single cells, RSL3, Lip1 or a combination of both were applied to cultures every two to three days. As expected, bulk primary HMECs gave rise to both branched organoids as well as spheres in the DMSO and Lip1 control (Figure 12A). Furthermore, branched organoids were established by B+ cells and spheres by LP cells (Figure 12B). Continuous RSL3-treatment strongly impaired organoid formation in all samples, leading to either the absence of colonies or the generation of smaller colonies that appeared fragmented (Figure 12A and B). Simultaneous Lip1 application during RSL3 treatment partially rescued organoid formation in bulk as well as sorted B+ and LP cells (60-100% of DMSO control) (Figure 12A and B). To analyze whether organoids present after RSL3 treatment were still proliferative, I performed immunofluorescent staining for the proliferation marker Ki67 and used DAPI to visualize cell nuclei. For organoids formed by basal B+ cells, vimentin staining was performed to visualize morphology of branched structures. Cells stained positive for Ki67 in the DMSO and Lip1 control as well as in Lip1-rescued RSL3-treated organoids for both B+- and LP-derived organoids (Figure 12C). However, Ki67 staining was absent in organoids that had been continuously treated with RSL3 and nuclear staining by DAPI indicated their fragmentation (Figure 12C). Moreover, B+-derived organoids displayed vimentin-positive cells at a basal position in DMSO, Lip1 and Lip1/RSL3 conditions. On the contrary, vimentin-positive cells appeared disordered and fragmented in RSL3-treated organoids (Figure 12C).

Together, these data indicated that both bulk cells, as well as prospectively sorted primary HMECs were highly susceptible to GPX4 inhibition by RSL3 at the single cell level. Thereby, continuous RSL3 treatment impaired proper organoid formation by primary HMECs, resulting in non-proliferative, disorganized organoids. Conclusively, a three dimensional matrix provided by Collagen I did not enable organoid formation of primary HMEC plated as single cells in presence of RSL3.

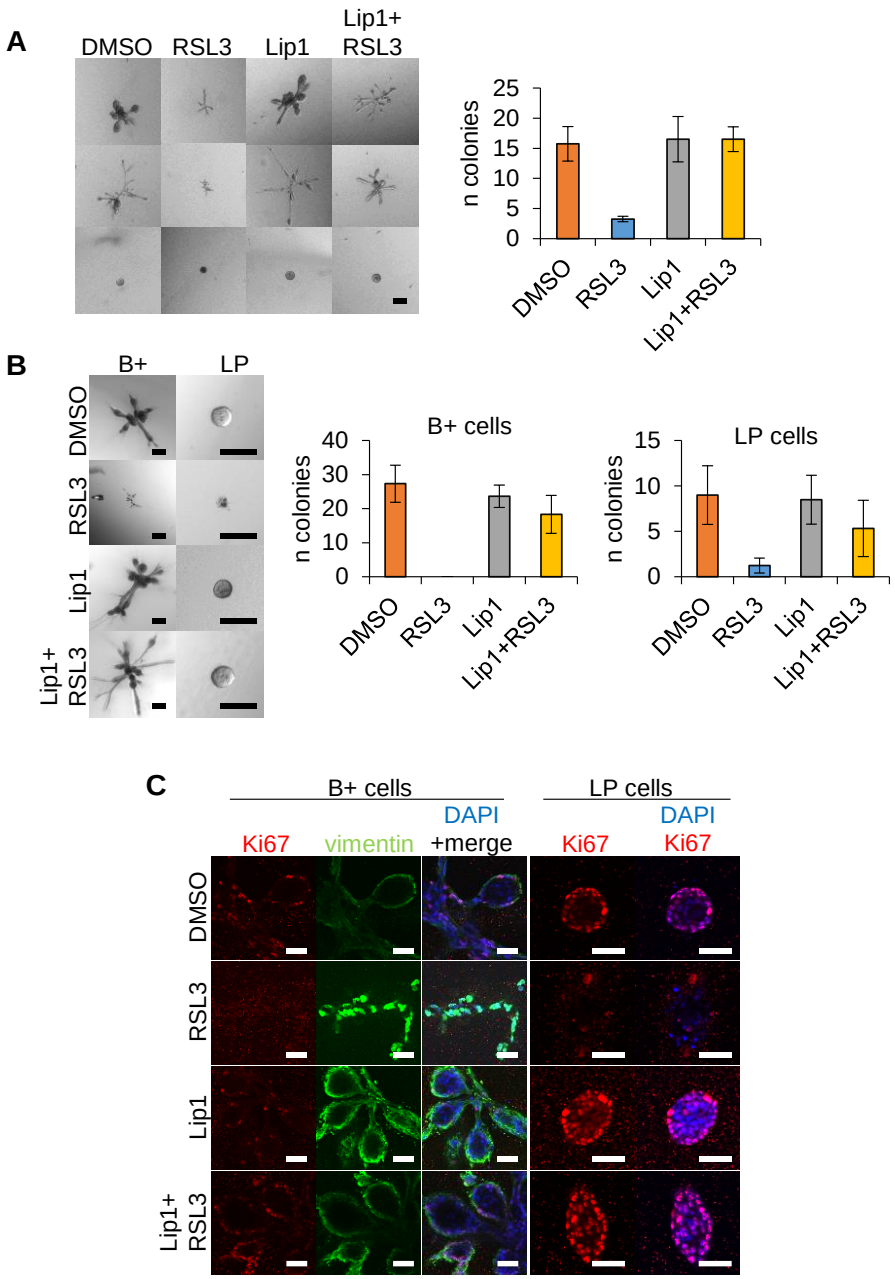

Figure 12: Cell density-dependent ferroptosis prevents organoid formation of primary HMECs

(A) 3D-collagen gels: bulk primary human mammary epithelial cells (HMECs) of donor M16 were treated with 0.1% DMSO, 100 nM RSL3, 500 nM Lip1 or a combination of RSL3 and Lip1 for 7 days prior to quantification of organoids. Representative bright-field images of organoids are shown on the left. Data shown represent mean ± SD of 3-4 collagen gels. Scale bar: 200 µm. (B): 3D-collagen gels: prospectively sorted CD10-positive basal (B+) or luminal progenitor (LP) primary HMECs were treated as indicated in A for 7-10d prior to quantification. Representative bright-field images of organoids are shown on the left. Data shown represent mean ± SD of 3-4 collagen gels from one representative experiment performed independently two times. Scale bar: 200 µm. (C) Confocal microscopy of 3D-collagen gels: staining of organoids cultured as described in B with Ki67 (red), vimentin (green) and DAPI (blue). DAPI was used as nuclear staining. Scale bar: 50 µm.

4.9 Knockdown or knockout of GPX4 impairs organoid formation in 3D-collagen gels by immortalized HMLE cells

In contrast to immortalized and tumorigenic MEFs (Schneider et al., 2010), inhibition of GPX4 impacted organoid formation of primary HMECs in a 3D environment. Primary HMECs plated in 3D-collagen gels require an initial five day survival phase prior to initiation of organoid formation (Linnemann et al., 2015), indicating elevated levels of cellular stress which might explain the observed sensitivity to GPX4 inhibition in 3D. Furthermore, although both primary as well as immortalized HMECs showed cell density-dependent ferroptosis upon RSL3 treatment, the immortalization process could potentially affect sensitivity to GPX4-inhibition in a 3D environment. Therefore, I wanted to determine whether colony formation of immortalized HMLE cells was influenced in 3D collagen gels as well. As previously shown, HMLE cells plated in 3D collagen gels give rise to multicellular spheres depending on the amount of seeded cells (Schmidt et al., 2015). For this purpose, HMLE cells with a partial knockdown of GPX4 or with a complete loss of GPX4 by CRISPR/Cas9-mediated gene knockout were plated into 3D collagen gels.

First, 500 HMLE 24^{hi} cells with (sh-GPX4) or without (sh-nt) a pTRIPZ construct targeting GPX4 were seeded into 3D collagen gels. Dox-treatment was immediately applied to induce expression of shRNAs and was refreshed every two days. Both HMLE 24^{hi} cells containing sh-nt or sh-GPX4 were able to form colonies in control conditions (DMSO) to the extent. On the contrary, 0.5 µg/ml Dox treatment led to a 5-fold decrease in arising colonies upon induction of GPX4 knockdown without impacting colony formation of sh-nt-containing cells (Figure 13A). These data showed that induction of GPX4 knockdown in immortalized HMLE 24^{hi} cells at the single cell level resulted in impaired colony formation in 3D collagen gels. Taken together, this indicated that both primary and immortalized HMECs are susceptible to ferroptosis induction in a 3D environment.

Since cell density predicts ferroptosis-sensitivity in 2D cultures, I wondered whether the latter was also influenced by seeded cell numbers or by the size of colonies (single cells *versus* small colonies) in a 3D environment. To address this question, I plated HMLE *GPX4*-KO SCCs (H5) at different densities in 3D collagen gels and cultured them in three different conditions. The medium was either supplemented with 500 nM Lip1 (+Lip1) or directly deprived of Lip1 (−Lip1). In a third condition,

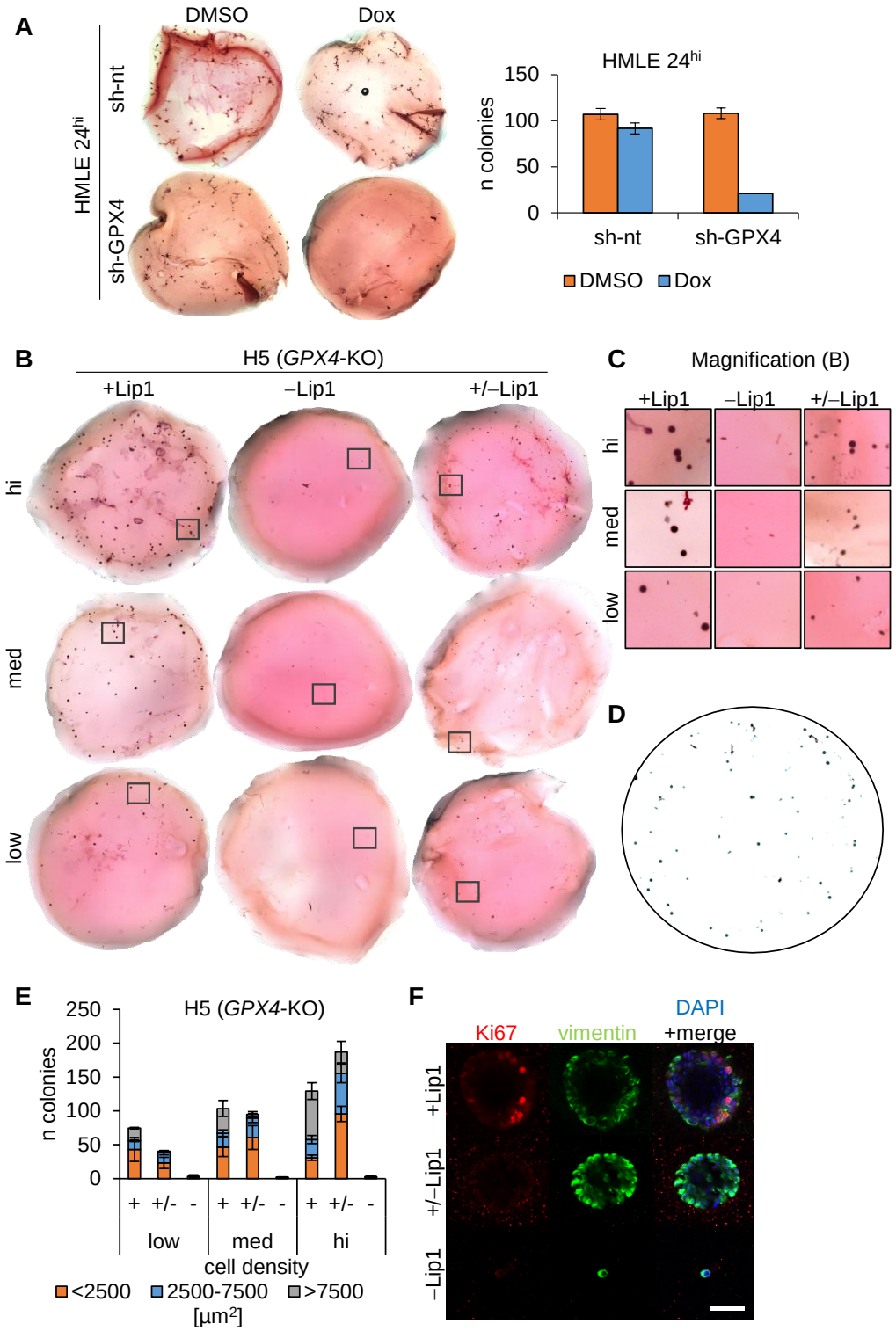

Figure 13: Cell density-dependent ferroptosis impairs colony formation of *GPX4*-knockdown and knockout cells

(A) Carmine staining and quantification of 3D-collagen gels: treatment of 500 plated HMLE 24^{hi} cells containing Dox-inducible non-targeting (sh-nt) or *GPX4*-targeting (sh-GPX4) shRNAs in 3D-collagen gels with DMSO solvent control or 0.5 µg/ml Dox for 9-11 days. Representative pictures of carmine-stained 3D-collagen gels are shown on the left and quantification of colonies is shown on the right. Data shown represent mean ± SD of three collagen gels from one representative experiment performed independently two times. (B) and (C) Carmine staining of

3D-collagen gels: HMLE single-cell clone (SCC) H5 with *GPX4*-knockout (KO) was seeded at indicated cell densities (75 (low), 225 (med), 675 (hi) cells) in 3D-collagen gels in medium with 500 nM Lip1 (+Lip1), without Lip1 (–Lip1) or for 3d in an initial Lip1-culture prior to withdrawal of Lip1 (+/–Lip1) for 7-10 days. Representative pictures of (B) carmine-stained 3D-collagen gels and (C) magnifications of colonies grown in 3D-collagen gels are shown. (D) Representative converted, binary picture for ImageJ quantification obtained from carmine-stained 3D-collagen gels as described in B. (E) Quantification of carmine-stained colonies formed by HMLE SCC H5 with *GPX4*-KO treated as described in B. Data shown represent mean ± SD of 3-4 collagen gels from one representative experiment performed independently two times. (F) Confocal microscopy of 3D-collagen gels: staining of colonies treated as described in B at an intermediate seeding density (225 cells, med) with Ki67 (red), vimentin (green) and DAPI (blue). DAPI was used as nuclear staining. Scale bar: 50 µm.

cells were grown for three days in Lip1-containing medium which allowed the generation of small colonies prior to withdrawal of Lip1 (+/−Lip1). As expected, I observed the formation of spheres in Lip1-containing medium irrespective of seeding density (Figure 13B). Direct withdrawal of Lip1 (−Lip1) from the culture medium led to complete growth inhibition, similar to what was observed at low seeding density in 2D cultures. In the third condition (+/−Lip1), Lip1 withdrawal after three days of culture still enabled outgrowth of colonies (Figure 13B). However, these colonies were smaller and appeared to be less proliferative compared to colonies generated during continuous Lip1-cultures (Figure 13C). In order to quantify the number and size of colonies, images were converted to binary pictures and automatically analyzed using ImageJ (Figure 13D). Indeed, ImageJ analysis confirmed that direct withdrawal of Lip1 (−Lip1) prevented colony formation independently of seeding density (Figure 13E). Moreover, ImageJ analysis revealed that upon delayed withdrawal of Lip1 (+/−Lip1), colonies were formed to a similar extend as in control Lip1 cultures (+Lip1). However, the number of colonies with an area greater than 7500 µm^2 were either strongly reduced (85-90% less for low and med cell density respectively) or reduced by 50% for high cell density in the +/−Lip1 condition compared to the +Lip1 condition (Figure 13E). These data suggested that proliferation has been disturbed when Lip1 was withdrawn at a later time point. Alternatively, the appearance of smaller colonies might be the consequence of cell death induction by GPX4 inhibition.

To differentiate between induction of cell death and inhibition of proliferation, I assessed whether the residual, smaller colonies contained proliferating cells. Immunofluorescent staining for the proliferation marker Ki67 was performed on spheres generated at the intermediate seeding density. Interestingly, Ki67-positive

cells were only observed in spheres cultured in Lip1-containing medium, while spheres arising in +/−Lip1 cultures did not stain positively for Ki67 (Figure 13F). Furthermore, based on immunostaining for vimentin, these spheres appeared to be less compact and fragmented when Lip1 was withdrawn after three days (+/–Lip1) compared to continuous Lip1 cultures (+Lip1) (Figure 13F). These results indicated that proliferation was impaired, but cell death was not induced in all cells within one colony, at least at the chosen endpoint of this experiment. For cultures grown without Lip1 (–Lip1), I could only detect some residual cells that neither stained positively for Ki67 nor showed any vimentin staining (Figure 13F), indicating induction of cell death in single cells. Together, these data suggested that GPX4 knockout, if induced at the single-cell level, prevented sphere formation of HMLE cells in 3D collagen gels. Of note, this effect occurred independently of the initial seeding density. However, once small colonies had formed, GPX4 knockout impaired expansion in 3D-cultures, but did not lead to complete disappearance of colonies, suggesting some resistance to GPX4 knockout-induced cell death.

Overall, these results showed that ferroptosis could be induced in a 3D environment in both primary as well as immortalized HMECs, as long as cells remained single cells. Since high cell density completely protected from ferroptosis in 2D culture and the formation of small colonies partially protected from ferroptosis in 3D cultures, it could be possible that not the absolute cell number, but the proximity and distance of cells to each other determined ferroptosis sensitivity in HMECs.

4.10 Cell density-dependent ferroptosis is not affected by secreted factors or cell-cell-adhesions

I established that cell density-dependent ferroptosis is an intrinsic property of both primary as well as immortalized HMECs. Furthermore, ferroptosis, induced by inhibition or knockout of GPX4, was independent of oncogenic signaling and occurred in cells cultured both in 2D and 3D cultures. To further shed light on what exactly might trigger ferroptosis at low density, I undertook a series of experiments addressing potential differences concerning proliferation, secreted factors and cell-cell adhesion signaling.

Since cell density is known to affect proliferation (Abercrombie; Stoker and Rubin, 1967), proliferation rates of HMLE and HMLE-Twist1 cells seeded at different

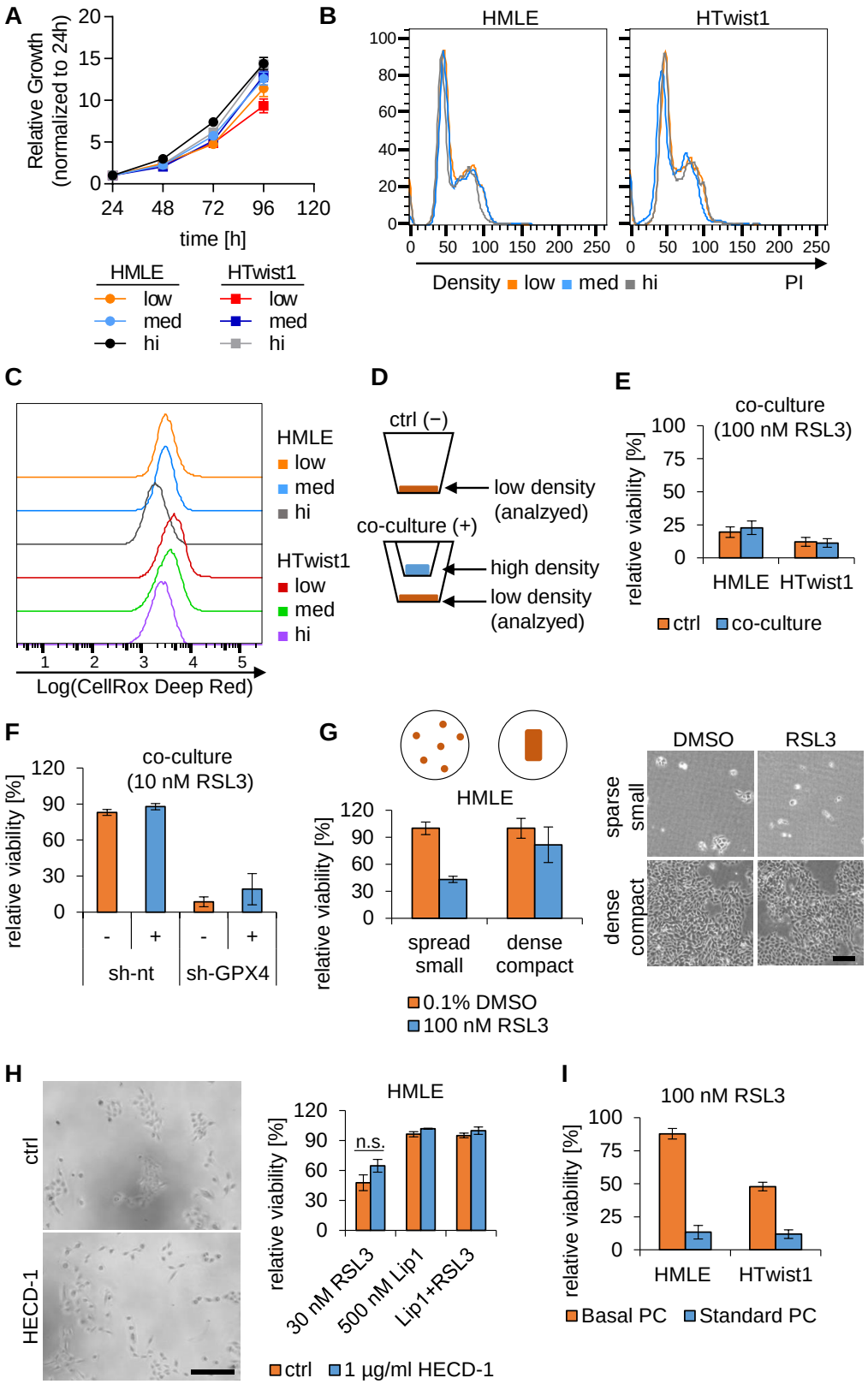

Figure 14: Cell density-dependent ferroptosis is not affected by secreted factors or cell-cell-adhesions

(A) Proliferation curve: measurement of metabolically active HMLE and HMLE-Twist1 cells plated at indicated densities in 96-wells every 24h for a period of 96h. Data shown represent mean ± SD of n=10 wells per time point normalized to the 24h measurement. (B) Cell-cycle analysis by flow

cytometry: staining of HMLE and HMLE-Twist1 cells seeded at indicated densities in 10-cm dishes for 48h prior to fixation and staining with propidium iodide (PI). X-axis: linear scale of PI fluorescence. Y-axis: percentage of maximum count. Data show one representative experiment performed independently two times. (C) Flow cytometry: CellRox Deep Red staining of HMLE and HMLE-Twist1 cells seeded at indicated densities in 6-cm dishes for 48h. X-axis: log10 of CellRox Deep Red fluorescence. Y-axis: percentage of the maximum count. Data show one representative experiment performed independently two times (D) Experimental setup for co-culture experiments. (E) Quantification of co-culture experiment as outlined in D: assessment of cell viability of HMLE and HMLE-Twist1 cells treated with 100 nM RSL3 for 20-24h without or during co-culture. Mean ± SEM is shown. n=5. Data were partly generated by Marie Bannier-Hélaouët (Intern). (F) Quantification of co-culture experiment (as outlined in D) using HMLE 24^{hi} cells expressing Dox-inducible non-targeting (sh-nt) or *GPX4*-targeting (sh-GPX4) shRNAs, pre-treated for 24h with 0.5 µg/ml Dox which was further applied during the experiment. Sh-nt cells were used for high seeding density co-culture (+). 10 nM RSL3 treatment was applied for 20-24h. Mean ± SD is shown. n=2. (G) Viability assay: the same cell number of HMLE cells was plated distributed or on one spot in 6 cm-dishes as illustrated followed by treatment with 100 nM RSL3 for 18h. Representative bright-field images of treated cells are shown on the right. Scale bar: 200 µm. Data shown represent mean ± SD of n=3 6-cm dishes. (H) Cell-scatter experiment: HMLE cells were pre-treated with 1 µg/ml HECD-1 prior to plating 600 cells in 96-well plates. Cells were treated for 24h with 30 nM RSL3 and 500 nM Lip1. Representative bright-field images of HECD-1-treated HMLE cells plated in 96-well plates prior to RSL3-treatment are shown. Scale bar: 200 µm. Mean ± SEM is shown. n=3. Statistics: two-tailed, unpaired T-test with Welch's correction (p-value: *<0.05, n.s. = not significant). (I) Viability assay: treatment of 450 plated HMLE and 1000 plated HMLE-Twist1 cells cultured in basal or growth-factor containing (Standard) PC medium in 96-well plates with 100 nM RSL3 for 24h. Mean ± SD is shown. n=2. Viability (E-I) was normalized to respective DMSO control within each cell line.

densities were assessed. Both cell lines showed similar proliferation rates which were not affected by density (Figure 14A), at least in short-term cultures that were also used for viability assays. Cell cycle analysis supported this finding (Figure 14B), ruling out differences in proliferation as regulator of ferroptosis sensitivity and resistance in cell density-dependent ferroptosis.

Moreover, it has been shown that ROS level vary between dense and sparse cultures (Limoli, 2004; Pani et al., 2000). Therefore, I assessed general ROS levels using the flow-cytometry compatible fluorescent dye CellRox Deep Red. Indeed, I observed an increase in ROS levels in low cell density culture compared to high cell density culture both in HMLE and HMLE-Twist1 cells (Figure 14C). These results revealed an elevation of oxidative stress at low density that was not directly related to proliferation.

In Burkitt' Lymphoma (BL) cells, low cell density leads to an oxidative stress-induced cell death that can be rescued by co-culture with irradiated fibroblasts (Falk et al., 1993, 1998). Mechanistically, secretion of cysteine by fibroblasts fuels a cystine/cysteine redox cycle within BL cells, thereby inducing a reducing

extracellular environment protecting BL cells from cell death induced by low seeding density (Banjac et al., 2008; Falk et al., 1993, 1998). To assess whether a similar mechanism sensitized cells in low density to ferroptosis, I asked whether one or several secreted factors, secreted by cells cultured at high density, might protect them from cell death induced by GPX4 inhibition. To test this hypothesis, HMLE and HMLE-Twist1 cells were seeded at a low density at the bottom of a 24-well plate and for co-cultures, cells were additionally seeded at a high density in inserts placed into the 24-well plate (Figure 14D). This system enabled a direct exchange of secreted factors between cultures seeded at low and high cell density. In the absence of a co-culture, RSL3 reduced the viability of cells seeded at low cell density by 80-88% compared to the DMSO control (Figure 14E). When cells were cultured in the co-culture condition, RSL3 reduced viability of cells seeded at low cell density to a similar extent (Figure 14E). These data indicated that co-culture with cells seeded at high cell density did not rescue cell death induction of cells seeded at low cell density. Experiments were repeated using HMLE 24^{hi} cells with (sh-GPX4) or without (sh-nt) a Dox-inducible GPX4 knockdown. Hereby, sh-nt cells were seeded into high cell density co-cultures for both GPX4 knockdown and sh-nt control HMLE 24^{hi} cells to avoid an impact of Dox-induction and 10 nM RSL3 treatment on the viability of cells seeded at high cell density (Figure 8). While sh-nt seeded at low cell density remained viable to a similar extent in both conditions (with or without co-culture), Dox and low-dose RSL3 treatment induced cell death in GPX4 knockdown cells which was again not rescued upon co-culture (Figure 14F). Together, these data suggested that cells seeded at high cell density did not secrete soluble factors that induced an environment that protected them from cell density-dependent ferroptosis induced by GPX4-inhibition.

In 3D cultures, ferroptosis was efficiently induced at the single-cell level, but once small colonies were generated, a partial protection was observed (Figure 13B, C and E). These indicated that the proximity of cells and the formation of cell-cell-adhesions might play a role in cell density-dependent ferroptosis. Since a major difference between low and dense 2D cultures are the size of colonies and the distance between cells (Figure 5C), I mimicked low and dense cultures by seeding the amount of cells in two different ways. HMLE cells were seeded either distributed at a low cell density on a 6-cm dish, thereby forming small, spread colonies. Alternatively, exactly the same amount of HMLE cells were seeded on a defined,

small area bordered by a sticky insert within a 6-cm dish, resulting in one large, dense and compact colony (Figure 14G). The next day, the sticky insert was removed and cells were treated for 18h with 100 nM RSL3 prior to measuring cell viability. Interestingly, although the same cell number was seeded, RSL3 induced cell death only in the condition where cells were distributed on the 6-cm dish while RSL3 failed to do so in the dense condition (Figure 14G). These results indicated that not the seeded cell number itself determined sensitivity to GPX4 inhibition, but rather the distribution and relationship of seeded cells to each other (proximity of cells).

HMLE-Twist1 cells did not form dense colonies connected by cell-cell adhesions such as E-cadherin (Figure 5F) (Mani et al., 2008), but still showed resistance at high cell densities to cell death induced by GPX4 inhibition (Figure 5D and E). However, HMLE-Twist1 cells are able to form weak cell-cell adhesion mediated by another cadherin, namely N-cadherin (Ganz et al., 2006; Mani et al., 2008), suggesting that cell-cell adhesions mediated by N-cadherin might be upregulated at high cell density. Intercellular contacts of HMLE cells are mainly formed by E-cadherin and disruption leads to cell scattering (Onder et al., 2008). Therefore, I determined whether treatment of HMLE with an E-cadherin neutralizing antibody (HECD-1), that has been shown to induce cell scattering (Chartier, 2006; Wong and Gumbiner, 2003), impacted cell death induction by GPX4-inhibition when cells were plated at an intermediate-low density (600 cells) in 96-well plates. Thereby, I wished to further clarify the mechanism of cell density-dependent ferroptosis. HMLE cells were pre-treated with HECD-1 for 24h and then plated into viability assays during which HECD-1 was further applied. As expected, HECD-1 treatment induced cell scattering and loosened the compactness of colonies formed by HMLE cells (Figure 14H). When cells were exposed to 30 nM RSL3 treatment, HECD-1-induced scattering did not impact RSL3-induced cell death induction compared to the RSL3-treated control (Figure 14H). Of note, Lip1 rescued RSL3-induced cell death in both conditions (Figure 14H). These results indicated that that cell-cell-adhesion-linked signaling did not determine cell density-dependent ferroptosis.

Interestingly, the absence (basal PC) and presence (Standard PC) of growth factor supplements in culture medium affected sensitivity to RSL3 treatment in both HMLE and HMLE-Twist1 cells. When 450 HMLE cells or 1000 HMLE-Twist1 cells were plated in 96-well plates, cells were less sensitive to RSL3-treatment when cultured

in basal PC medium compared to culture in Standard PC-medium (Figure 14I). These results suggested that metabolic pathways fueled by growth factors contributed to cell density-dependent ferroptosis induced by GPX4-inhibition.

Taken together, these data revealed that cell density-dependent ferroptosis was not directly linked to differences in proliferation, secreted factors or cell-cell adhesions. Overall, I could not yet determine one or several factors that explained cell density-dependent ferroptosis sensitivity of HMLE and HMLE-Twist1 cells to GPX4-inhibition.

4.11 Cell density is not a determinant of ferroptosis-sensitivity in a panel of breast cancer cell lines

Cell density-dependent ferroptosis induced by GPX4 is an intrinsic trait of both primary as well as immortalized HMECs. A recent study has revealed that triple-negative breast cancer (TNBC) cell lines are highly sensitive to ferroptosis induction due to the expression of the acyl-CoA synthetase long chain family member 4 (ACSL4). Thus, ACSL4 emerged as a marker for ferroptosis sensitivity that shapes lipid composition within cells (Doll et al., 2017). Moreover, another publication has revealed that in order to support glutamine-dependence of TNBC, expression of the system x_c^- is increased in TNBC cell lines (Timmerman et al., 2013). Together, these studies imply that ferroptosis sensitivity of TNBC cell lines is regulated by several pathways. For these reasons, I wondered whether cell density impacted ferroptosis-sensitivity in a panel of breast cancer cell lines as well. For this purpose, two epithelial hormone receptor-positive (MCF7 and T-47D) and three TNBC (epithelial MDA468 and mesenchymal MDA231 and MDA157) cell lines were seeded at different densities in 96-well plates and exposed to 100 nM RSL3 treatment. None of the analyzed breast cancer cell lines showed a cell density-dependent cell death induction by RSL3 treatment (Figure 15A). However, these experiments confirmed that MDA468, MDA231 and MDA157 cell lines were highly sensitive for ferroptosis, whereas MCF7 cells were resistant to RSL3 treatment (Figure 15A). In contrast to published data (Doll et al., 2017), I observed an intermediate sensitivity of T-47D cells. In T-47D cells, RSL3-treatment reduced viability by 60-67% compared to the DMSO control irrespective of seeding density (Figure 15A). Moreover, when different concentrations of RSL3 were employed for dose-response curves, I did not detect cell density-dependent ferroptosis in MCF7 and MDA231 cells (Figure 15B

and C). Immunoblotting for GPX4 revealed similar expression levels of GPX4 between cell lines (Figure 15D), suggesting that ferroptosis sensitivity was not directly linked to different GPX4 expression levels in this panel of breast cancer cell lines.

Conclusively, I did not determine a cell density-dependent ferroptosis-sensitivity in a panel of breast cancer cell lines. Furthermore, these data suggested that most likely a different mechanism than ACSL4 marker expression induced ferroptosis-sensitivity in primary and immortalized HMECs.

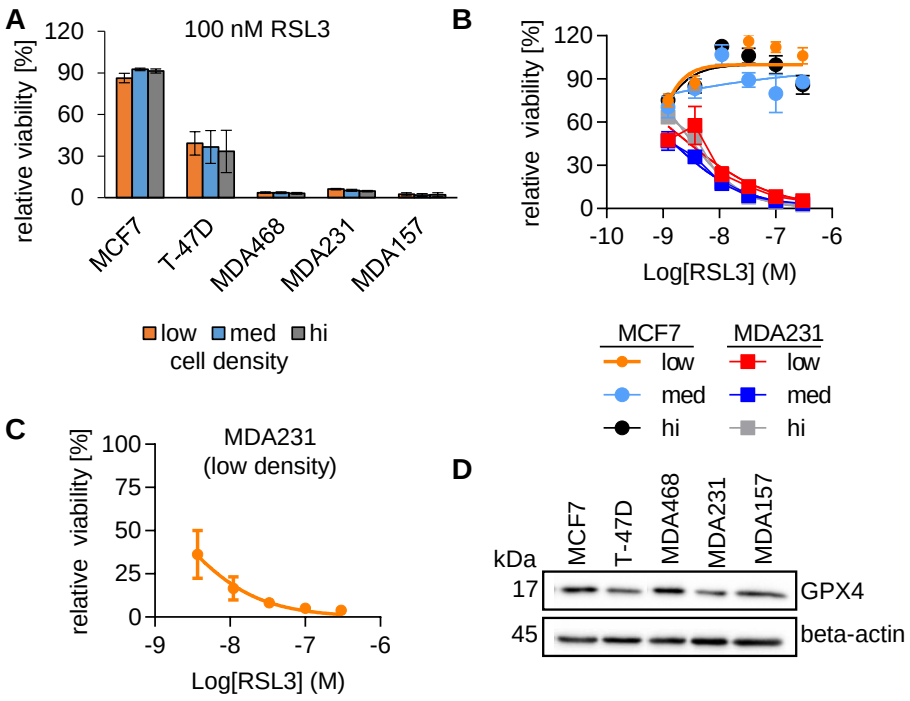

Figure 15: Cell density is not determining ferroptosis-sensitivity in a panel of breast cancer cell lines

(A) Viability assay: treatment of indicated breast cancer cell lines seeded at different densities in 96-well plates with 0.1% DMSO or 100 nM RSL3 for 24h. Mean ± SEM is shown. n=4. (B) Dose-response curves: treatment of MCF7 and MDA231 with 3-fold dilutions of RSL3 as described in A. Mean ± SD is shown of n=5 wells. (C) Viability assay: treatment of MDA231 plated at a cell density of 600 cells in 96-well plates with 3-fold dilutions of RSL3 for 24h. Mean ± SEM is shown. n=3. (D) Immunoblot: protein expression of GPX4 and beta-actin (loading control) in indicated breast cancer cell lines. kDa= kilo Dalton. Viability (A-C) was normalized to respective DMSO control within each cell line.

4.12 Iron availability and lipoxygenation, but not ACSL4 contribute to cell density-dependent ferroptosis induction by GPX4 inhibition

To further characterize cell density-dependent ferroptosis induced in primary and immortalized HMECs, known ferroptosis modulators were employed in viability

assays to examine their ability to rescue RSL3-induced cell death at intermediate-low density (600 cells) in HMLE and HMLE-Twist1 cells. Compared to the DMSO control, 100 nM RSL3 treatment alone reduced viability by 72% in HMLE and by 83% in HMLE-Twist1 cells, respectively (Figure 16A). RSL3-induced cell death was significantly rescued by DFO-mediated iron chelation, inhibition of lipoxygenases by both PD146176 (inhibition of Alox15) and BWA4C (inhibition of both Alox5 and 15) and by the lipophilic antioxidant α-toc (Figure 16A), as previously reported (Dixon et al., 2012; Friedmann Angeli et al., 2014; Seiler et al., 2008; Yang et al., 2016). In contrast to published data (Dixon et al., 2012), the iron chelator CPX did not rescue RSL3-induced cell death (Figure 16A). Mechanistically, CPX directly leads to intracellular iron chelation, thereby affecting iron-containing enzymes (Cao and Dixon, 2016), which might disturb cellular functions of HMLE and HMLE-Twist1 cells and thus counteract rescuing effects. This hypothesis was further supported by the fact that in CPX control treatment without RSL3, viability of HMLE-Twist1 cells was impacted, which I did not observe for the other modulators (Figure 16A). ACSL4 was described as a marker for ferroptosis sensitivity by increasing the pool of oxidation-sensitive PUFAs within membranes (Doll et al., 2017; Kagan et al., 2017). Therefore, cells were pre-treated with ROSI, a PPARγ agonist which has been shown to specifically inhibit ACSL4 as well (Kim et al., 2001), and its impact on RSL3-induced cell death was assessed. Surprisingly, ROSI failed to rescue RSL3-induced cell death both in HMLE and HMLE-Twist1 cells (Figure 16A), although both cell lines expressed ACSL4 at the protein level as confirmed by immunoblotting (Figure 16B). ACSL4 presence or absence at the protein level was linked to ferroptosis-sensitivity and –resistance (Doll et al., 2017) and the rescuing abilities of ROSI might be shaded due to effects on PPARγ (Lehmann et al., 1995). For these reasons, I performed CRISPR/Cas9-mediated gene knockout of *ACSL4* in HMLE *GPX4*-KO SCCs (H5). As assessed by immunoblotting, I obtained several SCCs without ACSL4 protein expression (*ACSL4*-KO: A1, A3, A4, A5, A7, A8) as well as WT-controls (*ACSL4*-WT: A2 and A6) (Figure 16C). Importantly, these SCCs did not show any differences on a morphological level (Figure 16D). For viability assays, these SCCs were plated at different cell densities into 96-well plates and exposed to *GPX4*-KO by Lip1 withdrawal. Again, cell density determined sensitivity towards *GPX4*-KO-induced cell death (Figure 16E). Surprisingly, presence or absence of ACSL4 at the protein level did not impact sensitivity towards *GPX4*-KO-induced cell

death at all (Figure 16E), suggesting that ACSL4 did not impact cell density-dependent cell death. Notably, dependence on ACSL4 in HMLE-Twist1 cells was not assessed, since no SCC with an ACSL4 knockout had been derived.

In sum, these data suggested that the labile iron pool as well as LOX-mediated oxidation processes contributed to cell density-dependent ferroptosis in both HMLE and HMLE-Twist1 cells. At least in HMLE cells, cell death induction upon GPX4 knockout was not dependent on ACSL4 expression.

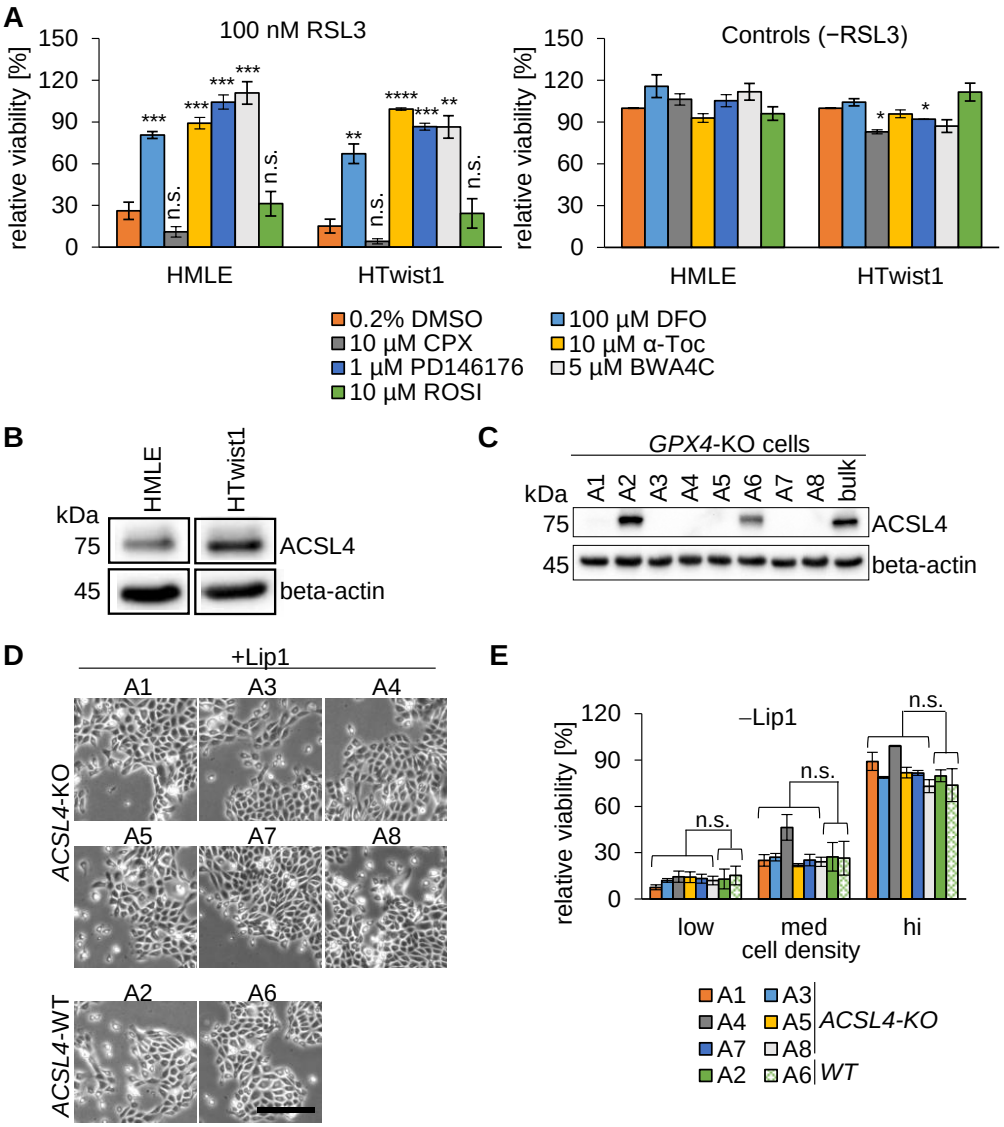

Figure 16: Cell density-dependent ferroptosis is dependent on iron and lipoxygenation, but independent of ACSL4

(A) Rescue-viability assay: treatment of HMLE and HMLE-Twist1 cells plated at 600 cells in 96-well plates with 100 nM RSL3 or a combination with the indicated compounds for 20-24h. Rosiglitazone (ROSI) treatment was additionally applied for 24h prior to RSL3 treatment. DFO: Deferoxamine, CPX: Ciclopirox α-toc: α-tocopherol. n=2-5. Data were partly generated by Felix Holstein (Master Student). (B) Immunoblot: protein expression of ACSL4 and beta-actin (loading control) in HMLE and HMLE-Twist1 cells plated at high cell density in 10-cm dishes.

kDa= kilo Dalton. (C) Immunoblot: ACSL4 and beta-actin (loading control) protein expression in single-cell clones (SCCs) derived by CRISPR/Cas9 genome-editing in the *ACSL4* locus of HMLE H5 SCC with *GPX4*-KO plated at intermediate cell density in 10-cm dishes. kDa= kilo Dalton. (D) Representative bright-field images of SCCs described in C. Scale bar: 200 µm. (E) Viability assay: withdrawal of 1 µM Liproxstatin (Lip1) for 48h of HMLE H5 *GPX4*-KO SCCs with or without ACSL4 expression as shown in C plated at indicated cell densities in 96-well plates. WT = wildtype. n=3. Data shown (A, E) represent mean ± SEM. Viability was normalized to respective DMSO control (A) or Lip1 control (E) within each cell line and cell density. Statistics: two-tailed, unpaired T-test with Welch's correction (p-value: *<0.05, **<0.01, ***<0.01, ****<0.0001, n.s. = not significant).

4.13 Lipid peroxidation levels do not correlate with cell density-dependent ferroptosis upon GPX4 inhibition or knockout

As a consequence of GPX4 inhibition, the accumulation of lipid hydroperoxides is regarded as a hallmark of ferroptosis (Dixon et al., 2012; Doll et al., 2017; Kagan et al., 2017; Yang et al., 2014). Furthermore, I established an involvement of lipoxygenases and iron in cell density-dependent ferroptosis which had been previously shown to contribute to lipid peroxidation (Dixon et al., 2012; Yang et al., 2014, 2016). Therefore, I measured lipid ROS levels in HMLE and HMLE-Twist1 using C11-BODIPY staining in flow cytometry analyses (Drummen et al., 2002). For this purpose, HMLE and HMLE-Twist1 cells were plated at intermediate cell density and treated for 6h or 20h with RSL3. Compared to unstained control (dashed), staining with C11-BODIPY led to a detectable increase in the fluorescence signal in the control staining (ctrl, orange) for both HMLE and HMLE-Twist1 cells (Figure 17A). However, I did not observe a further increase in C11-BODIPY fluorescence when these cell lines were treated for 6h (blue) or 20h (grey) with RSL3 (Figure 17A). These results were surprising since several reports showed that C11-BODIPY fluorescence increases upon RSL3 treatment (Friedmann Angeli et al., 2014; Yang et al., 2014). To rule out inappropriate handling of C11-BODIPY as a reason for these results, cumene hydroperoxide (CH) was used as a positive control. CH is a known inducer of lipid peroxidation (Weiss and Estabrook, 1986). Indeed, CH treatment led to a strong increase in C11-BODIPY fluorescence in both HMLE and HMLE-Twist1 cells compared to control treatment (Figure 17B). These data suggested that a pronounced increase in lipid peroxidation was not involved in cell density-dependent ferroptosis.

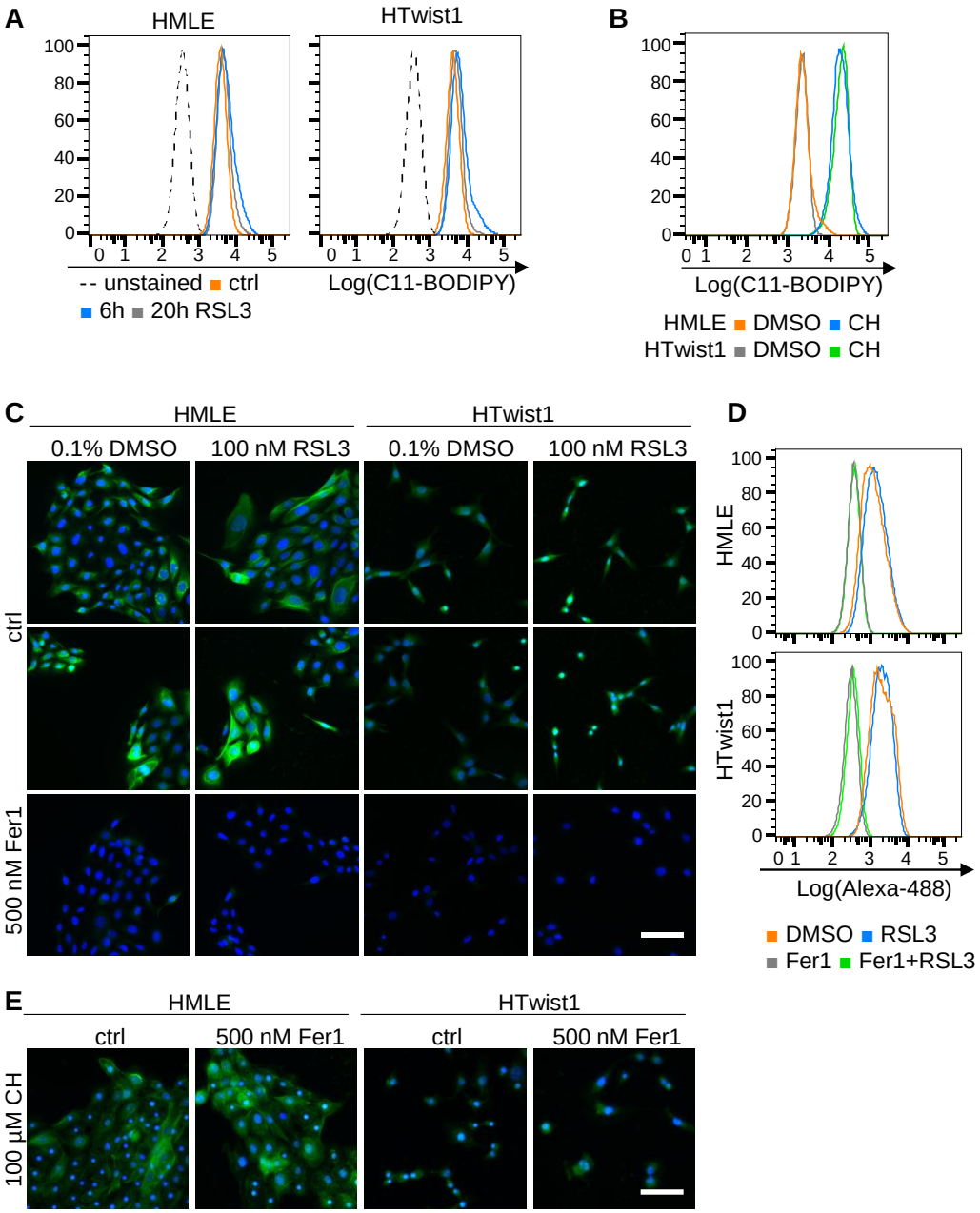

Figure 17: RSL3 treatment does not result in a global increase in lipid peroxidation

(A) Flow cytometry: C11-BODIPY staining of HMLE and HMLE-Twist1 cells plated at intermediate density in 6-cm dishes treated with 100 nM RSL3 for the indicated time points. X-axis: log10 of C11-BODIPY fluorescence. Y-axis: percentage of the maximum count. Data were partly generated by Marie Bannier-Hélaouët (Intern) and by Felix Holstein (Master Student). (B) Flow cytometry: C11-BODIPY staining of HMLE and HMLE-Twist1 cells as described in A treated for 1h with 100 µM cumene hydroperoxide (CH). Data were generated by Felix Holstein (Master Student). (C) Immunofluorescence: staining of lipid peroxidation (green) in HMLE and HMLE-Twist1 cells using Click-iT chemistry after treatment for 1.5h with 50 µM alkyne-modified linoleic acid (LAA) in presence or absence of 100 nM RSL3 and 500 nM Fer1. Cell nuclei were stained with DAPI (blue). Scale bar: 200 µm. (D) Flow cytometry: staining of lipid peroxidation in HMLE and HMLE-Twist1 cells using Click-iT chemistry as described in C. X-axis: log10 of Alexa-488 (lipid peroxidation detection) fluorescence. Y-axis: percentage of the maximum count. (E) Immunofluorescence: staining of lipid peroxidation (green) in HMLE and HMLE-Twist1 cells using Click-iT chemistry as described in C using 100 µM CH instead of RSL3-treatment. Cell nuclei were stained with DAPI (blue). Scale bar: 200 µm. Data (A-E) show one

representative experiment performed independently two (C, D, E), at least three (B) or four (A) times.

Next, I wanted to measure lipid peroxidation by other means than C11-BODIPY staining. The Click-iT® Lipid Peroxidation Imaging Kit (Thermo Fisher Scientific) has been previously shown to visualize ferroptosis-related lipid peroxidation occurring during neuronal reprogramming (Gascón et al., 2016). Thereby, cells are incubated with an alkyne-modified linoleic acid (LAA), a PUFA that incorporates into the cell membrane. In the presence of lipid peroxidation, oxygenation of LAA leads to chemical reactions with intracellular proteins that can be detected with Click-iT® chemistry, yielding green fluorescence. Therefore, I used the Click-iT® Lipid Peroxidation Imaging Kit to assess whether RSL3 induces lipid peroxidation in HMLE and HMLE-Twist1. For this purpose, 48h after seeding HMLE and HMLE-Twist1 cells on coverslips for immunofluorescence or in 6-well plates for flow cytometry, cells were incubated for 1.5h with 50 µM LAA in the presence or absence of 100 nM RSL3, 500 nM Fer1 or a combination of both. Then Click-iT® chemistry was performed prior to analyzing lipid peroxidation levels by immunofluorescence or by flow cytometry. Both analyses revealed that lipid peroxidation levels, indicated by a similar green fluorescence signals, did not increase upon RSL3-treatment compared to the DMSO control in both HMLE and HMLE-Twist1 cells (Figure 17C and D). In contrast, treatment with Fer1 alone or in combination with RSL3 completely abolished the green fluorescence signal (Figure 17C and D), indicating that Fer1 reduced lipid peroxidation. Furthermore, CH treatment led to the detection of lipid hydroperoxides in both cell lines, but levels were not increased compared to the control (Figure 17E). However, CH treatment induced cellular stress, indicated by small cell nuclei, stained with DAPI, and disorganized cell shapes, outlined by the lipid peroxidation staining (Figure 17E). These data indicated an induction of cell death by CH. Interestingly, lipid peroxidation levels were not reduced by Fer1 when cells were treated with CH. Additionally, Fer1 did not rescue cell death induction, since cell nuclei were still small and cell shapes were still disorganized upon simultaneous CH and Fer1 treatment (Figure 17E).

Notably, the levels of lipid peroxidation varied within the colonies formed by HMLE cells: smaller colonies showed higher lipid peroxidation levels than bigger colonies

(Figure 17C). Furthermore, cells at the border of colonies showed slightly elevated lipid peroxidation levels than cells in the middle of the colonies (Figure 17C).

Together, these data suggested that lipid peroxidation levels were overall high in HMLE and HMLE-Twist1 cells. However, RSL3 did not induce a further increase in lipid peroxidation. The observed differences in lipid peroxidation levels within colonies of HMLE cells might indicate a differential sensitivity of cells within one colony towards RSL3 treatment. Furthermore, since Fer1 treatment reduced lipid peroxidation levels in both DMSO and RSL3-treated cells, but not in CH-treated. These data indicated that cell death induced by CH was different to RSL3-induced cell death in HMLE and HMLE-Twist1 cells. This might explain why CH, but not RSL3 treatment increased lipid peroxidation level detected by C11-BODIPY. Overall, I was not able to detect an increase in lipid peroxidation upon RSL3 treatment in both HMLE and HMLE-Twist1 cells detected by C11-BODIPY staining or with the Click-iT® Lipid Peroxidation Imaging Kit.

Since these results were surprising and unexpected, lipid peroxidation levels were again measured as soon as I had derived *GPX4* knockout SCCs. Thereby, I wanted determine on a genetic level whether the GPX4 knockout correlated with lipid peroxidation and how this in turn correlated to ferroptosis sensitivity. To do so, SCCs were seeded at different cell densities either in presence or in absence of Lip1 in 6-cm dishes for 48h before staining the cells with C11-BODIPY. Unexpectedly, C11-BODIPY fluorescence increased upon Lip1-withdrawal (orange) in both HMLE and HMLE-Twist1 SCCs compared to Lip1-cultured cells (blue) (Figure 18A). The increase of C11-BODIPY fluorescence was not connected to the cell density. Moreover, the magnitude of C11-BODIPY levels greatly varied between the different SCCs upon Lip1-withdrawal (Figure 18A). On average, I observed at least a 2-fold increase in C11-BODIPY levels upon Lip1-withdrawal (Figure 18B). Despite an upregulation of C11-BODIPY levels upon Lip1-withdrawal at all cell densities, these SCCs were similarly sensitive to *GPX4* knockout at low cell density while being resistant at high cell density (Figure 9B).

Together, these data suggested that GPX4-inhibition by RSL3 did not induce a global increase in lipid peroxidation. In contrast, lipid peroxidation levels increased to some extent upon *GPX4* knockout which was not connected with the seeding density. Importantly, RSL3 treatment was sufficient to induce cell density-dependent ferroptosis and this effect was genetically confirmed by GPX4 knockout. Therefore,

these lipid peroxidation data indicated that global lipid peroxidation level did not directly contribute to cell density-dependent ferroptosis. Furthermore, these data suggested that cell death might be triggered by the oxidation of specific lipids, rather than by an overall increase in lipid peroxidation.

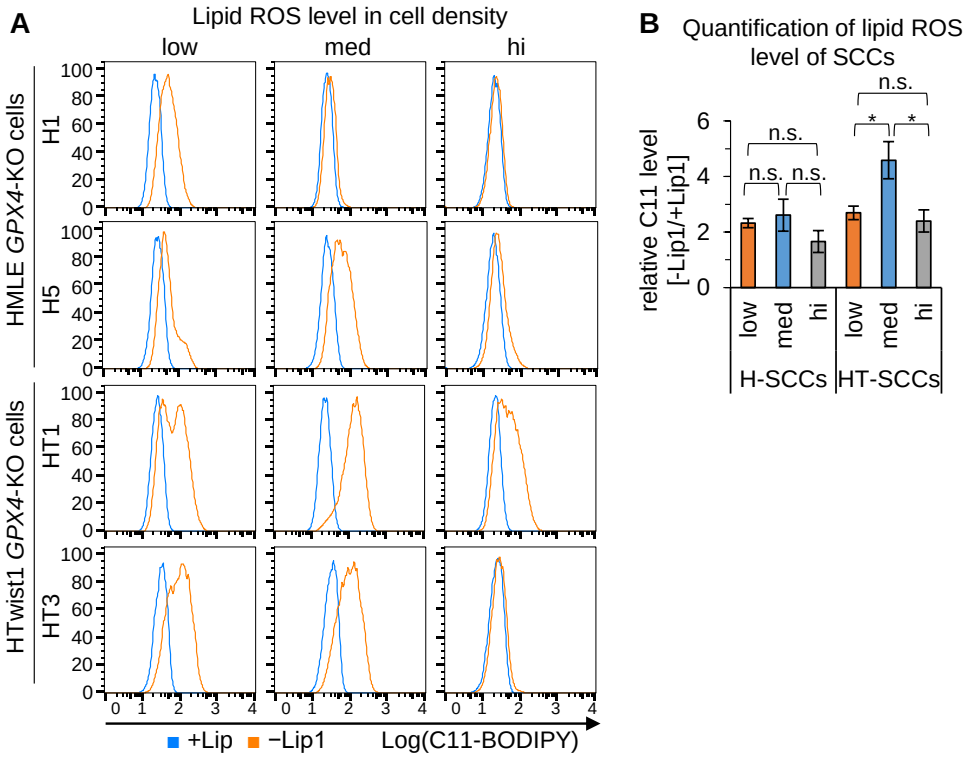

Figure 18: Lipid peroxidation level do not correlate with ferroptosis-sensitivity in *GPX4*-knockout single-cell clones

(A) Flow cytometry: C11-BODIPY staining of *GPX4*-knockout (KO) single-cell clones (SCCs) of HMLE and HMLE-Twist1 cells 48h after plating cells at different densities in 6-cm dishes in 1 µM Lip1 (+Lip1, blue) culture or in medium without Lip1 (–Lip1, orange). X-axis: log10 of C11-BODIPY fluorescence. Y-axis: percentage of the maximum count. One representative experiment visualizing variation of C11-BODIPY fluorescence between SCCs is shown. n=2-4 for each SCC (B) Quantification of C11-BODIPY fluorescence of HMLE (H) and HMLE-Twist1 (HT) SCCs (two SCCs of H-SCCs and three SCCs for HT-SCCs) as described in A. Data were normalized to respective Lip1-treated control and represent mean ± SEM. n=6. Statistics: two-tailed, unpaired T-test with Welch's correction (p-value: *<0.05, n.s. = not significant).

To this end, I showed that Fer1 rescued cell density-dependent cell death induction upon GPX4 inhibition or knockout (Figure 5A, Figure 6A and Figure 9C) and at the same time, Fer1 reduced lipid peroxidation levels in both HMLE and HMLE-Twist1 cells (Figure 17C and D). Moreover, ACSL4, increasing the amount of PUFAs within membranes, did not determine cell density-dependent ferroptosis sensitivity in HMLE cells (Figure 16E). Since culture of cells in basal medium protected from RSL3-induced cell death (Figure 14I), I hypothesized that metabolic pathways fueled

by growth factors might be involved in cell density-dependent ferroptosis. Moreover, I hypothesized that only some specific lipids might be oxidized during cell density-dependent ferroptosis. In turn, cells seeded at low or high density might cope differently with these oxidized lipids and as a result, a vulnerable cell state towards GPX4-inhibition might be induced.

4.14 Proteomic study reveals several regulated proteins both by cell density by RSL3 treatment

As described above, I showed that sensitivity to cell death upon GPX4 inhibition was dependent on cell density and that sensitivity was most likely regulated by some kind of proximity-sensing or short-distance paracrine signaling that was not directly linked with cell-cell-adhesion signaling. Therefore, I concluded that intracellular metabolic pathways might be regulated by cell density that led to a vulnerability of cells to GPX4 inhibition. Given that this regulation was a fast process immediately induced by plating cells at different densities, I hypothesized that analyzing the proteome of both HMLE and HMLE-Twist1 cells at cell density could provide insights into the mechanisms of cell density-dependent ferroptosis induced by GPX4 inhibition. Further, by assessing the proteins regulated by RSL3 treatment of cells seeded at intermediate cell density could further reveal mechanistic details. Therefore, a proteomic study of both HMLE and HMLE-Twist1 cells seeded at different densities as well as upon RSL3 treatment was performed in collaboration with the laboratory of Dr. Stefanie Hauck. For data analysis, I filtered on one hand for proteins that were at least 1.5-fold up- or downregulated ($p<0.05$) in low cell density compared to high cell density in both HMLE and HMLE-Twist1 cells and on the other hand for proteins that were at least 1.5-fold up- or downregulated ($p<0.05$) upon 5h RSL3 treatment compared to non-RSL3 treated control. Thereby, I obtained 190 up- and 57 down-regulated proteins at low cell density and 274 up- and 349 downregulated proteins upon RSL3 treatment. To further identify potential candidate proteins involved in cell density-dependent ferroptosis induced by GPX4-inhibition, I assessed the overlap between up- or downregulated overlapping proteins both at low cell density and by RSL3 treatment. The rationale behind this strategy was that proteins up- or downregulated by low density could confer sensitivity to cell density-dependent ferroptosis. Moreover, if the same proteins were similarly regulated

A

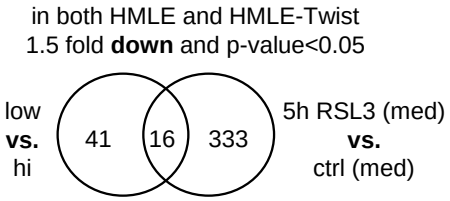

B

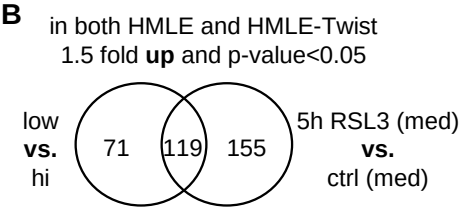

C

GeneID	Description	Fold decrease (low vs. high)
NEDD8	Ubiquitin-Like Protein Nedd8	16.27
IRS2	Insulin receptor substrate 2	6.10
LRRC58	Leucine-rich repeat-containing protein 58	3.17
OAS3	2'-5'-oligoadenylate synthase 3	3.01
PARP4	Poly [ADP-ribose] polymerase 4 OS	2.72
SPAG5	Sperm-associated antigen 5	2.50
SCD	Stearoyl-CoA Desaturase	2.47
PTPRE	Receptor-type tyrosine-protein phosphatase epsilon	1.96
YPEL5	Protein yippee-like 5	1.88
SPTBN2	Spectrin beta chain, non-erythrocytic 2	1.78

D

Term	p-Value	Gene names
transferrin transport (GO:0033572)	3.17E-09	ATP6V1A, ATP6V1B1, ATP6V1B2, ATP6V1D, ATP6V1E1, ATP6V1E2, ATP6V1H, RAB11B
regulation of macroautophagy (GO:0016241)	1.72E-08	ATP6V1A, ATP6V1B1, ATP6V1B2, ATP6V1D, ATP6V1E1, ATP6V1E2, ATP6V1H, UCHL1
phagosome acidification (GO:0090383)	2.26E-08	ATP6V1A, ATP6V1B1, ATP6V1B2, ATP6V1D, ATP6V1E1, ATP6V1E2, ATP6V1H
ATP hydrolysis coupled proton transport (GO:0015991)	2.30E-06	ATP6V1A, ATP6V1B1, ATP6V1B2, ATP6V1E1, ATP6V1E2, ATP6V1H
insulin receptor signaling pathway (GO:0008286)	1.48E-05	ATP6V1A, ATP6V1B1, ATP6V1B2, ATP6V1D, ATP6V1E1, ATP6V1E2, ATP6V1H
proton transport (GO:0015992)	3.37E-04	ATP6V1A, ATP6V1B1, ATP6V1B2, ATP6V1D, ATP6V1E1
positive regulation of exocytosis (GO:0045921)	3.71E-04	RAB3A, CADPS2, FGB, FGG
synaptic vesicle exocytosis (GO:0016079)	4.27E-04	RAB3A, CADPS2, CADPS, VAMP2
ion transmembrane transport (GO:0034220)	5.75E-04	ATP6V1A, ATP6V1B1, ATP6V1B2, ATP6V1D, ATP6V1E1, ATP6V1E2, ATP6V1H, GRIK3
positive regulation of triglyceride catabolic process (GO:0010898)	1.25E-03	ABHD5, APOA4, PNPLA2

Figure 19: Proteomic study identifies regulated proteins by both cell density and RSL3 treatment

(A) Venn diagram of proteomic data sets representing >1.5-fold downregulated proteins (p-value <0.05) in cell density (left) and upon 5h 100 nM RSL3-treatment (right). The left circle indicates commonly downregulated proteins in low cell density compared to high cell density in both HMLE and HMLE-Twist1 cells. The right circle indicates commonly downregulated proteins upon RSL3 treatment compared to non-RSL3 treated control cells at intermediate cell density in both cell lines. The overlapping 16 proteins are downregulated by both low cell density and RSL3 treatment. (B) Venn diagram of proteomic data sets representing >1.5-fold upregulated proteins (p-value<0.05) in cell density (left) and upon 5h 100 nM RSL3-treatment (right) as described in A. 119 proteins were upregulated by both low cell density and RSL3-treatment. (C) Top ten-downregulated proteins by both low cell density and RSL3-treatment in both cell lines as described in A. (D) GO-term analyses: top ten, significantly enriched terms (biological processes) using DAVID of upregulated proteins (119) by both cell density and RSL3-treatment as described in B.

during RSL3 treatment, this might imply a direct involvement in cell density-dependent ferroptosis induced by GPX4-inhibition.

With this strategy, I identified 16 proteins that were downregulated and 119 proteins that were upregulated in both low cell density and upon RSL3 treatment (Figure 19A and B, *Table 10 and Table 11 in the Appendix*). For instance, within the top ten-downregulated proteins, Stearoyl-CoA Desaturase (SCD) might be a potential hit involved in a lipid-mediated oxidative cell death (Figure 19C). SCD is a key enzyme in monounsaturated fatty acid metabolism (Paton and Ntambi, 2009) and its genetic absence was implied in increasing fatty acid oxidation (FAO) (Dobrzyn et al., 2004). Interestingly, Carnitine Palmitoyltransferase 1A (CPT1A), the rate-limiting enzyme for FAO, was upregulated at low cell density as well (*Appendix Table 11*). However, since more than 7-fold more proteins were upregulated by both low cell density and upon RSL3 treatment (Figure 19B), I submitted them to GO-term enrichment analysis of biological processes using DAVID (Figure 19D) (Huang et al., 2009b, 2009a). Thereby, some interesting terms were enriched. For example, the enriched term “transferrin transport” further indicated a contribution of iron to cell density-dependent ferroptosis (Figure 19D). Moreover, the upregulated protein Heme oxygenase 1 (HMOX1) (*Appendix Table 11*), shown to be involved in iron reutilization (Poss and Tonegawa, 1997a), was already implicated in Erastin-induced ferroptosis in HT-1080 fibrosarcoma cells (Kwon et al., 2015). Another interesting term within the top-ten regulated pathways was “positive regulation of triglyceride catabolic process”, further suggesting a regulation of lipid metabolism by cell density and an involvement in RSL3-induced cell death (Figure 19D).

Together, the proteomic analysis revealed candidate proteins that were potential candidates in the regulation of cell density-dependent ferroptosis.

4.15 HMOX1 does not impact cell density-dependent ferroptosis induced by GPX4 inhibition

Several studies have implied a role for HMOX1 in ferroptosis (Chang et al., 2018; Hassannia et al., 2018; Kwon et al., 2015) and therefore, I wanted to elucidate whether HMOX1 also contributed to cell density-dependent ferroptosis. To validate proteomics data, HMOX1 expression was assessed at both transcript as well as protein level. By qPCR, I found a 2-fold or 9-fold upregulation of *HMOX1*

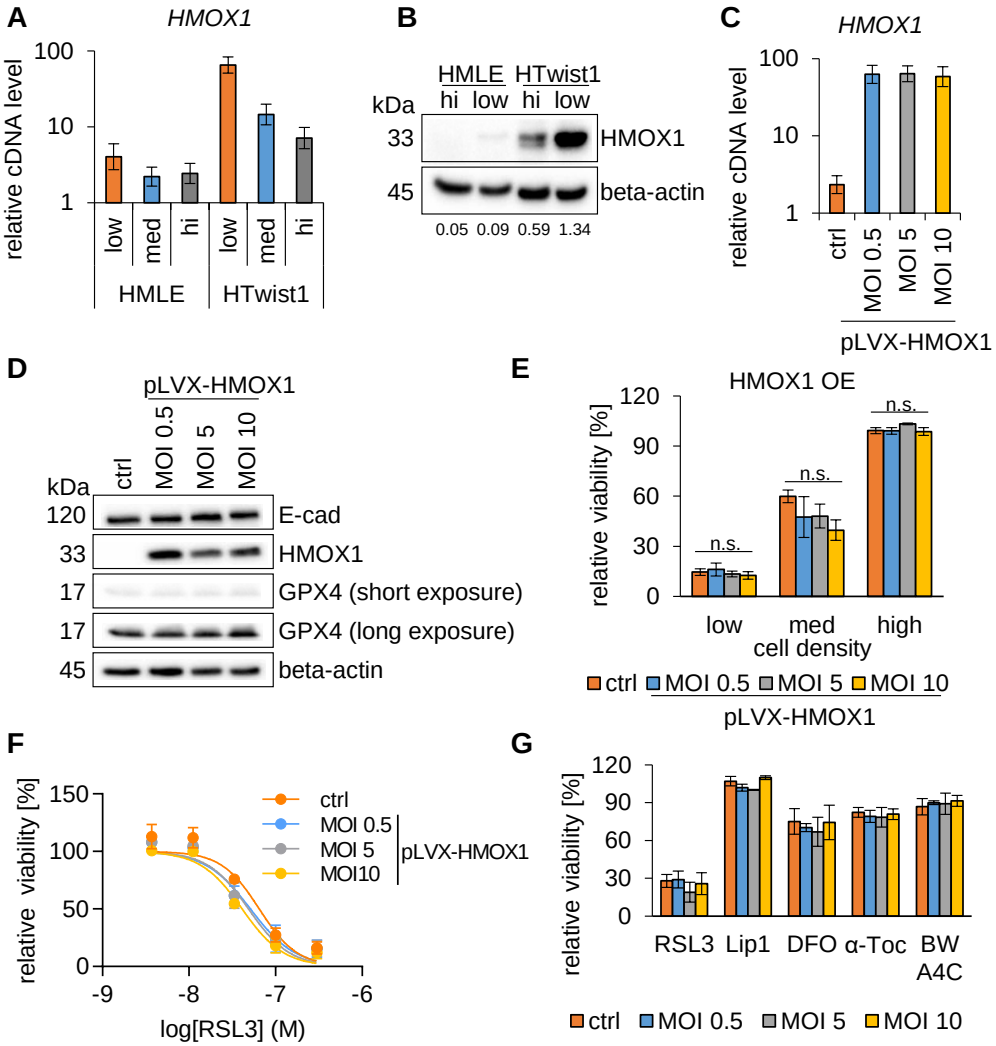

Figure 20: Overexpression of HMOX1 does not impact cell density-dependent ferroptosis induced by GPX4 inhibition

(A) qPCR: relative *HMOX1* mRNA expression of HMLE and HMLE-Twist1 cells seeded at different densities in 6-cm dishes for 48h. n=3. (B) Immunoblot: protein expression of HMOX1 and beta-actin (loading control) of HMLE and HMLE-Twist cells seeded at low or high cell density in 10-cm dishes for 48h. Numbers shown indicate densitometric ratios of detected HMOX1 to beta-actin protein band. One representative experiment performed independently two times is shown. (C) qPCR: relative *HMOX1* mRNA expression of non-transduced HMLE cells (control, ctrl) or of HMLE cells transduced with lentiviruses containing HMOX1 cDNA at indicated multiplicity of infections (MOIs). n=3. (D) Immunoblot: protein expression of E-cadherin (E-cad), HMOX1, GPX4 and beta-actin (loading control) in HMLE cells overexpressing HMOX1 as described in C. (E) Viability assay: treatment of HMLE cells overexpressing HMOX1 as described in C plated at indicated densities in 96-well plates with 100 nM RSL3 for 24h. n=3. Statistics: two-tailed, unpaired T-test with Welch's correction (p-value: *<0.05, n.s. = not significant). (F) Dose-response curve: treatment of HMLE cells overexpressing HMOX1 as described in C plated at 600 cells in 96-well plates with 3-fold dilutions of RSL3 for 24h. n=3. (G) Rescue-viability assay: treatment of HMLE cells over-expressing HMOX1 as described in C plated at 600 cells in 96-well plates with 100 nM RSL3, 500 nM Liproxstatin-1 (Lip1), 100 µM deferoxamine (DFO), 10 µM α-tocopherol (α-toc) , 5 µM BWA4C or a combination of these compounds for 24h. n=2. Data shown (A, C, E, F, G) represent mean ± SEM. Viability (E, F, G) was normalized to respective DMSO control within each cell line and cell density.

transcripts in low cell density compared to high cell density in HMLE and HMLE-Twist1 cells, respectively. However, expression levels were higher in HMLE-Twist1 cells (Figure 20A). By immunoblotting, I observed a strong expression of HMOX1 in HMLE-Twist1 cells seeded at low cell density, being more than 2-fold higher than the expression levels of cells seeded at high cell density (Figure 20B). In contrast, HMLE cells showed no expression of HMOX1 at high cell density and only a very low expression level at low cell density (Figure 20B), suggesting a minor role of HMOX1 for HMLE cells. To further elaborate the role of HMOX1 in cell density-dependent ferroptosis, HMOX1 cDNA was overexpressed in HMLE cells and its impact on cell viability was determined. For this purpose, HMOX1 cDNA transcribed from RNA extracted from HMLE-Twist1 cells was used since HMLE-Twist1 upregulated HMOX1 both at the RNA and protein level at low cell density. Then, HMLE cells were transduced with lentiviruses containing HMOX1 cDNA at three different MOIs (0.5, 5 and 10). After selection with 1 µg/ml puromycin, HMOX1 overexpression (OE) was confirmed by qPCR and immunoblotting, revealing in comparison to non-transduced control a successful increase in expression levels (Figure 20C), comparable to those of HMLE-Twist1 cells seeded at low cell density (Figure 20A). Of note, different MOIs used for transductions did not yield different HMOX1 expression levels (Figure 20C). Further, HMOX1 overexpression did also not impact E-cadherin or GPX4 expression levels, as assessed by immunoblotting (Figure 20D). Next, I plated HMOX1-overexpressing HMLE cells into viability assays at different cell densities and treated them the next day with 100 nM RSL3 for 24h. Again, as expected for control HMLE cells, I observed cell density-dependent ferroptosis upon RSL3 treatment with cells at low cell density being highly sensitive and cells at high cell density being resistant to GPX4-inhibition (Figure 20E). The amount of cell death induction was similar between HMOX1 OE and control cells (Figure 20E). In line, when cells seeded at an intermediate-low density (600 cells) were submitted to treatment with different concentrations of RSL3, I did not observe any difference in cell death induction between control and HMOX1 OE HMLE cells (Figure 20F). The ferroptosis inhibitors Lip1, α-Toc, DFO and BWA4C were able to rescue cell death induced by 100 nM RSL3 treatment in HMOX1 OE HMLE cells to comparable levels as observed in control cells (Figure 20G). Together, HMOX1 OE in HMLE cells suggested that HMOX1 did not impact sensitivity to cell density-dependent ferroptosis induced by GPX4 inhibition.

Since the assembly of a fully functional enzyme might be impacted by HMOX1 OE, CRISPR/Cas9-mediated HMOX1 knockout was performed in both HMLE and HMLE-Twist1 cells. Knockout efficiency was not high, but I derived one SCC with no HMOX1 expression for each cell line (SCC7-2 and SCC3-1, respectively) and several with low HMOX1 expression levels (Figure 21A and B). For SCCs of both HMLE and HMLE-Twist1 cells, cell density-dependent ferroptosis was observed upon 100 nM RSL3 treatment to a similar extent as in control SCCs (Cas9-only transfected cells without sgRNAs against HMOX1) and in HMOX1-modified SCCs (Figure 21C and D). Of note, SCC3-3, derived after CRISPR/Cas9-editing in HMLE-Twist1, showed increased sensitivity at high cell density (reduction in viability by 67% for SCC3-3 compared to 17% and 13% for SCC3-1 and SCC4-1 respectively) (Figure 21D). However, this SCC still showed low expression levels of HMOX1 by immunoblotting (Figure 21B), suggesting that increased sensitivity was most likely not induced through HMOX1 expression, but through other intrinsic properties of this SCC.

Conclusively, these data indicated that HMOX1 did not play a major role in cell density-dependent ferroptosis upon GPX4 inhibition.

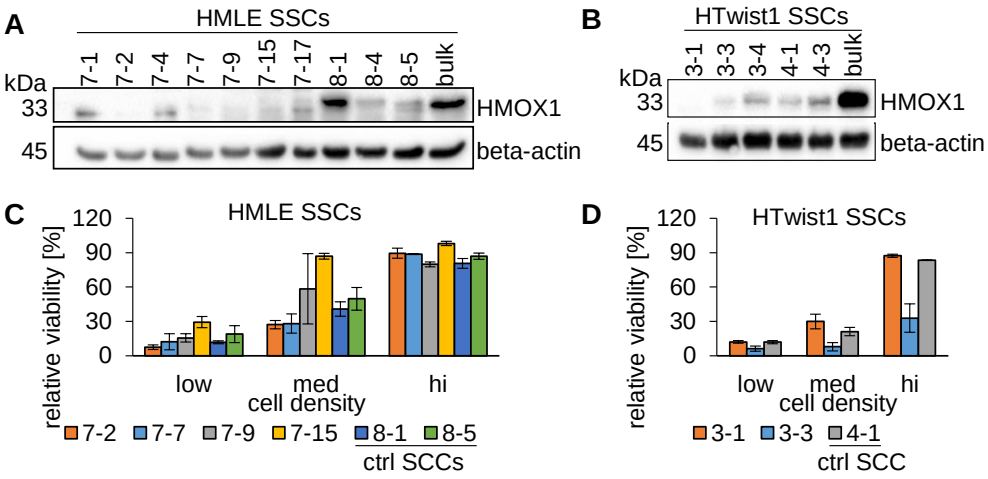

Figure 21: Genetic knockout of HMOX1 does not impact cell density-dependent ferroptosis induced by GPX4 inhibition

(A) and (B) Immunoblot: protein expression of HMOX1 and beta-actin (loading control) of single-cell clones (SCCs) derived by CRISPR/Cas9 genome-editing in the *HMOX1* locus of bulk (A) HMLE and (B) HMLE-Twist1 cells plated at intermediate cell density in 10-cm dishes. kDa= kilo Dalton. (C) Viability assay: treatment of HMLE SCCs derived by CRISPR/Cas9 with or without *HMOX1*-knockout (KO) as described in A plated at indicated cell densities in 96-well plates with 100 nM RSL3 for 24h. n=2. (D) Viability assay of HMLE-Twist1 SCCs as described in B with 100 nM RSL3 for 24h as described in C. n=2. Data shown (C, D) represent mean ± SD. Viability was normalized to respective DMSO control within each cell line and cell density.

4.16 ATGL-regulated lipid droplet catabolism at low cell density is connected with cell density-dependent ferroptosis

Since I hypothesized that specific lipids are oxidized during cell density-dependent ferroptosis (Figure 16-Figure 18), I next focused on the enriched GO Term “positive regulation of triglyceride catabolic process” (Figure 19D). As both the adipose triglyceride lipase (ATGL = PNPLA2) and its co-activator lipase 1-acylglycerol-3-phosphate O-acyltransferase (ABDH5) are involved in the turnover of triacylglycerides (TAGs) stored in lipid droplets (LDs) (Smirnova et al., 2006; Wang et al., 2011; Zimmermann et al., 2004), their expression was examined. By qPCR, I observed that both HMLE and HMLE-Twist1 cells expressed both *PNPLA2* and *ABDH5*, however, transcript levels were not regulated by cell density (Figure 22A and B). In contrast, regulation of ATGL expression by cell density was detectable by immunoblotting (Figure 22C). In line with the proteomic data, low cell density resulted in strongly upregulated ATGL protein levels compared to high cell density in both HMLE and HMLE-Twist1 cells (Figure 22C). Interestingly, HMLE cells did not express ATGL protein at high cell density in contrast to HMLE-Twist1 cells (Figure 22C). To connect the upregulation of ATGL to its function, the LD content was measured using the fluorescent dye BODIPY493/503, commonly used to stain LDs (Smirnova et al., 2006). Consequently, I found that BODIPY493/503 fluorescence intensity simultaneously declined with decreasing the seeding density in both HMLE and HMLE-Twist1 cells (Figure 22D), indicating that LD content was reduced from high to low cell density. At high cell density, BODIPY493/503 fluorescence intensity was higher in HMLE cells compared to HMLE-Twist1 cells, but decreased to a similar level in both cells lines at low seeding density (Figure 22D). These results reflected ATGL protein expression levels of HMLE and HMLE-Twist1 cells. Staining for lipid ROS using C11-BODIPY dye revealed the reverse regulation. Both cell lines showed higher lipid ROS levels at low cell density compared to high cell density (Figure 22D). These results suggested that cells suffered from increased lipid-mediated stress at low cell density.

Next, I inhibited ATGL by Atglistatin (ATGLi) during viability assays. To do so, I plated HMLE and HMLE-Twist1 cells at a low cell density and pre-incubated them with ATGLi prior to RSL3 treatment. RSL3 induced cell death by 70% compared to the DMSO control which was rescued by simultaneous ATGLi administration in both

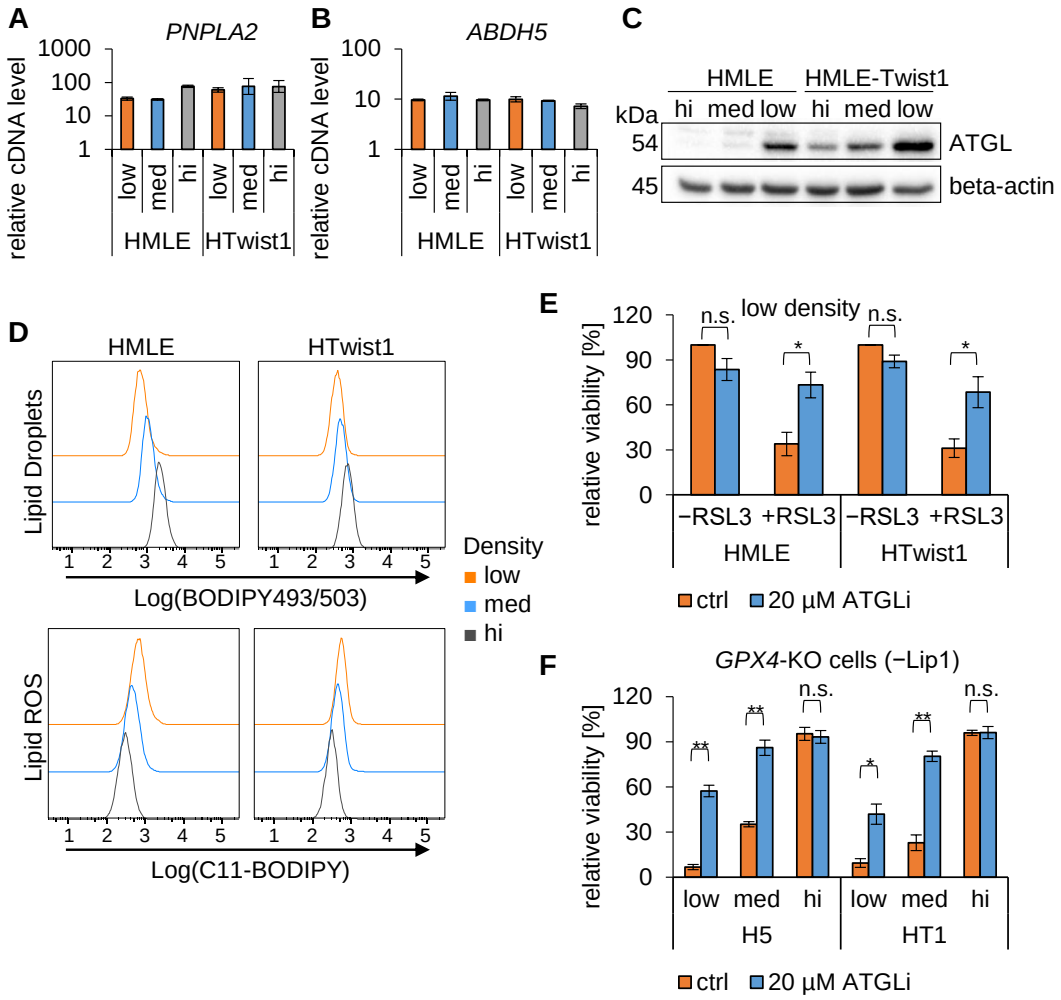

Figure 22: ATGL-regulated lipid droplet catabolism at low cell density is linked to cell density-dependent ferroptosis

(A) and (B) qPCR: relative (A) *PNPLA2* (ATGL) and (B) *ABDH5* mRNA expression of HMLE and HMLE-Twist1 cells seeded at different densities in 6-cm dishes for 48h. (C) Immunoblot: protein expression of ATGL and beta-actin (loading control) of HMLE and HMLE-Twist cells seeded at indicated cell densities in 10-cm dishes for 48h. (D) Flow cytometry: BODIPY493/503 (lipid droplets) and C11-BODIPY (lipid ROS) staining of HMLE and HMLE-Twist1 cells seeded at indicated densities in 6-cm dishes for 48h. X-axis: log10 of respective fluorescence, Y-axis: percentage of the maximum count. (E) Viability assay: treatment of HMLE and HMLE-Twist1 plated at low cell density in 96-well plates with 0.1% DMSO (–RSL3) or 100 nM RSL3 (+RSL3) without (control, ctrl) or in combination with 20 µM Atglistatin (ATGLi) for 24h. Cells were additionally pre-treated with ATGLi for 24h prior to DMSO/RSL3 treatment. n=4. (F) Viability assay: treatment of *GPX4*-knockout (KO) single-cell clones HMLE H5 and HMLE-Twist1 HT1 plated at indicated cell densities in 96-well plates without (ctrl) or with 20 µM ATGLi in presence or absence of 1 µM Lip1 for 48h. ATGLi-treated cells were additionally pre-treated with ATGLi in presence of Lip1 for 24h in 6-wells prior to the viability assay. n=3. Data shown (A, B, E, F) represent mean ± SEM. Viability was normalized to respective DMSO control (E) or respective Lip1 control (F) within each cell line and cell density. One representative experiment (A, B, C, D) performed independently two (A, B, C) or three (D) times is shown. Statistics: two-tailed, unpaired T-test with Welch's correction (p-value: *<0.05, **<0.01, n.s. = not significant).

HMLE and HMLE-Twist1 cells (Figure 22E). Notably, administration of only ATGLi did not affect viability compared to the DMSO controls (Figure 22E). Likewise, ATGLi incubation rescued cell density-dependent ferroptosis in *GPX4*-KO SCCs H5 and HT1, when they were cultured in the absence of Lip1 (Figure 22F).

ATGLi has been described to efficiently inhibit murine ATGL in adipocytes, but to target human ATGL only by 10% (Schweiger et al., 2017). To elucidate whether ATGLi non-specifically rescued RSL3-induced cell death, breast cancer cell lines, that did not show cell density-dependent ferroptosis induction upon GPX4-inhibition (Figure 15A), were pre-incubated with ATGLi prior to RSL3 treatment and viability was measured. ATGLi significantly rescued RSL3-mediated cell death in T-47D cells and in epithelial MDA468 cells, but did not do so in mesenchymal MDA231 and MDA157 cells (Figure 23A). These results revealed that ATGLi was not generally able to rescue RSL3-mediated cell death. Again, ATGLi did not impact viability in control treatments (Figure 23B). Notably, all breast cancer cell lines expressed ATGL at the protein level (Figure 23C), indicating that cells might rely to a different extent on the catabolic pathway mediated by ATGL.

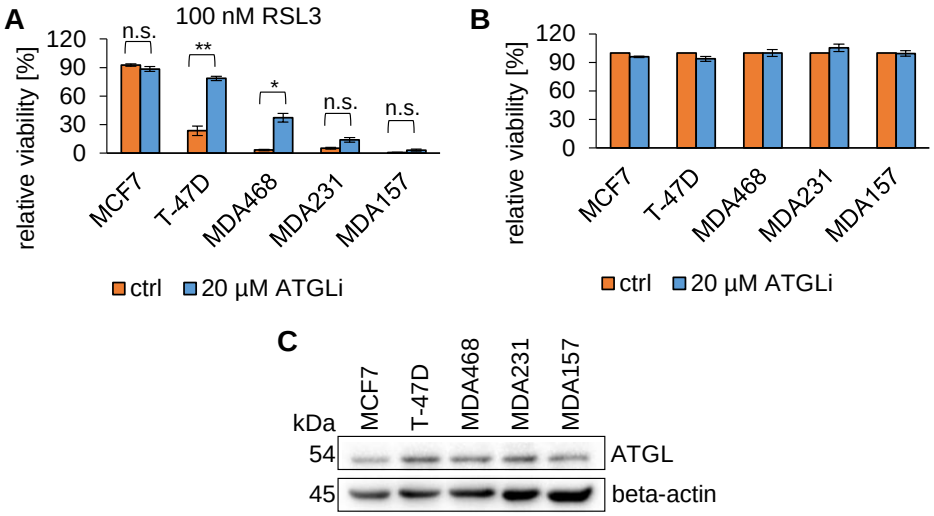

Figure 23: RSL3-induced ferroptosis of T-47D and MDA468 breast cancer cells is rescued by ATGLi

(A) Viability assay: treatment of indicated breast cancer cell lines plated at intermediate cell density in 96-well plates with 0.1% or 100 nM RSL3 without (ctrl) or in combination with 20 µM Atglistatin (ATGLi) for 24h. n=3. Statistics: two-tailed, unpaired T-test with Welch's correction (p-value: *<0.05, **<0.01, n.s. = not significant). (B) Viability assay as described in A. Data show DMSO-treated cells. n=3. (C) Immunoblot: protein expression of ATGL and beta-actin (loading control) of indicated breast cancer cell lines seeded at intermediate cell density in 10-cm dishes for 48h. Data shown (A, B) represent mean ± SEM. Viability was normalized to respective DMSO control within each cell line.

Conclusively, these data implied that ATGL expression, upregulated by low cell density, controlled liberation of TAGs from LDs in a cell density-dependent manner in both HMLE and HMLE-Twist1 cells. Thereby, lipid-mediated ROS level were increased that might indicate a vulnerability of cells at low cell density to GPX4-inhibition.

4.17 Oleic acid supplementation rescues cell density-dependent ferroptosis

To better understand the connection between ATGL-mediated turnover of LDs and sensitivity to cell density-dependent ferroptosis, I wished to interfere with LD metabolism in a different manner than by inhibiting ATGL. An earlier study has shown that the monounsaturated fatty acid oleic acid (OA) increases the amount of LDs within cells in cell culture (Smirnova et al., 2006). Therefore, I supplemented the culture medium of HMLE and HMLE-Twist1 cells, that were seeded at different cell densities, with 100 µM OA for 24h and measured the LD content using BODIPY493/503 staining. BODIPY493/503 fluorescence intensity increased upon OA treatment compared to the control in all cell densities for both cell lines (Figure 24A). These data indicated that the amount of LDs increased upon OA treatment. By contrast, OA supplementation decreased C11-BODIPY fluorescence (Figure 24A), suggesting that lipid ROS level decreased in OA-treated cells and again, indicating an opposite correlation between LD amount and lipid ROS level. In order to assess how this translated to RSL3-sensitivity, control and OA-supplemented HMLE and HMLE-Twist1 cells plated at different cells densities were submitted to 100 nM RSL3 treatment during viability assays. For both cell lines, I observed that cell density-dependent ferroptosis, induced by RSL3 treatment, was rescued by OA supplementation (Figure 24B). Furthermore, I noticed a minor impact on cell viability by OA treatment alone (Figure 24C).

In sum, these data suggested that the OA-induced increase in the amount of LD resulted in lower lipid ROS level within cells, thereby lowering lipid-mediated stress and protecting cells from RSL3-mediated cell death. These data supported the hypothesis that the turnover of LDs was indeed connected with an induced vulnerability to GPX4 inhibition at low cell density.

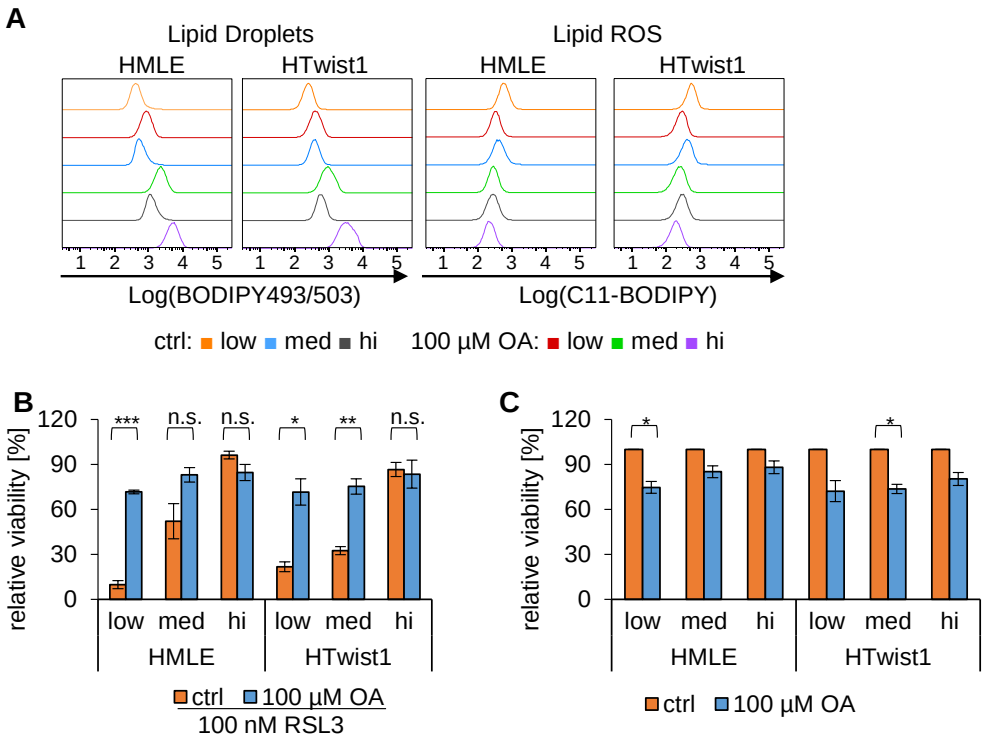

Figure 24: Oleic acid supplementation rescues cell density-dependent ferroptosis
(A) Flow cytometry: BODIPY493/503 (lipid droplets) and C11-BODIPY (lipid ROS) staining of HMLE and HMLE-Twist1 cells seeded at indicated densities in 6-cm dishes for 48h treated without (ctrl) or for 24h with 100 µM oleic acid (OA). X-axis: log10 of respective fluorescence, Y-axis: percentage of the maximum count. One representative experiment performed independently two times is shown. (B) Viability assay: treatment of HMLE and HMLE-Twist1 cells plated at indicated cell densities in 96-well plates with 0.1% DMSO or 100 nM RSL3 without (ctrl, orange) or with 100 µM oleic acid (OA, blue) for 24h. OA was additionally applied for 24h prior to the viability assay. n=3. (C) Viability assay as described in B. Data show DMSO-treated cells. n=3. Data shown (B, C) represent mean ± SEM. Viability was normalized to respective DMSO control within each cell line and cell density. Statistics: two-tailed, unpaired T-test with Welch's correction (p-value: *<0.05, **<0.01, ***<0.001, n.s. = not significant).

4.18 Energy metabolism shifts to beta-oxidation by cell density

Next, I wanted to determine why low cell density upregulated LD catabolism at the expense of inducing a vulnerable cell state. Recent studies indicated that fatty acids (FAs), stored within LDs, are liberated by ATGL during periods of starvation or cellular stress in order to enable oxidative metabolism within mitochondria (Jarc et al., 2018; Rambold et al., 2015; Wright et al., 2017). Since the proteomic data suggested a regulation of the enzyme CPT1A which is essential for β-oxidation (*Appendix Table 11*), I hypothesized that low cell density might trigger ATGL-mediated LD turnover in order to fuel β-oxidation.

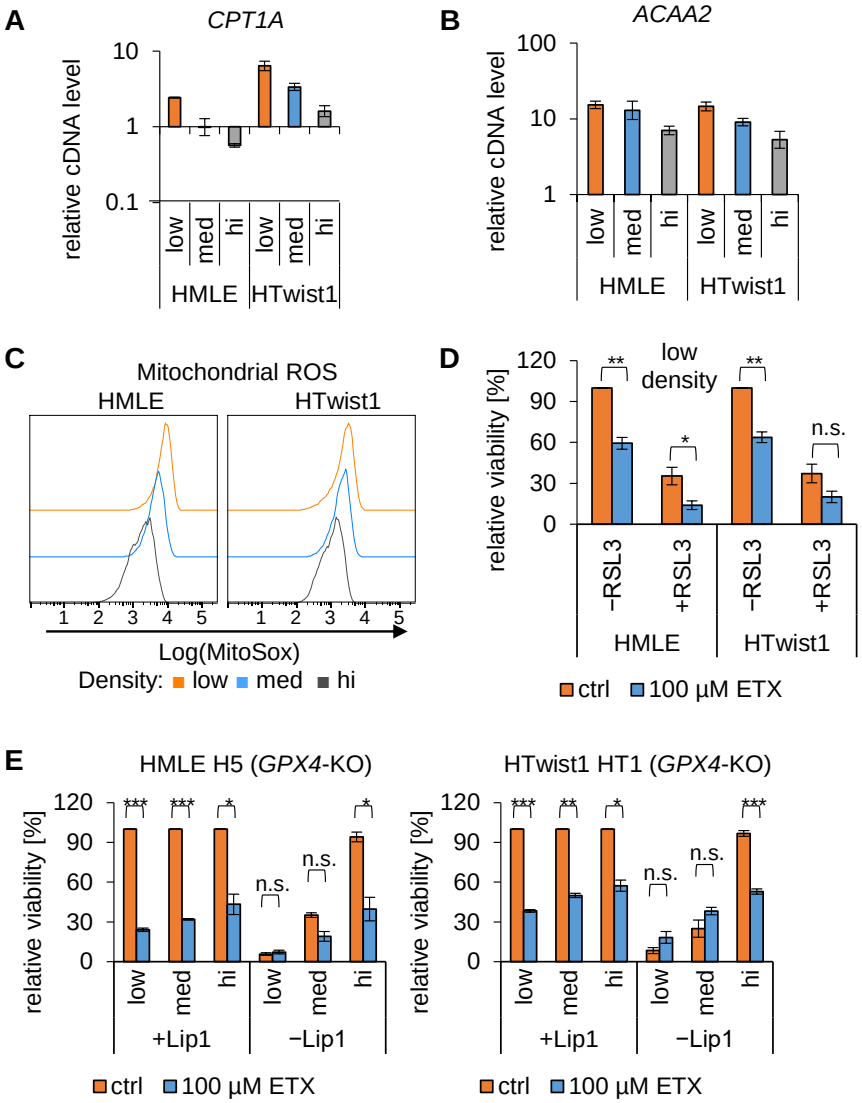

Figure 25: Energy metabolism shifts to beta-oxidation by low cell density

(A) and (B) qPCR: relative (A) *CPT1A* and (B) *ACAA2* mRNA expression of HMLE and HMLE-Twist1 cells seeded at different densities in 6-cm dishes for 48h. (C) Flow cytometry: MitoSox (mitochondrial ROS) staining of HMLE and HMLE-Twist1 cells seeded at indicated densities in 6-cm dishes for 48h. X-axis: log10 of MitoSox fluorescence, Y-axis: percentage of the maximum count. (D) Viability assay: treatment of HMLE and HMLE-Twist1 plated at low cell density in 96-well plates with 0.1% DMSO (–RSL3) or 100 nM RSL3 (+RSL3) without (ctrl) or in combination with 100 µM Etomoxir (ETX) for 24h. n=4. (E) Viability assay: treatment of *GPX4*-knockout (KO) single-cell clones HMLE H5 and HMLE-Twist1 HT1 plated at indicated cell densities in 96-well plates without (ctrl) or with 100 µM Etomoxir (ETX) for 48h in presence or absence of 1 µM Lip1. n=3. Data shown (A, B, D, E) represent mean ± SEM. Viability was normalized to respective DMSO control (D) or respective Lip1 control (E) within each cell line and cell density. One representative experiment (A, B, C) performed independently two (A, B) or four (C) times is shown. Statistics: two-tailed, unpaired T-test with Welch's correction (p-value: *<0.05, **<0.01, ***<0.01, n.s. = not significant).

First, I assessed the expression of β-oxidation related enzymes by qPCR in both HMLE and HMLE-Twist1 cells. In line with the proteomic data, *CPT1A* transcript levels as well as those of Acetyl-CoA Acyltransferase 2 (*ACAA2*), catalyzing the last step of β-oxidation, were increased at low cell density compared to high cell density (Figure 25A and B). Next, basal mitochondrial ROS levels were assessed by MitoSox staining, which serves as a proxy of mitochondrial activity. MitoSox fluorescence shifted to higher levels from high to low cell density in both cell lines (Figure 25C). These data indicated increased levels of mitochondrial ROS at low cell density, thus pointing to higher mitochondrial activity, potentially induced by increased level of β-oxidation. To further analyze β-oxidation in HMLE and HMLE-Twist1 cells, CPT1A function was inhibited by Etomoxir (ETX) treatment at low cell density during viability assays. Treatment with 100 µM ETX diminished cell viability compared to controls in both cell lines, while a combination of ETX with RSL3 did not further impact cell viability (Figure 25D). Furthermore, when *GPX4*-KO SCCs H5 and HT1 were exposed to ETX treatment in presence of Lip1, viability was strongly reduced at all seeding densities. However, cells at low cell density were around 1.5-fold less viable compared to cells at high cell density (Figure 25E). Again, Lip1-withdrawal unveiled *GPX4*-KO effects leading to cell density-dependent ferroptosis in both SCCs, but simultaneous ETX treatment did not reveal sound additive effects on cell viability (Figure 25E).

Collectively, these data suggested that cell density regulated the expression of enzymes required for β-oxidation which led to a greater dependence of HMLE and HMLE-Twist1 cells seeded at low density on β-oxidation. At the same time, both cell lines were generally sensitive to inhibition of β-oxidation.

Overall, these data indicated that in order to fuel β-oxidation, cells at low density increased LD turnover by ATGL upregulation which, in turn, induced lipid-mediated toxicity. With respect to cell density-dependent ferroptosis, this mechanism induced a vulnerability towards lipid-mediated stress provoked by GPX4 inhibition.

5 Discussion

Worldwide, breast cancer is the most frequently diagnosed cancer and the leading cause of cancer-related death in women (Bray et al., 2018). Importantly, whereas localized breast cancer is associated with a good prognosis, 5-year survival is below 30% for advanced and metastatic disease (Noone et al., 2017). The identification and characterization of molecular breast cancer subtypes based on global gene expression have helped to better understand this complex and heterogeneous disease. Specifically, a subset of breast cancer belonging to the molecular subtypes of basal-like or claudin-low breast cancer has been associated with a poor clinical outcome. Together they represent approximately 80% of all TNBC which are characterized by a lack of HR and HER2 expression and therefore are limited in targeted therapies opportunities (Prat and Perou, 2011). Both claudin-low and basal-like breast cancer have been shown to correlate with an EMT and a stem-cell-like signature (Herschkowitz et al., 2007; Sarrió et al., 2008). Since activation of EMT-TFs and the process of EMT are implicated in tumor progression and metastasis and confer resistance to conventional therapies like radio- or chemotherapy (Ansieau et al., 2014; Nieto et al., 2016), using EMT models and thus studying EMT may enable to develop novel therapies for TNBC patients as well as for patients with metastatic and therapy refractory breast cancer.

Ferroptosis is a regulated non-apoptotic cell death, induced through genetic inactivation or pharmacological inhibition of GPX4 (Dixon et al., 2012; Yang et al., 2014). Several players and metabolic regulators such as glutathione biosynthesis and iron metabolism have been identified to be involved in ferroptosis (Hao et al., 2018). Central to ferroptosis is the accumulation of lipid peroxidation of specific phospholipids like phosphatidylethanolamines (PE) containing long-chain polyunsaturated fatty acids (such as arachidonic acid (AA) and adrenic acid (AdA)) prior to cell death. Specifically, ACSL4 leads to AA and AdA esterification into PEs while lipoxygenases oxygenate this PE species, thereby converting them into a ferroptotic death signal (Doll et al., 2017; Kagan et al., 2017). Several reports have associated EMT with changes in cellular metabolism along with altered redox regulation and lipid metabolism (Dong et al., 2013; Sciacovelli and Frezza, 2017; Shaul et al., 2014), leading to the hypothesis that ferroptosis might be used to target EMT-induced cells. My work focused on studying ferroptosis in the context of

mammary epithelial cells (HMECs) and during Twist1-induced EMT. More precisely, I wished to elucidate molecular determinants of ferroptosis sensitivity in human mammary epithelial cells. The major finding of this work is the establishment of cell density, independently of EMT and other oncogenic signaling, as an important predictor of ferroptosis sensitivity in both primary as well as immortalized human mammary epithelial cells (HMECs). Specifically, cells at high cell density acquire resistance to ferroptosis while cells at low cell density are sensitive to ferroptosis induced by pharmacologic or genetic inhibition of GPX4 (Figure 5, Figure 8, Figure 9 and Figure 11). To my knowledge, cell density has not yet been described as a regulator of ferroptosis sensitivity.

5.1 Cell density determines ferroptosis-sensitivity in both epithelial and Twist1-induced HMLE cells

Since I hypothesized that EMT-induction might sensitize cells to ferroptosis, I initially elicited ferroptosis in a cellular model of EMT. For this purpose, I used immortalized mammary epithelial cells (HMLE) and induced EMT by activating Twist1 in a conditional manner by TAM-administration or in a constitutive manner (Mani et al., 2008; Schmidt et al., 2015). Doing so, I observed a strong reduction in viability at low seeding density upon inhibition of GPX4 in both epithelial and Twist1-induced mesenchymal cells. Irrespective of the cellular phenotype, both cell types became resistant to GPX4-inhibition with increasing cell densities (Figure 5A, C, D and E). Similarly, RSL3 treatment led to cell density-dependent ferroptosis in Snail1-induced EMT cells (Figure 5B). Moreover, I ruled out necrosis or apoptosis as cell death modalities (Figure 6). My findings are to some extent in contrast with a recent paper stating that therapy-resistant high mesenchymal cell states sensitize cells to ferroptosis (Viswanathan et al., 2017), since I did not observe a consistent difference in sensitivity in HMLE cells before and after EMT. Instead, my data indicate a different mechanism of cell density-dependent ferroptosis irrespective of cell state. However, in support of my data, although the mesenchymal-state vulnerability has been previously correlated with sensitivity in diverse cancer line lineages, no such correlation has been observed in breast cancer cell lines (Viswanathan et al., 2017). Additionally, the authors do not provide any information about seeding densities during viability assays in their research paper (Viswanathan et al., 2017), it is

impossible to directly compare my finding of a cell density-dependent ferroptosis to the finding of a mesenchymal cell state-dependent ferroptosis.

5.2 Thiol and glutathione metabolism do not directly impact cell density-dependent ferroptosis but could be linked to metastasis

Upstream of GPX4, the system x_c^- supplies cysteine for GSH biosynthesis which, in turn, is necessary for proper GPX4 activity (Friedmann Angeli et al., 2014; Yang et al., 2014). In contrast to RSL3, ERA treatment, which inhibits system x_c^- upstream of GPX4, did not impact cell viability at any cell density in both HMLE and HMLE-Twist1 (Figure 5A, D and E, Figure 7A). In line with these observations, cell density did not regulate key genes of the system x_c^- like *SLC7A11* and of GSH biosynthesis like *GCLC* (Figure 7B) that have been shown to modulate sensitivity to cystine deprivation (Dixon et al., 2012; Gao et al., 2015). Although this observation was surprising to some extent, ERA-resistant cell lines have been described before. For instance, oncogenic RAS-expressing fibroblasts (BJ-TERT/LT/ST/RAS^{V12}), but not their parental counterparts, are sensitive to ERA treatment, which led to its terminology “eradicator of Ras and ST”-expressing cells (Erastin) (Dolma et al., 2003). Since the generation of BJ and HMLE cells is based on the same genetic elements like the introduction of hTERT and the SV40 large T early region (Elenbaas et al., 2001; Hahn et al., 1999), oncogenic Ras expression in HMLE cells might induce ERA-sensitivity. Although one would need to test this possibility, it is quite unlikely. BJ-TERT/LT/ST/RAS^{V12} cells also undergo ferroptosis upon RSL3 treatment compared to BJ-TERT/LT/ST cells (Yang and Stockwell, 2008), but oncogenic Ras did not confer further sensitivity to RSL3 treatment in HMLE and HMLE-Twist1 beyond the cell density-dependency (Figure 10A and B). Another explanation might be that HMLE and HMLE-Twist1 cells derive cysteine by other means than the system x_c^-. Recently, resistance to ERA-induced ferroptosis has been linked to the transsulfuration pathway which provides intracellular cysteine from methionine (Hayano et al., 2016). Indeed, an active transsulfuration pathway has been shown to participate in GSH biosynthesis in primary HMECs (Belalcázar et al., 2014). Burkitt’s Lymphoma (BL) cells suffer from oxidative stress-induced cell death when they are seeded at low densities. Co-culture of BL-cells with irradiated fibroblasts has been reported to rescue cell death since fibroblasts supply cysteine to cells (Falk et al., 1993, 1998). By overexpression of SLC7A11 in BL-cells, it has

been shown that cysteine induces protection from low seeding densities by generating a reducing extracellular microenvironment fueled by cystine/cysteine redox cycle, but not by increasing GSH metabolism (Banjac et al., 2008). However, in my own experiments, co-culture with cells seeded at high cell density did not protect cells seeded at low cell density from ferroptosis (Figure 14D-F). Hence, this implies another mechanism in cell density-dependent cell death induction by GPX4 inhibition in HMECs than that observed for BL cells. Together, these data suggest that system x_c^- and GSH metabolism do not directly impact cell density-dependent ferroptosis observed upon GPX4 inhibition or knockout.

Interestingly, compared to parental HMLE cells, Twist1-induced EMT reduced both *SLC7A11* and *GCLC* expression which led to a reduction in thiols, serving as a proxy for cysteine levels, and to a reduction in reduced as well as total GSH levels (Figure 7B-F). A possible mechanism for a reduction of SLC7A11 and GSH levels upon Twist1-induced EMT could be the isoform switch of the cell surface marker CD44 that occurs during EMT (Brown et al., 2011; Ishimoto et al., 2011). A shift in expression of CD44 from variant isoforms (CD44v) to the standard isoform (CD44s) is as a critical event during Twist1-induced EMT in HMLE cells. Expression of the CD44s isoform has been connected to apoptosis-resistance by inducing survival signaling via AKT and has been found to be expressed in high-grade breast tumor samples (Brown et al., 2011). By contrast, the CD44v isoform has been shown to stabilize SLC7A11, thereby regulating GSH levels in gastrointestinal cancer cell lines. Further, stabilization of SLC7A11 by CD44v has been shown to promote tumor growth (Ishimoto et al., 2011). Since metastasizing melanoma cells have been shown to suffer from elevated oxidative stress which has to be reduced for metastatic outgrowth (Piskounova et al., 2015), reduction in the antioxidant capacity during Twist1-induced EMT might facilitate invasion and progression. Further experiments are required to elaborate this mechanism which might constitute an opportunity to therapeutically target metastatic progression.

Alternatively, one could hypothesize that these observations might explain why Twist1-induced cells seeded at intermediate seeding densities were slightly more sensitive to RSL3 treatment (Figure 5D and E). A small reduction in reducing equivalents might impact the threshold when cells are pushed into cell death upon RSL3 inhibition. At intermediate seeding densities, this deadly threshold might be reached earlier in HMLE-Twist1 cells compared to HMLE cells upon RSL3 inhibition.

However, this explanation contrasts to some extent with the observations that the reductions in thiol and GSH metabolism that I detected upon Twist1-induced EMT did not directly alter GPX4 activity (Figure 7G). Further, I did not observe that *GPX4*-KO resulted in different sensitivities of HMLE and HMLE-Twist1 SCCs seeded at intermediate cell densities (Figure 9B and C). Together, these data suggest that Twist1-induced changes in thiol and GSH metabolism might modulate RSL3 sensitivity at intermediate cell densities, however, upon complete loss of GPX4, these upstream mechanisms do not have a significant role in impacting sensitivity to ferroptosis. Furthermore, GPX4 might not only utilize GSH as a cofactor but also other thiol-containing substrates (Roveri et al., 1994) or protein thiols (Maiorino et al., 2005; Ursini et al., 1999), explaining why GPX4-activity is not altered in Twist1-induced cells. Additionally, it is possible that the thioredoxin antioxidant system might compensate for a reduction in GSH levels (Mandal et al., 2010). Although loss of GCL, the rate-limiting enzyme in GSH biosynthesis, is lethal to cells, Mandal and colleagues have been shown that GCL knockout cells are able to proliferate when SLC7A11 is simultaneously overexpressed, leading to higher cystine import into cells. Within the cells, TXNRD1 reduces cystine to cysteine, thereby enabling these cells to maintain a reducing microenvironment independently of GSH (Mandal et al., 2010). Again, as explained before, other cysteine sources could compensate for the reduction of system x_c^-. For example, a recent study has shown by metabolomics profiling that Cystathionine, a precursor of homocysteine in the transsulfuration pathway, was 11-fold enriched in HMLE-Twist1 cells compared to parental HMLE cells (Bhowmik et al., 2015).

5.3 Cell density-dependent ferroptosis is an intrinsic property of mammary epithelial cells

After establishing that cell density-dependent ferroptosis occurred irrespective of the epithelial or mesenchymal phenotype and was consistently observed upon RSL3-mediated GPX4 inhibition or GPX4 knockout, I set out to further elaborate the underlying mechanisms. Despite the recognition that RAS-expressing fibroblast are particularly sensitive to RSL3 treatment (Yang and Stockwell, 2008), I was not able to link oncogenic RAS expression or PTEN loss to cell density-dependent ferroptosis in the HMLE system (Figure 10). This is not too surprising since it has been shown that sensitivity to ferroptosis is not necessarily predicted by the *RAS* mutation status

across a large panel of cancer cell lines (Yang et al., 2014). Another study has reported a similar finding for other known tumor mutations in *RAF*, *PIK3CA* and *TP53* (Lachaier et al., 2014). Moreover, I discovered that cell density-dependent sensitivity towards RSL3-induced cell death was already present in primary HMECs (Figure 11). These data suggest that ferroptosis might be an intrinsic mechanism in the mammary gland to promote elimination of single detached cells when the epithelial integrity is disturbed. Accordingly, a recent study has shown that in immortalized non-tumorigenic MCF10A cells and a panel of breast cancer cell lines, detachment of cells from the extracellular matrix (ECM) triggers ferroptosis (Brown et al., 2017). In this context, ECM detachment has been modeled by culturing cells in low-adhesion plates which had been previously shown to induce anoikis, a form of programmed cell death (Frisch and Francis, 1994). Mechanistically, the authors have shown that α6β4 integrin expression leads to ferroptosis resistance during ECM detachment. At the molecular level, α6β4 integrin inhibits ACSL4 expression in a Src-dependent manner, thereby suppressing pro-ferroptotic changes in membrane composition (Brown et al., 2017). In a follow-up study, the authors have reported that in the absence of α6β4, cell-clustering during detachment mediated through PVRL4 (Nectin-4) dictates ferroptosis sensitivity. In contrast, without this clustering during detachment, susceptibility to anoikis is increased in single cells (Brown et al., 2018). However, I did not establish a link to ACSL4 expression because *ACSL4*-KO did not impact cell density-dependent ferroptosis, at least not in HMLE cells (Figure 16C-E). Therefore, the mechanism proposed by Brown and colleagues might be different from cell density-dependent ferroptosis. Furthermore, I observed that RSL3 prevented the organoid formation of primary HMECs seeded into 3D-collagen gels (Figure 13). Collagen I provides an ECM enabling growth as branched organoids of primary HMECs that resemble terminal ductal-lobular units of the mammary gland. Integrin α6 is expressed at a basal position in organoids formed by primary HMECs (Linnemann et al., 2015). Therefore, it is very interesting to assess how GPX4 inhibition impacts organoids that were already formed or whether they become resistant to GPX4 inhibition. It has been shown that TAM-inducible *GPX4*-KO fibroblasts are able to form colonies in a 3D Matrigel assay at a similar number as control cells. In these assays, 5×10^4 cells per gel have been seeded, a cell density at which cells die in 2D cultures (Schneider et al., 2010). In contrast, by culturing a *GPX4*-KO SCC of HMLE cells in 3D-collagen gels, I

observed that exposure to *GPX4*-KO by withdrawal of Lip1 at the single-cell level completely abolished sphere formation. After three days of culture in presence of Lip1, small colonies appeared and here, withdrawal of Lip1 impaired further proliferation, but did not induce complete regression of spheres (Figure 13B-F). In these 3D-collagen gels, I did not establish a direct correlation between seeded cell densities and resistance to ferroptosis (Figure 13B-F). However, the cell numbers that I have seeded into 3D collagen gels were 10-fold to 74-fold lower than those employed by Schneider and colleagues (Schneider et al., 2010). Although that study does not provide a mechanism for the difference between 2D and 3D ferroptosis-sensitivity, I propose that cell density-dependent ferroptosis observed in HMECs is mechanistically different to the sensitivity observed in fibroblasts. This hypothesis is further corroborated by a series of additional experiments using HMLE cells. There, I was able to induce cell death by RSL3 treatment if cells were distributed at low cell density in several small colonies spread across the entire surface of 6-cm dishes. In contrast, seeding the same cell number as one large dense and compact colony in the middle of such a dish resulted in resistance to RSL3-treatment (Figure 14G). Moreover, scattering epithelial colonies by neutralization of E-cadherin-mediated cell-cell adhesions did not alter RSL3 sensitivity. Notably, despite the disruption of adherens junctions, these scattered cells were still in close distance to each other (Figure 14H). Together, my data gained from 3D and 2D experiments imply that not necessarily the number of seeded cells determines ferroptosis sensitivity, but the proximity of cells to each other might play an additional role in ferroptosis sensitivity. Hence, organoids grown in 3D cultures or large colonies grown in 2D cultures might be considered as a cluster of cells in very close proximity that provides resistance, possibly by some specific integrin signaling like α6β4, as recently proposed (Brown et al., 2017). However, how integrin signaling is linked with cell-cell proximity signaling constitutes an aim of future studies. Another explanation how cell density, cell-cell adhesions and ferroptosis-sensitivity might be linked is discussed in *Section 5.6*.

However, cell-cell adhesions might be important for ferroptosis sensitivity after all. First, HMLE cells seeded at low cell density form small epithelial clusters as well although they are sensitive to ferroptosis (Figure 5C-E). Second, EMT-induced HMLE-Twist1 cells also form cell-cell adhesions mediated by N-cadherin (Ganz et al., 2006; Mani et al., 2008). These interactions might be increased at high cell

density since cells are in close-proximity and have more contact points to each other (Figure 5C). Similarly, neural crest cells are connected by N-cadherin-mediated cell-cell adhesions during collective migration which leads to cell polarity and formation of protrusions at the leading edge of the cluster (Theveneau et al., 2010). A similar mechanism with respect to N-cadherin-induced polarity has been found in HeLa cells which involves integrin signaling molecules (Yano et al., 2004). Therefore, I hypothesize that the threshold of ferroptosis sensitivity might be determined by integrin signaling. Again, how exactly ferroptosis-sensitivity regulated by cell density is linked with integrin signaling remains to be determined in future studies.

There might be yet another mechanism how cells sense their neighbors. For instance, Calcium signaling could play a possible role. It has been proposed that calcium released into the surrounding medium informs adjacent cells via the extracellular Ca^{2+}-sensing receptor about their Ca^{2+}-signaling status (Hofer et al., 2004). Furthermore, an increase in intracellular calcium concentrations has been linked to cytotoxicity induced by peroxynitrite and hydrogen-peroxide oxidative stress in HaCaT cells (a keratinocyte cell line). The authors have connected this oxidative stress-induced cell toxicity with cell density. Moreover, at high cell densities, PARP activation and thus apoptotic pathways have been reduced (Bakondi et al., 2003). In support of this hypothesis, intracellular calcium chelators have been found to be protective in hydrogen peroxide-induced renal tubular cell injury as well as in ischemic neuronal injury (Tymianski et al., 1993; Ueda and Shah, 1992). These observations might constitute a link between ferroptosis and calcium signaling since ferroptosis has been implied in ischemia-reperfusion injuries of the brain and kidney (Friedmann Angeli et al., 2014; Linkermann et al., 2014; Tuo et al., 2017). Although calcium chelation did not rescue ERA-induced cell death in HT-1080 cells (Dixon et al., 2012), but ERA also did not impact viability in HMECs (Figure 7A), the assessment of calcium-signaling in cell density-dependent ferroptosis might be an avenue to consider in future experiments.

5.4 An increase in lipid peroxidation is not directly linked to cell density-dependent ferroptosis

Generation and accumulation of lipid peroxidation caused by GPX4 inhibition or *GPX4* knockout is considered a hallmark and mediator of ferroptosis (Dixon et al., 2012; Doll et al., 2017; Friedmann Angeli et al., 2014; Kagan et al., 2017; Yang et

al., 2014). To detect an increase in lipid peroxidation upon GPX4 inhibition, fluorescent C11-BODIPY dye and the Click-iT Lipid Peroxidation Imaging Kit are in widespread use (Dixon et al., 2012; Gascón et al., 2016; Yang et al., 2014). By contrast, I did not detect a significant increase in lipid peroxidation in RSL3-treated HMLE and HMLE-Twist1 cells when using these dyes (Figure 17A, C and D). This was unexpected since I had ruled out necrosis and apoptosis as cell death modalities and established that cell density-dependent cell death was rescued by a variety of agents that block ferroptosis (Figure 6 and Figure 16A). Importantly, I used cumene hydroperoxide as a positive control to measure lipid peroxidation (Figure 17B and E) (Weiss and Estabrook, 1986), ruling out technical issues with these assays. Even more surprising was my finding that when using *GPX4*-KO HMLE and HMLE-Twist1 SCCs, I discovered an increase in lipid peroxidation levels by C11-BODIPY staining which (I) was highly variable between different SCCs and which (II) was not directly linked to cell density (Figure 18A). However, low seeding density reliably sensitized all these SCCs to ferroptosis (Figure 9C). Specifically, Lip1 withdrawal increased lipid peroxidation levels on average by 2-fold in all densities (low, intermediate and high seeding densities) compared to Lip1-cultured cells (Figure 18B). Since both RSL3 and *GPX4*-KO lead to cell density-dependent ferroptosis, I conclude that a general increase in lipid peroxidation is not the direct cause of cell death in cell density-dependent ferroptosis. However, since both lipophilic antioxidants and LOX inhibitors rescued RSL3-induced ferroptosis in HMLE and HMLE-Twist1 cells (Figure 16A), my data suggest that lipid peroxidation is critically involved. Indeed, LOX enzymes have been shown to oxidize PUFAs which sensitize cells to ferroptosis (Seiler et al., 2008; Yang et al., 2016). Moreover, it has been reported that ALOX15, a specific LOX enzyme, is involved in lipoprotein oxygenation and organelle degradation (Belkner et al., 1993; van Leyen et al., 1998). Therefore, instead of inducing a global increase in lipid peroxidation, it could be possible that very specific lipid metabolites are oxidized in HMLE and HMLE-Twist1 cells that serve as mediators of cell death. These metabolites might be crucial for cell survival or might serve as metabolites for other cellular processes. Based on my proteomics screen, I propose that cell density regulates the liberation of fatty acids from lipid droplets which are used for fatty acid oxidation in the mitochondria. This mechanism will be discussed in more detail in *Section 5.6*. Another report has established ACSL4 as a determinant in ferroptosis by increasing oxidation-prone

PUFAs in membranes (Doll et al., 2017). Specifically, ACSL4 expression leads to the enrichment of PEs, a specific class of phospholipids, containing AA and AdA species, within cellular membranes. Furthermore, double and triple oxygenated AA- and AdA-containing PEs have been identified as mediators in ferroptosis (Doll et al., 2017; Kagan et al., 2017). However, I discovered that although both HMLE and HMLE-Twist1 cells expressed ACSL4 (Figure 16B), neither inhibition of ACSL4 by rosiglitazone (ROSI) nor genetic deletion of *ACSL4* rescued cell density-dependent ferroptosis (Figure 16A, C and E). I cannot rule out that another ACSL enzyme compensates for ACSL4 activity during *ACSL4*-KO. For instance, ACSL3 can use AA as a substrate as well (Ansari et al., 2017; Van Horn et al., 2005). Moreover, a regulation of another lipid-metabolizing enzyme by cell density, namely lysophosphatidylcholine acyltransferase 3 (LPCAT3), which incorporates ACSL-activated acyl-CoAs into phospholipids (PL) (Shindou and Shimizu, 2009) may play a role in cell density-dependent ferroptosis. LPCAT3 has been identified to contribute to RSL3 and ML162, but not ERA-induced ferroptosis (Dixon et al., 2015). Since ERA-treatment does not elicit cell density-dependent ferroptosis, LPCAT3 could be considered in future experiments. To clarify mechanisms of cell density-dependent ferroptosis, experiments involving the deletion of other ACSL proteins will provide further insights.

I did not observe cell density-dependent ferroptosis upon GPX4 inhibition in a panel of breast cancer cell lines (Figure 15). In this panel, ACSL4 expression has been described to confer ferroptosis sensitivity. For instance, MCF7 and T-47D cells showed resistance while MDA468, MDA231 and MDA157 cells were sensitive to RSL3-induced ferroptosis correlating to absence (MCF7 and T-47D) and presence (MDA231 and MDA157) of ACSL4 expression (Doll et al., 2017). These data again support the hypothesis that another mechanism confers sensitivity in cell density-dependent ferroptosis. ACSL4 expression might be a predictor for ferroptosis sensitivity depending on the cellular context. Likewise, oncogenic RAS confers ferroptosis sensitivity only in specific cellular contexts (Dolma et al., 2003; Lachaier et al., 2014; Yang and Stockwell, 2008; Yang et al., 2014).

Moreover the role of LOX enzymes in ferroptosis is highly debated. For instance, deletion of the 12/15-lipoxygenase (*ALOX15*) resulted in resistance to BSO-induced ferroptosis (Seiler et al., 2008), but did not rescue mice with an inducible *GPX4*-KO from ferroptosis-induced acute renal failure and early death (Friedmann Angeli et

al., 2014). In the latter case, a possible compensation by ALOX5, another LOX enzyme, was excluded (Friedmann Angeli et al., 2014). Moreover, the authors from a recently published study suggest that ferroptosis sensitivity is simply determined by the pool of autoxidizable lipids. Every modulation increasing this pool then induces ferroptosis susceptibility (Shah et al., 2018). Further, this study showed that LOX inhibitors possess unspecific radical scavenging properties. Nonetheless, additional studies involving genetic modulation of LOX genes and PUFA-related genes would be required to better understand how cellular context shapes sensitivity to ferroptosis. Accordingly, large-scale analyses of cellular lipids (lipidomics), especially of PUFAs in phospholipids, in HMLE and HMLE-Twist1 cells seeded at different cell densities will be performed in addition to further loss-of function analyses of PUFA-modifying enzymes. Likewise, as previously reported (Kagan et al., 2017), assessing the oxi-lipidome will enable us to shed light on which lipid metabolites are oxidized during cell density-dependent ferroptosis. Together, these experiments will provide further insights into the mechanisms of ferroptosis sensitivity induced by low cell density in HMECs.

5.5 The role of iron in cell density-dependent ferroptosis remains unclear

5.5.1 Does ferritinophagy play a role in cell density-dependent ferroptosis?

Iron-dependent lipid peroxidation is considered as a hallmark in ferroptosis and even informed its terminology (Cao and Dixon, 2016; Dixon et al., 2012). Indeed, I observed that iron chelation by deferoxamine (DFO), but not by ciclopirox (CPX) partially rescued cell density-dependent ferroptosis induced by RSL3 treatment (Figure 16A). Both iron chelators have been described to protect from ferroptosis (Dixon et al., 2012, 2015; Yang and Stockwell, 2008). However, they possess distinct modes of action due to differential abilities to cross cellular membranes (Hao et al., 2018). Since DFO chelates lysosomal iron while CPX binds the cytoplasmic labile iron pool (Hao et al., 2018), one could hypothesize that lysosomal iron plays a role in cell density-dependent ferroptosis. For instance, it has been shown that oxidative-stress-induced cell death was prevented by DFO-mediated chelation of redox-active iron in lysosomes (Kurz et al., 2004; Persson et al., 2003; Yu et al., 2003). Only recently, lysosomal degradation of ferritin providing labile iron (Fe^{2+}) that involves an autophagic process termed ferritinophagy has been connected to ferroptosis (Gao et al., 2016; Hou et al., 2016; Torii et al., 2016). Mechanistically,

inhibition of autophagy by chemical inhibitors or knockdown of autophagy-related proteins (for instance Atg5, Atg7, Atg3 and Atg13) protected from FIN-induced ferroptosis in fibroblasts and cancer cells by preventing the accumulation of labile iron and ROS (Gao et al., 2016; Hou et al., 2016; Torii et al., 2016). Further, the nuclear receptor coactivator 4 (NCOA4), which is a selective cargo receptor for ferritinophagy, has been linked to modulate ferroptosis when NCOA4 was knocked down or overexpressed during ferroptosis induction (Gao et al., 2016; Hou et al., 2016). Interestingly, senescent MEFs, induced by oncogenic Ras expression, have been shown to accumulate iron due to impaired ferritinophagy. In addition, they were resistant to ERA and RSL3-induced ferroptosis (Masaldan et al., 2018). Overall, these data hint to an association between autophagy, and more specifically ferritinophagy with ferroptosis. Notably, “transferrin transport” and “regulation of macroautophagy” are two biological GO-terms enriched in low cell density in both HMLE and HMLE-Twist1 identified during my proteomic study (Figure 19D). Therefore, it might be that cell density impacts ferritinophagy and thereby ferroptosis-sensitivity. However, in the study performed by Masaldan and colleagues, pharmacological induction of ferritinophagy did not re-sensitize senescent cells to ferroptosis (Masaldan et al., 2018), further showing that more research is necessary to assess the contribution of ferritinophagy in ferroptosis. Future experiments are required to address the role of lysosomal iron, possibly provided during ferritinophagy, in cell density-dependent ferroptosis.

5.5.2 HMOX1 does not contribute to cell density-dependent ferroptosis

Another iron metabolism-related protein that was enriched in low density in my proteomic study was heme oxygenase 1 (HMOX1) (Appendix Table 11). By degrading heme and heme-containing proteins, HMOX1 leads to the release of ferrous iron (Fe^{2+}). In contrast to the ubiquitously expressed isoform HMOX2, HMOX1 is induced by a variety of external stimuli like oxidative stress, hypoxia or iron starvation (Dunn et al., 2014). It has been shown that HMOX1 expression increases ERA-induced ferroptosis (Kwon et al., 2015). Therefore, HMOX1 was validated as one potential protein which might influence cell density-dependent ferroptosis. Indeed, I discovered that cell density upregulates HMOX1 at the transcriptional and protein level in HMLE-Twist1 cells. However, HMLE cells expressed HMOX1 only at very low levels that were very slightly upregulated by low

cell density (Figure 20A and B). Moreover, although lentiviral-mediated HMOX1 overexpression resulted in high HMOX1 levels in HMLE cells (Figure 20C and D), no impact on cell density-dependent ferroptosis induced by RSL3 treatment was observed (Figure 20E and F). Likewise, CRISPR/Cas9 genome-editing in the HMOX1 locus in both HMLE and HMLE-Twist1 cells, yielding at least one SCCs with HMOX1-KO, did not alter cell density-dependent ferroptosis (Figure 21). Together, my data suggested that HMOX1 does not contribute to cell density-dependent ferroptosis in HMLE and HMLE-Twist1. One explanation is that overexpression of HMOX1, which was derived from cloned cDNA transcribed from HMOX1 RNA expressed by HMLE-Twist1 cells at low cell density, did not result in the assembly of a fully functional enzyme in HMLE cells (Figure 20D). Furthermore, CRISPR/Cas9 genome-editing in the HMOX1 locus had a low efficiency resulting in only one SCCs with a full HMOX1 knockout (Figure 21A and B), opening the possibility that these data might not be sufficient to exclude HMOX1 as a potential candidate. For instance, further evidence could be provided by experiments modulating HMOX1 activity either by addition of the HMOX1 inhibitor zinc protoporphyrin IX or the inducer Hemin during RSL3-induced ferroptosis, as previously described (Kwon et al., 2015). Since endogenous HMOX1 levels are very low in HMLE cells (Figure 20B), a contribution of HMOX1 at least in HMLE-observed cell density-dependent ferroptosis is unlikely. A controversial role of HMOX1 in ferroptosis has been also reported in recent literature. Genetic deletion of *HMOX1* in renal proximal tubule cells increased sensitivity to ERA- and RSL3-induced ferroptosis compared to *HMOX1* wildtype cells (Adedoyin et al., 2018). Likewise, knockdown of *HMOX1* in hepatocellular carcinoma cells (HCCs) augmented their sensitivity to ferroptosis. In HCCs cells, the nuclear factor erythroid 2-related factor 2 (NRF2), as a master regulator of antioxidant response inducing, for instance, the transcription of *HMOX1*, conferred resistance to ferroptosis (Sun et al., 2016). Similarly, the NRF2-HMOX1 pathway has been associated with resistance to artesunate-induced ferroptosis in cisplatin-resistant head and neck cancer cells (Roh et al., 2017). By contrast, several reports have linked *HMOX1* expression to ferroptosis sensitivity (Chang et al., 2018; Hassannia et al., 2018; Kwon et al., 2015). For instance, withaferin A increases the labile Fe^{2+} pool by inducing HMOX1 which results in increased ferroptosis induction in neuroblastoma cell lines (Hassannia et al., 2018). Moreover, BAY 11-7085-induced ferroptosis has been shown to be mediated by an upregulation of an NRF2-

SLC7A11-HMOX1. Here, HMOX1 overexpression accelerated ferroptosis (Chang et al., 2018). These studies clearly demonstrate that HMOX1 might have a dual role in ferroptosis. HMOX1-deficient mice were shown to be susceptible to oxidative stress (Poss and Tonegawa, 1997b). By contrast, depending on the expression levels of HMOX1, HMOX1 either induced a cytoprotective or, at higher expression levels due to an increase in labile Fe^{2+}, a cytotoxic response (Suttner and Dennery, 1999). Therefore, upregulation of HMOX1 during ferroptosis, possibly through NRF2-mediated response to oxidative stress, might occur as a compensatory mechanism at the expense of increasing the redox-sensitive labile iron pool. Depending on the ability to buffer iron, for instance by iron storage in ferritin or iron export, these contradictory results might be explained. Similarly, upregulation of SLC7A11 during ERA-induced ferroptosis has been shown to occur as a compensatory mechanism (Dixon et al., 2012). Likewise, one could hypothesize that the observed upregulation of HMOX1 at low density in both cell lines is a consequence of increased oxidative stress which is indicated by increased cytosolic, mitochondrial and lipid-derived ROS levels (Figure 14C, Figure 22D and Figure 25C).

Heme degradation by both HMOX1 and HMOX2 leads as another product to biliverdin which is reduced to bilirubin by the biliverdin reductase (BVR) (Dunn et al., 2014). The redox cycle of biliverdin and bilirubin by BVR has been shown to possess potent antioxidant activity (Baranano et al., 2002). However, in a recent study, bilirubin have been associated to protect from lipid peroxidation in contrast to GSH which was more connected to protect from protein oxidation (Sedlak et al., 2009). Indeed, earlier studies have shown that HMOX2 has a neuroprotective role by protecting against oxidative stress and lipid peroxidation (Chang et al., 2003; Chen et al., 2005a; Doré et al., 1999). For instance, *HMOX2*-KO mice were still able to induce HMOX1 after traumatic brain injury, but compared to *HMOX2*-WT littermates, protection against lipid peroxidation and neuronal loss was greatly reduced (Chang et al., 2003). Therefore, it is possible that cell density regulates HMOX2 and BVR in HMECs. The induction of HMOX1 observed at low cell density might be a marker for increased cellular stress, but neither sufficient nor driving protection against cell density-dependent ferroptosis.

5.6 Cell density-dependent regulation of lipid droplet metabolism linked to a switch to oxidative metabolism might explain differential vulnerability to GPX4-mediated ferroptosis at low and high cell density

During the analysis of the proteomics data, the GO Term “positive regulation of triglyceride catabolic process” attracted my attention (Figure 19D). Since I hypothesized that specific lipids might be oxidized during cell density-dependent ferroptosis (see also *Section 5.4*), I decided to validate the two hits adipose triglyceride lipase (ATGL = PNPLA2) and its co-activator lipase 1-acylglycerol-3-phosphate O-acyltransferase (ABDH5). ATGL catalyzes the first step in the lipolytic breakdown of triacylglycerides (TAGs) from intracellular lipid droplets to liberate one fatty acid (FA) and yield diacylglycerol (DAG). FAs are subsequently hydrolyzed from DAG by the hormone-sensitive lipase (HSL) and monoacylglycerol lipase (MAGL). Thereby, liberated FAs from TAGs can be transferred to mitochondrial β-oxidation as an energy source, serve as a source for the synthesis of membrane lipids or can be re-esterified as TAGs (Walther and Farese, 2012). Indeed, I observed that low cell density upregulated ATGL protein in both HMLE and HMLE-Twist1 cells which inversely correlated with the LD droplet amount measured by the fluorescent dye BODIPY493/503 (Figure 22C and D). In support of my data, a key role of ATGL-induced lipolysis of LDs was described for mammalian cells (Smirnova et al., 2006). Interestingly, at the transcript level, regulation of *ATGL* and *ABDH5* by cell density was not evident (Figure 22A), indicating that either mRNA is degraded or protein stability of ATGL is modulated. For instance, short-term fasting of worms have been shown to result in ATGL-1-mediated lipolysis that was activated by LID-1, an orthologue of human ABDH5. Thereby, increased cyclic AMP (cAMP) levels activated protein kinase A (PKA) activation which in turn stabilized ATGL-1 together with LID-1 at LDs (Lee et al., 2014). Perilipins (PLIN) are another protein family that regulates LD metabolism and ATGL-mediated lipolysis (Khor et al., 2013). During hepatic nutrient starvation, LD-associated PLIN2 and PLIN3 has been shown to be degraded via chaperone-mediated autophagy (CMA), followed by an increase in ATGL levels and association of macroautophagy proteins on LDs (Kaushik and Cuervo, 2015). Further, both ATGL and ABDH5 are bound by PLIN5 at the surface of LDs, thereby inhibiting lipolysis. In that study, PKA activation only modestly increased lipolysis (Wang et al., 2011). On the contrary, in C.elegans, the AMP-

activated protein kinase (AMPK) has been shown to phosphorylate the C.elegans homolog of ATGL (ATGL-1), thereby inducing binding sites for the C.elegans homolog of 14-3-3 protein (PAR5). PAR5 interaction with ATGL-1 removes ATGL-1 from LDs, guiding it to proteasome-mediated degradation (Xie and Roy, 2015). AMPK is activated by binding of AMP or ADP when ATP levels drop for instance during low nutrient supply. Furthermore, AMPK has to be phosphorylated at Thr172 which occurs by the serine/threonine kinase LKB1 or in response to calcium flux (Mihaylova and Shaw, 2011). Together, these studies suggest that depending on the cellular context, lipolysis is tightly regulated at the basal level and during nutrient stress. In this study, cell density might be the trigger to stimulate ATGL-mediated LD breakdown. Importantly, a decrease of LD content at low cell density was associated with an increase in lipid ROS level in both HMLE and HMLE-Twist1 cells (Figure 22D), suggesting that lipid peroxidation increases. Moreover, inhibition of ATGL by Atglistatin rescued RSL3-induced and *GPX4*-KO-mediated ferroptosis (Figure 22E and F). Likewise, supplementation with the mono-unsaturated fatty acid oleic acid (OA), increasing the amount of LDs, rescued RSL3-induced cell death (Figure 24). Previously, it has been shown that OA supplementation induces the translocation of the LD-associated hydrolase (LDAH) from the endoplasmic reticulum to newly formed LDs where it induces LD fusion. Moreover, polyubiquitination and proteasomal degradation of ATGL is increased by LDAH (Goo et al., 2017), suggesting a possible contribution of LDAH in regulating ATGL levels at high cell density. Furthermore, OA supplementation was associated with a decrease in lipid ROS level (Figure 24A), indicating that LDs might buffer lipid peroxidation. A recent study has shown that LDs might serve as an antioxidant organelle protecting breast cancer cells from nutrient and lipotoxic stress. Thereby, the breakdown of LDs by ATGL increased PUFA-mediated lipotoxicity during starvation. Importantly, utilization of fatty acids in β-oxidation was shown to enhance cell survival during nutrient-stress. Two compensatory mechanisms were described. First, MDA-MB-231 breast cancer cells were protected from PUFA-induced lipotoxicity during nutrient starvation by the liberation of unsaturated FAs from phospholipid membranes by the human group X secreted phospholipase (hGX sPLA2), thereby increasing the abundance of low-level unsaturated FAs like OA in LDs. Second, inhibition of ATGL-induced lipolysis further protected from PUFA-induced lipotoxicity during nutrient starvation (Jarc et al., 2018). Therefore, my data

suggest that ATGL-mediated degradation of LDs increase lipotoxic stress at low cell density at a basal level. Then, simultaneous inhibition of GPX4, resulting in a decreased ability to remove lipid peroxides, might increase lipid-mediated stress to a level that cells are no longer able to cope with. However, lipid ROS were not significantly different when GPX4 was inhibited at different cell densities (Figure 17 and Figure 18). Therefore, while cell density appears to increase on its own lipid-mediated stress, this cellular stress is more detrimental at low cell density than at high cell density. One reason might be that liberated FAs, especially PUFAs, are used in β-oxidation as previously described (Ong et al., 2011). I discovered that HMLE and HMLE-Twist1 cells rely on β-oxidation (Figure 25). Therefore, when GPX4 is inhibited at low cell density, the elevated lipid-mediated stress might lead to oxidation of these FAs, thereby inhibiting β-oxidation and resulting in cell death. This mechanism will be explained in more detail in the following paragraphs.

Of note, my data provide a possible explanation for the beneficial effect OA. Another study has been already observing that OA strongly rescued RSL3-induced ferroptosis in BJeLR, HT-1080 and G-401 cells (Yang et al., 2016). Accordingly, generation of LDs has been found to reduce FA-induced lipotoxicity. Mechanistically, supplementation with OA or increased stearoyl-CoA desaturase 1 (SCD-1) activity increased the amount of unsaturated fatty acids like OA, which in turn promoted TAG accumulation of both saturated and unsaturated FA (Listenberger et al., 2003). Interestingly, my proteomic study indicated an upregulation of SCD at high cell density (Figure 19C), further suggesting a possible difference of cells seeded at low and high cell density with respect to LD biogenesis. Importantly, it has been recently suggested that reducing the pool of autooxidizable lipids will inevitably inhibit ferroptosis, no matter by what means (Shah et al., 2018). Thus, the amount of LD present in cells or changing the fraction of highly unsaturated PUFAs by OA supplementation might buffer lipotoxic effects as recently proposed (Jarc et al., 2018; Listenberger et al., 2003). Further, a recent report suggested that cells at high cell density might have a greater cell-to-cell heterogeneity of the LD content (overall higher than at low cell density), thereby reducing lipotoxicity for the whole population (Herms et al., 2013). In Drosophila, the proliferation of neuronal stem cells during oxidative stress was enabled by a mechanism involving LD biogenesis in adjacent niche glia cells. Here, oxidative stress induced the generation of TAGs by enzymes like diacylglycerol

acyltransferase1 (DGAT-1) that were stored as LDs in glial cells. These newly generated LDs sequestered PUFAs, thereby limited ROS and lipid peroxidation of PUFAs and in turn, protected neighboring neural stem cells (Bailey et al., 2015). Diacylglycerol acyltransferase1 (DGAT-1) has been shown to promote LD biogenesis of FAs liberated by autophagy during nutrient-stress. With this mechanism, mitochondrial function was preserved and lipotoxicity limited (Nguyen et al., 2017). Likewise, deletion of DGAT-1 impaired TAG synthesis and induced lipotoxicity mediated by both OA and palmitate overload (Listenberger et al., 2003). Together, these data suggest that cells suffer from higher oxidative stress at all cell densities, but cell-to-cell heterogeneity in LD metabolism at high cell density provides protection at the population level. Indeed, I observed that lipid peroxidation levels are higher in HMLE cells that are located at the border of bigger colonies formed by HMLE cells compared to those located within colonies (Figure 17C), indicating heterogeneity of lipid peroxidation levels within colonies. Since I observed a correlation between LD content and lipid ROS level, cells at the border might also have higher ATGL expression, less LD abundance and as a result higher lipid peroxidation levels. In contrast, LD biogenesis might be increased in cells located inside these colonies. In cases of increased lipid stress, i.e. during GPX4 inhibition, this heterogeneity might provide protection as indicated by previous studies (Bailey et al., 2015; Herms et al., 2013). Therefore, the balance between LD catabolism mediated by ATGL and biogenesis mediated by DGAT-1 might be crucial for cell density-dependent ferroptosis. Further, these observations indicate a connection between LD metabolism, autophagy and ferroptosis sensitivity that opens yet another interesting avenue for future research. Autophagy has been linked with ferroptosis previously (Gao et al., 2016; Hou et al., 2016; Torii et al., 2016) (see also *Section 5.5.1*). Interestingly, one of the top enriched GO Terms at low cell density in my proteomics data was “regulation of macroautophagy” (Figure 19D). With respect to LD metabolism, it has been previously shown that LD catabolism and fatty acid oxidation (FAO) was impaired when autophagy was inhibited in mouse hepatocytes and mice liver (Singh et al., 2009). Different mechanisms for this mechanism have been provided recently. For instance, during nutrient-stress in hepatocytes, ATGL levels and, presumably, lipolysis increased through the degradation of PLIN2 and PLIN3 by chaperone-mediated autophagy followed by the localization of macroautophagy proteins on LDs (Kaushik and Cuervo, 2015). Furthermore, it has

been shown that ATGL is both required and sufficient for LD breakdown by an autophagic/lipophagic process in hepatocytes. Specifically, ATGL was shown to control sirtuin 1 (SIRT1) activity which in turn regulates autophagy. Together, LD catabolism is induced which in turn fuels FAO (Sathyanarayan et al., 2017).

Based on all of these data, I hypothesize that fatty acids, particularly PUFAs required for β-oxidation might be oxidized during GPX4-inhibition, thereby inducing an energy crisis and cell death at low cell density. In hepatocytes, ATGL-regulated LD turnover has been implicated in channeling fatty acids to mitochondrial FAO (Ong et al., 2011). ATGL-mediated lipolysis has been shown to activate both peroxisome proliferator-activated receptor alpha activity (PPAR-α) and PPAR-γ coactivator 1-α (PGC-1α) signaling, thereby inducing mitochondrial biogenesis and oxidative gene expression (Haemmerle et al., 2011; Ong et al., 2011; Sapiro et al., 2009). Adding to this, a recent report has shown that LD lipolysis, autophagy and mitochondrial fusion dynamics are crucial to channel FAs to mitochondria to enable oxidative phosphorylation during nutrient-stress (Rambold et al., 2015). Indeed, I observed upregulation of genes involved in mitochondrial FAO like *CPT1A* and *ACAA2* as well as increased mitochondrial ROS levels at low cell density (Figure 25A-C). Treatment with Etomoxir, an inhibitor of β-oxidation, elicited cell death induction in both HMLE and HMLE-Twist1 cells in all cell densities (Figure 25D and E), indicating that β-oxidation is in general crucial for the survival of HMLE and HMLE-Twist1 cells. Together, these data indicate that cell density induces ATGL-dependent LD breakdown. In turn, liberated FAs might induce both mitochondrial biogenesis and fuel β-oxidation at low cell density. This mechanism might be induced at the expense of increasing the vulnerability of cells toward lipid toxicity at low cell density. One explanation, why these pathways are induced at low cell density, might be that thereby, migratory and invasive traits are induced. For instance, it has been shown that expression of the connected transmembrane glycoprotein, CUB-domain-containing protein 1 (CDCP1) decreases LD abundance along with an increase FAO. This mechanism has been linked to metastasis of TNBC cell lines (Wright et al., 2017). Likewise, FAO driven by CPT1 and CPT2 have been implicated in migration, invasion and metastasis *in vitro* and in patient-derived xenograft models of TNBC (Park et al., 2016). Interestingly, PGC-1α has been linked to increased mitochondrial biogenesis and oxidative metabolism, necessary for migration, invasion and distant metastasis. However, while a knockdown of *PGC-1α* impacted

invasive properties, proliferation and EMT were not affected, implying that the EMT program is not directly connected to PGC-1α (LeBleu et al., 2014). These data could explain why the presumed metabolic switch to β-oxidation at low cell density that I observed occurs in both epithelial and Twist1-induced mesenchymal HMLE cells. Interestingly, a link between ferroptosis, fatty acid metabolism and FAO has been recently described involving yet another mechanism: the inhibitor CIL56 induces ferroptotic and necrotic cell death by acting on fatty acid synthesis by the rate-limiting enzyme Acetyl-CoA Carboxylase 1 (ACC1). CIL56 led to an accumulation of long-chain saturated, monounsaturated and polyunsaturated fatty acids, possibly by inhibiting the mitochondrial breakdown of fatty acids or increased malonyl-CoA production by ACC-1, which is a negative regulator of β-oxidation (Dixon et al., 2015).

However, further experiments are necessary to elaborate on the proposed mechanism in detail. Since it has been shown that Atglistatin targets human ATGL only by 10% (Schweiger et al., 2017), loss-of-function experiments for ATGL are required. Further, measuring lipolysis and staining of LDs by immunofluorescence will shed further light on the contribution and localization of LDs and how this impacts cell density-dependent ferroptosis. Of note, RSL3-induced cell death was not generally rescued by Atglistatin, indicating that Atglistatin does not have generalized unspecific, antioxidative capacity. For example, Atglistatin rescued T-47D cells from RSL3-induced ferroptosis, but not MDA231 or MDA157 cells (Figure 23A). This finding could be interesting with respect to different mechanisms of ferroptosis. Furthermore, I did not establish a contribution of ACSL4 in cell density-dependent ferroptosis (Figure 16E) although ACSL4 expression has been shown to directly correlate with ferroptosis sensitivity by increasing oxidation-prone PUFAs in cellular membranes (Doll et al., 2017; Kagan et al., 2017) (see also *Section 5.4*). T-47D cells do not express ACSL4 and have been shown to be resistant to RSL3-induced ferroptosis (Doll et al., 2017). Therefore, the differences that I observed with respect to RSL3-sensitivity might be elicited by culturing cells in different growth media that modulate signaling and intracellular metabolism. T-47D cells might be used to study the proposed mechanism of cell density-dependent ferroptosis when culturing these cells in different growth media. Accordingly, HMLE and HMLE-Twist1 cells were less sensitive to RSL3-induced cell death when they were cultured in basal medium compared to growth-factor containing medium (Figure 14I). These data indicated

that metabolic pathways activated through factors in the growth medium play an important role in cell density-dependent ferroptosis. Interestingly, transcription levels of genes involved in LD breakdown like ATGL and MAGL and in FAO like CPT1A are enriched in HR+ breast cancer compared to TNBC (Monaco, 2017). Further, ACSL3 expression is enriched in HR+ breast cancer while ACSL4 expression marks TNBC (Monaco, 2017). In KRAS mutated non-small cell lung cancer cells (NSCLCs), ACSL3, activating long-chain FAs, has been shown to be required for β-oxidation and lipid storage of TAGs. Suppression of ACSL3 highly impaired tumorigenesis and led to cell death in NSCLC (Padanad et al., 2016). Together, these data further support the notion that T-47D, an HR+ breast cancer cell line, could be used to study mechanisms of cell density-dependent ferroptosis. Moreover, these data indicate that other ACSL isoforms might contribute to ferroptosis depending on the cellular context. However, the proposed switch to oxidative metabolism needs to be addressed in more detail as well. In this regard, a recent report suggested that in T-cells depending on the concentration employed, ETX could either inhibit β-oxidation or inhibit ATP generation during mitochondrial respiration through inhibition of adenine nucleotide translocase (ANT), thereby inducing an uncoupling of the electron transport chain (Raud et al., 2018). Therefore, genetic interference by overexpression or knockdown of CPT1A and measurement of β-oxidation, for example by Seahorse analysis, are required to provide further evidence of the proposed metabolic switch to FAO. Furthermore, analysis of global metabolic changes of cells seeded in different cell densities as well as during GPX4 inhibition/knockout using metabolomics, lipidomics as well as oxi-lipidomics will narrow down the mechanisms of cell density-dependent ferroptosis.

5.7 Concluding remarks

In this study, I elucidated the mechanisms of ferroptosis susceptibility in the context of human mammary epithelial cells. Initially, I was interested in determining whether ferroptosis could be employed to specifically target EMT-induced cells, previously shown to be chemotherapy-resistant (Ansieau et al., 2014; Nieto et al., 2016). Although the mesenchymal cell state has been connected to promote ferroptosis sensitivity in different cellular contexts (Viswanathan et al., 2017), I was not able to show that Twist1-induced mesenchymal HMLE cells are particularly sensitive to ferroptosis compared their epithelial counterparts. Instead, I discovered that cell

density plays a critical role in determining the sensitivity to ferroptosis in both immortalized and primary HMECs. Further, my data indicate that GPX4-inhibition in HMECs does not result in a consistent increase in lipid peroxidation. Therefore, ferroptosis induction is not directly linked to a global increase in lipid peroxidation in HMECs. To find potential candidates that contribute to cell density-dependent ferroptosis, I analyzed the proteome of HMLE and HMLE-Twist1 regulated by cell density and during GPX4-inhibition. The proteomic analysis provides several regulated proteins that might contribute to cell density-dependent ferroptosis whose exact role will be assessed in future studies. As one example, I identified ATGL as a potential hit that was further evaluated. Mechanistically, my data suggest that cell density-dependent vulnerability to ferroptosis depends on changes in lipid droplet metabolism that modulates lipid-mediated stress. Further, low cell density might induce a metabolic switch to fatty acid oxidation which is fueled by ATGL-liberated FAs. The proposed switch might potentially impact migratory and invasive behavior and might be elicited when tissue integrity is disturbed. Metastatic cells, at least in melanoma, have been shown to have increased oxidative stress which has to be limited at the distant site to enable metastatic outgrowth (Piskounova et al., 2015). Therefore, ferroptosis might be employed to target breast cancer cells during early stages of metastases as long as cells are present as single cells or small cluster clusters. However, the intrinsic property of mammary epithelial cells, i.e. being sensitive to ferroptosis at low cell density, has an important impact when considering ferroptosis as a treatment strategy in cancer treatment. Moreover, it will be interesting to determine whether ferroptosis has a physiological role in mammary gland development and function. For instance, ferroptosis might play a role during involution of the mammary gland after cessation of lactation. Interestingly, involution has been described to involve a lysosomal, non-apoptotic cell death triggered by OA liberated from TAGs (Magtanong et al., 2016). Further, it will be crucial to understand at the molecular level how cell density is sensed and how this sensing impacts LD metabolism and lipotoxicity. Therefore, on one hand, elucidating the molecular and genetic mechanisms of cell density-dependent ferroptosis in human mammary epithelial cells might yield fundamental insights into epithelial tissue function. On the other hand, a better understanding in the context of breast cancer will enable stratification of patient samples into sensitive and resistant tumors as the basis to translate mechanisms of ferroptosis sensitivity into therapeutic strategies.

6 References

van ’t Veer, L.J., Dai, H., van de Vijver, M.J., He, Y.D., Hart, A.A.M., Mao, M., Peterse, H.L., van der Kooy, K., Marton, M.J., Witteveen, A.T., et al. (2002). Gene expression profiling predicts clinical outcome of breast cancer. Nature *415*, 530–536.

Abe, O., Abe, R., Enomoto, K., Kikuchi, K., Koyama, H., Masuda, H., Nomura, Y., Ohashi, Y., Sakai, K., Sugimachi, K., et al. (2011). Relevance of breast cancer hormone receptors and other factors to the efficacy of adjuvant tamoxifen: Patient-level meta-analysis of randomised trials. Lancet *378*, 771–784.

Abercrombie, M. Contact inhibition in tissue culture. In Vitro *6*, 128–142.

Abeysinghe, R.D., Roberts, P.J., Cooper, C.E., MacLean, K.H., Hider, R.C., and Porter, J.B. (1996). The environment of the lipoxygenase iron binding site explored with novel hydroxypyridinone iron chelators. J. Biol. Chem. *271*, 7965–7972.

Aceto, N., Bardia, A., Miyamoto, D.T., Donaldson, M.C., Wittner, B.S., Spencer, J.A., Yu, M., Pely, A., Engstrom, A., Zhu, H., et al. (2014). Circulating tumor cell clusters are oligoclonal precursors of breast cancer metastasis. Cell *158*, 1110–1122.

Adedoyin, O., Boddu, R., Traylor, A., Lever, J.M., Bolisetty, S., George, J.F., and Agarwal, A. (2018). Heme oxygenase-1 mitigates ferroptosis in renal proximal tubule cells. Am. J. Physiol. Renal Physiol. *314*, F702–F714.

Agrawal, S. (2014). Late effects of cancer treatment in breast cancer survivors. South Asian J. Cancer *3*, 112–115.

Al-Hajj, M., Wicha, M.S., Benito-Hernandez, A., Morrison, S.J., and Clarke, M.F. (2003). Prospective identification of tumorigenic breast cancer cells. Proc. Natl. Acad. Sci. *100*, 3983–3988.

Allemani, C., Minicozzi, P., Berrino, F., Bastiaannet, E., Gavin, A., Galceran, J., Ameijide, A., Siesling, S., Mangone, L., Ardanaz, E., et al. (2013). Predictions of survival up to 10 years after diagnosis for European women with breast cancer in 2000-2002. Int. J. Cancer *132*, 2404–2412.

American Cancer Society (2017). Breast Cancer Facts & Figures 2017-2018. Atlanta Am. Cancer Soc. Inc 2017.

Ansari, I.H., Longacre, M.J., Stoker, S.W., Kendrick, M.A., O’Neill, L.M., Zitur, L.J., Fernandez, L.A., Ntambi, J.M., and MacDonald, M.J. (2017). Characterization of Acyl-CoA synthetase isoforms in pancreatic beta cells: Gene silencing shows participation of ACSL3 and ACSL4 in insulin secretion. Arch. Biochem. Biophys. *618*, 32–43.

Ansieau, S., Bastid, J., Doreau, A., Morel, A.P., Bouchet, B.P., Thomas, C., Fauvet, F., Puisieux, I., Doglioni, C., Piccinin, S., et al. (2008). Induction of EMT by Twist Proteins as a Collateral Effect of Tumor-Promoting Inactivation of Premature Senescence. Cancer Cell *14*, 79–89.

Ansieau, S., Collin, G., and Hill, L. (2014). EMT or EMT-Promoting Transcription Factors, Where to Focus the Light? Front. Oncol. *4*, 353.

Bailey, A.P., Koster, G., Guillermier, C., Hirst, E.M.A., MacRae, J.I., Lechene, C.P., Postle, A.D., and Gould, A.P. (2015). Antioxidant Role for Lipid Droplets in a Stem Cell Niche of Drosophila. Cell *163*, 340–353.

Bakondi, E., Gönczi, M., Szabó, É., Bai, P., Pacher, P., Gergely, P., Kovács, L., Hunyadi, J., Szabó, C., Csernoch, L., et al. (2003). Role of intracellular calcium mobilization and cell-density-dependent signaling in oxidative-stress-induced cytotoxicity in HaCaT

keratinocytes. J. Invest. Dermatol. *121*, 88–95.

Banjac, A., Perisic, T., Sato, H., Seiler, A., Bannai, S., Weiss, N., Kölle, P., Tschoep, K., Issels, R.D., Daniel, P.T., et al. (2008). The cystine/cysteine cycle: a redox cycle regulating susceptibility versus resistance to cell death. Oncogene *27*, 1618–1628.

Bannai, S. (1986). Exchange of cystine and glutamate across plasma membrane of human fibroblasts. J. Biol. Chem. *261*, 2256–2263.

Bannai, S., and Ishii, T. (1982). Transport of cystine and cysteine and cell growth in cultured human diploid fibroblasts: Effect of glutamate and homocysteate. J. Cell. Physiol. *112*, 265–272.

Bannai, S., and Tateishi, N. (1986). Role of membrane transport in metabolism and function of glutathione in mammals. J. Membr. Biol. *89*, 1–8.

Baranano, D.E., Rao, M., Ferris, C.D., and Snyder, S.H. (2002). Biliverdin reductase: A major physiologic cytoprotectant. Proc. Natl. Acad. Sci. *99*, 16093–16098.

Barradas, M.A., Jeremy, J.Y., Kontoghiorghes, G.J., Mikhailidis, D.P., Hoflbrand, A.V., and Dandona, P. (1989). Iron chelators inhibit human platelet aggregation, thromboxane A2 synthesis and lipoxygenase activity. FEBS Lett. *245*, 105–109.

Batlle, E., Sancho, E., Francí, C., Domínguez, D., Monfar, M., Baulida, J., and García De Herreros, A. (2000). The transcription factor snail is a repressor of E-cadherin gene expression in epithelial tumour cells. Nat. Cell Biol. *2*, 84–89.

Beck, B., Lapouge, G., Rorive, S., Drogat, B., Desaedelaere, K., Delafaille, S., Dubois, C., Salmon, I., Willekens, K., Marine, J.C., et al. (2015). Different levels of Twist1 regulate skin tumor initiation, stemness, and progression. Cell Stem Cell *16*, 67–79.

Beerling, E., Seinstra, D., de Wit, E., Kester, L., van der Velden, D., Maynard, C., Schäfer, R., van Diest, P., Voest, E., van Oudenaarden, A., et al. (2016). Plasticity between Epithelial and Mesenchymal States Unlinks EMT from Metastasis-Enhancing Stem Cell Capacity. Cell Rep. *14*, 2281–2288.

Belalcázar, A.D., Ball, J.G., Frost, L.M., Valentovic, M.A., and Wilkinson, J. (2014). Transsulfuration Is a Significant Source of Sulfur for Glutathione Production in Human Mammary Epithelial Cells. ISRN Biochem. *2013*, 637897.

Belkner, J., Wiesner, R., Rathman, J., Barnett, J., Sigal, E., and Kühn, H. (1993). Oxygenation of lipoproteins by mammalian lipoxygenases. Eur. J. Biochem. *213*, 251–261.

Bellinger, F.P., Bellinger, M.T., Seale, L.A., Takemoto, A.S., Raman, A. V., Miki, T., Manning-Boğ, A.B., Berry, M.J., White, L.R., and Ross, G.W. (2011). Glutathione peroxidase 4 is associated with neuromelanin in substantia nigra and dystrophic axons in putamen of Parkinson's brain. Mol. Neurodegener. *6*.

Berry, D.A., Cronin, K.A., Plevritis, S.K., Fryback, D.G., Clarke, L., Zelen, M., Mandelblatt, J.S., Yakovlev, A.Y., Habbema, J.D.F., Feuer, E.J., et al. (2005). Effect of screening and adjuvant therapy on mortality from breast cancer. N. Engl. J. Med. *353*, 1784–1792.

Bhowmik, S.K., Ramirez-Peña, E., Arnold, J.M., Putluri, V., Sphyris, N., Michailidis, G., Putluri, N., Ambs, S., Sreekumar, A., and Mani, S.A. (2015). EMT-induced metabolite signature identifies poor clinical outcome. Oncotarget *6*, 42651–42660.

Boulares, a H., Yakovlev, A.G., Ivanova, V., Stoica, B. a, Wang, G., Iyer, S., Smulson, M., and Chem, M.J.B. (1999). Role of Poly (ADP-ribose) Polymerase (PARP) Cleavage in Apoptosis. J. Biol. Chem. *274*, 22932–22940.

Bray, F., Ferlay, J., Soerjomataram, I., Siegel, R.L., Torre, L.A., and Jemal, A. (2018). Global cancer statistics 2018: GLOBOCAN estimates of incidence and mortality worldwide for 36 cancers in 185 countries. CA. Cancer J. Clin. *68*, 394–424.

Breunig, C.T., Durovic, T., Neuner, A.M., Baumann, V., Wiesbeck, M.F., Köferle, A., Götz, M., Ninkovic, J., and Stricker, S.H. (2018). One step generation of customizable gRNA vectors for multiplex CRISPR approaches through string assembly gRNA cloning (STAgR). PLoS One *13*, 1–12.

Brigelius-Flohé, R., and Maiorino, M. (2013). Glutathione peroxidases. Biochim. Biophys. Acta *1830*, 3289–3303.

Brown, C.W., Amante, J.J., Goel, H.L., and Mercurio, A.M. (2017). The α6β4 integrin promotes resistance to ferroptosis. J. Cell Biol. *216*, 4287–4297.

Brown, C.W., Amante, J.J., and Mercurio, A.M. (2018). Cell clustering mediated by the adhesion protein PVRL4 is necessary for 64 integrin–promoted ferroptosis resistance in matrix-detached cells. J. Biol. Chem. *293*, 12741–12748.

Brown, R.L., Reinke, L.M., Damerow, M.S., Perez, D., Chodosh, L.A., Yang, J., and Cheng, C. (2011). CD44 splice isoform switching in human and mouse epithelium is essential for epithelial-mesenchymal transition and breast cancer progression. J. Clin. Invest. *121*, 1064–1074.

Bryant, H.E., Schultz, N., Thomas, H.D., Parker, K.M., Flower, D., Lopez, E., Kyle, S., Meuth, M., Curtin, N.J., and Helleday, T. (2005). Specific killing of BRCA2-deficient tumours with inhibitors of poly(ADP-ribose) polymerase. Nature *434*, 913–917.

Bukholm, I.K., Nesland, J.M., and Børresen-Dale, A.L. (2000). Re-expression of E-cadherin, alpha-catenin and beta-catenin, but not of gamma-catenin, in metastatic tissue from breast cancer patients [seecomments]. J. Pathol. *190*, 15–19.

von Burstin, J., Eser, S., Paul, M.C., Seidler, B., Brandl, M., Messer, M., von Werder, A., Schmidt, A., Mages, J., Pagel, P., et al. (2009). E-Cadherin Regulates Metastasis of Pancreatic Cancer In Vivo and Is Suppressed by a SNAIL/HDAC1/HDAC2 Repressor Complex. Gastroenterology *137*, 361–371.e5.

Cano, A., Pérez-Moreno, M. a, Rodrigo, I., Locascio, A., Blanco, M.J., del Barrio, M.G., Portillo, F., and Nieto, M.A. (2000). The transcription factor snail controls epithelial-mesenchymal transitions by repressing E-cadherin expression. Nat. Cell Biol. *2*, 76–83.

Cao, J.Y., and Dixon, S.J. (2016). Mechanisms of ferroptosis. Cell. Mol. Life Sci. *73*, 2195–2209.

Carlson, B.A., Tobe, R., Yefremova, E., Tsuji, P.A., Hoffmann, V.J., Schweizer, U., Gladyshev, V.N., Hatfield, D.L., and Conrad, M. (2016). Glutathione peroxidase 4 and vitamin E cooperatively prevent hepatocellular degeneration. Redox Biol. *9*, 22–31.

Casas, E., Kim, J., Bendesky, A., Ohno-Machado, L., Wolfe, C.J., and Yang, J. (2011). Snail2 is an essential mediator of twist1-induced epithelial mesenchymal transition and metastasis. Cancer Res. *71*, 245–254.

Celià-Terrassa, T., Meca-Cortés, O., Mateo, F., Martínez de Paz, A., Rubio, N., Arnal-Estapé, A., Ell, B.J., Bermudo, R., Díaz, A., Guerra-Rebollo, M., et al. (2012). Epithelial-mesenchymal transition can suppress major attributes of human epithelial tumor-initiating cells. J. Clin. Invest. *122*, 1849–1868.

Chang, E.F., Wong, R.J., Vreman, H.J., Igarashi, T., Galo, E., Sharp, F.R., Stevenson, D.K., and Noble-Haeusslein, L.J. (2003). Heme oxygenase-2 protects against lipid peroxidation-mediated cell loss and impaired motor recovery after traumatic brain injury. J.

Neurosci. *23*, 3689–3696.

Chang, L.-C., Chiang, S.-K., Chen, S.-E., Yu, Y.-L., Chou, R.-H., and Chang, W.-C. (2018). Heme oxygenase-1 mediates BAY 11-7085 induced ferroptosis. Cancer Lett. *416*, 124–137.

Chartier, N.T. (2006). Laminin-5-integrin interaction signals through PI 3-kinase and Rac1b to promote assembly of adherens junctions in HT-29 cells. J. Cell Sci. *119*, 31–46.

Chen, J., Tu, Y., Connolly, E.C., and Ronnett, G. V (2005a). Heme oxygenase-2 protects against glutathione depletion-induced neuronal apoptosis mediated by bilirubin and cyclic GMP. Curr. Neurovasc. Res. *2*, 121–131.

Chen, L., Na, R., Gu, M., Richardson, A., and Ran, Q. (2008). Lipid peroxidation up-regulates BACE1 expression in vivo: a possible early event of amyloidogenesis in Alzheimer's disease. J. Neurochem. *107*, 197–207.

Chen, Z., Trotman, L.C., Shaffer, D., Lin, H.-K., Dotan, Z.A., Niki, M., Koutcher, J.A., Scher, H.I., Ludwig, T., Gerald, W., et al. (2005b). Crucial role of p53-dependent cellular senescence in suppression of Pten-deficient tumorigenesis. Nature *436*, 725–730.

Cheng, G.Z., Chan, J., Wang, Q., Zhang, W., Sun, C.D., and Wang, L.H. (2007). Twist transcriptionally up-regulates AKT2 in breast cancer cells leading to increased migration, invasion, and resistance to paclitaxel. Cancer Res. *67*, 1979–1987.

Cheung-Ong, K., Giaever, G., and Nislow, C. (2013). DNA-damaging agents in cancer chemotherapy: Serendipity and chemical biology. Chem. Biol. *20*, 648–659.

Côme, C., Magnino, F., Bibeau, F., De Barbara, P.S., Becker, K.F., Theillet, C., and Savagner, P. (2006). Snail and slug play distinct roles during breast carcinoma progression. Clin. Cancer Res. *12*, 5395–5402.

Comijn, J., Berx, G., Vermassen, P., Verschueren, K., van Grunsven, L., Bruyneel, E., Mareel, M., Huylebroeck, D., and van Roy, F. (2001). The two-handed E box binding zinc finger protein SIP1 downregulates E-cadherin and induces invasion. Mol. Cell *7*, 1267–1278.

Conrad, M., Angeli, J.P.F., Vandenabeele, P., and Stockwell, B.R. (2016). Regulated necrosis: disease relevance and therapeutic opportunities. Nat. Rev. Drug Discov. *15*, 348–366.

De Craene, B., and Berx, G. (2013). Regulatory networks defining EMT during cancer initiation and progression. Nat. Rev. Cancer *13*, 97–110.

Creighton, C.J., Li, X., Landis, M., Dixon, J.M., Neumeister, V.M., Sjolund, A., Rimm, D.L., Wong, H., Rodriguez, A., Herschkowitz, J.I., et al. (2009). Residual breast cancers after conventional therapy display mesenchymal as well as tumor-initiating features. Proc Natl Acad Sci U S A *106*, 13820–13825.

Curtis, C., Shah, S.P., Chin, S.F., Turashvili, G., Rueda, O.M., Dunning, M.J., Speed, D., Lynch, A.G., Samarajiwa, S., Yuan, Y., et al. (2012). The genomic and transcriptomic architecture of 2,000 breast tumours reveals novel subgroups. Nature *486*, 346–352.

Degterev, A., Huang, Z., Boyce, M., Li, Y., Jagtap, P., Mizushima, N., Cuny, G.D., Mitchison, T.J., Moskowitz, M.A., and Yuan, J. (2005). Chemical inhibitor of nonapoptotic cell death with therapeutic potential for ischemic brain injury. Nat. Chem. Biol. *1*, 112–119.

Deichmann, R., Lavie, C., and Andrews, S. (2010). Coenzyme q10 and statin-induced mitochondrial dysfunction. Ochsner J *10*, 16–21.

Dixon, S.J., Lemberg, K.M., Lamprecht, M.R., Skouta, R., Zaitsev, E.M., Gleason, C.E.,

Patel, D.N., Bauer, A.J., Cantley, A.M., Yang, W.S., et al. (2012). Ferroptosis: an iron-dependent form of nonapoptotic cell death. Cell *149*, 1060–1072.

Dixon, S.J., Patel, D., Welsch, M., Skouta, R., Lee, E., Hayano, M., Thomas, A.G., Gleason, C., Tatonetti, N., Slusher, B.S., et al. (2014). Pharmacological inhibition of cystine-glutamate exchange induces endoplasmic reticulum stress and ferroptosis. Elife *2014*, 1–25.

Dixon, S.J., Winter, G.E., Musavi, L.S., Lee, E.D., Snijder, B., Rebsamen, M., Superti-Furga, G., and Stockwell, B.R. (2015). Human Haploid Cell Genetics Reveals Roles for Lipid Metabolism Genes in Nonapoptotic Cell Death. ACS Chem. Biol. *10*, 1604–1609.

Dobrzyn, P., Dobrzyn, A., Miyazaki, M., Cohen, P., Asilmaz, E., Hardie, D.G., Friedman, J.M., and Ntambi, J.M. (2004). Stearoyl-CoA desaturase 1 deficiency increases fatty acid oxidation by activating AMP-activated protein kinase in liver. Proc. Natl. Acad. Sci. *101*, 6409–6414.

Doll, S., and Conrad, M. (2017). Iron and ferroptosis: A still ill-defined liaison. IUBMB Life *69*, 423–434.

Doll, S., Proneth, B., Tyurina, Y.Y., Panzilius, E., Kobayashi, S., Ingold, I., Irmler, M., Beckers, J., Aichler, M., Walch, A., et al. (2017). ACSL4 dictates ferroptosis sensitivity by shaping cellular lipid composition. Nat. Chem. Biol. *13*, 91–98.

Dolma, S., Lessnick, S.L., Hahn, W.C., and Stockwell, B.R. (2003). Identification of genotype-selective antitumor agents using synthetic lethal chemical screening in engineered human tumor cells. Cancer Cell *3*, 285–296.

Dong, C., Yuan, T., Wu, Y., Wang, Y., Fan, T.W.M., Miriyala, S., Lin, Y., Yao, J., Shi, J., Kang, T., et al. (2013). Loss of FBP1 by Snail-mediated repression provides metabolic advantages in basal-like breast cancer. Cancer Cell *23*, 316–331.

Doré, S., Takahashi, M., Ferris, C.D., Zakhary, R., Hester, L.D., Guastella, D., and Snyder, S.H. (1999). Bilirubin, formed by activation of heme oxygenase-2, protects neurons against oxidative stress injury. Proc. Natl. Acad. Sci. U. S. A. *96*, 2445–2450.

Drummen, G.P.C., Van Liebergen, L.C.M., Op den Kamp, J.A.F., and Post, J.A. (2002). C11-BODIPY581/591, an oxidation-sensitive fluorescent lipid peroxidation probe: (Micro)spectroscopic characterization and validation of methodology. Free Radic. Biol. Med. *33*, 473–490.

DuBridge, R.B., Tang, P., Hsia, H.C., Leong, P.M., Miller, J.H., and Calos, M.P. (1987). Analysis of mutation in human cells by using an Epstein-Barr virus shuttle system. Mol. Cell. Biol. *7*, 379–387.

Dunn, L.L., Midwinter, R.G., Ni, J., Hamid, H.A., Parish, C.R., and Stocker, R. (2014). New Insights into Intracellular Locations and Functions of Heme Oxygenase-1. Antioxid. Redox Signal. *20*, 1723–1742.

Easton, D.F., Ford, D., and Bishop, D.T. (1995). Breast and ovarian cancer incidence in BRCA1-mutation carriers. Breast Cancer Linkage Consortium. Am. J. Hum. Genet. *56*, 265–271.

Elenbaas, B., Spirio, L., Koerner, F., Fleming, M.D., Zimonjic, D.B., Donaher, J.L., Popescu, N.C., Hahn, W.C., and Weinberg, R.A. (2001). Human breast cancer cells generated by oncogenic transformation of primary mammary epithelial cells. Genes Dev. *15*, 50–65.

Ellsworth, R.E., Toro, A.L., Blackburn, H.L., Decewicz, A., Mamula, K. a, Costantino, N.S., Hooke, J. a, Shriver, C.D., and Ellsworth, D.L. (2015). Molecular Heterogeneity in Primary

Breast Carcinomas and Axillary Lymph Node Metastases Assessed by Genomic Fingerprinting Analysis. 15–24.

Falk, M.H., Bornkamm, G.W., Hültner, L., Milner, A., and Gregory, C.D. (1993). Irradiated fibroblasts protect burkitt lymphoma cells from apoptosis by a mechanism independent of BCL-2. Int. J. Cancer *55*, 485–491.

Falk, M.H., Meier, T., Issels, R.D., Brielmeier, M., Scheffer, B., and Bornkamm, G.W. (1998). Apoptosis in Burkitt lymphoma cells is prevented by promotion of cysteine uptake. Int. J. Cancer *75*, 620–625.

Farmer, H., McCabe, N., Lord, C.J., Tutt, A.N.J., Johnson, D.A., Richardson, T.B., Santarosa, M., Dillon, K.J., Hickson, I., Knights, C., et al. (2005). Targeting the DNA repair defect in BRCA mutant cells as a therapeutic strategy. Nature *434*, 917–921.

Fernandes-Alnemri, T., Litwack, G., and Alnemri, E.S. (1994). CPP32, a novel human apoptotic protein with homology to Caenorhabditis elegans cell death protein Ced-3 and mammalian interleukin-1 beta-converting enzyme. J. Biol. Chem. *269*, 30761–30764.

Fischer, K.R., Durrans, A., Lee, S., Sheng, J., Li, F., Wong, S.T.C., Choi, H., El Rayes, T., Ryu, S., Troeger, J., et al. (2015). Epithelial-to-mesenchymal transition is not required for lung metastasis but contributes to chemoresistance. Nature *527*, 472–476.

Ford, D., Easton, D.F., Stratton, M., Narod, S., Goldgar, D., Devilee, P., Bishop, D.T., Weber, B., Lenoir, G., Chang-Claude, J., et al. (1998). Genetic heterogeneity and penetrance analysis of the BRCA1 and BRCA2 genes in breast cancer families. The Breast Cancer Linkage Consortium. Am. J. Hum. Genet. *62*, 676–689.

Fornari, F.A., Randolph, J.K., Yalowich, J.C., Ritke, M.K., and Gewirtz, D.A. (1994). Interference by doxorubicin with DNA unwinding in MCF-7 breast tumor cells. Mol. Pharmacol. *45*, 649–656.

Friedmann Angeli, J.P., Schneider, M., Proneth, B., Tyurina, Y.Y., Tyurin, V. a, Hammond, V.J., Herbach, N., Aichler, M., Walch, A., Eggenhofer, E., et al. (2014). Inactivation of the ferroptosis regulator Gpx4 triggers acute renal failure in mice. Nat. Cell Biol. *16*, 1180–1191.

Frisch, S.M., and Francis, H. (1994). Disruption of epithelial cell-matrix interactions induces apoptosis. J. Cell Biol. *124*, 619–626.

Ganz, A., Lambert, M., Saez, A., Silberzan, P., Buguin, A., Mège, R.M., and Ladoux, B. (2006). Traction forces exerted through N-cadherin contacts. Biol. Cell *98*, 721–730.

Gao, M., Monian, P., Quadri, N., Ramasamy, R., and Jiang, X. (2015). Glutaminolysis and Transferrin Regulate Ferroptosis. Mol. Cell *59*, 298–308.

Gao, M., Monian, P., Pan, Q., Zhang, W., Xiang, J., and Jiang, X. (2016). Ferroptosis is an autophagic cell death process. Cell Res. *26*, 1021–1032.

Gascón, S., Murenu, E., Masserdotti, G., Ortega, F., Russo, G.L., Petrik, D., Deshpande, A., Heinrich, C., Karow, M., Robertson, S.P., et al. (2016). Identification and Successful Negotiation of a Metabolic Checkpoint in Direct Neuronal Reprogramming. Cell Stem Cell *18*, 396–409.

Goo, Y.H., Son, S.H., and Paul, A. (2017). Lipid droplet-associated hydrolase promotes lipid droplet fusion and enhances ATGL degradation and triglyceride accumulation. Sci. Rep. *7*, 1–13.

Graff, J.R., Gabrielson, E., Fujii, H., Baylin, S.B., and Herman, J.G. (2000). Methylation patterns of the E-cadherin 5' CpG island are unstable and reflect the dynamic,

heterogeneous loss of E-cadherin expression during metastatic progression. J. Biol. Chem. *275*, 2727–2732.

Greenberg, P.A., Hortobagyi, G.N., Smith, T.L., Ziegler, L.D., Frye, D.K., and Buzdar, A.U. (1996). Long-term follow-up of patients with complete remission following combination chemotherapy for metastatic breast cancer. J. Clin. Oncol. *14*, 2197–2205.

Grosche, A., Hauser, A., Lepper, M.F., Mayo, R., von Toerne, C., Merl-Pham, J., and Hauck, S.M. (2016). The Proteome of Native Adult Müller Glial Cells From Murine Retina. Mol. Cell. Proteomics *15*, 462–480.

Grzegrzolka, J., Biala, M., Wojtyra, P., Kobierzycki, C., Olbromski, M., Gomulkiewicz, A., Piotrowska, A., Rys, J., Podhorska-Okolow, M., and Dziegiel, P. (2015). Expression of EMT Markers SLUG and TWIST in Breast Cancer. Anticancer Res. *35*, 3961–3968.

Guarneri, V., Broglio, K., Kau, S.-W., Cristofanilli, M., Buzdar, A.U., Valero, V., Buchholz, T., Meric, F., Middleton, L., Hortobagyi, G.N., et al. (2006). Prognostic value of pathologic complete response after primary chemotherapy in relation to hormone receptor status and other factors. J. Clin. Oncol. *24*, 1037–1044.

Guha, M., Srinivasan, S., Ruthel, G., Kashina, A.K., Carstens, R.P., Mendoza, A., Khanna, C., Van Winkle, T., and Avadhani, N.G. (2014). Mitochondrial retrograde signaling induces epithelial-mesenchymal transition and generates breast cancer stem cells. Oncogene *33*, 5238–5250.

Haemmerle, G., Moustafa, T., Woelkart, G., Büttner, S., Schmidt, A., van de Weijer, T., Hesselink, M., Jaeger, D., Kienesberger, P.C., Zierler, K., et al. (2011). ATGL-mediated fat catabolism regulates cardiac mitochondrial function via PPAR-α and PGC-1. Nat. Med. *17*, 1076–1085.

Hahn, W.C., Counter, C.M., Lundberg, A.S., Beijersbergen, R.L., Brooks, M.W., and Weinberg, R.A. (1999). Creation of human tumour cells with defined genetic elements. Nature *400*, 464–468.

Hajra, K.M., Chen, D.Y.-S., and Fearon, E.R. (2002). The SLUG zinc-finger protein represses E-cadherin in breast cancer. Cancer Res. *62*, 1613–1618.

Hanahan, D., and Weinberg, R.A. (2011). Hallmarks of cancer: the next generation. Cell *144*, 646–674.

Hao, S., Liang, B., Huang, Q., Dong, S., Wu, Z., He, W., and Shi, M. (2018). Metabolic networks in ferroptosis (Review). Oncol. Lett. *15*, 5405–5411.

Hassannia, B., Vandenabeele, P., and Vanden Berghe, T. (2018). Nano-targeted induction of dual ferroptotic mechanisms eradicates high-risk neuroblastoma Graphical abstract The Journal of Clinical Investigation. J Clin Invest *128*, 3341–3355.

Hay, E.D. (1968). Organization and fine structure of epithelium and mesenchyme in the developing chick embryo. Proceedings of the 18th Hahnemann Symposium: 31-55.

Hay, E.D. (1995). An overview of epithelio-mesenchymal transformation. Acta Anat. (Basel). *154*, 8–20.

Hayano, M., Yang, W.S., Corn, C.K., Pagano, N.C., and Stockwell, B.R. (2016). Loss of cysteinyl-tRNA synthetase (CARS) induces the transsulfuration pathway and inhibits ferroptosis induced by cystine deprivation. Cell Death Differ. *23*, 270–278.

Herms, A., Bosch, M., Ariotti, N., Reddy, B.J.N., Fajardo, A., Fernández-Vidal, A., Alvarez-Guaita, A., Fernández-Rojo, M.A., Rentero, C., Tebar, F., et al. (2013). Cell-to-cell heterogeneity in lipid droplets suggests a mechanism to reduce lipotoxicity. Curr. Biol. *23*,

1489–1496.

Hernandez, L., Wilkerson, P.M., Lambros, M.B., Campion-Flora, A., Rodrigues, D.N., Gauthier, A., Cabral, C., Pawar, V., Mackay, A., A'Hern, R., et al. (2012). Genomic and mutational profiling of ductal carcinomas in situ and matched adjacent invasive breast cancers reveals intra-tumour genetic heterogeneity and clonal selection. J. Pathol. *227*, 42–52.

Herschkowitz, J.I., Simin, K., Weigman, V.J., Mikaelian, I., Usary, J., Hu, Z., Rasmussen, K.E., Jones, L.P., Assefnia, S., Chandrasekharan, S., et al. (2007). Identification of conserved gene expression features between murine mammary carcinoma models and human breast tumors. Genome Biol. *8*, R76.

Heselmeyer-Haddad, K., Berroa Garcia, L.Y., Bradley, A., Ortiz-Melendez, C., Lee, W.J., Christensen, R., Prindiville, S.A., Calzone, K.A., Soballe, P.W., Hu, Y., et al. (2012). Single-cell genetic analysis of ductal carcinoma in situ and invasive breast cancer reveals enormous tumor heterogeneity yet conserved genomic imbalances and gain of MYC during progression. Am. J. Pathol. *181*, 1807–1822.

Hofer, A.M., Gerbino, A., Caroppo, R., and Curci, S. (2004). The extracellular calcium-sensing receptor and cell-cell signaling in epithelia. Cell Calcium *35*, 297–306.

Van Horn, C.G., Caviglia, J.M., Li, L.O., Wang, S., Granger, D.A., and Coleman, R.A. (2005). Characterization of recombinant long-chain rat Acyl-CoA synthetase isoforms 3 and 6: Identification of a novel variant of isoform 6. Biochemistry *44*, 1635–1642.

Hou, W., Xie, Y., Song, X., Sun, X., Lotze, M.T., Zeh, H.J., Kang, R., and Tang, D. (2016). Autophagy promotes ferroptosis by degradation of ferritin. Autophagy *12*, 1425–1428.

Hu, Z., Fan, C., Oh, D.S., Marron, J.S., He, X., Qaqish, B.F., Livasy, C., Carey, L.A., Reynolds, E., Dressler, L., et al. (2006). The molecular portraits of breast tumors are conserved across microarray platforms. BMC Genomics *7*, 96.

Huang, D.W., Sherman, B.T., and Lempicki, R.A. (2009b). Bioinformatics enrichment tools: Paths toward the comprehensive functional analysis of large gene lists. Nucleic Acids Res. *37*, 1–13.

Huang, D.W., Sherman, B.T., and Lempicki, R.A. (2009a). Systematic and integrative analysis of large gene lists using DAVID bioinformatics resources. Nat. Protoc. *4*, 44–57.

Hyun, T., Yam, A., Pece, S., Xie, X., Zhang, J., Miki, T., Gutkind, J.S., and Li, W. (2000). Loss of PTEN expression leading to high Akt activation in human multiple myelomas. Blood *96*, 3560–3568.

Ikenouchi, J., Matsuda, M., Furuse, M., and Tsukita, S. (2003). Regulation of tight junctions during the epithelium-mesenchyme transition: direct repression of the gene expression of claudins/occludin by Snail. J. Cell Sci. *116*, 1959–1967.

Imai, H., Hirao, F., Sakamoto, T., Sekine, K., Mizukura, Y., Saito, M., Kitamoto, T., Hayasaka, M., Hanaoka, K., and Nakagawa, Y. (2003). Early embryonic lethality caused by targeted disruption of the mouse PHGPx gene. Biochem. Biophys. Res. Commun. *305*, 278–286.

Ince, T.A., Richardson, A.L., Bell, G.W., Saitoh, M., Godar, S., Karnoub, A.E., Iglehart, J.D., and Weinberg, R. a (2007). Transformation of different human breast epithelial cell types leads to distinct tumor phenotypes. Cancer Cell *12*, 160–170.

Ishii, T., Sugita, Y., and Bannai, S. (1987). Regulation of glutathione levels in mouse spleen lymphocytes by transport of cysteine. J. Cell. Physiol. *133*, 330–336.

Ishimoto, T., Nagano, O., Yae, T., Tamada, M., Motohara, T., Oshima, H., Oshima, M., Ikeda, T., Asaba, R., Yagi, H., et al. (2011). CD44 variant regulates redox status in cancer cells by stabilizing the xCT subunit of system xc(-) and thereby promotes tumor growth. Cancer Cell *19*, 387–400.

Jaramillo, M.C., and Zhang, D.D. (2013). The emerging role of the Nrf2-Keap1 signaling pathway in cancer. Genes Dev. *27*, 2179–2191.

Jarc, E., Kump, A., Malavašič, P., Eichmann, T.O., Zimmermann, R., and Petan, T. (2018). Lipid droplets induced by secreted phospholipase A2and unsaturated fatty acids protect breast cancer cells from nutrient and lipotoxic stress. Biochim. Biophys. Acta - Mol. Cell Biol. Lipids *1863*, 247–265.

Jeschke, U., Mylonas, I., Kuhn, C., Shabani, N., Kunert-Keil, C., Schindlbeck, C., Gerber, B., and Friese, K. (2007). Expression of E-cadherin in human ductal breast cancer carcinoma in situ, invasive carcinomas, their lymph node metastases, their distant metastases, carcinomas with recurrence and in recurrence. Anticancer Res. *27*, 1969–1974.

Jiang, L., Kon, N., Li, T., Wang, S.J., Su, T., Hibshoosh, H., Baer, R., and Gu, W. (2015). Ferroptosis as a p53-mediated activity during tumour suppression. Nature *520*, 57–62.

Jones, N., Bonnet, F., Sfar, S., Lafitte, M., Lafon, D., Sierankowski, G., Brouste, V., Banneau, G., Tunon de Lara, C., Debled, M., et al. (2013). Comprehensive analysis of PTEN status in breast carcinomas. Int. J. Cancer *133*, 323–334.

Kagan, V.E., Mao, G., Qu, F., Angeli, J.P.F., Doll, S., Croix, C.S., Dar, H.H., Liu, B., Tyurin, V.A., Ritov, V.B., et al. (2017). Oxidized arachidonic and adrenic PEs navigate cells to ferroptosis. Nat. Chem. Biol. *13*, 81–90.

Kajita, M., McClinic, K.N., and Wade, P.A. (2004). Aberrant expression of the transcription factors snail and slug alters the response to genotoxic stress. Mol. Cell. Biol. *24*, 7559–7566.

Kalluri, R., and Weinberg, R.A. (2009). The basics of epithelial-mesenchymal transition. J. Clin. Invest. *119*, 1420–1428.

Kaushik, S., and Cuervo, A.M. (2015). Degradation of lipid droplet-associated proteins by chaperone-mediated autophagy facilitates lipolysis. Nat. Cell Biol. *17*, 759.

Kayl, A.E., and Meyers, C.A. (2006). Side-effects of chemotherapy and quality of life in ovarian and breast cancer patients. Curr. Opin. Obstet. Gynecol. *18*, 24–28.

Khor, V.K., Shen, W.-J., and Kraemer, F.B. (2013). Lipid droplet metabolism. Curr. Opin. Clin. Nutr. Metab. Care *16*, 632–637.

Kim, J.H., Lewin, T.M., and Coleman, R.A. (2001). Expression and characterization of recombinant rat acyl-CoA synthetases 1, 4, and 5: Selective inhibition by triacsin C and thiazolidinediones. J. Biol. Chem. *276*, 24667–24673.

Koboldt, D.C., Fulton, R.S., McLellan, M.D., Schmidt, H., Kalicki-Veizer, J., McMichael, J.F., Fulton, L.L., Dooling, D.J., Ding, L., Mardis, E.R., et al. (2012). Comprehensive molecular portraits of human breast tumours. Nature *490*, 61–70.

Kowalski, P.J., Rubin, M. a, and Kleer, C.G. (2003). E-cadherin expression in primary carcinomas of the breast and its distant metastases. Breast Cancer Res. *5*, 217–222.

Kryukov, G. V, Castellano, S., Novoselov, S. V, Lobanov, A. V, Zehtab, O., Guigó, R., and Gladyshev, V.N. (2003). Characterization of mammalian selenoproteomes. Science *300*, 1439–1443.

Kuhn, H., Banthiya, S., and van Leyen, K. (2015). Mammalian lipoxygenases and their biological relevance. Biochim. Biophys. Acta *1851*, 308–330.

Kurrey, N.K., Jalgaonkar, S.P., Joglekar, A. V., Ghanate, A.D., Chaskar, P.D., Doiphode, R.Y., and Bapat, S.A. (2009). Snail and slug mediate radioresistance and chemoresistance by antagonizing p53-mediated apoptosis and acquiring a stem-like phenotype in ovarian cancer cells. Stem Cells *27*, 2059–2068.

Kurz, T., Leake, A., Von Zglinicki, T., and Brunk, U.T. (2004). Relocalized redox-active lysosomal iron is an important mediator of oxidative-stress-induced DNA damage. Biochem. J. *378*, 1039–1045.

Kwon, M.-Y., Park, E., Lee, S.-J., and Chung, S.W. (2015). Heme oxygenase-1 accelerates erastin-induced ferroptotic cell death. Oncotarget *6*.

Lachaier, E., Louandre, C., Godin, C., Saidak, Z., Baert, M., Diouf, M., Chauffert, B., and Galmiche, A. (2014). Sorafenib induces ferroptosis in human cancer cell lines originating from different solid tumors. Anticancer Res. *34*, 6417–6422.

LeBleu, V.S., O'Connell, J.T., Gonzalez Herrera, K.N., Wikman, H., Pantel, K., Haigis, M.C., de Carvalho, F.M., Damascena, A., Domingos Chinen, L.T., Rocha, R.M., et al. (2014). PGC-1α mediates mitochondrial biogenesis and oxidative phosphorylation in cancer cells to promote metastasis. Nat. Cell Biol. *16*, 992–1003, 1–15.

Lee, J.H., Kong, J., Jang, J.Y., Han, J.S., Ji, Y., Lee, J., and Kim, J.B. (2014). Lipid Droplet Protein LID-1 Mediates ATGL-1-Dependent Lipolysis during Fasting in Caenorhabditis elegans. Mol. Cell. Biol. *34*, 4165–4176.

Lehmann, B.D., Jovanović, B., Chen, X., Estrada, M. V., Johnson, K.N., Shyr, Y., Moses, H.L., Sanders, M.E., and Pietenpol, J.A. (2016). Refinement of Triple-Negative Breast Cancer Molecular Subtypes: Implications for Neoadjuvant Chemotherapy Selection. PLoS One *11*, e0157368.

Lehmann, B.D.B., Bauer, J. a J., Chen, X., Sanders, M.E., Chakravarthy, A.B., Shyr, Y., Pietenpol, J.A., Pegram, M., Wiggans, R., Carey, L., et al. (2011). Identification of human triple-negative breast cancer subtypes and preclinical models for selection of targeted therapies. J. Clin. Invest. *121*, 2750–2767.

Lehmann, J.M., Moore, L.B., Smith-Oliver, T.A., Wilkison, W.O., Willson, T.M., and Kliewer, S.A. (1995). An antidiabetic thiazolidinedione is a high affinity ligand for peroxisome proliferator-activated receptor gamma (PPAR gamma). J. Biol. Chem. *270*, 12953–12956.

van Leyen, K., Duvoisin, R.M., Engelhardt, H., and Wiedmann, M. (1998). A function for lipoxygenase in programmed organelle degradation. Nature *395*, 392–395.

Li, J., Yen, C., Liaw, D., Podsypanina, K., Bose, S., Wang, S.I., Puc, J., Miliaresis, C., Rodgers, L., McCombie, R., et al. (1997). PTEN, a putative protein tyrosine phosphatase gene mutated in human brain, breast, and prostate cancer. Science *275*, 1943–1947.

Li, Q.Q., Xu, J. Da, Wang, W.J., Cao, X.X., Chen, Q., Tang, F., Chen, Z.Q., Liu, X.P., and Xu, Z. De (2009). Twist1-mediated adriamycin-induced epithelial-mesenchymal transition relates to multidrug resistance and invasive potential in breast cancer cells. Clin. Cancer Res. *15*, 2657–2665.

Liedtke, C., Mazouni, C., Hess, K.R., André, F., Tordai, A., Mejia, J.A., Symmans, W.F., Gonzalez-Angulo, A.M., Hennessy, B., Green, M., et al. (2008). Response to neoadjuvant therapy and long-term survival in patients with triple-negative breast cancer. J. Clin. Oncol. *26*, 1275–1281.

Limoli, C.L. (2004). Cell-density-dependent regulation of neural precursor cell function. Proc. Natl. Acad. Sci. *101*, 16052–16057.

Lin, N.U., Vanderplas, A., Hughes, M.E., Theriault, R.L., Edge, S.B., Wong, Y.-N., Blayney, D.W., Niland, J.C., Winer, E.P., and Weeks, J.C. (2012). Clinicopathologic features, patterns of recurrence, and survival among women with triple-negative breast cancer in the National Comprehensive Cancer Network. Cancer *118*, 5463–5472.

Linkermann, A., Skouta, R., Himmerkus, N., Mulay, S.R., Dewitz, C., De Zen, F., Prokai, A., Zuchtriegel, G., Krombach, F., Welz, P.-S., et al. (2014). Synchronized renal tubular cell death involves ferroptosis. Proc. Natl. Acad. Sci. *111*, 16836–16841.

Linnemann, J.R., Miura, H., Meixner, L.K., Irmler, M., Kloos, U.J., Hirschi, B., Bartsch, H.S., Sass, S., Beckers, J., Theis, F.J., et al. (2015). Quantification of regenerative potential in primary human mammary epithelial cells. Development *142*, 3239–3251.

Listenberger, L.L., Han, X., Lewis, S.E., Cases, S., Farese, R. V, Ory, D.S., and Schaffer, J.E. (2003). Triglyceride accumulation protects against fatty acid-induced lipotoxicity. Proc. Natl. Acad. Sci. U. S. A. *100*, 3077–3082.

Liu, Y., Sánchez-Tilló, E., Lu, X., Huang, L., Clem, B., Telang, S., Jenson, A.B., Cuatrecasas, M., Chesney, J., Postigo, A., et al. (2013). Sequential inductions of the ZEB1 transcription factor caused by mutation of Rb and then Ras proteins are required for tumor initiation and progression. J. Biol. Chem. *288*, 11572–11580.

Livak, K.J., and Schmittgen, T.D. (2001). Analysis of relative gene expression data using real-time quantitative PCR and the 2(-Delta Delta C(T)) Method. Methods *25*, 402–408.

Lomax, M.E., Folkes, L.K., and O'Neill, P. (2013). Biological consequences of radiation-induced DNA damage: Relevance to radiotherapy. Clin. Oncol. *25*, 578–585.

Louandre, C., Ezzoukhry, Z., Godin, C., Barbare, J.C., Mazière, J.C., Chauffert, B., and Galmiche, A. (2013). Iron-dependent cell death of hepatocellular carcinoma cells exposed to sorafenib. Int. J. Cancer *133*, 1732–1742.

Lowry, O.H., Rosebrough, N.J., Farr, A.L., and Randall, R.J. (1951). Protein measurement with the Folin phenol reagent. J. Biol. Chem. *193*, 265–275.

Magtanong, L., Ko, P.J., and Dixon, S.J. (2016). Emerging roles for lipids in non-apoptotic cell death. Cell Death Differ. *23*, 1099.

Maiorino, M., Roveri, A., Benazzi, L., Bosello, V., Mauri, P., Toppo, S., Tosatto, S.C.E., and Ursini, F. (2005). Functional interaction of phospholipid hydroperoxide glutathione peroxidase with sperm mitochondrion-associated cysteine-rich protein discloses the adjacent cysteine motif as a new substrate of the selenoperoxidase. J. Biol. Chem. *280*, 38395–38402.

Mandal, P.K., Seiler, A., Perisic, T., Kölle, P., Banjac Canak, A., Förster, H., Weiss, N., Kremmer, E., Lieberman, M.W., Bannai, S., et al. (2010). System x(c)- and thioredoxin reductase 1 cooperatively rescue glutathione deficiency. J. Biol. Chem. *285*, 22244–22253.

Mani, S. a, Guo, W., Liao, M.-J., Eaton, E.N., Ayyanan, A., Zhou, A.Y., Brooks, M., Reinhard, F., Zhang, C.C., Shipitsin, M., et al. (2008). The epithelial-mesenchymal transition generates cells with properties of stem cells. Cell *133*, 704–715.

Mani, S.A., Yang, J., Brooks, M., Schwaninger, G., Zhou, A., Miura, N., Kutok, J.L., Hartwell, K., Richardson, A.L., and Weinberg, R.A. (2007). Mesenchyme Forkhead 1 (FOXC2) plays a key role in metastasis and is associated with aggressive basal-like breast cancers. Proc. Natl. Acad. Sci. *104*, 10069–10074.

Martínez-Estrada, O.M., Cullerés, A., Soriano, F.X., Peinado, H., Bolós, V., Martínez, F.O., Reina, M., Cano, A., Fabre, M., and Vilaró, S. (2006). The transcription factors Slug and Snail act as repressors of Claudin-1 expression in epithelial cells. Biochem. J. *394*, 449–457.

Masaldan, S., Clatworthy, S.A.S., Gamell, C., Meggyesy, P.M., Rigopoulos, A., Haupt, S., Haupt, Y., Denoyer, D., Adlard, P.A., Bush, A.I., et al. (2018). Iron accumulation in senescent cells is coupled with impaired ferritinophagy and inhibition of ferroptosis. Redox Biol. *14*, 100–115.

Masin, M., Vazquez, J., Rossi, S., Groeneveld, S., Samson, N., Schwalie, P.C., Deplancke, B., Frawley, L.E., Gouttenoire, J., Moradpour, D., et al. (2014). GLUT3 is induced during epithelial-mesenchymal transition and promotes tumor cell proliferation in non-small cell lung cancer. Cancer Metab. *2*, 11.

Matsushita, M., Freigang, S., Schneider, C., Conrad, M., Bornkamm, G.W., and Kopf, M. (2015). T cell lipid peroxidation induces ferroptosis and prevents immunity to infection. J. Exp. Med. *212*, 555–568.

Mauri, D., Pavlidis, N., and Ioannidis, J.P.A. (2005). Neoadjuvant versus adjuvant systemic treatment in breast cancer: A meta-analysis. J. Natl. Cancer Inst. *97*, 188–194.

McCubrey, J.A., Steelman, L.S., Chappell, W.H., Abrams, S.L., Wong, E.W.T., Chang, F., Lehmann, B., Terrian, D.M., Milella, M., Tafuri, A., et al. (2007). Roles of the Raf/MEK/ERK pathway in cell growth, malignant transformation and drug resistance. Biochim. Biophys. Acta *1773*, 1263–1284.

Mejlvang, J., Kriajevska, M., Vandewalle, C., Chernova, T., Sayan, A.E., Berx, G., Mellon, J.K., and Tulchinsky, E. (2007). Direct repression of cyclin D1 by SIP1 attenuates cell cycle progression in cells undergoing an epithelial mesenchymal transition. Mol. Biol. Cell *18*, 4615–4624.

Ménard, S., Pupa, S.M., Campiglio, M., and Tagliabue, E. (2003). Biologic and therapeutic role of HER2 in cancer. Oncogene *22*, 6570–6578.

Miess, H., Dankworth, B., Gouw, A.M., Rosenfeldt, M., Schmitz, W., Jiang, M., Saunders, B., Howell, M., Downward, J., Felsher, D.W., et al. (2018). The glutathione redox system is essential to prevent ferroptosis caused by impaired lipid metabolism in clear cell renal cell carcinoma. Oncogene 1–16.

Mihaylova, M.M., and Shaw, R.J. (2011). The AMPK signalling pathway coordinates cell growth, autophagy and metabolism. Nat. Cell Biol. *13*, 1016–1023.

Monaco, M.E. (2017). Fatty acid metabolism in breast cancer subtypes. Oncotarget *8*, 29487–29500.

Moody, S.E., Perez, D., Pan, T.C., Sarkisian, C.J., Portocarrero, C.P., Sterner, C.J., Notorfrancesco, K.L., Cardiff, R.D., and Chodosh, L.A. (2005). The transcriptional repressor Snail promotes mammary tumor recurrence. Cancer Cell *8*, 197–209.

Morel, A.-P., Lièvre, M., Thomas, C., Hinkal, G., Ansieau, S., and Puisieux, A. (2008). Generation of breast cancer stem cells through epithelial-mesenchymal transition. PLoS One *3*, e2888.

Morel, A.P., Hinkal, G.W., Thomas, C., Fauvet, F., Courtois-Cox, S., Wierinckx, A., Devouassoux-Shisheboran, M., Treilleux, I., Tissier, A., Gras, B., et al. (2012). EMT inducers catalyze malignant transformation of mammary epithelial cells and drive tumorigenesis towards claudin-low tumors in transgenic mice. PLoS Genet. *8*.

Moreno-Bueno, G., Cubillo, E., Sarrió, D., Peinado, H., Rodríguez-Pinilla, S.M., Villa, S.,

Bolós, V., Jordá, M., Fabra, A., Portillo, F., et al. (2006). Genetic profiling of epithelial cells expressing E-cadherin repressors reveals a distinct role for snail, Slug, and E47 Factors in epithelial- mesenchymal transition. Cancer Res. *66*, 9543–9556.

Muckenthaler, M.U., Rivella, S., Hentze, M.W., and Galy, B. (2017). A Red Carpet for Iron Metabolism. Cell *168*, 344–361.

Muenst, S., Däster, S., Obermann, E.C., Droeser, R.A., Weber, W.P., Von Holzen, U., Gao, F., Viehl, C., Oertli, D., and Soysal, S.D. (2013). Nuclear expression of snail is an independent negative prognostic factor in human breast cancer. Dis. Markers *35*, 337–344.

Nass, S.J., Herman, J.G., Gabrielson, E., Iversen, P.W., Parl, F.F., Davidson, N.E., and Graff, J.R. (2000). Aberrant methylation of the estrogen receptor and E-cadherin 5′ CpG islands increases with malignant progression in human breast cancer. Cancer Res. *60*, 4346–4348.

Navin, N., Krasnitz, A., Rodgers, L., Cook, K., Meth, J., Kendall, J., Riggs, M., Eberling, Y., Troge, J., Grubor, V., et al. (2010). Inferring tumor progression from genomic heterogeneity. Genome Res. *20*, 68–80.

Navin, N., Kendall, J., Troge, J., Andrews, P., Rodgers, L., McIndoo, J., Cook, K., Stepansky, A., Levy, D., Esposito, D., et al. (2011). Tumour evolution inferred by single-cell sequencing. Nature *472*, 90–95.

Van Nes, J.G.H., De Kruijf, E.M., Putter, H., Faratian, D., Munro, A., Campbell, F., Smit, V.T.H.B.M., Liefers, G.J., Kuppen, P.J.K., Van De Velde, C.J.H., et al. (2012). Co-expression of SNAIL and TWIST determines prognosis in estrogen receptor-positive early breast cancer patients. Breast Cancer Res. Treat. *133*, 49–59.

Neshat, M.S., Mellinghoff, I.K., Tran, C., Stiles, B., Thomas, G., Petersen, R., Frost, P., Gibbons, J.J., Wu, H., and Sawyers, C.L. (2001). Enhanced sensitivity of PTEN-deficient tumors to inhibition of FRAP/mTOR. Proc. Natl. Acad. Sci. *98*, 10314–10319.

Ng, C.K.Y., Bidard, F.-C., Piscuoglio, S., Geyer, F.C., Lim, R.S., de Bruijn, I., Shen, R., Pareja, F., Berman, S.H., Wang, L., et al. (2017). Genetic Heterogeneity in Therapy-Naïve Synchronous Primary Breast Cancers and Their Metastases. Clin. Cancer Res. *23*, 4402–4415.

Nguyen, T.B., Louie, S.M., Daniele, J.R., Tran, Q., Dillin, A., Zoncu, R., Nomura, D.K., and Olzmann, J.A. (2017). DGAT1-Dependent Lipid Droplet Biogenesis Protects Mitochondrial Function during Starvation-Induced Autophagy. Dev. Cell *42*, 9–21.e5.

Nicholson, D.W., Ali, A., Thornberry, N.A., Vaillancourt, J.P., Ding, C.K., Gallant, M., Gareau, Y., Griffin, P.R., Labelle, M., and Lazebnik, Y.A. (1995). Identification and inhibition of the ICE/CED-3 protease necessary for mammalian apoptosis. Nature *376*, 37–43.

Nieto, M.A., Huang, R.Y.Y.J., Jackson, R.A.A., and Thiery, J.P.P. (2016). Emt: 2016. Cell *166*, 21–45.

Noone, A., Howlader, N., Krapcho, M., Miller, D., Brest, A., Yu, M., Ruhl, J., Tatalovich, Z., Mariotto, A., Lewis, D., et al. (2017). SEER Cancer Statistics Review, 1975-2014.

O'Shaughnessy, J., Osborne, C., Pippen, J., Yoffe, M., Patt, D., Monaghan, G., Rocha, C., Ossovskaya, V., Sherman, B., and Bradley, C. (2009). Efficacy of BSI-201, a poly (ADP-ribose) polymerase-1 (PARP1) inhibitor, in combination with gemcitabine/carboplatin (G/C) in patients with metastatic triple-negative breast cancer (TNBC): Results of a randomized phase II trial. J. Clin. Oncol. *27*, 3.

Ocaña, O.H., Córcoles, R., Fabra, A., Moreno-Bueno, G., Acloque, H., Vega, S., Barrallo-Gimeno, A., Cano, A., and Nieto, M.A. (2012). Metastatic colonization requires the repression of the epithelial-mesenchymal transition inducer Prrx1. Cancer Cell *22*, 709–724.

Ohnuma, T., Arkin, H., and Holland, J.F. (1986). Effects of cell density on drug-induced cell kill kinetics in vitro (inoculum effect). Br. J. Cancer *54*, 415–421.

Onder, T.T., Gupta, P.B., Mani, S. a, Yang, J., Lander, E.S., and Weinberg, R. a (2008). Loss of E-cadherin promotes metastasis via multiple downstream transcriptional pathways. Cancer Res. *68*, 3645–3654.

Ong, K.T., Mashek, M.T., Bu, S.Y., Greenberg, A.S., and Mashek, D.G. (2011). Adipose triglyceride lipase is a major hepatic lipase that regulates triacylglycerol turnover and fatty acid signaling and partitioning. Hepatology *53*, 116–126.

Padanad, M.S., Konstantinidou, G., Venkateswaran, N., Melegari, M., Rindhe, S., Mitsche, M., Yang, C., Batten, K., Huffman, K.E., Liu, J., et al. (2016). Fatty Acid Oxidation Mediated by Acyl-CoA Synthetase Long Chain 3 Is Required for Mutant KRAS Lung Tumorigenesis. Cell Rep. *16*, 1614–1628.

Paddison, P.J., Caudy, A.A., Bernstein, E., Hannon, G.J., and Conklin, D.S. (2002). Short hairpin RNAs (shRNAs) induce sequence-specific silencing in mammalian cells. 948–958.

Pani, G., Colavitti, R., Bedogni, B., Anzevino, R., Borrello, S., and Galeotti, T. (2000). A redox signaling mechanism for density-dependent inhibition of cell growth. J. Biol. Chem. *275*, 38891–38899.

Panzilius, E., Holstein, F., Bannier-Hélaouët, M., von Toerne, C., Koenig, A.-C., Hauck, S.M., Ganz, H.M., Friedmann Angeli, J.P., Conrad, M., and Scheel, C.H. (2018). A cell-density dependent metabolic switch sensitizes breast cancer cells to ferroptosis. BioRxiv 417949.

Park, J.H., Vithayathil, S., Kumar, S., Sung, P.L., Dobrolecki, L.E., Putluri, V., Bhat, V.B., Bhowmik, S.K., Gupta, V., Arora, K., et al. (2016). Fatty Acid Oxidation-Driven Src Links Mitochondrial Energy Reprogramming and Oncogenic Properties in Triple-Negative Breast Cancer. Cell Rep. *14*, 2154–2165.

Paton, C.M., and Ntambi, J.M. (2009). Biochemical and physiological function of stearoyl-CoA desaturase. Am. J. Physiol. Endocrinol. Metab. *297*, E28-37.

Pear, W.S., Nolan, G.P., Scott, M.L., and Baltimore, D. (1993). Production of high-titer helper-free retroviruses by transient transfection. Proc. Natl. Acad. Sci. *90*, 8392–8396.

Perou, C.M., Jeffrey, S.S., van de Rijn, M., Rees, C.A., Eisen, M.B., Ross, D.T., Pergamenschikov, A., Williams, C.F., Zhu, S.X., Lee, J.C.F., et al. (1999). Distinctive gene expression patterns in human mammary epithelial cells and breast cancers. Proc. Natl. Acad. Sci. *96*, 9212–9217.

Perou, C.M., Sorlie, T., Eisen, M.B., Rijn, M. Van De, Jeffrey, S.S., Rees, C.A., Pollack, J.R., Ross, D.T., Johnsen, H., Akslen, L.A., et al. (2000). Molecular Portraits Breast Cancer. Nature *406*, 747–752.

Persson, H.L., Yu, Z., Tirosh, O., Eaton, J.W., and Brunk, U.T. (2003). Prevention of oxidant-induced cell death by lysosomotropic iron chelators. Free Radic. Biol. Med. *34*, 1295–1305.

Piskounova, E., Agathocleous, M., Murphy, M.M., Hu, Z., Huddlestun, S.E., Zhao, Z., Leitch, A.M., Johnson, T.M., DeBerardinis, R.J., and Morrison, S.J. (2015). Oxidative

stress inhibits distant metastasis by human melanoma cells. Nature *527*, 186–191.

Porporato, P.E., Payen, V.L., Pérez-Escuredo, J., De Saedeleer, C.J., Danhier, P., Copetti, T., Dhup, S., Tardy, M., Vazeille, T., Bouzin, C., et al. (2014). A mitochondrial switch promotes tumor metastasis. Cell Rep. *8*, 754–766.

Poss, K.D., and Tonegawa, S. (1997a). Heme oxygenase 1 is required for mammalian iron reutilization. Proc. Natl. Acad. Sci. *94*, 10919–10924.

Poss, K.D., and Tonegawa, S. (1997b). Reduced stress defense in heme oxygenase 1-deficient cells. Proc. Natl. Acad. Sci. U. S. A. *94*, 10925–10930.

Prat, A., and Perou, C.M. (2011). Deconstructing the molecular portraits of breast cancer. Mol. Oncol. *5*, 5–23.

Prat, A., Parker, J.S., Karginova, O., Fan, C., Livasy, C., Herschkowitz, J.I., He, X., and Perou, C.M. (2010). Phenotypic and molecular characterization of the claudin-low intrinsic subtype of breast cancer. Breast Cancer Res. *12*, R68.

Rambold, A.S., Cohen, S., and Lippincott-Schwartz, J. (2015). Fatty acid trafficking in starved cells: Regulation by lipid droplet lipolysis, autophagy, and mitochondrial fusion dynamics. Dev. Cell *32*, 678–692.

Ran, F.A., Hsu, P.D., Wright, J., Agarwala, V., Scott, D.A., and Zhang, F. (2013). Genome engineering using the CRISPR-Cas9 system. Nat. Protoc. *8*, 2281–2308.

Raud, B., Roy, D.G., Divakaruni, A.S., Tarasenko, T.N., Franke, R., Ma, E.H., Samborska, B., Hsieh, W.Y., Wong, A.H., Stüve, P., et al. (2018). Etomoxir Actions on Regulatory and Memory T Cells Are Independent of Cpt1a-Mediated Fatty Acid Oxidation. Cell Metab. *28*, 504–515.e7.

Richards, M.A., Westcombe, A.M., Love, S.B., Littlejohns, P., and Ramirez, A.J. (1999). Influence of delay on survival in patients with breast cancer: A systematic review. Lancet *353*, 1119–1126.

Roh, J.L., Kim, E.H., Jang, H., and Shin, D. (2017). Nrf2 inhibition reverses the resistance of cisplatin-resistant head and neck cancer cells to artesunate-induced ferroptosis. Redox Biol. *11*, 254–262.

Romond, E.H., Perez, E.A., Bryant, J., Suman, V.J., Geyer, C.E., Davidson, N.E., Tan-Chiu, E., Martino, S., Paik, S., Kaufman, P.A., et al. (2005). Trastuzumab plus Adjuvant Chemotherapy for Operable HER2-Positive Breast Cancer. N. Engl. J. Med. *353*, 1673–1684.

Rottenberg, S., Jaspers, J.E., Kersbergen, A., van der Burg, E., Nygren, A.O.H., Zander, S.A.L., Derksen, P.W.B., de Bruin, M., Zevenhoven, J., Lau, A., et al. (2008). High sensitivity of BRCA1-deficient mammary tumors to the PARP inhibitor AZD2281 alone and in combination with platinum drugs. Proc. Natl. Acad. Sci. U. S. A. *105*, 17079–17084.

Roveri, A., Maiorino, M., Nisii, C., and Ursini, F. (1994). Purification and characterization of phospholipid hydroperoxide glutathione peroxidase from rat testis mitochondrial membranes. Biochim. Biophys. Acta *1208*, 211–221.

Sabatier, R., Finetti, P., Guille, A., Adelaide, J., Chaffanet, M., Viens, P., Birnbaum, D., and Bertucci, F. (2014). Claudin-low breast cancers: Clinical, pathological, molecular and prognostic characterization. Mol. Cancer *13*, 1–14.

Sapiro, J.M., Mashek, M.T., Greenberg, A.S., and Mashek, D.G. (2009). Hepatic triacylglycerol hydrolysis regulates peroxisome proliferator-activated receptor alpha activity. J. Lipid Res. *50*, 1621–1629.

Sarrió, D., Rodriguez-Pinilla, S.M., Hardisson, D., Cano, A., Moreno-Bueno, G., and Palacios, J. (2008). Epithelial-mesenchymal transition in breast cancer relates to the basal-like phenotype. Cancer Res. *68*, 989–997.

Sathyanarayan, A., Mashek, M.T., and Mashek, D.G. (2017). ATGL Promotes Autophagy/Lipophagy via SIRT1 to Control Hepatic Lipid Droplet Catabolism. Cell Rep. *19*, 1–9.

Sato, H., Tamba, M., Ishii, T., and Bannai, S. (1999). Cloning and expression of a plasma membrane cystine/glutamate exchange transporter composed of two distinct proteins. J. Biol. Chem. *274*, 11455–11458.

Scheel, C., and Weinberg, R.A. (2012). Cancer stem cells and epithelial-mesenchymal transition: concepts and molecular links. Semin. Cancer Biol. *22*, 396–403.

Schmidt, J.M., Panzilius, E., Bartsch, H.S., Irmler, M., Beckers, J., Kari, V., Linnemann, J.R., Dragoi, D., Hirschi, B., Kloos, U.J., et al. (2015). Stem-Cell-like Properties and Epithelial Plasticity Arise as Stable Traits after Transient Twist1 Activation. Cell Rep. *10*, 131–139.

Schmittgen, T.D., and Livak, K.J. (2008). Analyzing real-time PCR data by the comparative C(T) method. Nat. Protoc. *3*, 1101–1108.

Schneider, M., Wortmann, M., Mandal, P.K., Arpornchayanon, W., Jannasch, K., Alves, F., Strieth, S., Conrad, M., and Beck, H. (2010). Absence of Glutathione Peroxidase 4 Affects Tumor Angiogenesis through Increased 12/15-Lipoxygenase Activity. Neoplasia *12*, 254–263.

Schnitt, S.J. (2010). Classification and prognosis of invasive breast cancer: From morphology to molecular taxonomy. Mod. Pathol. *23*, 60–64.

Schweiger, M., Romauch, M., Schreiber, R., Grabner, G.F., Hütter, S., Kotzbeck, P., Benedikt, P., Eichmann, T.O., Yamada, S., Knittelfelder, O., et al. (2017). Pharmacological inhibition of adipose triglyceride lipase corrects high-fat diet-induced insulin resistance and hepatosteatosis in mice. Nat. Commun. *8*.

Sciacovelli, M., and Frezza, C. (2017). Metabolic reprogramming and epithelial-to-mesenchymal transition in cancer. FEBS J. *284*, 3132–3144.

Sciacovelli, M., Gonçalves, E., Johnson, T.I., Zecchini, V.R., da Costa, A.S.H., Gaude, E., Drubbel, A.V., Theobald, S.J., Abbo, S.R., Tran, M.G.B., et al. (2016). Fumarate is an epigenetic modifier that elicits epithelial-to-mesenchymal transition. Nature *537*, 544–547.

Sedlak, T.W., Saleh, M., Higginson, D.S., Paul, B.D., Juluri, K.R., and Snyder, S.H. (2009). Bilirubin and glutathione have complementary antioxidant and cytoprotective roles. Proc. Natl. Acad. Sci. *106*, 5171–5176.

Seiler, A., Schneider, M., Förster, H., Roth, S., Wirth, E.K., Culmsee, C., Plesnila, N., Kremmer, E., Rådmark, O., Wurst, W., et al. (2008). Glutathione peroxidase 4 senses and translates oxidative stress into 12/15-lipoxygenase dependent- and AIF-mediated cell death. Cell Metab. *8*, 237–248.

Sengupta, A., Lichti, U.F., Carlson, B.A., Cataisson, C., Ryscavage, A.O., Mikulec, C., Conrad, M., Fischer, S.M., Hatfield, D.L., and Yuspa, S.H. (2013). Targeted disruption of glutathione peroxidase 4 in mouse skin epithelial cells impairs postnatal hair follicle morphogenesis that is partially rescued through inhibition of COX-2. J. Invest. Dermatol. *133*, 1731–1741.

Shah, R., Shchepinov, M.S., and Pratt, D.A. (2018). Resolving the Role of Lipoxygenases in the Initiation and Execution of Ferroptosis. ACS Cent. Sci. *4*, 387–396.

Shah, S.P., Morin, R.D., Khattra, J., Prentice, L., Pugh, T., Burleigh, A., Delaney, A., Gelmon, K., Guliany, R., Senz, J., et al. (2009). Mutational evolution in a lobular breast tumour profiled at single nucleotide resolution. Nature *461*, 809–813.

Shah, S.P., Roth, A., Goya, R., Oloumi, A., Ha, G., Zhao, Y., Turashvili, G., Ding, J., Tse, K., Haffari, G., et al. (2012). The clonal and mutational evolution spectrum of primary triple-negative breast cancers. Nature *486*, 395–399.

Shamir, E.R., Pappalardo, E., Jorgens, D.M., Coutinho, K., Tsai, W., Aziz, K., Auer, M., Tran, P.T., Bader, J.S., and Ewald, A.J. (2014). Twist1-induced dissemination preserves epithelial identity and requires E-cadherin. *204*, 839–856.

Shargh, S.A., Sakizli, M., Khalaj, V., Movafagh, A., Yazdi, H., Hagigatjou, E., Sayad, A., Mansouri, N., Mortazavi-Tabatabaei, S.A., and Khorram Khorshid, H.R. (2014). Downregulation of E-cadherin expression in breast cancer by promoter hypermethylation and its relation with progression and prognosis of tumor. Med. Oncol. *31*, 1–6.

Shaul, Y.D., Freinkman, E., Comb, W.C., Cantor, J.R., Tam, W.L., Thiru, P., Kim, D., Kanarek, N., Pacold, M.E., Chen, W.W., et al. (2014). Dihydropyrimidine Accumulation Is Required for the Epithelial-Mesenchymal Transition. Cell *158*, 1094–1109.

Shimada, K., Hayano, M., Pagano, N.C., and Stockwell, B.R. (2016a). Cell-Line Selectivity Improves the Predictive Power of Pharmacogenomic Analyses and Helps Identify NADPH as Biomarker for Ferroptosis Sensitivity. Cell Chem. Biol. *23*, 225–235.

Shimada, K., Skouta, R., Kaplan, A., Yang, W.S., Hayano, M., Dixon, S.J., Brown, L.M., Valenzuela, C.A., Wolpaw, A.J., and Stockwell, B.R. (2016b). Global survey of cell death mechanisms reveals metabolic regulation of ferroptosis. Nat. Chem. Biol. *12*, 497–503.

Shindou, H., and Shimizu, T. (2009). Acyl-CoA:lysophospholipid acyltransferases. J. Biol. Chem. *284*, 1–5.

Shirakihara, T., Saitoh, M., and Miyazono, K. (2007). Differential regulation of epithelial and mesenchymal markers by deltaEF1 proteins in epithelial mesenchymal transition induced by TGF-beta. Mol. Biol. Cell *18*, 3533–3544.

Singh, R., Kaushik, S., Wang, Y., Xiang, Y., Novak, I., Komatsu, M., Tanaka, K., Cuervo, A.M., and Czaja, M.J. (2009). Autophagy regulates lipid metabolism. Nature *458*, 1131–1135.

Skouta, R., Dixon, S.J., Wang, J., Dunn, D.E., Orman, M., Shimada, K., Rosenberg, P.A., Lo, D.C., Weinberg, J.M., Linkermann, A., et al. (2014). Ferrostatins inhibit oxidative lipid damage and cell death in diverse disease models. J. Am. Chem. Soc. *136*, 4551–4556.

Slamon, D.J., Leyland-Jones, B., Shak, S., Fuchs, H., Paton, V., Bajamonde, A., Fleming, T., Eiermann, W., Wolter, J., Pegram, M., et al. (2001). Use of chemotherapy plus a monoclonal antibody against HER2 for metastatic breast cancer that overexpresses HER2. N. Engl. J. Med. *344*, 783–792.

SLEE, E.A., ZHU, H., CHOW, S.C., MacFARLANE, M., NICHOLSON, D.W., and COHEN, G.M. (1996). Benzyloxycarbonyl-Val-Ala-Asp (OMe) fluoromethylketone (Z-VAD.FMK) inhibits apoptosis by blocking the processing of CPP32. Biochem. J. *315*, 21–24.

Smirnova, E., Goldberg, E.B., Makarova, K.S., Lin, L., Brown, W.J., and Jackson, C.L. (2006). ATGL has a key role in lipid droplet/adiposome degradation in mammalian cells. EMBO Rep. *7*, 106–113.

Sørlie, T., Perou, C.M., Tibshirani, R., Aas, T., Geisler, S., Johnsen, H., Hastie, T., Eisen, M.B., van de Rijn, M., Jeffrey, S.S., et al. (2001). Gene expression patterns of breast carcinomas distinguish tumor subclasses with clinical implications. Proc. Natl. Acad. Sci.

U. S. A. *98*, 10869–10874.

Sørlie, T., Tibshirani, R., Parker, J., Hastie, T., Marron, J.S., Nobel, A., Deng, S., Johnsen, H., Pesich, R., Geisler, S., et al. (2003). Repeated observation of breast tumor subtypes in independent gene expression data sets. Proc. Natl. Acad. Sci. *100*, 8418–8423.

Soupene, E., and Kuypers, F.A. (2008). Mammalian long-chain acyl-CoA synthetases. Exp. Biol. Med. (Maywood). *233*, 507–521.

Sparano, J.A., Gray, R.J., Makower, D.F., Pritchard, K.I., Albain, K.S., Hayes, D.F., Geyer, C.E., Dees, E.C., Perez, E.A., Olson, J.A., et al. (2015). Prospective Validation of a 21-Gene Expression Assay in Breast Cancer. N. Engl. J. Med. *373*, 2005–2014.

Steck, P.A., Pershouse, M.A., Jasser, S.A., Yung, W.K., Lin, H., Ligon, A.H., Langford, L.A., Baumgard, M.L., Hattier, T., Davis, T., et al. (1997). Identification of a candidate tumour suppressor gene, MMAC1, at chromosome 10q23.3 that is mutated in multiple advanced cancers. Nat. Genet. *15*, 356–362.

Stingl, J., Emerman, J.T., and Eaves, C.J. (2005). Enzymatic dissociation and culture of normal human mammary tissue to detect progenitor activity. Methods Mol. Biol. *290*, 249–263.

Stockwell, B.R., Friedmann Angeli, J.P., Bayir, H., Bush, A.I., Conrad, M., Dixon, S.J., Fulda, S., Gascón, S., Hatzios, S.K., Kagan, V.E., et al. (2017). Ferroptosis: A Regulated Cell Death Nexus Linking Metabolism, Redox Biology, and Disease. Cell *171*, 273–285.

Stoker, M.G., and Rubin, H. (1967). Density dependent inhibition of cell growth in culture. Nature *215*, 171–172.

Sun, X., Ou, Z., Chen, R., Niu, X., Chen, D., Kang, R., and Tang, D. (2016). Activation of the p62-Keap1-NRF2 pathway protects against ferroptosis in hepatocellular carcinoma cells. Hepatology *63*, 173–184.

Suttner, D.M., and Dennery, P.A. (1999). Reversal of HO-1 related cytoprotection with increased expression is due to reactive iron. FASEB J. *13*, 1800–1809.

Tacar, O., Sriamornsak, P., and Dass, C.R. (2013). Doxorubicin: an update on anticancer molecular action, toxicity and novel drug delivery systems. J. Pharm. Pharmacol. *65*, 157–170.

Takemura, Y., Kobayashi, H., Miyachi, H., Hayashi, K., Sekiguchi, S., and Ohnuma, T. (1991). The influence of tumor cell density on cellular accumulation of doxorubicin or cisplatin in vitro. Cancer Chemother. Pharmacol. *27*, 417–422.

Taube, J.H., Herschkowitz, J.I., Komurov, K., Zhou, A.Y., Gupta, S., Yang, J., Hartwell, K., Onder, T.T., Gupta, P.B., Evans, K.W., et al. (2010). Core epithelial-to-mesenchymal transition interactome gene-expression signature is associated with claudin-low and metaplastic breast cancer subtypes. Proc. Natl. Acad. Sci. *107*, 19132–19132.

Tevaarwerk, A.J., Gray, R.J., Schneider, B.P., Smith, M. Lou, Wagner, L.I., Fetting, J.H., Davidson, N., Goldstein, L.J., Miller, K.D., and Sparano, J.A. (2013). Survival in patients with metastatic recurrent breast cancer after adjuvant chemotherapy: Little evidence of improvement over the past 30 years. Cancer *119*, 1140–1148.

Tewari, M., Quan, L.T., O'Rourke, K., Desnoyers, S., Zeng, Z., Beidler, D.R., Poirier, G.G., Salvesen, G.S., and Dixit, V.M. (1995). Yama/CPP32 beta, a mammalian homolog of CED-3, is a CrmA-inhibitable protease that cleaves the death substrate poly(ADP-ribose) polymerase. Cell *81*, 801–809.

Theveneau, E., Marchant, L., Kuriyama, S., Gull, M., Moepps, B., Parsons, M., and Mayor,

R. (2010). Collective Chemotaxis Requires Contact-Dependent Cell Polarity. Dev. Cell *19*, 39–53.

Thiery, J.P., Acloque, H., Huang, R.Y.J., and Nieto, M.A. (2009). Epithelial-mesenchymal transitions in development and disease. Cell *139*, 871–890.

Tietze, F. (1969). Enzymic method for quantitative determination of nanogram amounts of total and oxidized glutathione: applications to mammalian blood and other tissues. Anal. Biochem. *27*, 502–522.

Timmerman, L.A., Holton, T., Yuneva, M., Louie, R.J., Padró, M., Daemen, A., Hu, M., Chan, D.A., Ethier, S.P., van'tVeer, L.J., et al. (2013). Glutamine Sensitivity Analysis Identifies the xCT Antiporter as a Common Triple-Negative Breast Tumor Therapeutic Target. Cancer Cell *24*, 450–465.

Torii, S., Shintoku, R., Kubota, C., Yaegashi, M., Torii, R., Sasaki, M., Suzuki, T., Mori, M., Yoshimoto, Y., Takeuchi, T., et al. (2016). An essential role for functional lysosomes in ferroptosis of cancer cells. Biochem. J. *473*, 769–777.

Torres, L., Ribeiro, F.R., Pandis, N., Andersen, J.A., Heim, S., and Teixeira, M.R. (2007). Intratumor genomic heterogeneity in breast cancer with clonal divergence between primary carcinomas and lymph node metastases. Breast Cancer Res. Treat. *102*, 143–155.

Trelstad, R.L., Hay, E.D., and Revel, J.P. (1967). Cell contact during early morphogenesis in the chick embryo. Dev. Biol. *16*, 78–106.

Tsai, J.H., Donaher, J.L., Murphy, D.A., Chau, S., and Yang, J. (2012). Spatiotemporal regulation of epithelial-mesenchymal transition is essential for squamous cell carcinoma metastasis. Cancer Cell *22*, 725–736.

Tuo, Q.Z., Lei, P., Jackman, K.A., Li, X.L., Xiong, H., Li, X.L., Liuyang, Z.Y., Roisman, L., Zhang, S.T., Ayton, S., et al. (2017). Tau-mediated iron export prevents ferroptotic damage after ischemic stroke. Mol. Psychiatry *22*, 1520–1530.

Tymianski, M., Wallace, M.C., Spigelman, I., Uno, M., Carlen, P.L., Tator, C.H., and Charlton, M.P. (1993). Cell-permeant Ca2+ chelators reduce early excitotoxic and ischemic neuronal injury in vitro and in vivo. Neuron *11*, 221–235.

Ueda, N., and Shah, S. V (1992). Role of Intracellular Calcium in Hydrogen Peroxide-Induced Renal Tubular Cell Injury. Am. J. Physiol. *263*, F214–F221.

Ueta, T., Inoue, T., Furukawa, T., Tamaki, Y., Nakagawa, Y., Imai, H., and Yanagi, Y. (2012). Glutathione peroxidase 4 is required for maturation of photoreceptor cells. J. Biol. Chem. *287*, 7675–7682.

Ursini, F., Maiorino, M., Valente, M., Ferri, L., and Gregolin, C. (1982). Purification from pig liver of a protein which protects liposomes and biomembranes from peroxidative degradation and exhibits glutathione peroxidase activity on phosphatidylcholine hydroperoxides. Biochim. Biophys. Acta *710*, 197–211.

Ursini, F., Maiorino, M., and Gregolin, C. (1985). The selenoenzyme phospholipid hydroperoxide glutathione peroxidase. Biochim. Biophys. Acta *839*, 62–70.

Ursini, F., Heim, S., Kiess, M., Maiorino, M., Roveri, A., Wissing, J., and Flohé, L. (1999). Dual function of the selenoprotein PHGPx during sperm maturation. Science *285*, 1393–1396.

Do Van, B., Gouel, F., Jonneaux, A., Timmerman, K., Gelé, P., Pétrault, M., Bastide, M., Laloux, C., Moreau, C., Bordet, R., et al. (2016). Ferroptosis, a newly characterized form

of cell death in Parkinson's disease that is regulated by PKC. Neurobiol. Dis. *94*, 169–178.

Vandewalle, C., Comijn, J., De Craene, B., Vermassen, P., Bruyneel, E., Andersen, H., Tulchinsky, E., Van Roy, F., and Berx, G. (2005). SIP1/ZEB2 induces EMT by repressing genes of different epithelial cell-cell junctions. Nucleic Acids Res. *33*, 6566–6578.

Vega, S., Morales, A. V., Ocaña, O.H., Valdés, F., Fabregat, I., and Nieto, M.A. (2004). Snail blocks the cell cycle and confers resistance to cell death. Genes Dev. *18*, 1131–1143.

van de Vijver, M.J., He, Y.D., van't Veer, L.J., Dai, H., Hart, A.A.M., Voskuil, D.W., Schreiber, G.J., Peterse, J.L., Roberts, C., Marton, M.J., et al. (2002). A gene-expression signature as a predictor of survival in breast cancer. N. Engl. J. Med. *347*, 1999–2009.

Visvader, J.E. (2009). Keeping abreast of the mammary epithelial hierarchy and breast tumorigenesis. Genes Dev. *23*, 2563–2577.

Viswanathan, V.S., Ryan, M.J., Dhruv, H.D., Gill, S., Eichhoff, O.M., Seashore-Ludlow, B., Kaffenberger, S.D., Eaton, J.K., Shimada, K., Aguirre, A.J., et al. (2017). Dependency of a therapy-resistant state of cancer cells on a lipid peroxidase pathway. Nature *547*, 453–457.

Wahba, A., El-Hadaad, H., Ahmed Wahba, H., and Ahmed El-Hadaad, H. (2015). Current approaches in treatment of triple-negative breast cancer. Cancer Biol Med | v. June | PMC4493381 Citations Cancer Biol Med *12*, 106–116.

Walther, T.C., and Farese, R. V (2012). Lipid droplets and cellular lipid metabolism. Annu. Rev. Biochem. *81*, 687–714.

Wan, X., and Helman, L.J. (2003). Levels of PTEN protein modulate Akt phosphorylation on serine 473, but not on threonine 308, in IGF-II-overexpressing rhabdomyosarcomas cells. Oncogene *22*, 8205–8211.

Wang, H., Bell, M., Sreenevasan, U., Hu, H., Liu, J., Dalen, K., Londos, C., Yamaguchi, T., Rizzo, M.A., Coleman, R., et al. (2011). Unique regulation of adipose triglyceride lipase (ATGL) by perilipin 5, a lipid droplet-associated protein. J. Biol. Chem. *286*, 15707–15715.

Wang, S.-J., Li, D., Ou, Y., Jiang, L., Chen, Y., Zhao, Y., and Gu, W. (2016). Acetylation Is Crucial for p53-Mediated Ferroptosis and Tumor Suppression. Cell Rep. *17*, 366–373.

Wang, T., Wei, J.J., Sabatini, D.M., and Lander, E.S. (2014). Genetic screens in human cells using the CRISPR-Cas9 system. Science *343*, 80–84.

Warner, G.J., Berry, M.J., Moustafa, M.E., Carlson, B.A., Hatfield, D.L., and Faust, J.R. (2000). Inhibition of selenoprotein synthesis by selenocysteine tRNA[Ser]Sec lacking isopentenyladenosine. J. Biol. Chem. *275*, 28110–28119.

Weiss, R.H., and Estabrook, R.W. (1986). The mechanism of cumene hydroperoxide-dependent lipid peroxidation: the function of cytochrome P-450. Arch. Biochem. Biophys. *251*, 348–360.

Wendt, M.K., Taylor, M.A., Schiemann, B.J., and Schiemann, W.P. (2011). Down-regulation of epithelial cadherin is required to initiate metastatic outgrowth of breast cancer. Mol. Biol. Cell *22*, 2423–2435.

Wirth, E.K., Conrad, M., Winterer, J., Wozny, C., Carlson, B.A., Roth, S., Schmitz, D., Bornkamm, G.W., Coppola, V., Tessarollo, L., et al. (2010). Neuronal selenoprotein expression is required for interneuron development and prevents seizures and neurodegeneration. FASEB J. *24*, 844–852.

Wirth, E.K., Bharathi, B.S., Hatfield, D., Conrad, M., Brielmeier, M., and Schweizer, U.

(2014). Cerebellar hypoplasia in mice lacking selenoprotein biosynthesis in neurons. Biol. Trace Elem. Res. *158*, 203–210.

Wiśniewski, J.R., Zougman, A., Nagaraj, N., and Mann, M. (2009). Universal sample preparation method for proteome analysis. Nat. Methods *6*, 359–362.

Wolf, B.B., Schuler, M., Echeverri, F., and Green, D.R. (1999). Caspase-3 is the primary activator of apoptotic DNA fragmentation via DNA fragmentation factor-45/inhibitor of caspase-activated DNase inactivation. J. Biol. Chem. *274*, 30651–30656.

Wong, A.S.T., and Gumbiner, B.M. (2003). Adhesion-independent mechanism for suppression of tumor cell invasion by E-cadherin. J. Cell Biol. *161*, 1191–1203.

Wong, H., Lau, S., Yau, T., Cheung, P., and Epstein, R.J. (2010). Presence of an in situ component is associated with reduced biological aggressiveness of size-matched invasive breast cancer. Br. J. Cancer *102*, 1391–1396.

Wright, H.J., Hou, J., Xu, B., Cortez, M., Potma, E.O., Tromberg, B.J., and Razorenova, O. V. (2017). CDCP1 drives triple-negative breast cancer metastasis through reduction of lipid-droplet abundance and stimulation of fatty acid oxidation. Proc. Natl. Acad. Sci. *114*, E6556–E6565.

Xie, M., and Roy, R. (2015). AMP-Activated Kinase Regulates Lipid Droplet Localization and Stability of Adipose Triglyceride Lipase in C. elegans Dauer Larvae. PLoS One *10*, e0130480.

Yagoda, N., Von Rechenberg, M., Zaganjor, E., Bauer, A.J., Yang, W.S., Fridman, D.J., Wolpaw, A.J., Smukste, I., Peltier, J.M., Boniface, J.J., et al. (2007). RAS-RAF-MEK-dependent oxidative cell death involving voltage-dependent anion channels. Nature *447*, 864–868.

Yang, J., and Weinberg, R.A. (2008). Epithelial-mesenchymal transition: at the crossroads of development and tumor metastasis. Dev. Cell *14*, 818–829.

Yang, W.S., and Stockwell, B.R. (2008). Synthetic Lethal Screening Identifies Compounds Activating Iron-Dependent, Nonapoptotic Cell Death in Oncogenic-RAS-Harboring Cancer Cells. Chem. Biol. *15*, 234–245.

Yang, W.S., and Stockwell, B.R. (2016). Ferroptosis: Death by Lipid Peroxidation. Trends Cell Biol. *26*, 165–176.

Yang, J., Mani, S.A., Donaher, J.L., Ramaswamy, S., Itzykson, R.A., Come, C., Savagner, P., Gitelman, I., Richardson, A., Weinberg, R.A., et al. (2004). Twist , a Master Regulator of Morphogenesis , Plays an Essential Role in Tumor Metastasis Ben Gurion University of the Negev. Cell *117*, 927–939.

Yang, L., Venneti, S., and Nagrath, D. (2017). Glutaminolysis: A Hallmark of Cancer Metabolism. Annu. Rev. Biomed. Eng. *19*, 163–194.

Yang, W.S., SriRamaratnam, R., Welsch, M.E., Shimada, K., Skouta, R., Viswanathan, V.S., Cheah, J.H., Clemons, P.A., Shamji, A.F., Clish, C.B., et al. (2014). Regulation of ferroptotic cancer cell death by GPX4. Cell *156*, 317–331.

Yang, W.S., Kim, K.J., Gaschler, M.M., Patel, M., Shchepinov, M.S., and Stockwell, B.R. (2016). Peroxidation of polyunsaturated fatty acids by lipoxygenases drives ferroptosis. Proc. Natl. Acad. Sci. *113*, E4966–E4975.

Yano, H., Mazaki, Y., Kurokawa, K., Hanks, S.K., Matsuda, M., and Sabe, H. (2004). Roles played by a subset of integrin signaling molecules in cadherin-based cell-cell adhesion. J. Cell Biol. *166*, 283–295.

Yant, L.J., Ran, Q., Rao, L., Van Remmen, H., Shibatani, T., Belter, J.G., Motta, L., Richardson, A., and Prolla, T.A. (2003). The selenoprotein GPX4 is essential for mouse development and protects from radiation and oxidative damage insults. Free Radic. Biol. Med. *34*, 496–502.

Yoo, M.-H., Gu, X., Xu, X.-M., Kim, J.-Y., Carlson, B.A., Patterson, A.D., Cai, H., Gladyshev, V.N., and Hatfield, D.L. (2010). Delineating the Role of Glutathione Peroxidase 4 in Protecting Cells Against Lipid Hydroperoxide Damage and in Alzheimer's Disease. Antioxid. Redox Signal. *12*, 819–827.

Yoo, S.E., Chen, L., Na, R., Liu, Y., Rios, C., Van Remmen, H., Richardson, A., and Ran, Q. (2012). Gpx4 ablation in adult mice results in a lethal phenotype accompanied by neuronal loss in brain. Free Radic. Biol. Med. *52*, 1820–1827.

Yu, J.S.L., and Cui, W. (2016). Proliferation, survival and metabolism: the role of PI3K/AKT/mTOR signalling in pluripotency and cell fate determination. Development *143*, 3050–3060.

Yu, Z., Persson, H.L., Eaton, J.W., and Brunk, U.T. (2003). Intralysosomal iron: a major determinant of oxidant-induced cell death. Free Radic. Biol. Med. *34*, 1243–1252.

Zardavas, D., Irrthum, A., Swanton, C., and Piccart, M. (2015). Clinical management of breast cancer heterogeneity. Nat. Rev. Clin. Oncol. *12*, 381–394.

Zeichner, S.B., Terawaki, H., and Gogineni, K. (2016). A review of systemic treatment in metastatic triple-negative breast cancer. Breast Cancer Basic Clin. Res. *10*, 25–36.

Zhang, P., Wei, Y., Wang, L. i., Debeb, B.G., Yuan, Y., Zhang, J., Yuan, J., Wang, M., Chen, D., Sun, Y., et al. (2014). ATM-mediated stabilization of ZEB1 promotes DNA damage response and radioresistance through CHK1. Nat. Cell Biol. *16*, 864–875.

Zheng, L., Cardaci, S., Jerby, L., Mackenzie, E.D., Sciacovelli, M., Johnson, T.I., Gaude, E., King, A., Leach, J.D.G., Edrada-Ebel, R., et al. (2015a). Fumarate induces redox-dependent senescence by modifying glutathione metabolism. Nat. Commun. *6*, 1–12.

Zheng, X., Carstens, J.L., Kim, J., Scheible, M., Kaye, J., Sugimoto, H., Wu, C.-C., LeBleu, V.S., and Kalluri, R. (2015b). Epithelial-to-mesenchymal transition is dispensable for metastasis but induces chemoresistance in pancreatic cancer. Nature *527*, 525–530.

Zimmermann, R., Strauss, J.G., Haemmerle, G., Schoiswohl, G., Birner-Gruenberger, R., Riederer, M., Lass, A., Neuberger, G., Eisenhaber, F., Hermetter, A., et al. (2004). Fat mobilization in adipose tissue is promoted by adipose triglyceride lipase. Science *306*, 1383–1386.

7 Appendix

Proteins that were at least 1.5-fold down- or upregulated both by low cell density and by 5h RSL3 treatment in both HMLE and HMLE-Twist1 cells ($p<0.05$, unpaired T-test with Welch's correction) in the proteomics are listed in the following, (related to Figure 19).

Table 10: Fold changes of downregulated proteins in low cell density and upon 5h RSL3 treatment in both HMLE and HMLE-Twist1 cells

Uniprot Accession	GeneID	low vs. high density	RSL3 vs. Ctrl (med density)
Q15843	NEDD8	16.27	15.42
Q9Y4H2	IRS2	6.10	3.96
Q96CX6	LRRC58	3.17	5.66
Q9Y6K5	OAS3	3.01	4.90
Q9UKK3	PARP4	2.72	2.14
Q96R06	SPAG5	2.50	2.05
O00767	SCD	2.47	1.72
P23469	PTPRE	1.96	1.76
P62699	YPEL5	1.88	1.75
O15020	SPTBN2	1.78	1.92
P53384	NUBP1	1.74	2.26
Q9UBT7	CTNNAL1	1.59	1.72
Q16832;Q53FD0	DDR2	1.59	1.65
Q96JH7	VCPIP1	1.57	1.78
Q6PJG2	ELMSAN1	1.57	2.09
P62241	RPS8	1.57	1.51

Table 11: Fold changes of upregulated proteins in low cell density and upon 5h RSL3 treatment in both HMLE and HMLE-Twist1 cells

Uniprot Accession	GeneID	low vs. high density	RSL3 vs. Ctrl (med density)
Q99969	RARRES2	316.58	154.78
P02679	FGG	254.12	23.05
P02649	APOE	56.88	7.75
Q8NDH3	NPEPL1	47.35	18.74
Q8WTS1	ABHD5	38.77	4.36
P51888	PRELP	37.95	32.27
P13796	LCP1	33.39	6.03
Q14894	CRYM	29.93	19.47
Q8IW45	NAXD	29.56	12.88
P01185;P01178	AVP	29.25	23.34
Q6NW29	RWDD4	28.97	9.58
P51649	ALDH5A1	25.26	10.33
Q9BUP3	HTATIP2	24.61	11.52
Q96DC8	ECHDC3	22.00	13.25
Q9HCE0	EPG5	21.16	8.08
I1YAP6	TRIM77	19.49	8.78
Q8TDX9	PKD1L1	17.29	5.16
P09936	UCHL1	16.56	7.25

Uniprot Accession	GeneID	low vs. high density	RSL3 vs. Ctrl (med density)
Q9UQ10	DHDH	15.71	7.65
P09471	GNAO1	15.61	6.41
Q9HBL8	NMRAL1	15.58	5.25
Q8NBE8	KLHL23	15.32	8.51
A6NC98	CCDC88B	13.79	5.67
Q96E35	ZMYND19	13.04	6.61
Q7RTP6	MICAL3	12.41	4.44
P02774	GC	11.93	7.19
O94915	FRYL	11.68	4.47
P01024	C3	11.65	9.15
Q8TEB9	RHBDD1	11.33	6.27
Q9P258	RCC2	11.26	5.58
Q9NZR1	TMOD2	11.24	4.08
Q7Z4S6	KIF21A	11.23	6.53
F8WCM5	INS-IGF2	10.38	4.52
P69905	HBA1	9.82	3.99
Q5SZQ8	CELF3	9.57	8.36
P08247	SYP	8.92	4.95
Q9ULU8;Q86UW7	CADPS	8.65	5.99
Q6Q4G3	LVRN	8.60	3.28
Q9Y3E0	GOLT1B	8.42	4.74
P21266	GSTM3	8.06	3.19
Q9H4G4	GLIPR2	7.52	7.98
P02788	LTF	6.64	3.71
P54652	HSPA2	6.63	4.78
P13929	ENO3	6.40	3.67
P02675	FGB	6.12	3.70
Q9UGM3	DMBT1	6.11	3.30
Q96L91	EP400	6.09	3.92
P28161	GSTM2	6.09	3.23
P08910	ABHD2	5.90	3.28
Q8N0Y7	PGAM4	5.84	4.41
Q8WUH6	TMEM263	5.68	5.91
Q9H1E3	NUCKS1	5.53	4.23
Q13003	GRIK3	5.44	2.92
O95834	EML2	5.30	2.84
Q9UHG2	PCSK1N	5.22	3.90
Q9H4F8	SMOC1	4.94	3.15
Q96AD5	PNPLA2	4.74	3.75
O43426	SYNJ1	4.63	2.22
Q16527	CSRP2	4.26	2.16
P09104	ENO2	4.22	2.51
P51608	MECP2	4.20	2.24
Q9P2J5	LARS	3.88	2.83
P06727	APOA4	3.84	2.29
Q8IZW8	TNS4	3.80	2.29
P48506	GCLC	3.75	2.35
Q9Y3E1	HDGFRP3	3.72	2.87
Q02252	ALDH6A1	3.64	3.52
Q96BY9	SARAF	3.64	2.73
P09601	HMOX1	3.58	2.90
Q5T0D9	TPRG1L	3.32	1.99
P12277;P06732	CKB	3.32	2.14
Q9Y5K8	ATP6V1D	3.28	2.33

Uniprot Accession	GeneID	low vs. high density	RSL3 vs. Ctrl (med density)
P13521	SCG2	3.16	2.50
P20336	RAB3A	3.06	2.64
P55327	TPD52	3.00	1.88
Q8IVF2	AHNAK2	2.98	3.30
Q8N8N7	PTGR2	2.98	3.35
Q53EL6	PDCD4	2.97	2.38
Q9UI12	ATP6V1H	2.96	2.43
Q96DG6	CMBL	2.95	1.65
Q6UWR7	ENPP6	2.95	1.77
Q99536	VAT1	2.90	2.39
Q01995	TAGLN	2.72	2.07
Q02880	TOP2B	2.70	1.57
A6ZKI3	FAM127A	2.68	2.03
Q96G21	IMP4	2.64	1.72
P01189	POMC	2.58	2.36
P63027	VAMP2	2.56	2.29
P36543;Q96A05	ATP6V1E1	2.52	1.67
Q96HU1	SGSM3	2.50	2.35
Q9NRF8	CTPS2	2.46	1.99
P21281;P15313	ATP6V1B2	2.40	1.75
Q9NP66	HMG20A	2.37	1.91
P36871	PGM1	2.35	1.87
P61020	RAB5B	2.27	1.98
P32320	CDA	2.26	2.65
Q9BYP7	WNK3	2.17	2.30
P38606	ATP6V1A	2.17	1.74
P23526	AHCY	2.15	1.53
Q99500	S1PR3	2.10	1.59
O94903	PROSC	2.08	1.62
P52926	HMGA2	2.07	1.60
Q8IWA0	WDR75	2.07	1.93
Q8N9N2	ASCC1	2.06	1.69
Q16537	PPP2R5E	1.96	1.92
Q15907	RAB11B	1.92	1.53
Q15061	WDR43	1.88	1.94
Q9H8H0	NOL11	1.83	1.76
O43818	RRP9	1.73	1.69
O75367	H2AFY	1.72	2.33
Q86SQ9	DHDDS	1.72	1.50
Q9UNP9	PPIE	1.70	1.80
Q8N128	FAM177A1	1.68	1.58
O00566	MPHOSPH10	1.67	1.57
P62805	HIST1H4A	1.58	2.42
Q9P031	CCDC59	1.57	2.05
O14974	PPP1R12A	1.57	1.54
P07910	HNRNPC	1.52	1.66
O15091	KIAA0391	1.50	1.57

List of figures

List of tables

Acknowledgements

The time as a PhD Student was demanding and challenging, but at the same time exciting and instructive. During this time, I gained many new experiences and important skills that have tremendously broadened my perspective in both my work and personal life. However, this thesis would not have been possible without the help and support of several people that I want to thank in the following paragraph.

In the beginning, I want to thank Prof. Dr. Magdalena Götz, head of the Institute of Stem Cell Research, for enabling my thesis in her institute and for being my supervisor at the university. Thank you for your great scientific support and valuable input not only during thesis committee meetings and during progress reports.

Foremost, I wish to thank my supervisor Dr. Christina Scheel for giving me the opportunity to complete my thesis in her mammary stem cells group. Thank you for guiding me through my PhD with numerous ideas, helpful advice and constructive discussions. I am very thankful for all the things that you taught me, for your constant encouragement and for sharing your passion of science with me.

I want to extent my gratitude to all other and former members of the Scheel Group including Dr. Diana Dragoi, Dr. Jelena Krendl, Dr. Johanna Bartsch, Dr. Benjamin Hirschi, Dr. Anja Krattenmacher, Dr. Alecia-Jane Twigger, Dr. Stefania Petricca, Dr. Massimo Saini, Uwe Kloos, Artur Schmidt, Lisa Meixner, Laura Eichelberger, Hilary Ganz, Aristeidis Papargyriou, Felix Holstein, Marie Bannier-Hélaouët and Nina Frey. I am really thankful for the great working atmosphere in the Scheel lab which made daily work enjoyable and fun, for all the scientific and non-scientific advice, help and discussions. I am especially grateful to my master student Felix Holstein and my intern Marie Bannier-Hélaouët for their contributions to this thesis. It was a pleasure working with you and a great experience for me. Special thanks goes to Lisa Meixner for her help with primary mammary epithelial cell culture, with the FACS and with confocal microscopy, to Dr. Anja Krattenmacher and Dr. Massimo Saini for their valuable advices for cloning and to Hilary Ganz for providing cell lines used in this thesis. Moreover, I want to thank Dr. Johanna Bartsch and Laura Eichelberger for being valuable office and bench neighbors in the past and present. Additionally, I

want to thank Karen Biniossek, Elsa Melo and Nina Fuchs for their great help in all organizational matters.

I also want to acknowledge all the other members of the Institute of Stem Cell Research that supported me throughout the course of this thesis. Especially, I owe gratitude to Dr. Stefan Stricker and Christopher Breunig for sharing experimental expertise and reagents that helped a lot to establish CRISPR/Cas9 in our lab.

I would like to thank my thesis committee members Prof. Dr Magdalena Götz, Dr. Christina Scheel and Prof. Dr. Andreas Jung for their valuable input and advice and the fruitful discussions about my project.

Many thanks goes to my collaborators who enabled me to gain a deeper understanding of my project. Thanks to Dr. Stefanie Hauck, Dr. Christine von Törne and Dr. Ann-Christine König who conducted the proteomic study and analyzed the data. I would like to thank Dr. Marcus Conrad and his research group for sharing expertise in the field of ferroptosis and for all the great discussions, we had. Special thanks goes to Dr. José Pedro Friedman Angeli for his great suggestions and for the measurement of thiols and total GSH content and to Dr. Irina Ingold for the GPX4-acitivity measurement.

I want to thank the Boehringer Ingelheim Fonds who supported me with a PhD Fellowship. Many thanks for the outstanding scientific as well personal support in particular to Dr. Claudia Walther, Dr. Anja Petersen and Sandra Schedler.

I want to extent my gratitude to all my friends inside and outside Munich who constantly supported and motivated me during the long way as a PhD student.

I am thankful to Michael Wöllhaf for his understanding support, his help to maintain my positive attitude and for being by my side.

Finally yet importantly I want to deeply thank my family and in particular my mum. Thank you for your love, your constant support, your belief in me ever since and all the invaluable advice.

Eidesstattliche Versicherung

Panzilius, Elena
Name, Vorname

Ich erkläre hiermit an Eides statt,
dass ich die vorliegende Dissertation mit dem Thema

Dissection and identification of cellular contexts that determine sensitivity to ferroptosis in human mammary epithelial cells and breast cancer

selbständig verfasst, mich außer der angegebenen keiner weiteren Hilfsmittel bedient und alle Erkenntnisse, die aus dem Schrifttum ganz oder annähernd übernommen sind, als solche kenntlich gemacht und nach ihrer Herkunft unter Bezeichnung der Fundstelle einzeln nachgewiesen habe.

Ich erkläre des Weiteren, dass die hier vorgelegte Dissertation nicht in gleicher oder in ähnlicher Form bei einer anderen Stelle zur Erlangung eines akademischen Grades eingereicht wurde.

München, den 14.07.2020	Elena Panzilius
Ort, Datum	Unterschrift Doktorand